A.2　不均質性を持つ特性化震源モデルによる強震動評価（付録資料）

A.2.1　Goodness of fit between recorded and simulated response spectra

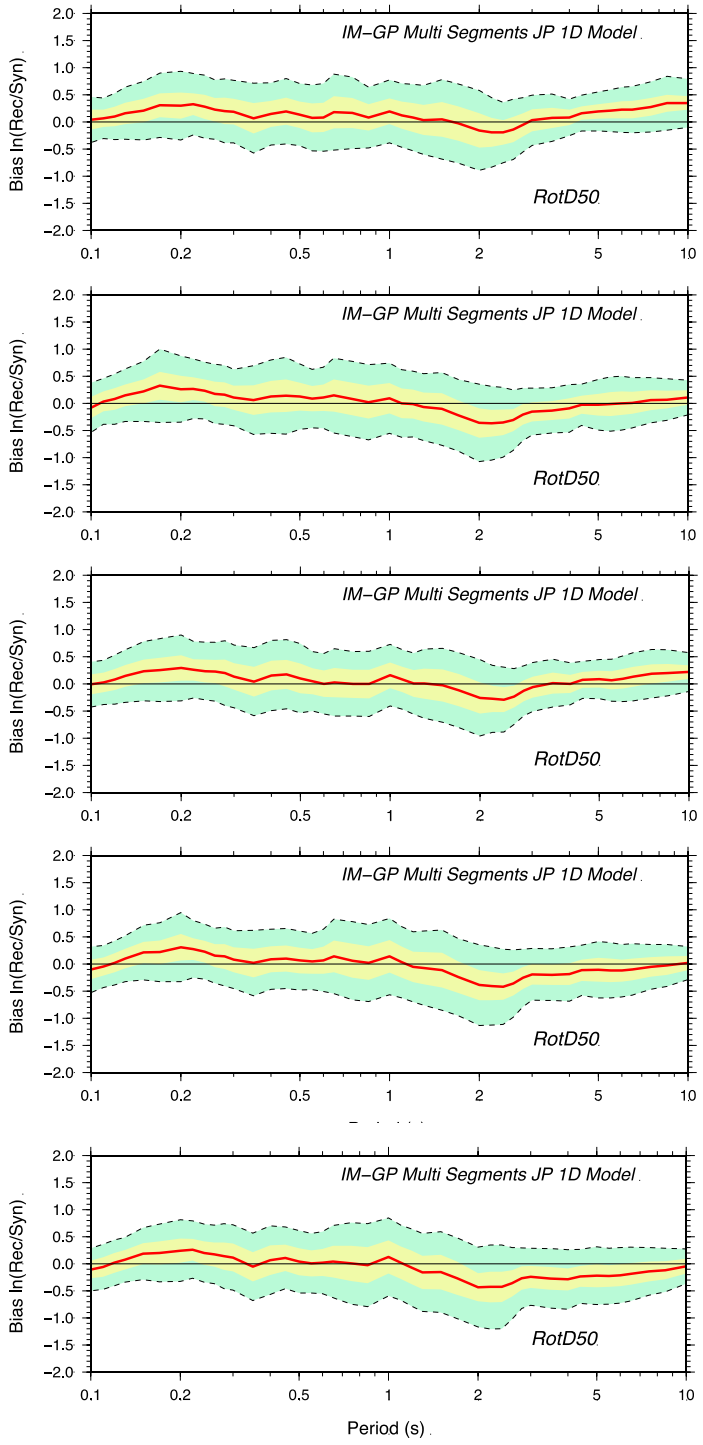

Figure A.2.1-1. Goodness of fit between recorded (Rec) and simulated (Syn) acceleration response spectra for different **Vr/Vs ratios**: 0.538,0.616,0.0694,0.772,0.850 from top to bottom panels, respectively. Note, bias (red line) positive means recorded ground motion is higher that simulated ground motion

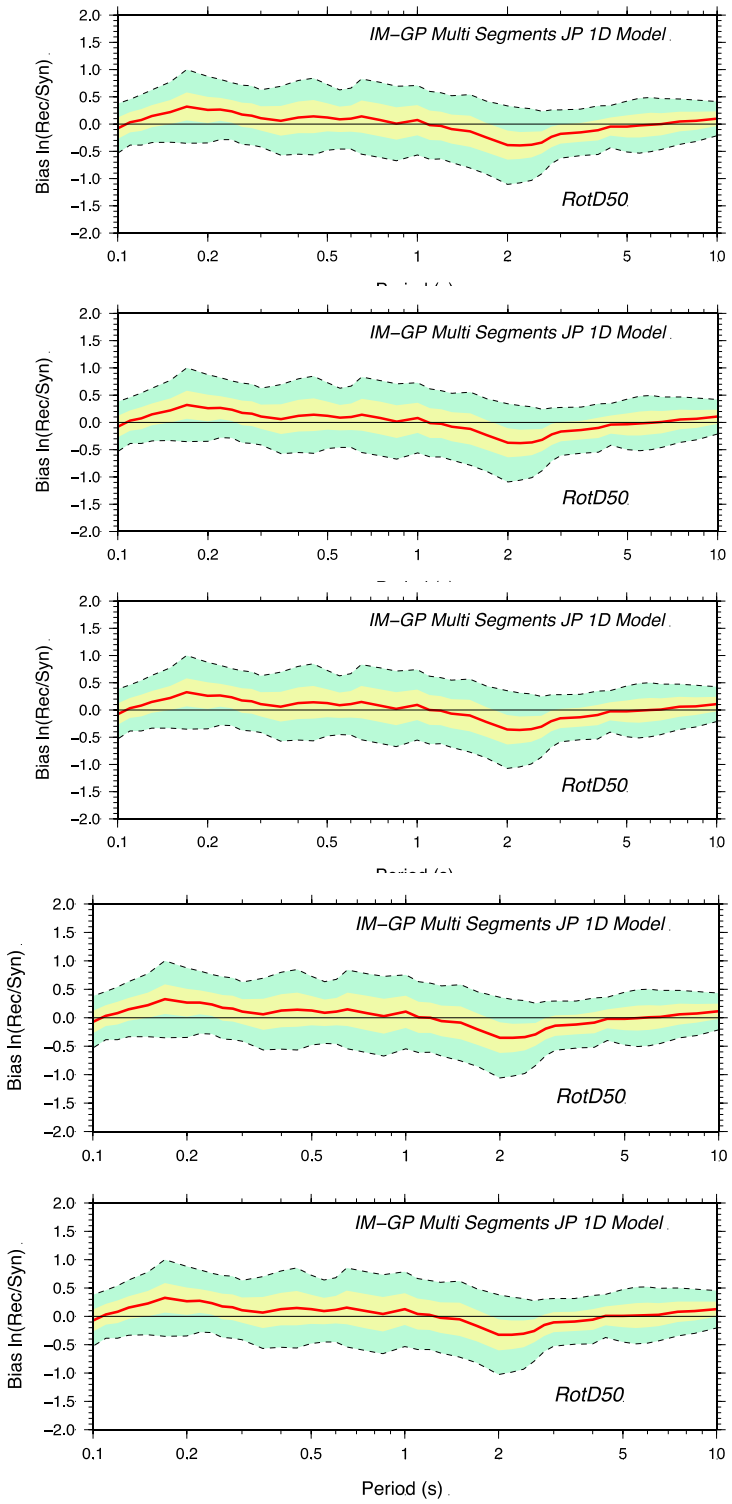

Figure A.2.1-2. Goodness of fit between recorded (Rec) and simulated (Syn) acceleration response spectra for different **rise time factors**: 1.44, 1.52,1.60,1.68,1.76 from top to bottom panels, respectively. Note, bias (red line) positive means recorded ground motion is higher that simulated ground motion

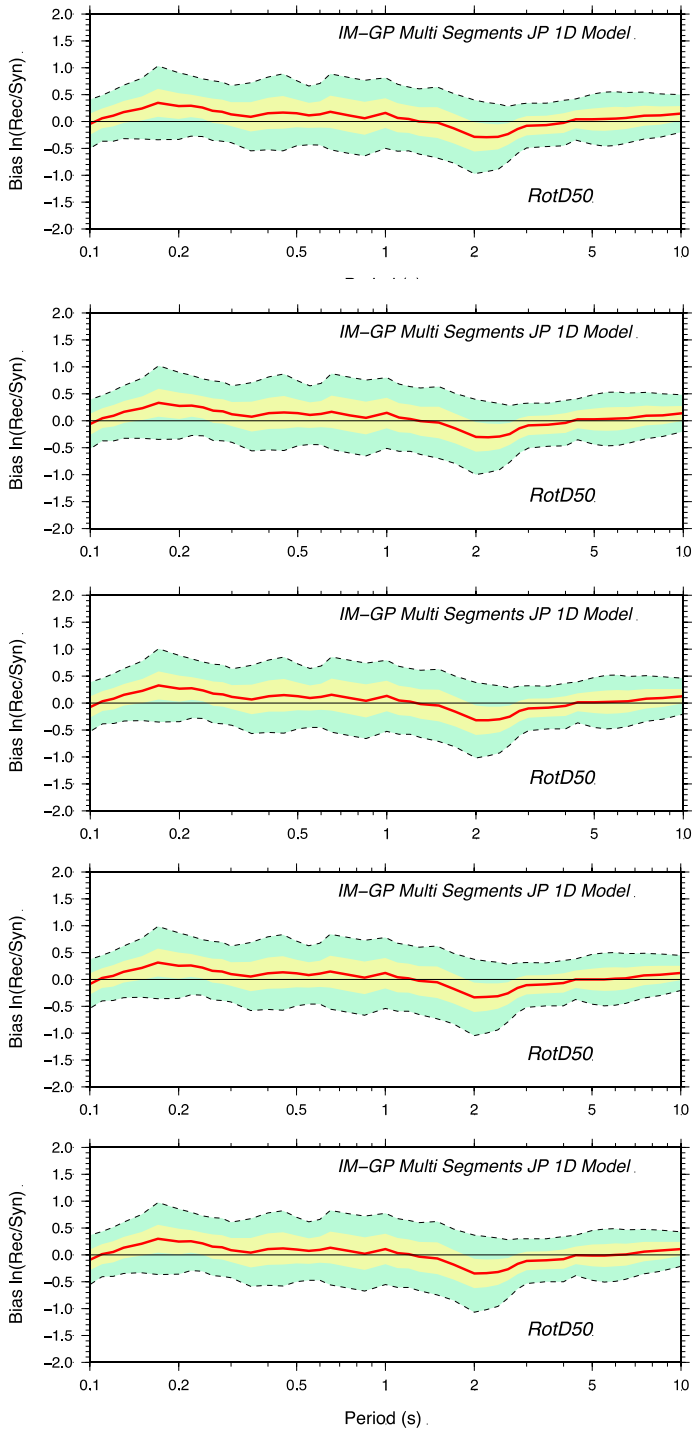

Figure A.2.1-3. Goodness of fit between recorded (Rec) and simulated (Syn) acceleration response spectra for different **slip roughness factors**: 0.75, 0.80, 0.85, 0.90, 0.95 from top to bottom panels, respectively. Note, bias (red line) positive means recorded ground motion is higher that simulated ground motion

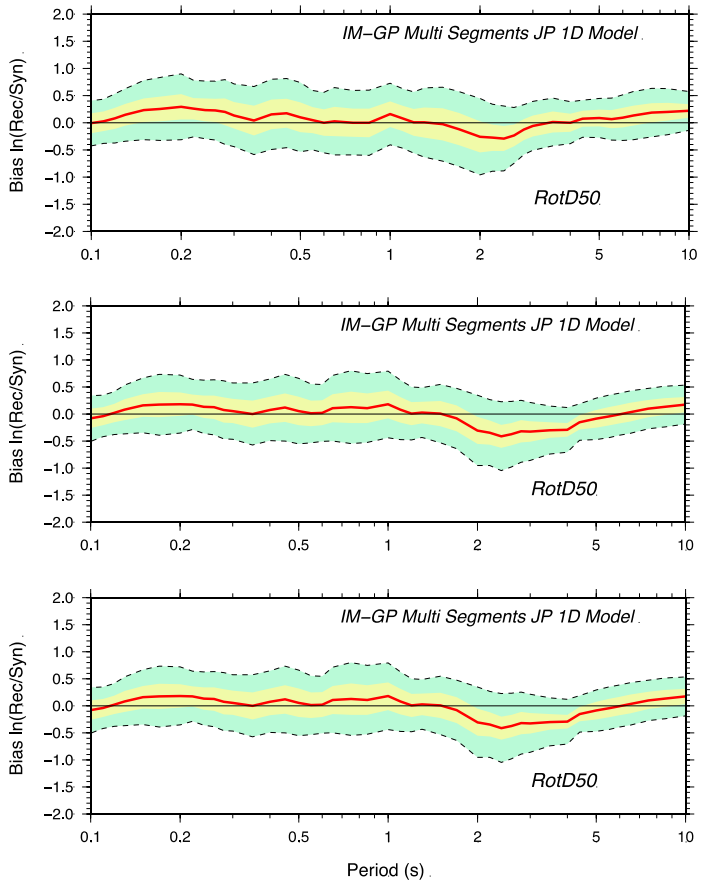

Figure A.2.1-4. Goodness of fit between recorded (Rec) and simulated (Syn) acceleration response spectra for different **rupture starting point location**: left (top panel), center (middle panel), right (bottom panel), respectively. Note, bias (red line) positive means recorded ground motion is higher that simulated ground motion

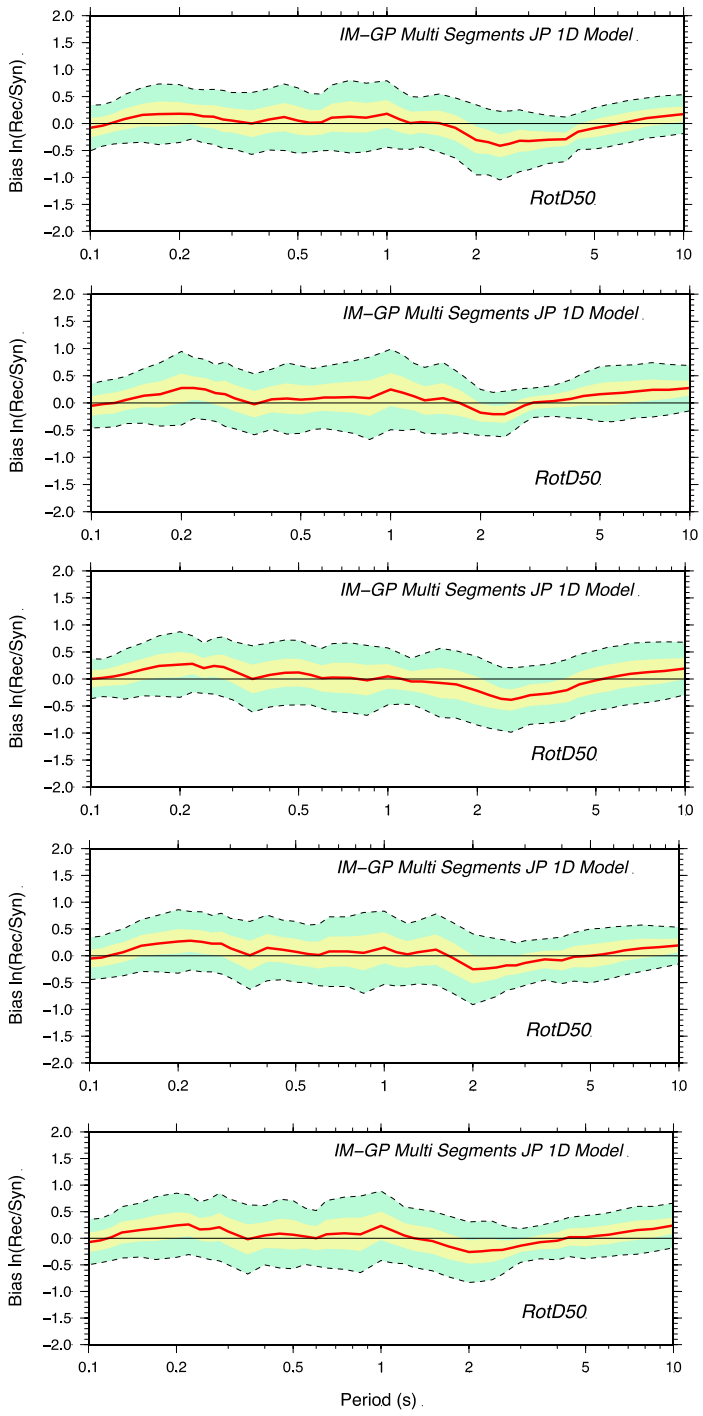

Figure A.2.1-5. Goodness of fit between recorded (Rec) and simulated (Syn) acceleration response spectra for different **slip generator seeds** : s1,s2,s3,s4,s5 from top to bottom panels, respectively. Note, bias (red line) positive means recorded ground motion is higher that simulated ground motion

A.2.2 Comparison of computed acceleration response spectra with four GMPEs

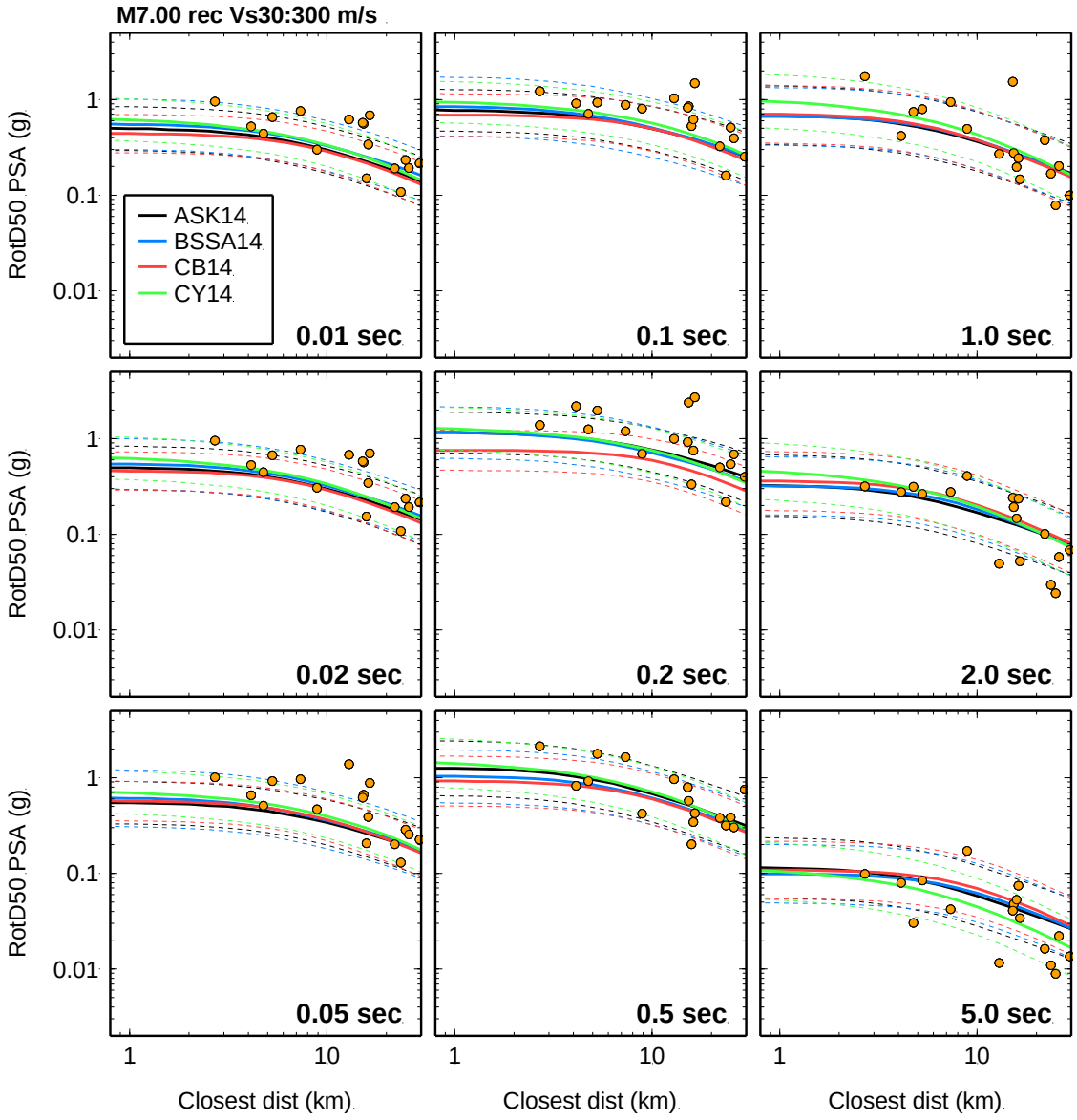

Figure A.2.2-1. Comparison of RotD50 acceleration response spectra (yellow circles), recorded at 17 near-fault stations, with four GMPEs for Vs30=300m/s

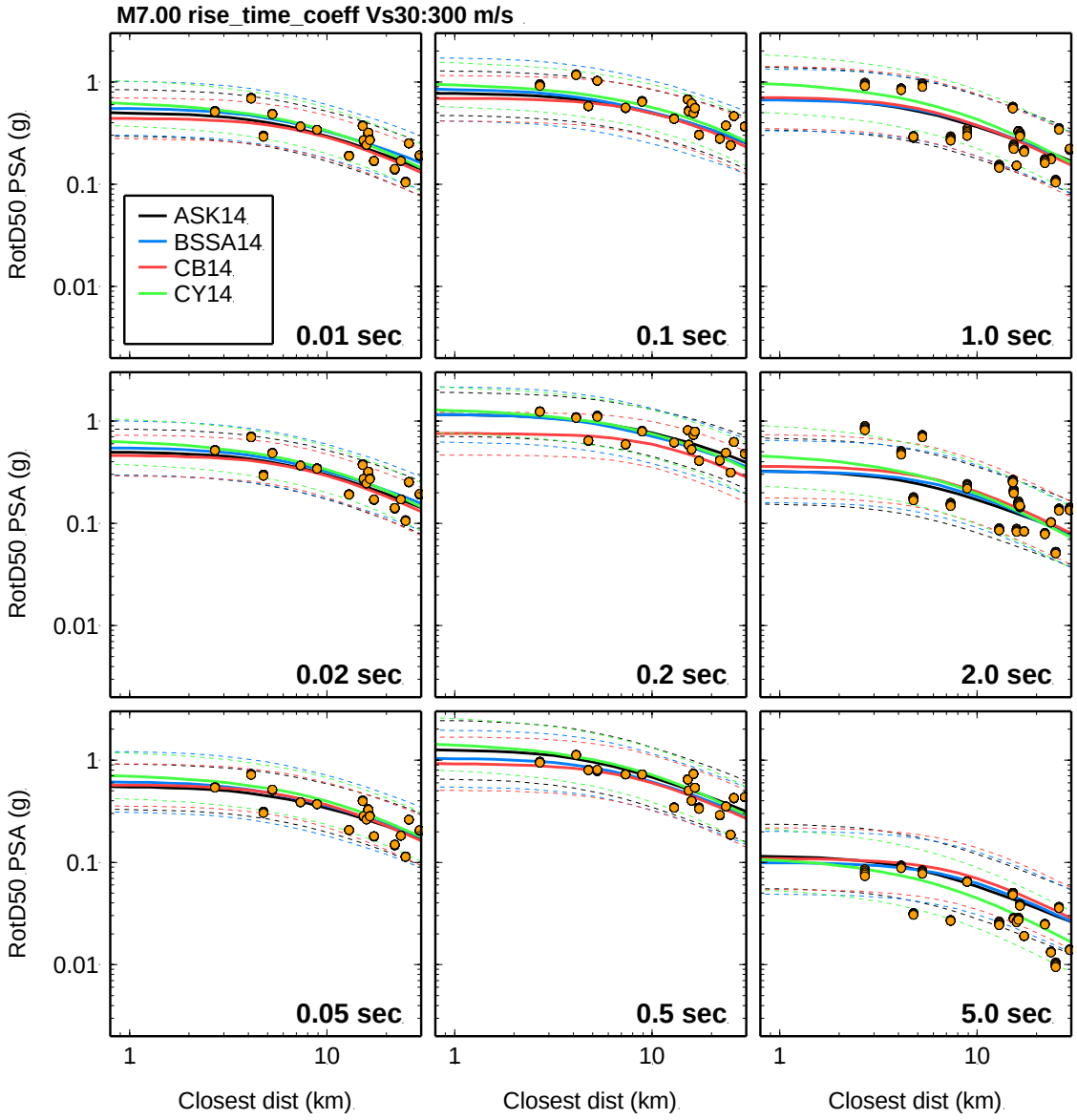

Figure A.2.2-2. Comparison of RotD50 acceleration response spectra (yellow circles), computed at 17 near-fault stations using five rupture scenarios with different **rise time coefficients**, with four GMPEs for Vs30=300m/s

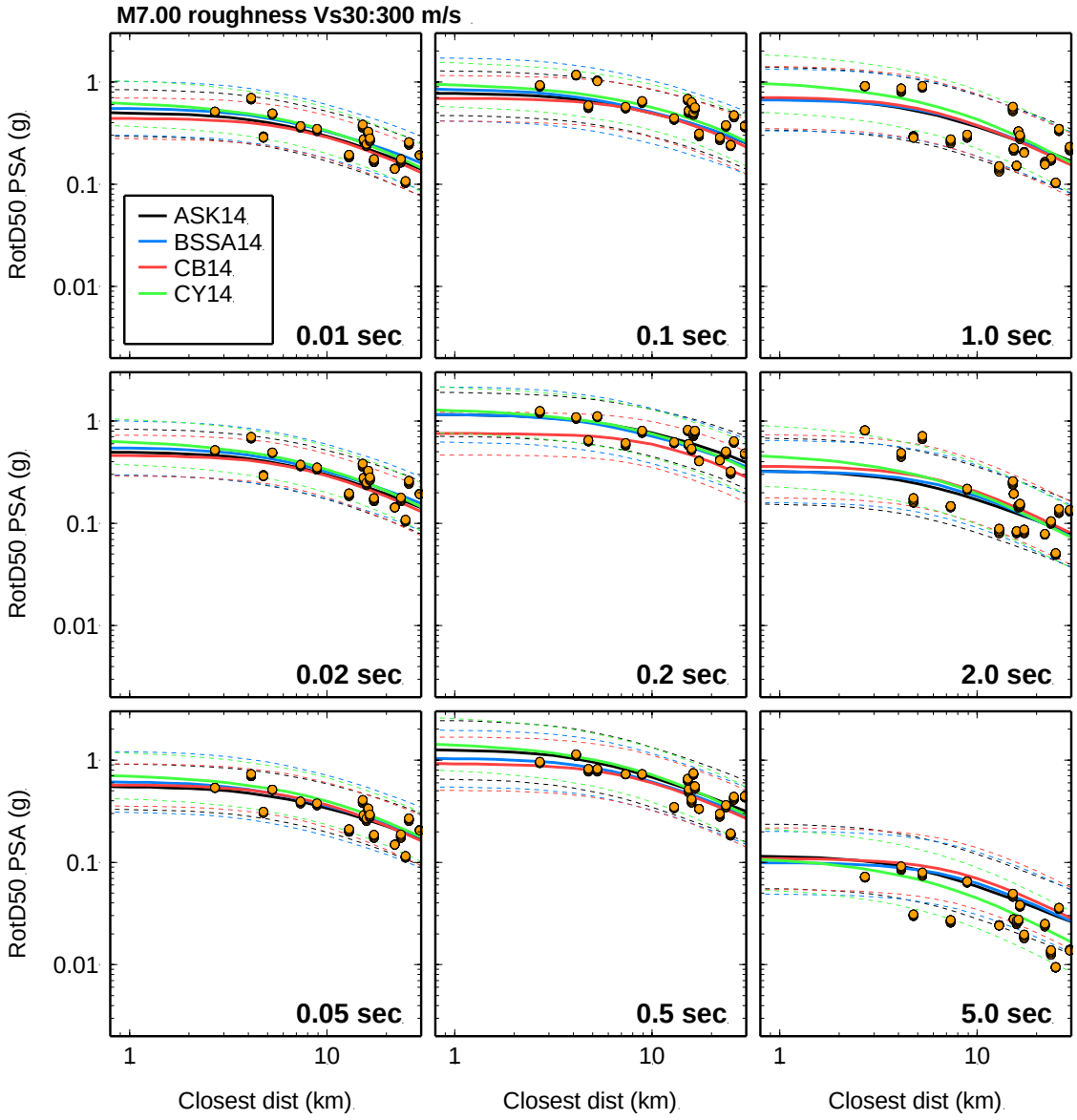

Figure A.2.2-3. Comparison of RotD50 acceleration response spectra (yellow circles), computed at 17 near-fault stations, using five rupture scenarios with different **slip roughness coefficients**, with four GMPEs for Vs30=300m/s

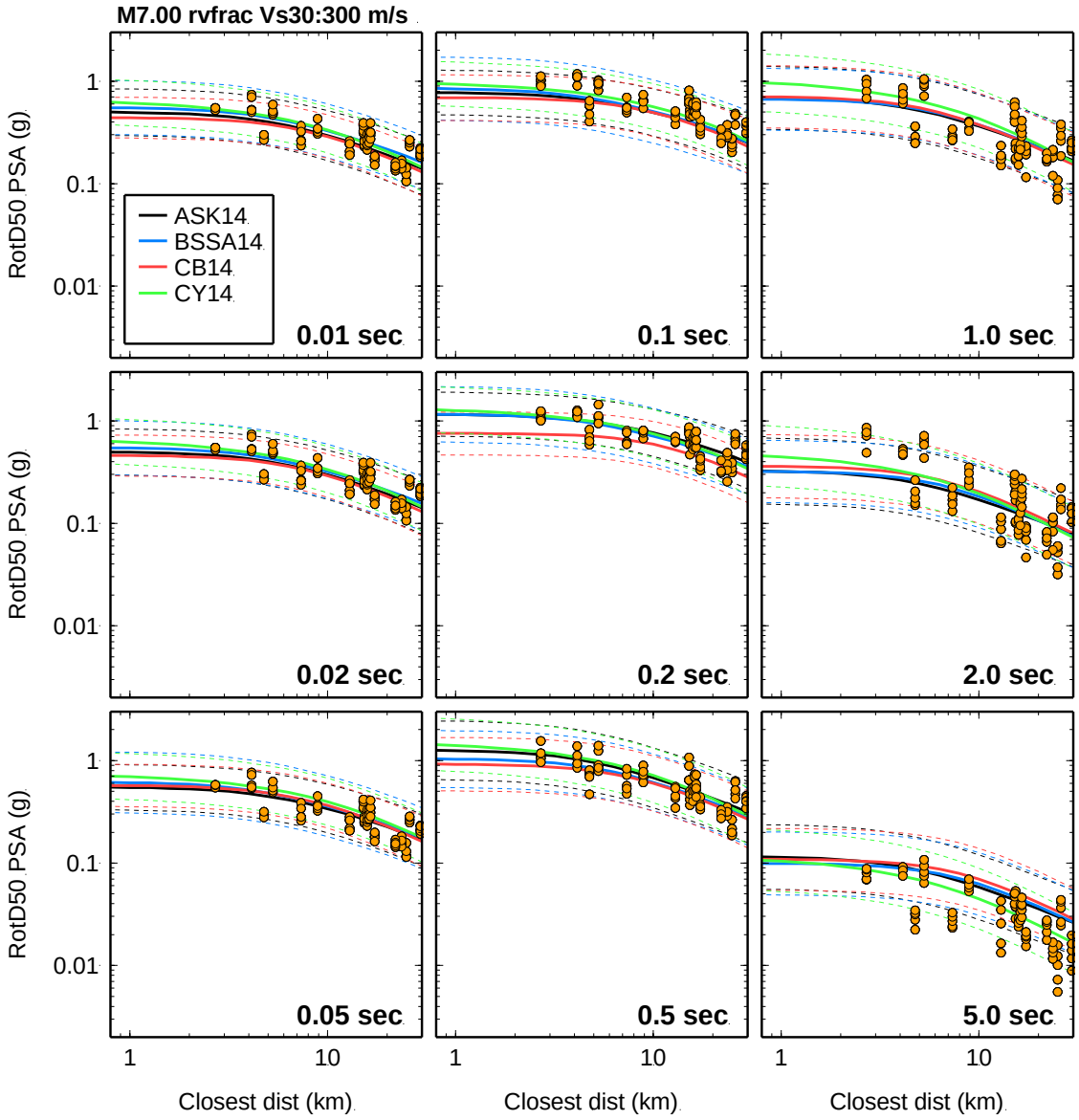

Figure A.2.2-4. Comparison of RotD50 acceleration response spectra (yellow circles), computed at 17 near-fault stations, using five rupture scenarios with different **Vr/Vs factors**, with four GMPEs for Vs30=300m/s

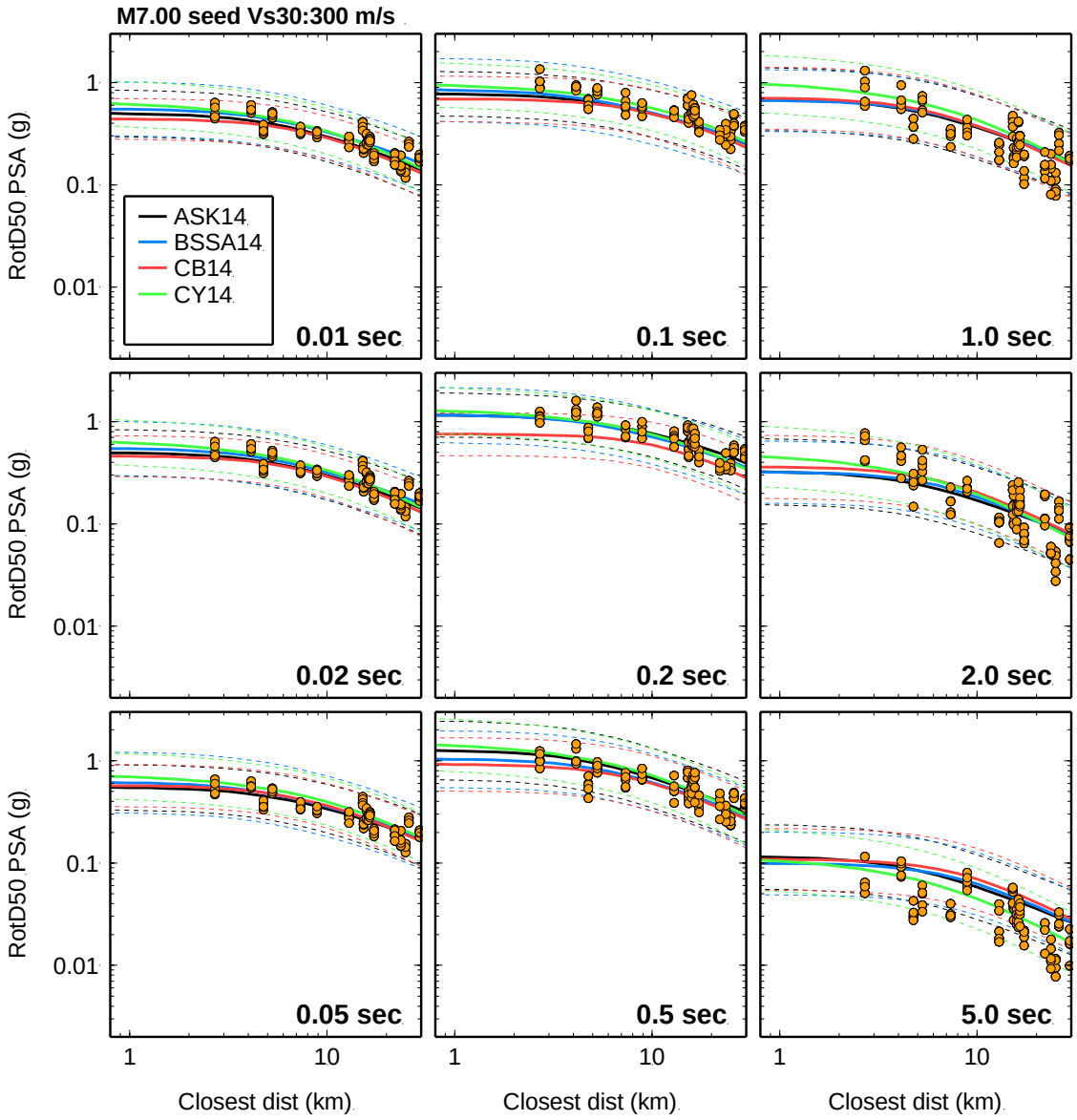

Figure A.2.2-5. Comparison of RotD50 acceleration response spectra (yellow circles), computed at 17 near-fault stations, using five rupture scenarios with different **rupture seeds**, with four GMPEs for Vs30=300m/s

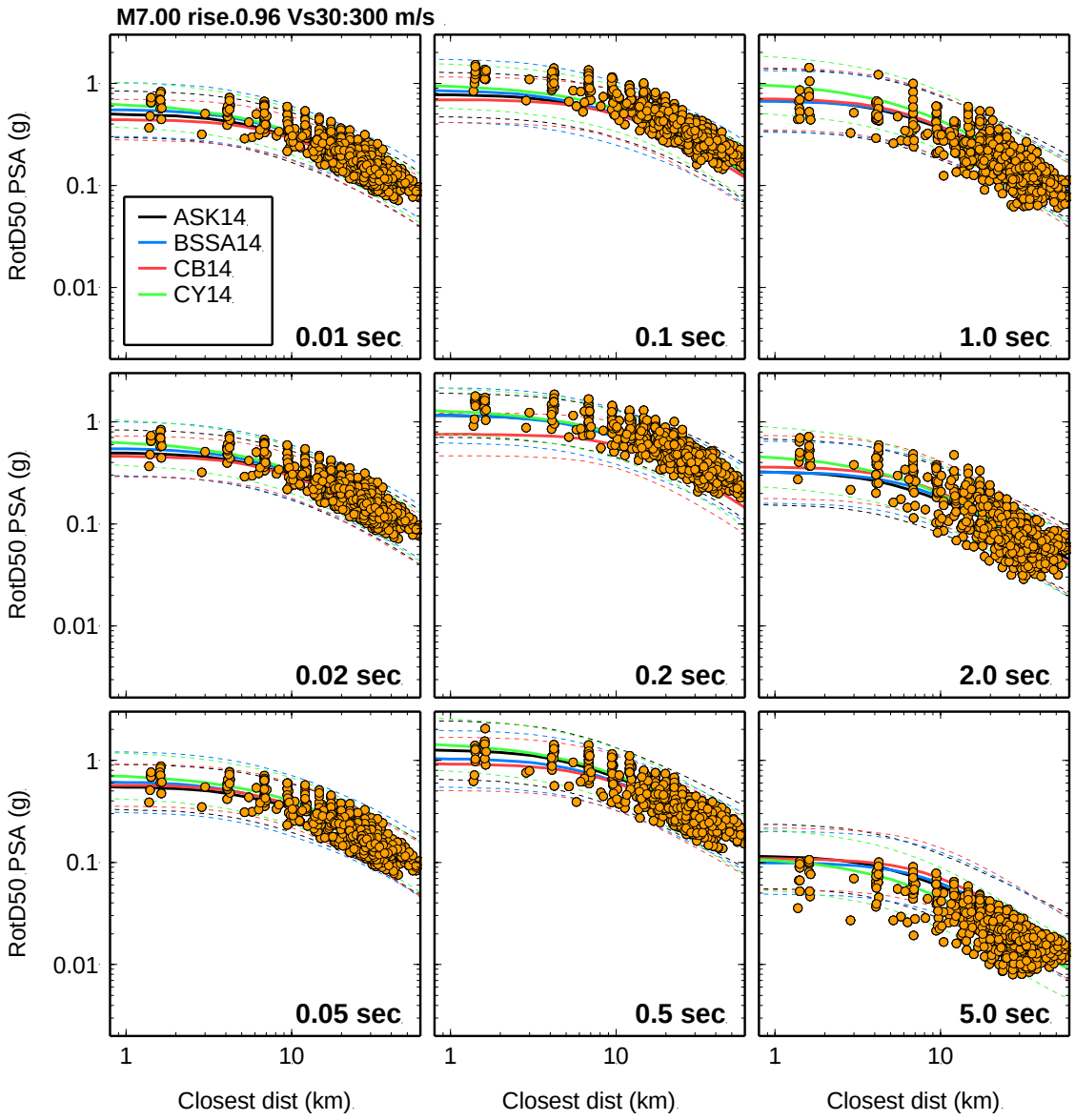

Figure A.2.2-6. Comparison of RotD50 acceleration response spectra (yellow circles), computed at 500 near-fault stations, using rupture scenario with **rise time coeff=0.96**, with four GMPEs for Vs30=300m/s

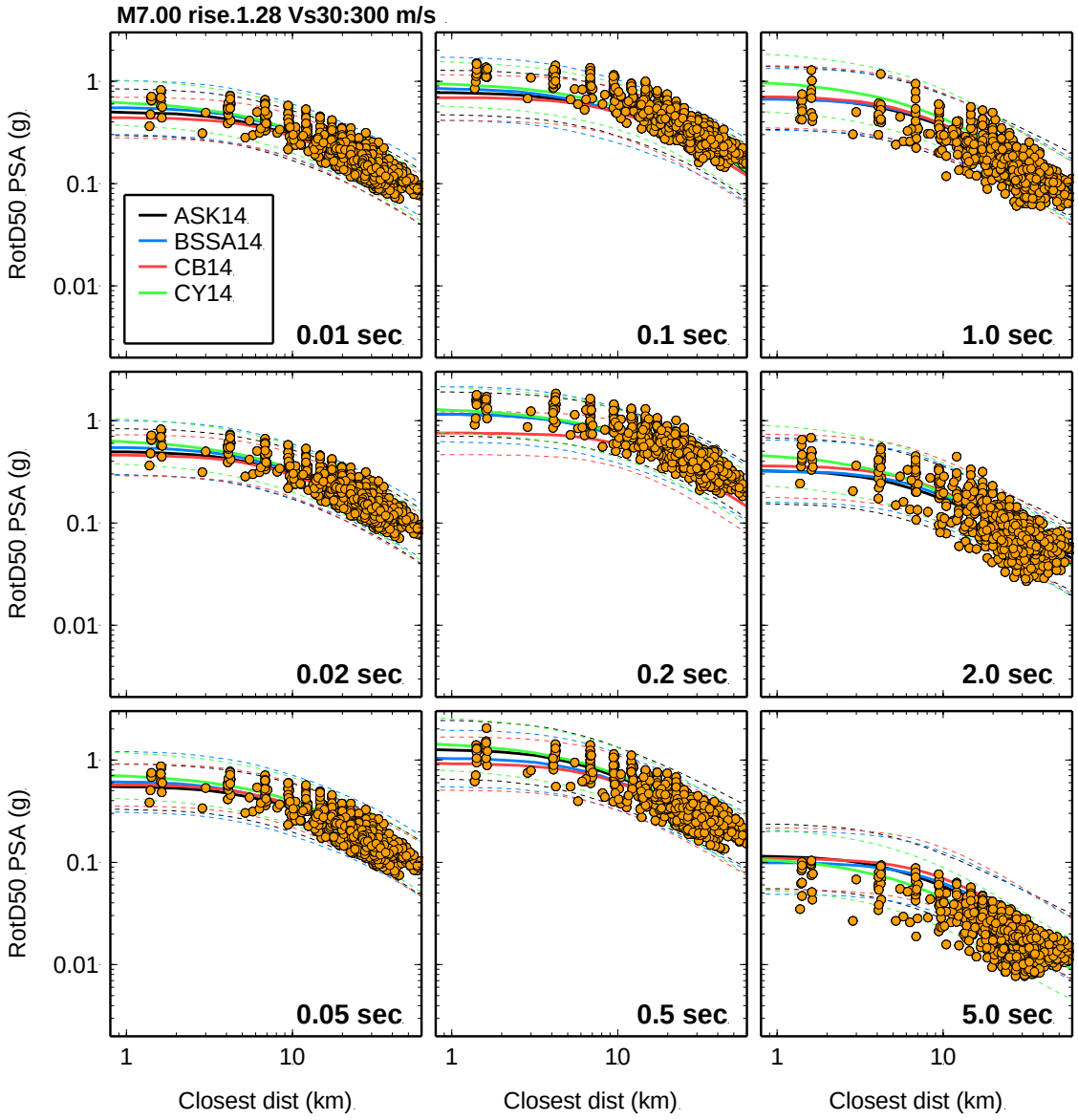

Figure A.2.2-7. Comparison of RotD50 acceleration response spectra (yellow circles), computed at 500 near-fault stations, using rupture scenario with **rise time coeff=1.28**, with four GMPEs for Vs30=300m/s

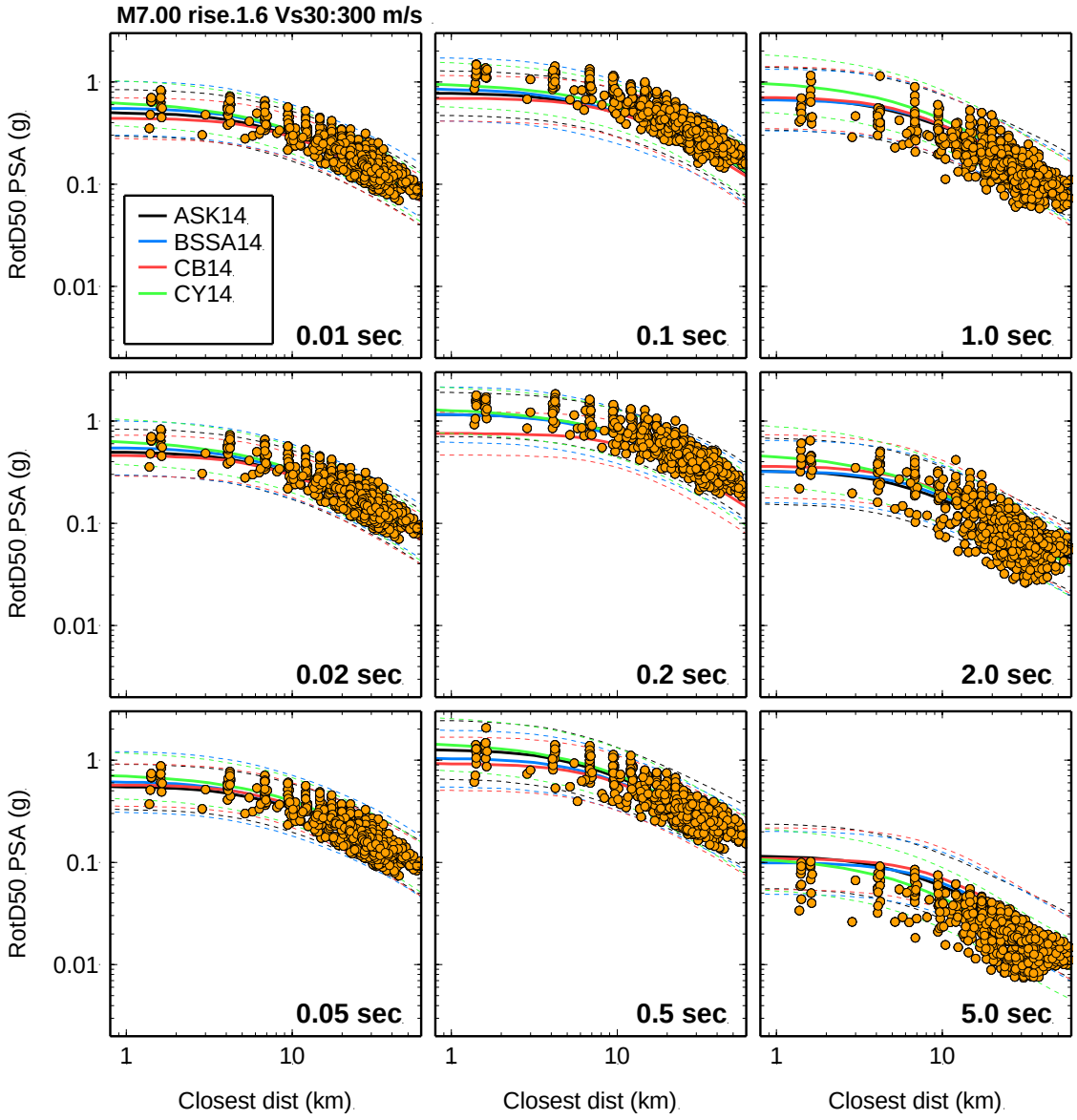

Figure A.2.2-8. Comparison of RotD50 acceleration response spectra (yellow circles), computed at 500 near-fault stations, using rupture scenario with **rise time coeff=1.60**, with four GMPEs for Vs30=300m/s

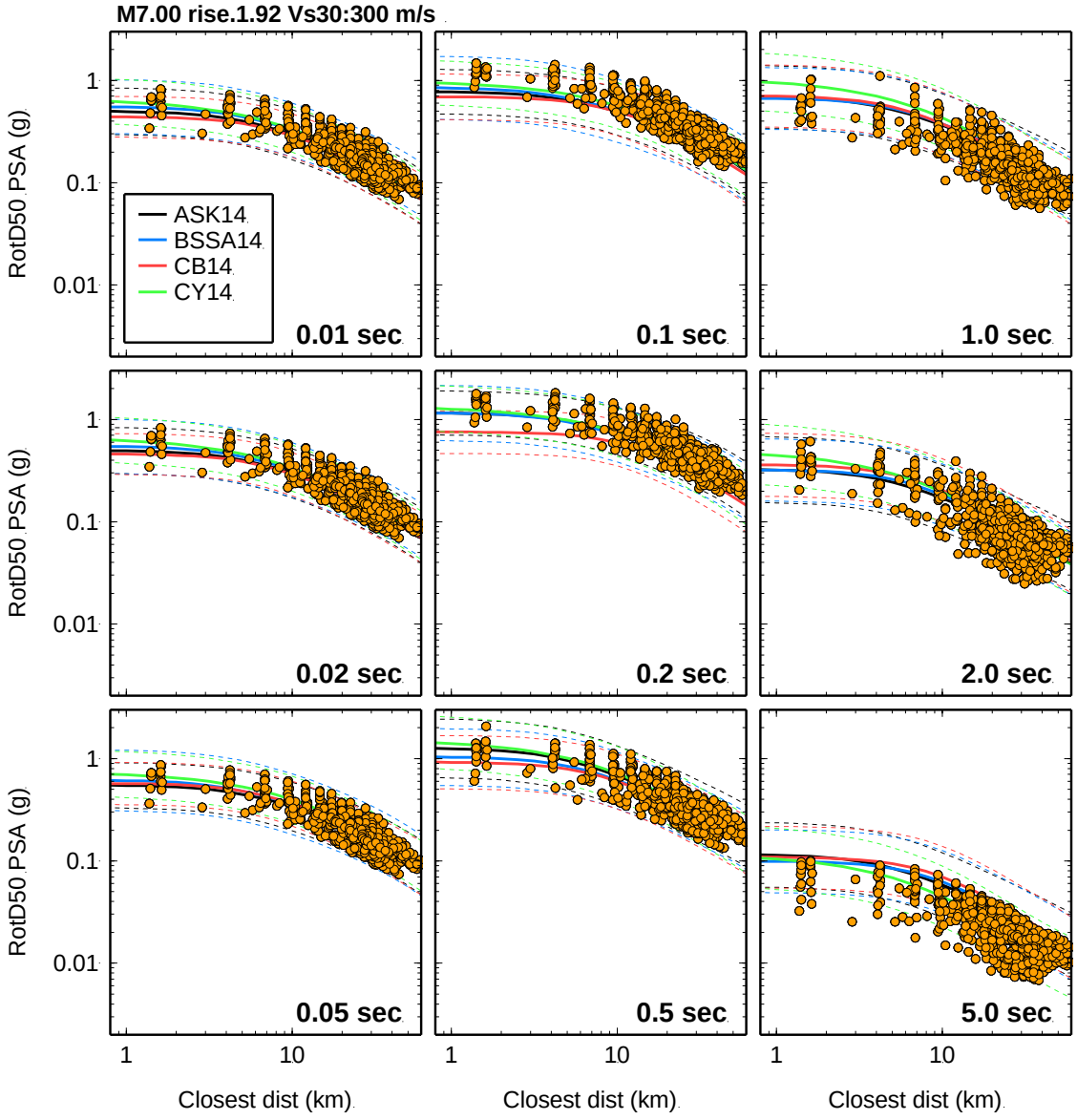

Figure A.2.2-9. Comparison of RotD50 acceleration response spectra (yellow circles), computed at 500 near-fault stations, using rupture scenario with **rise time coeff=1.92**, with four GMPEs for Vs30=300m/s

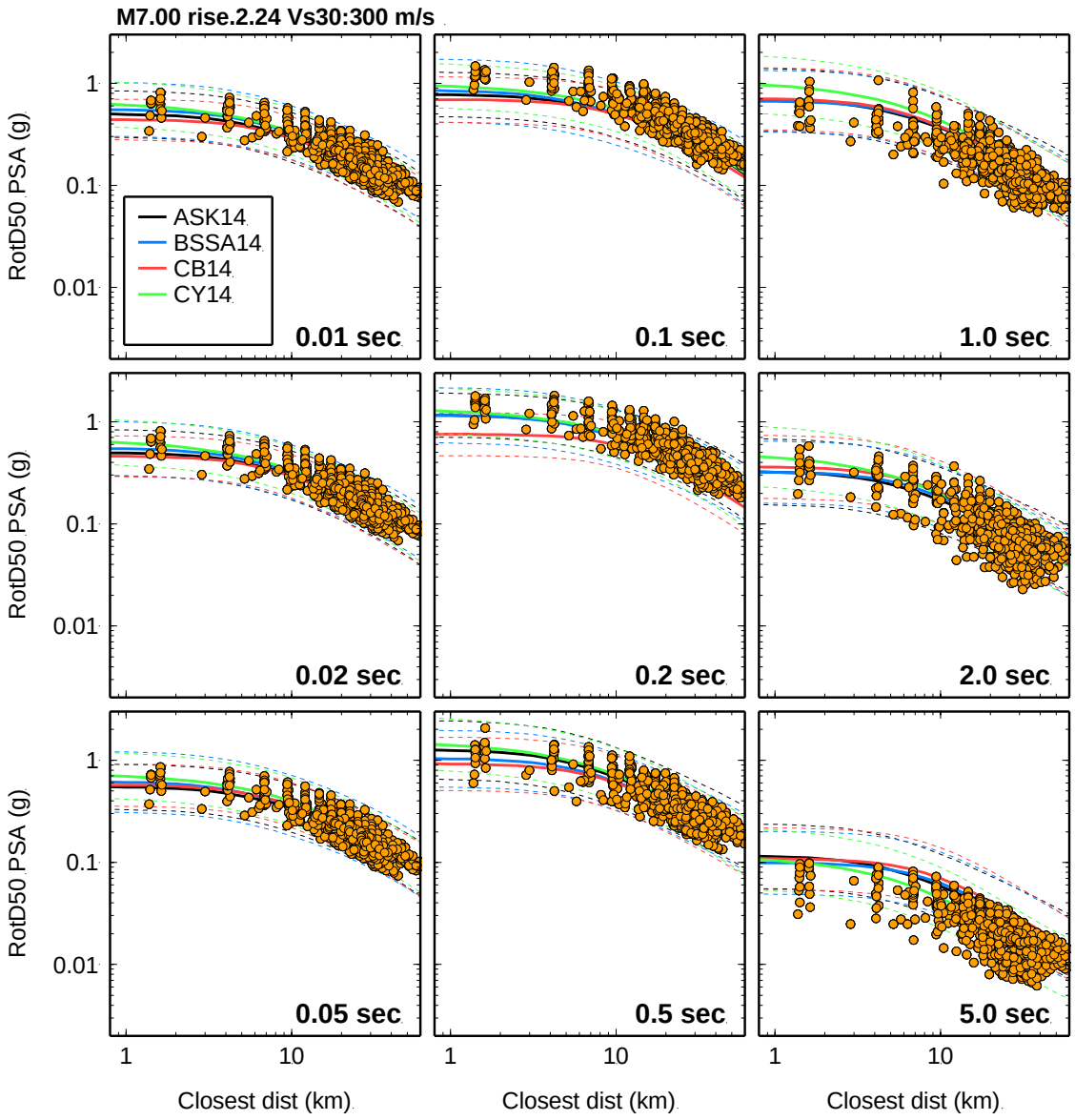

Figure A.2.2-10. Comparison of RotD50 acceleration response spectra (yellow circles), computed at 500 near-fault stations, using rupture scenario with **rise time coeff=2.24**, with four GMPEs for Vs30=300m/s

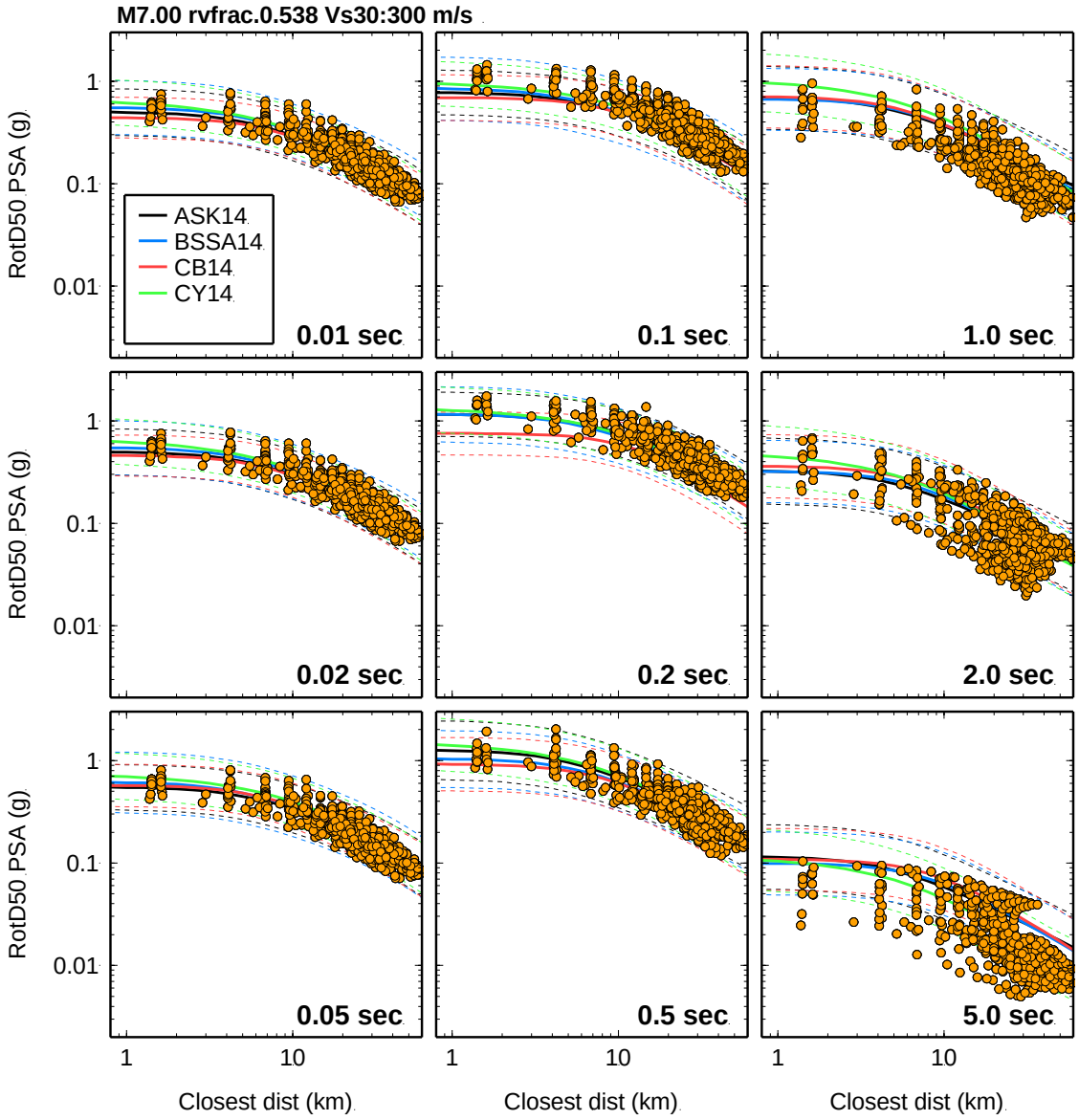

Figure A.2.2-11. Comparison of RotD50 acceleration response spectra (yellow circles), computed at 500 near-fault stations, using rupture scenario with **Vr/Vs ratio =0.538**, with four GMPEs for Vs30=300m/s

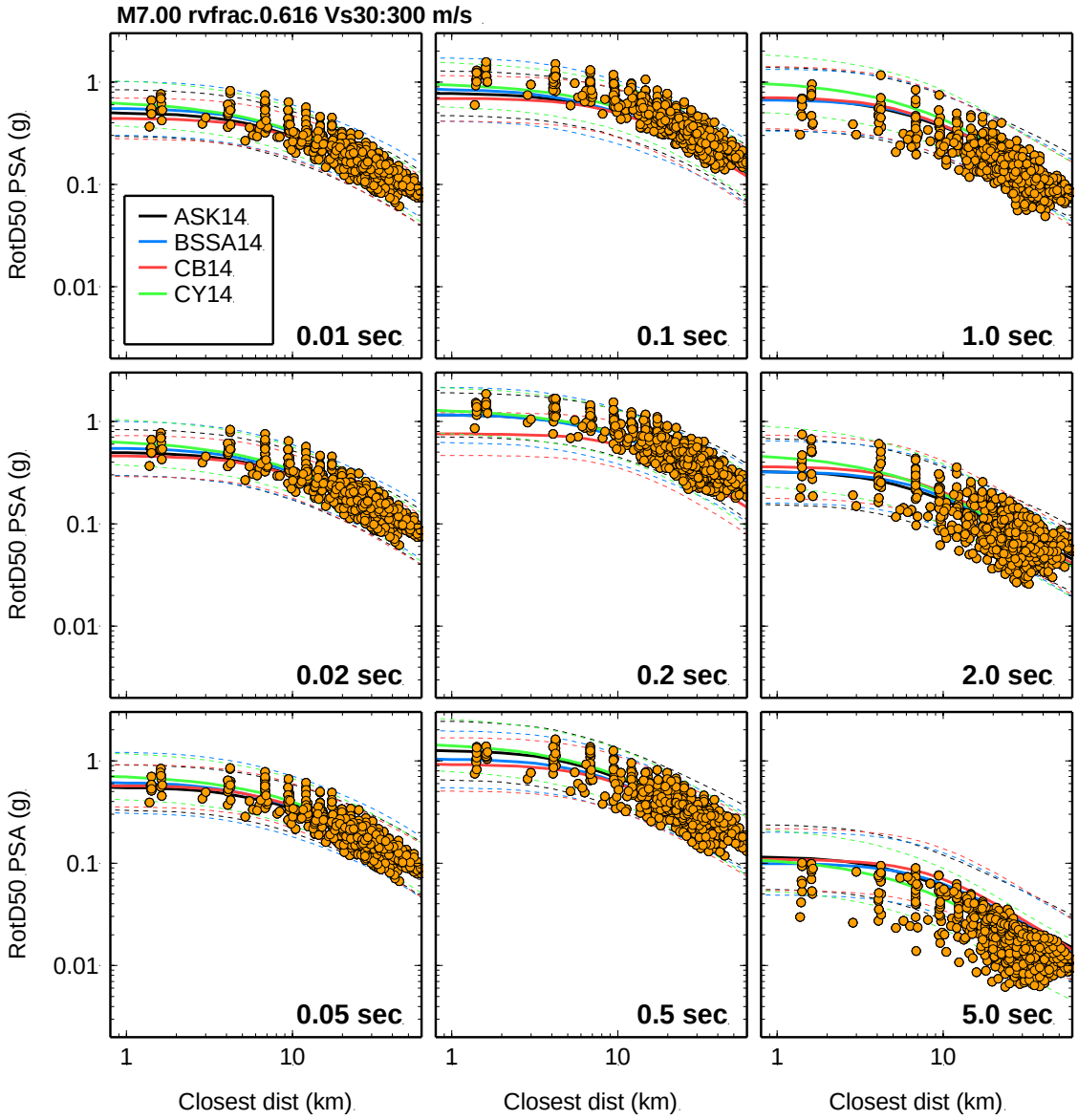

Figure A.2.2-12. Comparison of RotD50 acceleration response spectra (yellow circles), computed at 500 near-fault stations, using rupture scenario with **Vr/Vs ratio =0.616**, with four GMPEs for Vs30=300m/s

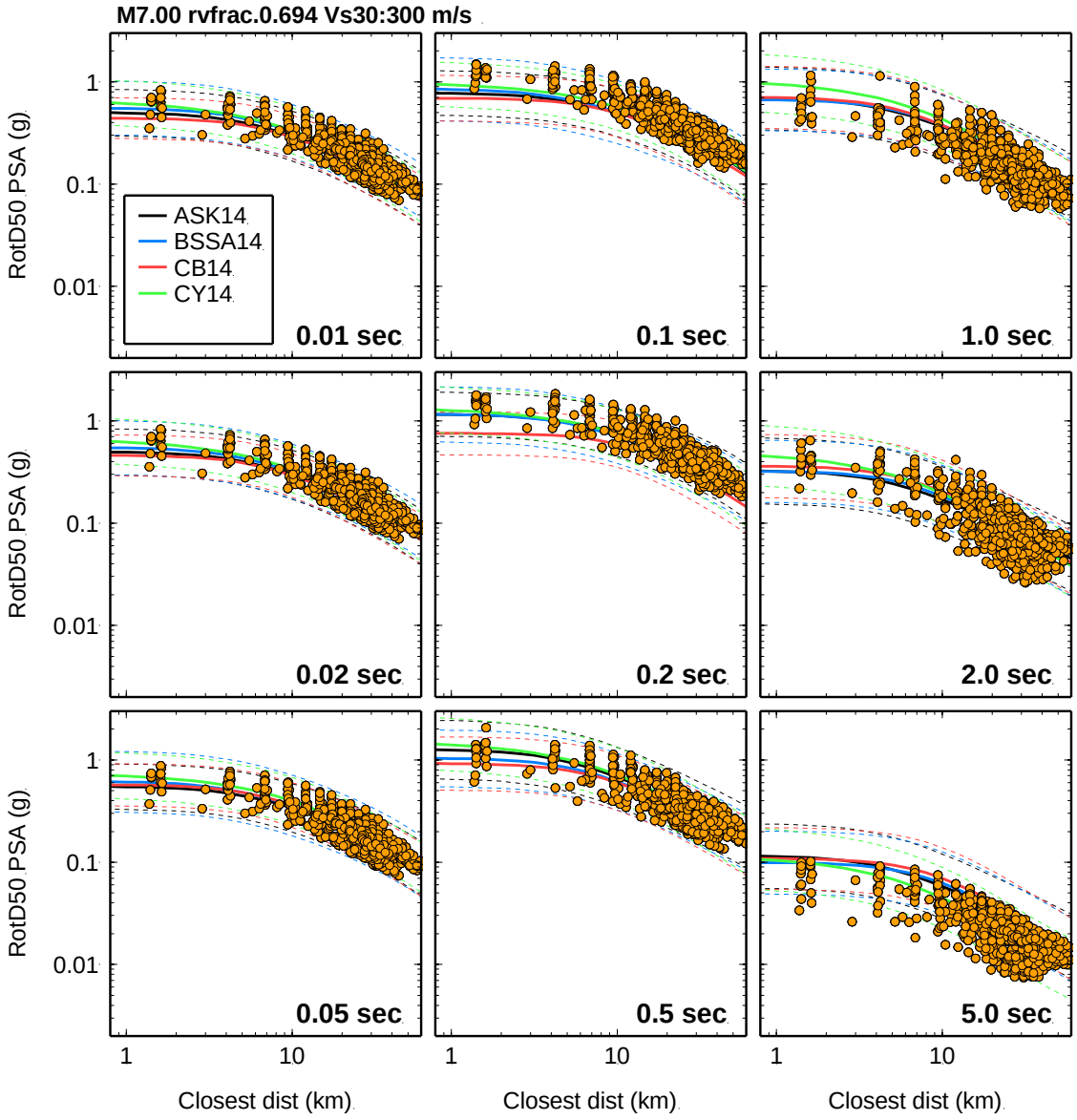

Figure A.2.2-13. Comparison of RotD50 acceleration response spectra (yellow circles), computed at 500 near-fault stations, using rupture scenario with **Vr/Vs ratio =0.694**, with four GMPEs for Vs30=300m/s

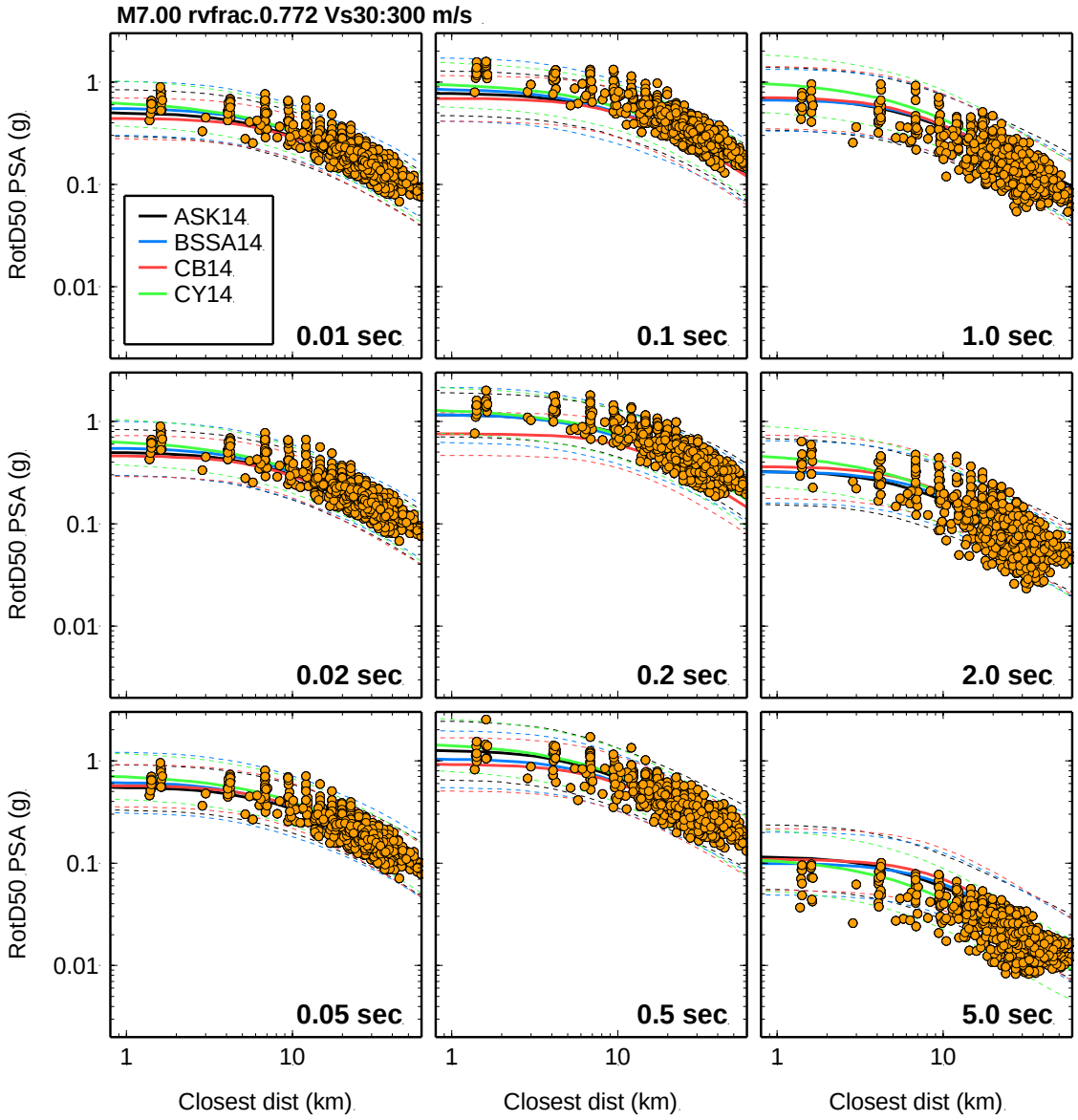

Figure A.2.2-14. Comparison of RotD50 acceleration response spectra (yellow circles), computed at 500 near-fault stations, using rupture scenario with **Vr/Vs ratio =0.772**, with four GMPEs for Vs30=300m/s

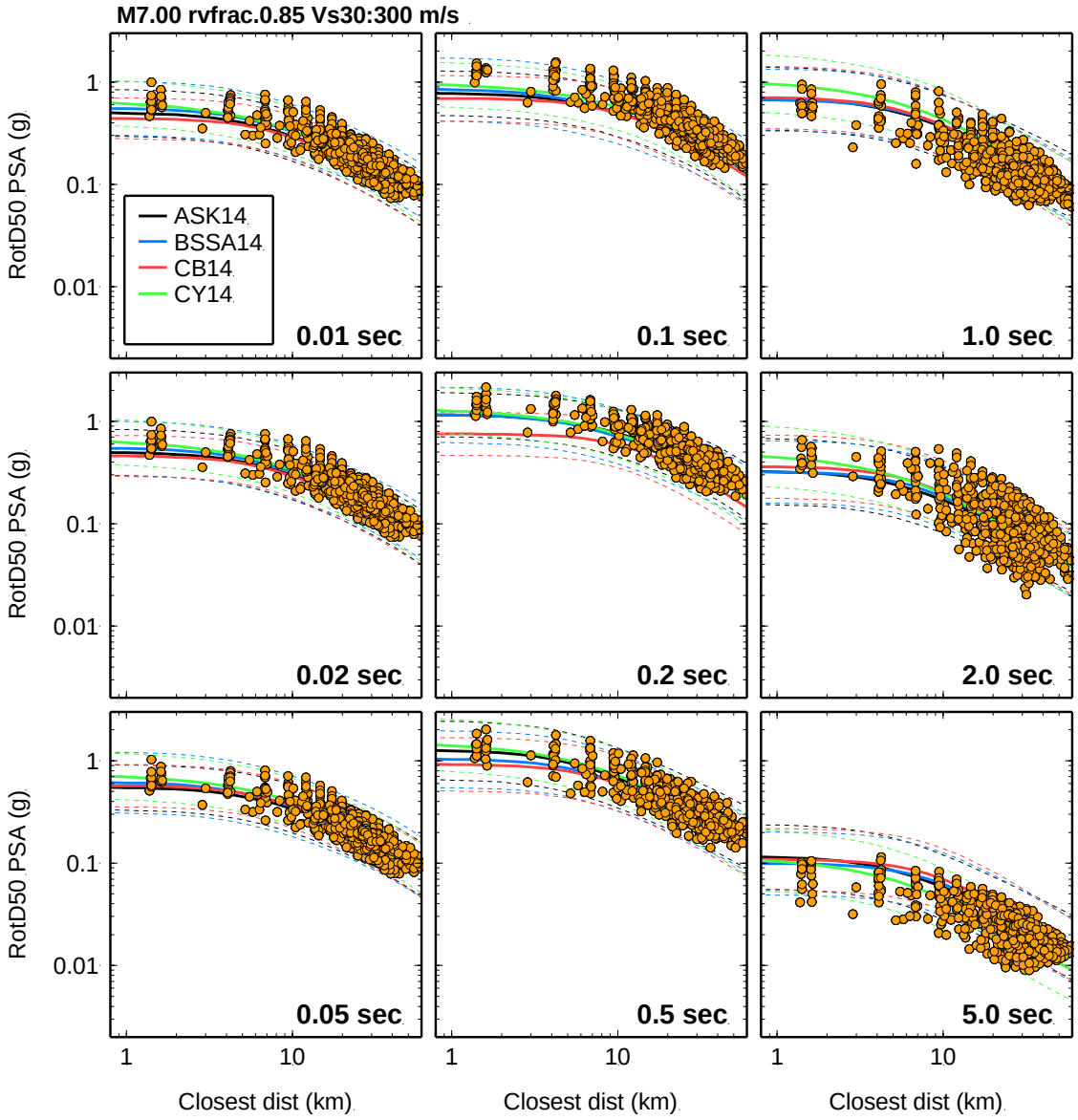

Figure A.2.2-15. Comparison of RotD50 acceleration response spectra (yellow circles), computed at 500 near-fault stations, using rupture scenario with **Vr/Vs ratio =0.85,** with four GMPEs for Vs30=300m/s

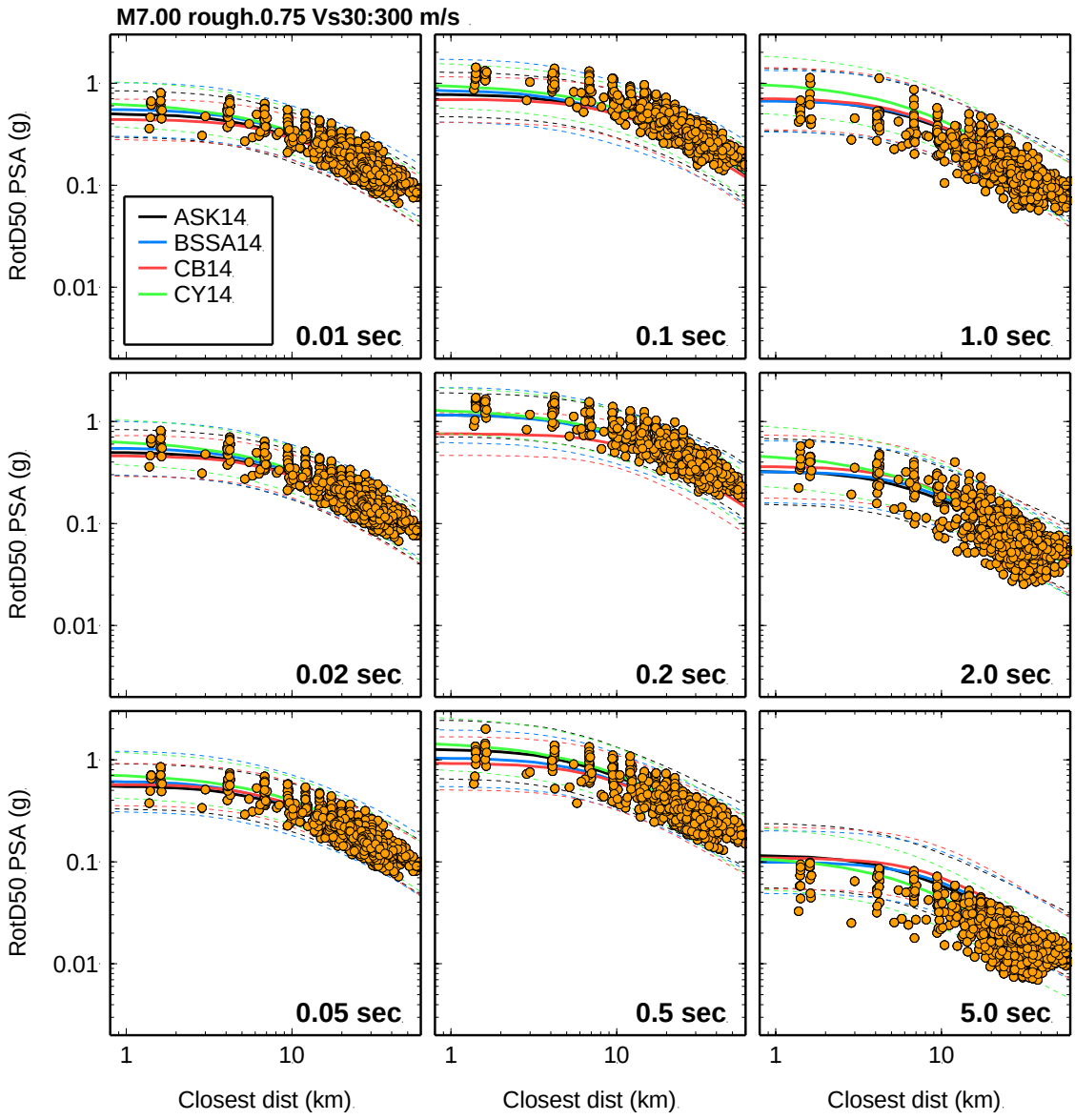

Figure A.2.2-16. Comparison of RotD50 acceleration response spectra (yellow circles), computed at 500 near-fault stations, using rupture scenario with **slip roughness coeff =0.75,** with four GMPEs for Vs30=300m/s

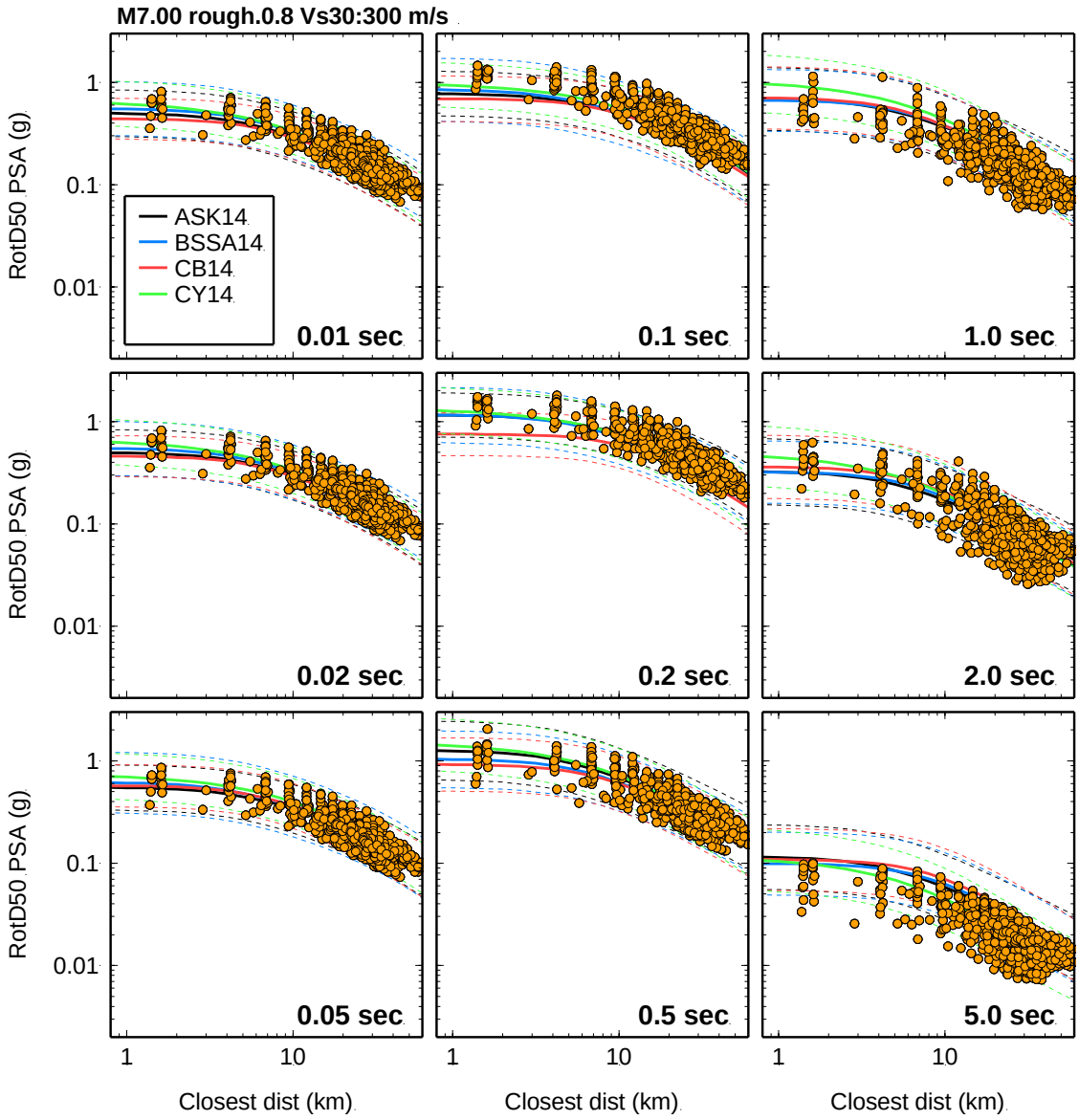

Figure A.2.2-17. Comparison of RotD50 acceleration response spectra (yellow circles), computed at 500 near-fault stations, using rupture scenario with **slip roughness coeff =0.80,** with four GMPEs for Vs30=300m/s

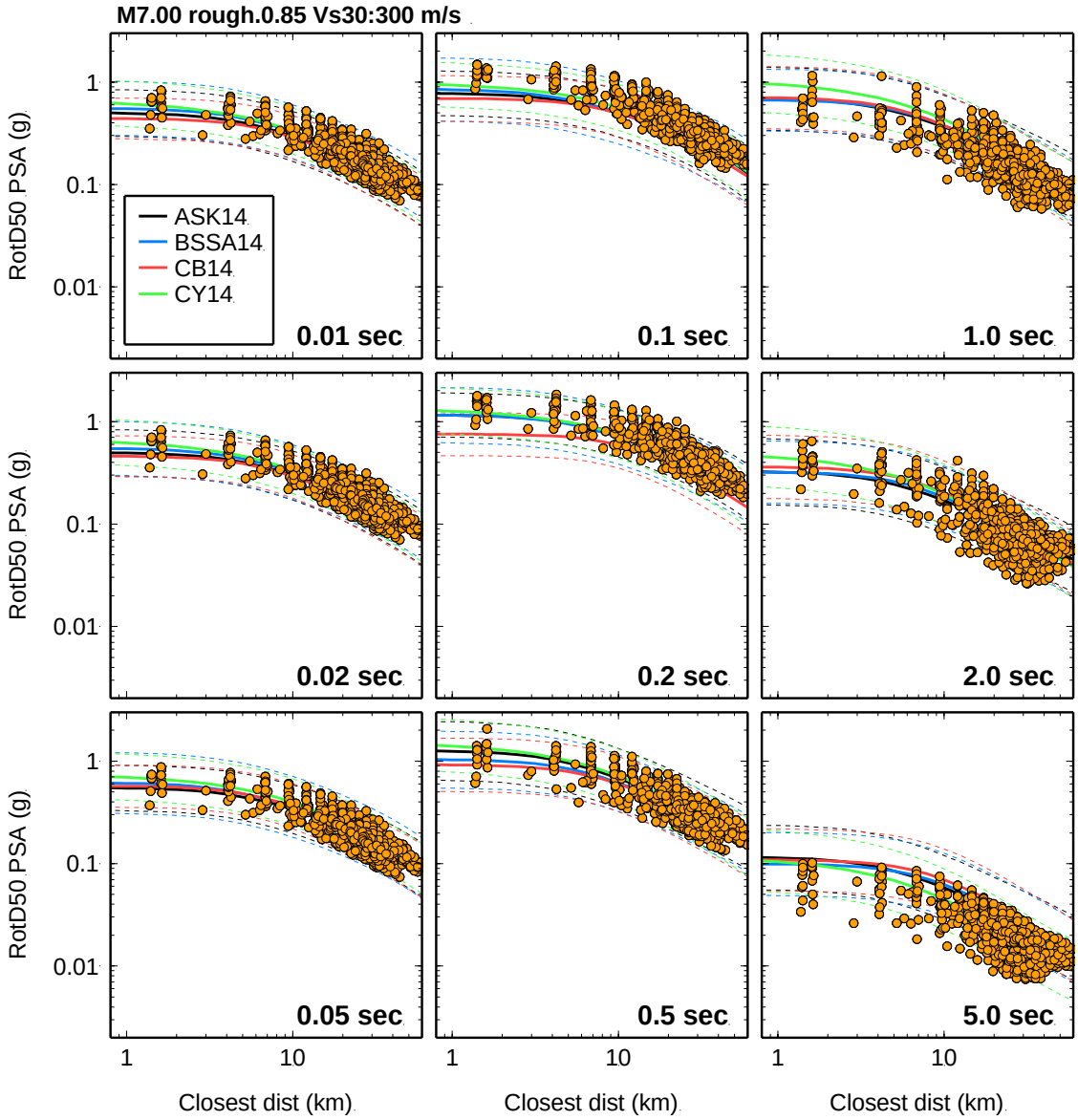

Figure A.2.2-18. Comparison of RotD50 acceleration response spectra (yellow circles), computed at 500 near-fault stations, using rupture scenario with **slip roughness coeff =0.85,** with four GMPEs for Vs30=300m/s

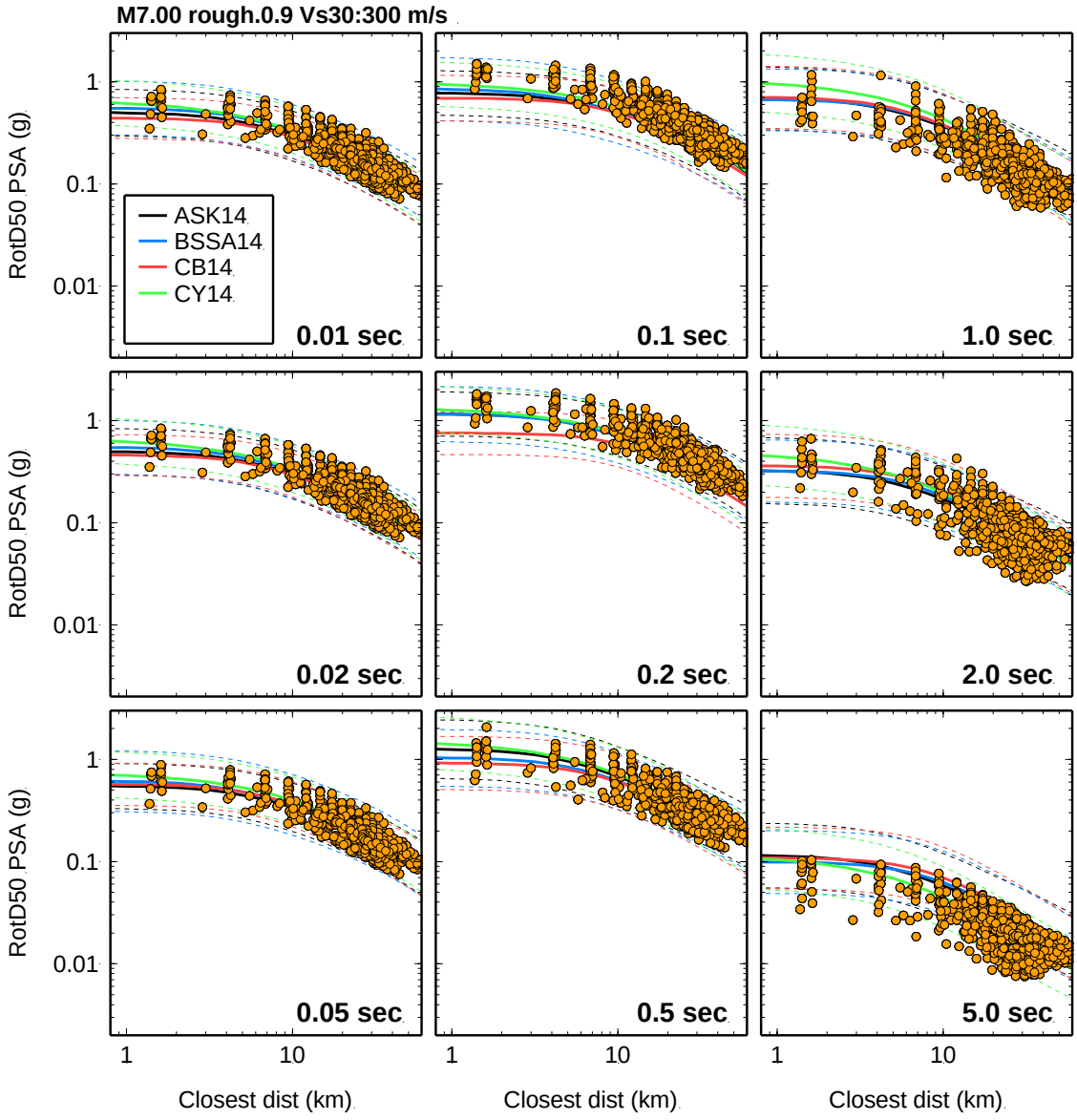

Figure A.2.2-19. Comparison of RotD50 acceleration response spectra (yellow circles), computed at 500 near-fault stations, using rupture scenario with **slip roughness coeff =0.90,** with four GMPEs for Vs30=300m/s

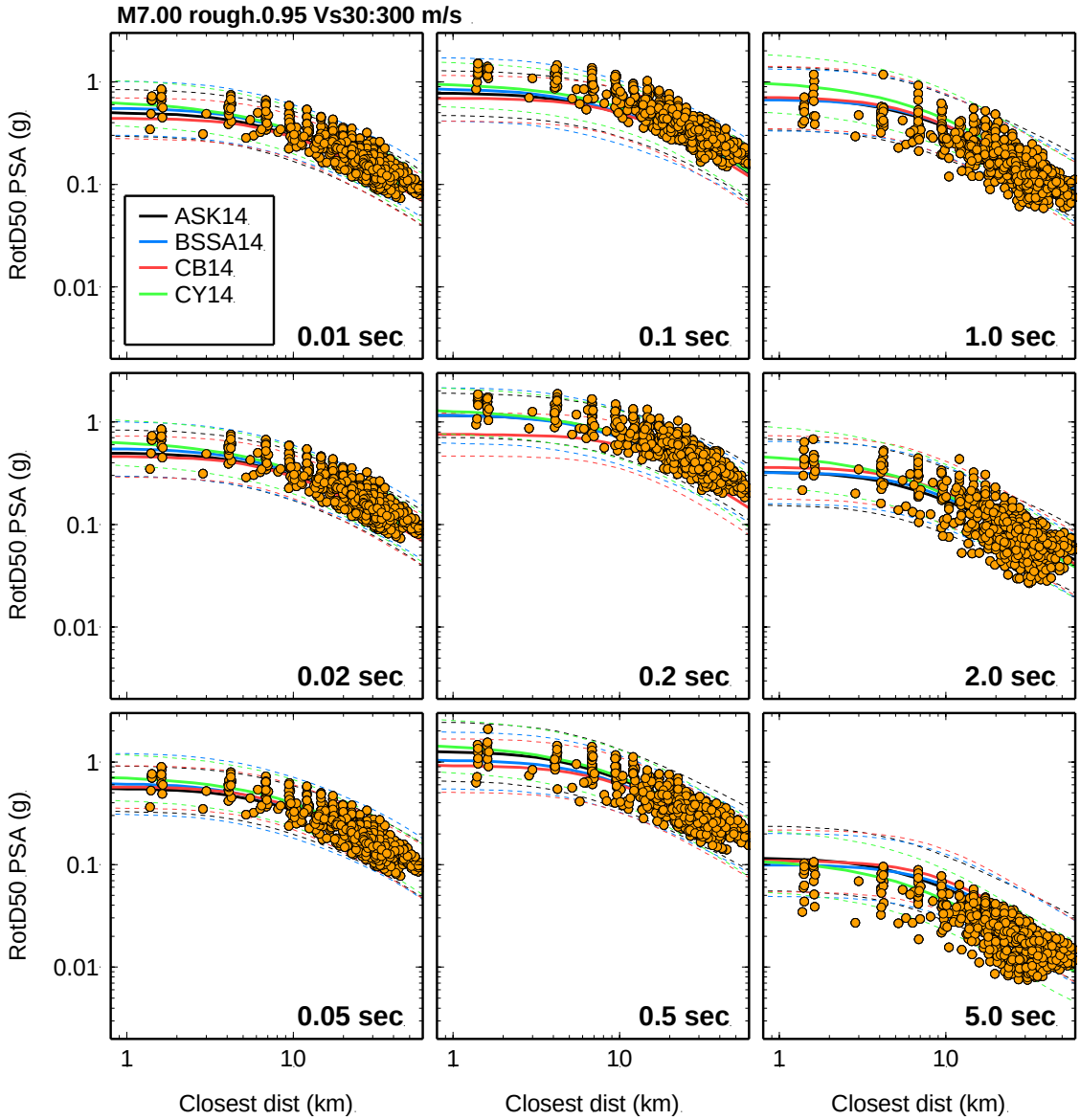

Figure A.2.2-20. Comparison of RotD50 acceleration response spectra (yellow circles), computed at 500 near-fault stations, using rupture scenario with **slip roughness coeff =0.95,** with four GMPEs for Vs30=300m/s

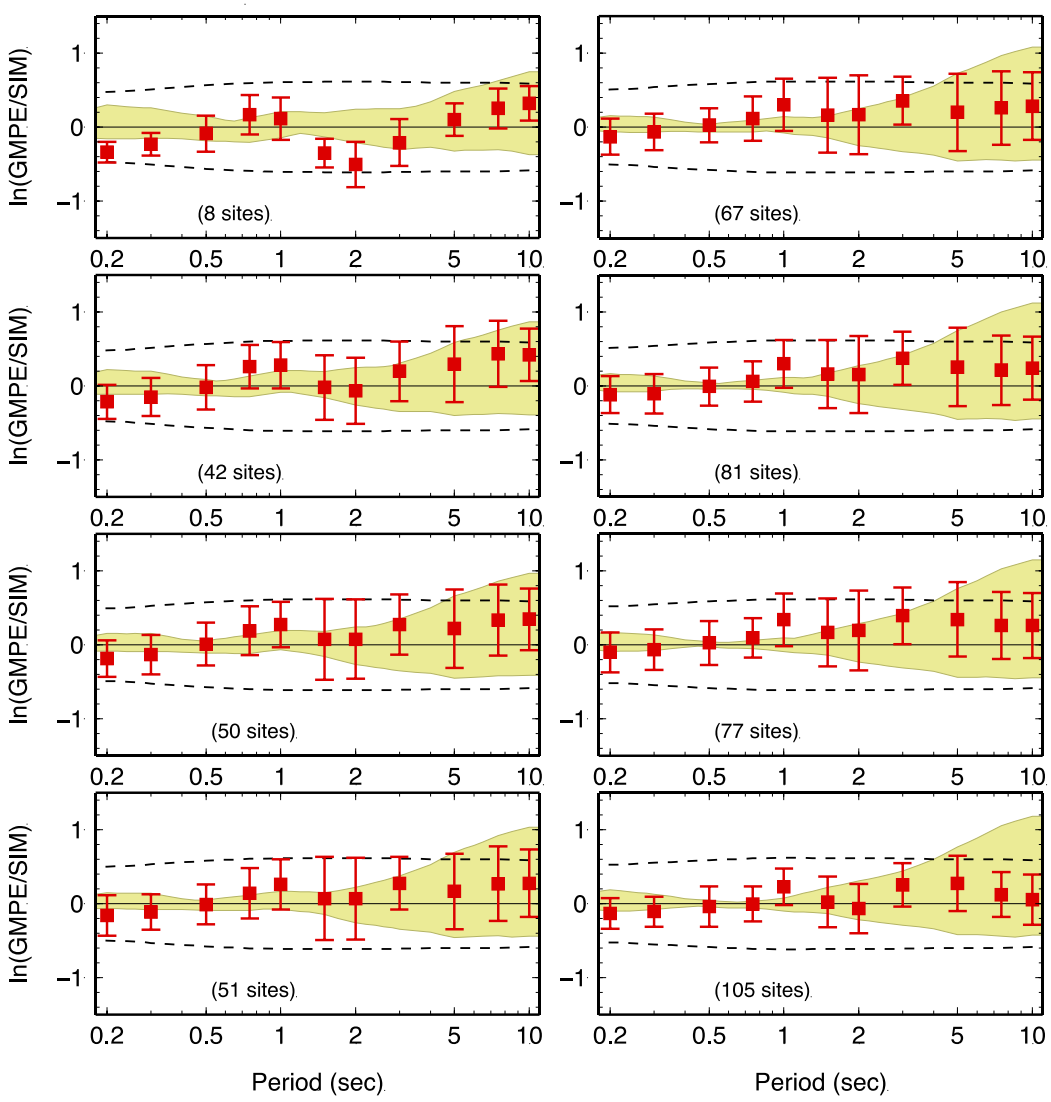

Figure A.2.2-21. Bias between the GMPEs and simulated ground motion computed as the ln(GMPE/SIM) RotD50 spectral acceleration ratio as a function of period, averaged over stations with same fault distance. The fault distance and the number of sites for each distance bin is indicated on each panel. Red squares and red vertical lines indicate the median value and +/- one standard deviation of the bias. The synthetics are computed for a rupture scenario with **Vr/Vs ratio = 0.538.**

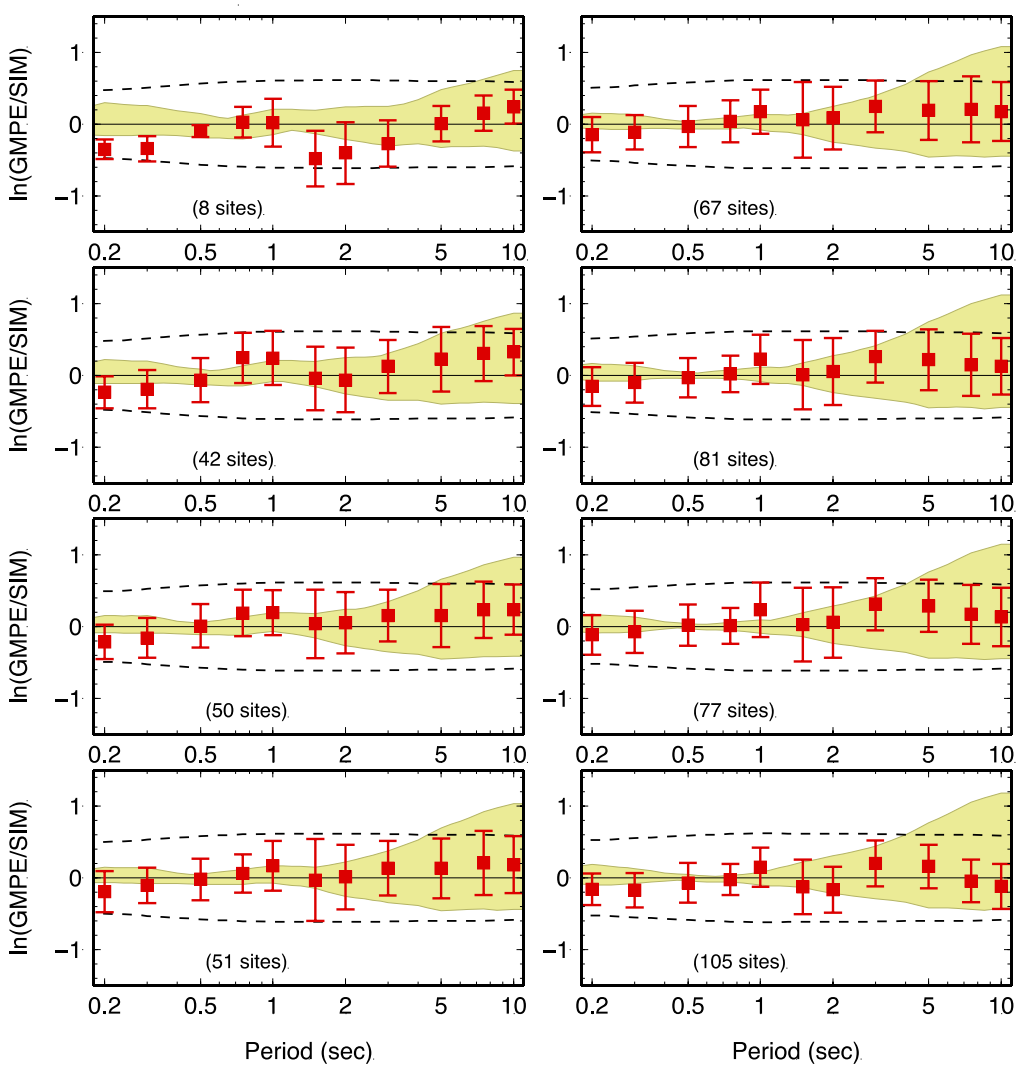

Figure A.2.2-22. Bias between the GMPEs and simulated ground motion computed as the ln(GMPE/SIM) RotD50 spectral acceleration ratio as a function of period, averaged over stations with same fault distance. The fault distance and the number of sites for each distance bin is indicated on each panel. Red squares and red vertical lines indicate the median value and +/- one standard deviation of the bias. The synthetics are computed for a rupture scenario with

Vr/Vs ratio = 0.616

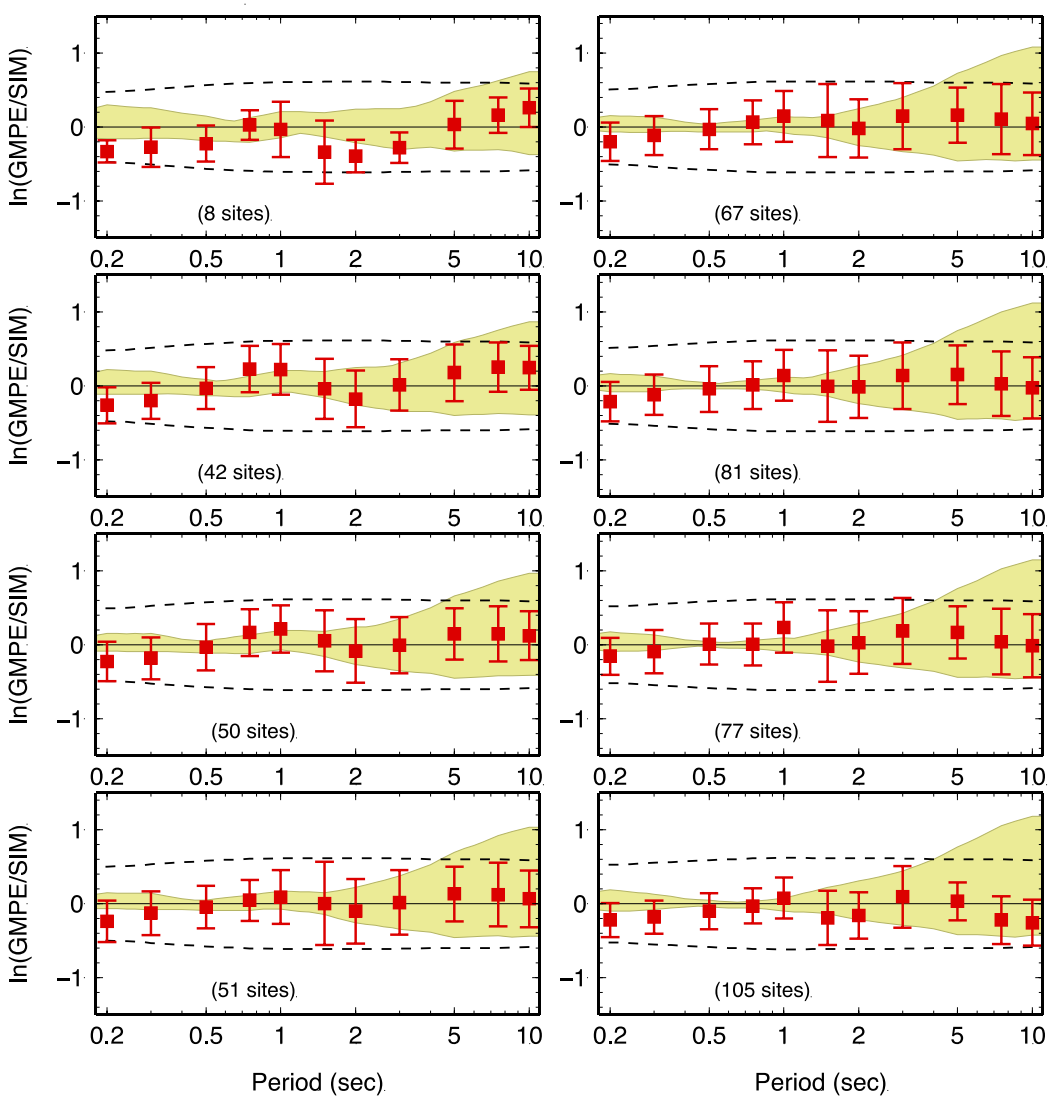

Figure A.2.2-23. Bias between the GMPEs and simulated ground motion computed as the ln(GMPE/SIM) RotD50 spectral acceleration ratio as a function of period, averaged over stations with same fault distance. The fault distance and the number of sites for each distance bin is indicated on each panel. Red squares and red vertical lines indicate the median value and +/- one standard deviation of the bias. The synthetics are computed for a rupture scenario with

Vr/Vs ratio = 0.694

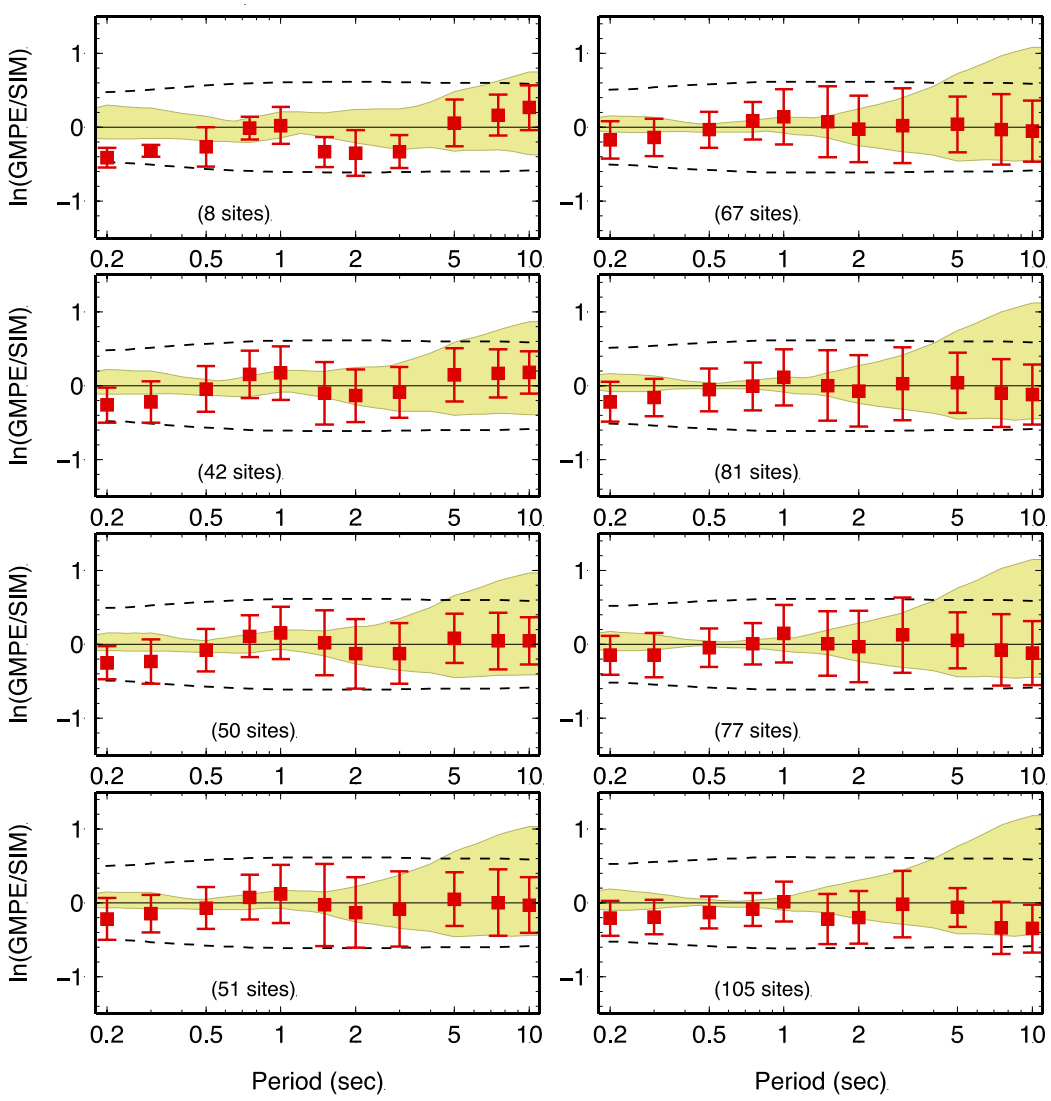

Figure A.2.2-24. Bias between the GMPEs and simulated ground motion computed as the ln(GMPE/SIM) RotD50 spectral acceleration ratio as a function of period, averaged over stations with same fault distance. The fault distance and the number of sites for each distance bin is indicated on each panel. Red squares and red vertical lines indicate the median value and +/- one standard deviation of the bias. The synthetics are computed for a rupture scenario with

Vr/Vs ratio = 0.772

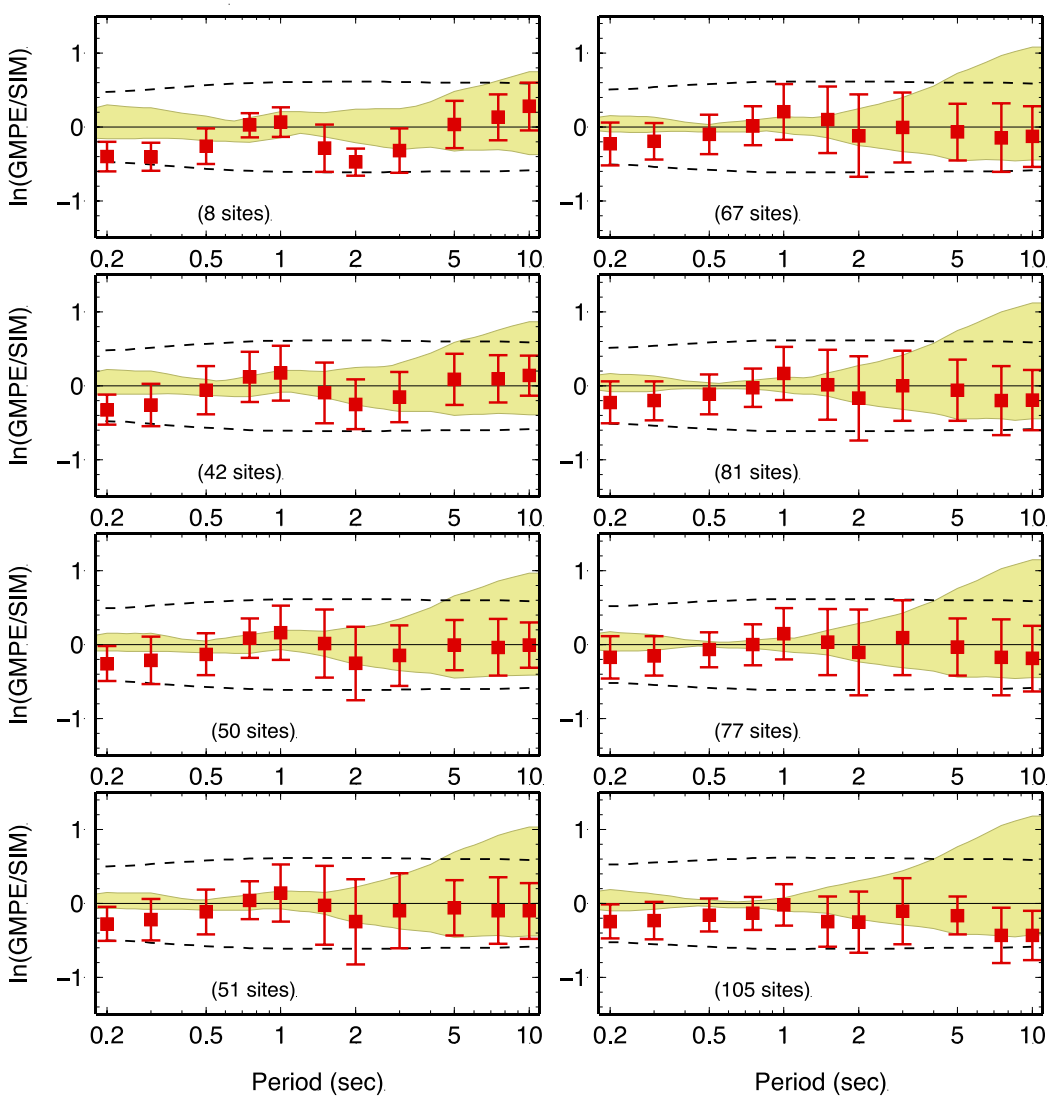

Figure A.2.2-25. Bias between the GMPEs and simulated ground motion computed as the ln(GMPE/SIM) RotD50 spectral acceleration ratio as a function of period, averaged over stations with same fault distance. The fault distance and the number of sites for each distance bin is indicated on each panel. Red squares and red vertical lines indicate the median value and +/- one standard deviation of the bias. The synthetics are computed for a rupture scenario with **Vr/Vs ratio = 0.85**

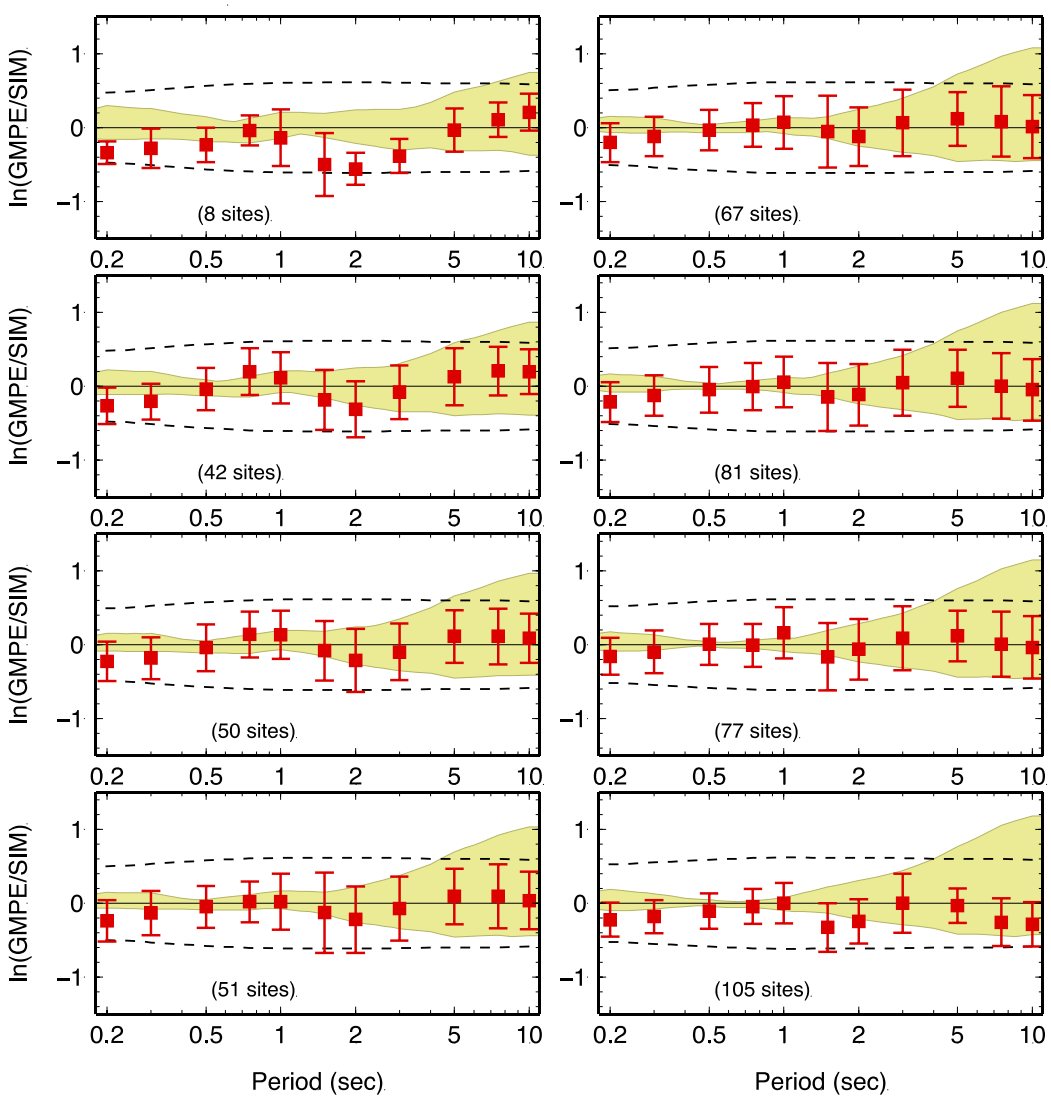

Figure A.2.2-26. Bias between the GMPEs and simulated ground motion computed as the ln(GMPE/SIM) RotD50 spectral acceleration ratio as a function of period, averaged over stations with same fault distance. The fault distance and the number of sites for each distance bin is indicated on each panel. Red squares and red vertical lines indicate the median value and +/- one standard deviation of the bias. The synthetics are computed for a rupture scenario with

Vr/Vs ratio = 0.96

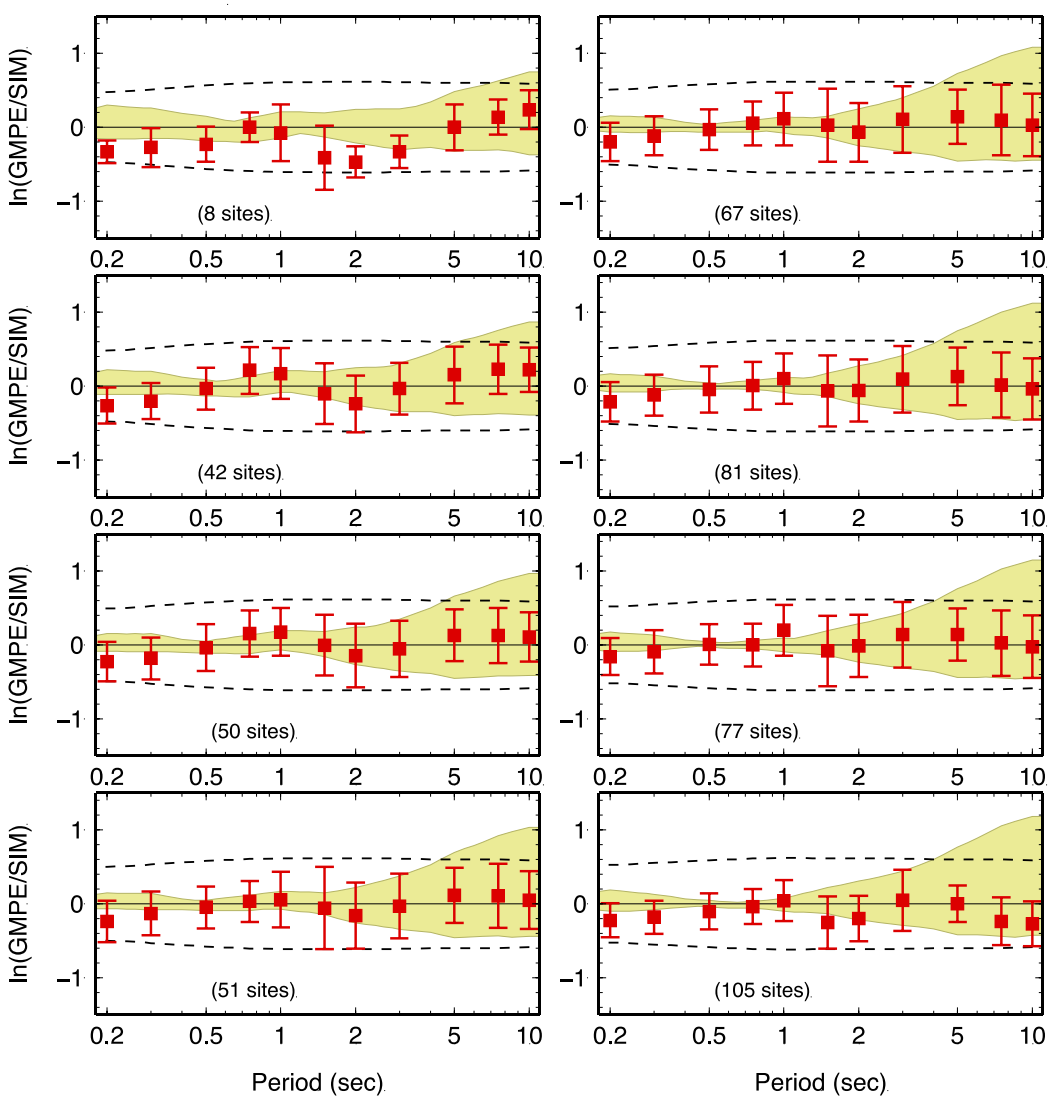

Figure A.2.2-27. Bias between the GMPEs and simulated ground motion computed as the ln(GMPE/SIM) RotD50 spectral acceleration ratio as a function of period, averaged over stations with same fault distance. The fault distance and the number of sites for each distance bin is indicated on each panel. Red squares and red vertical lines indicate the median value and +/- one standard deviation of the bias. The synthetics are computed for a rupture scenario with **rise time factor = 1.28**

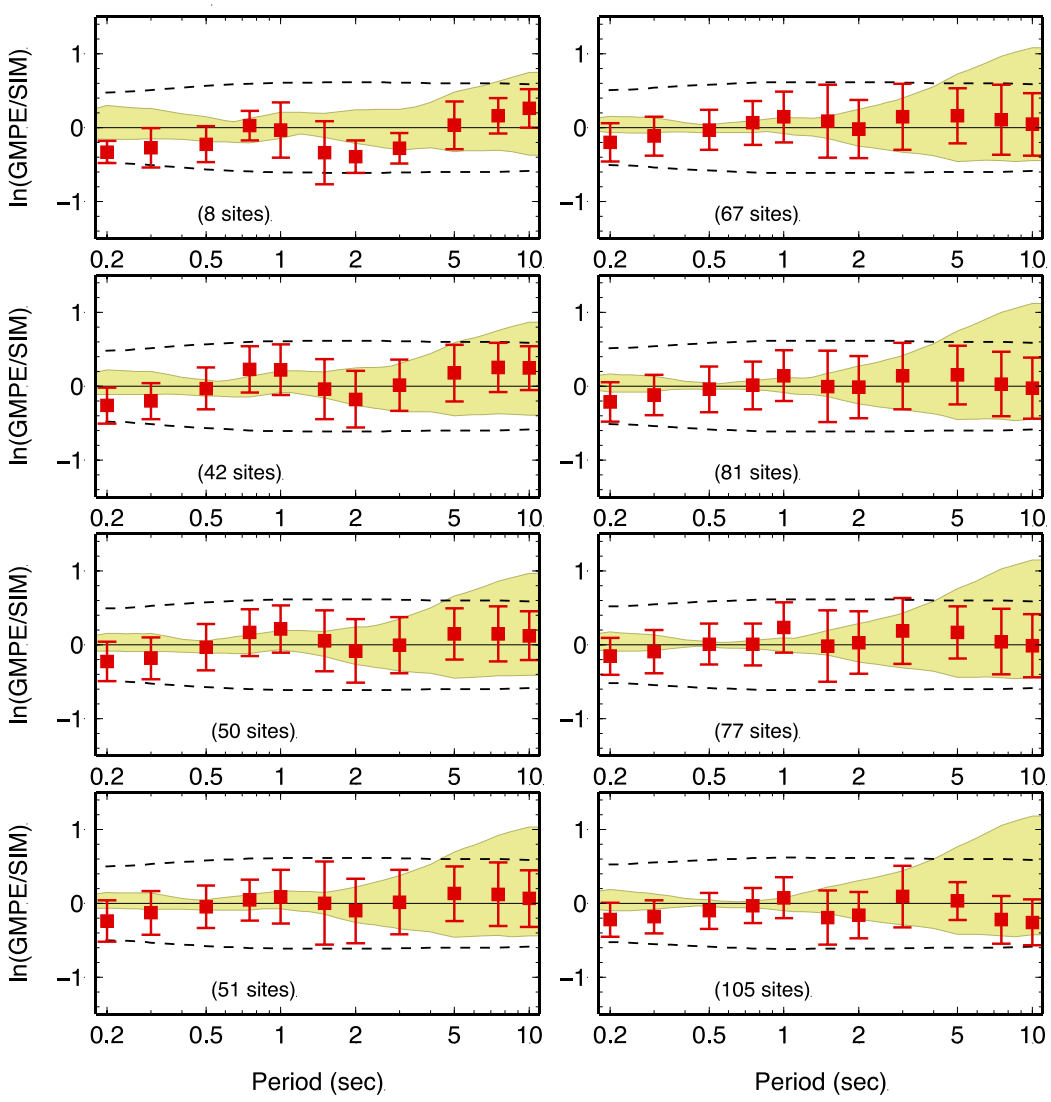

Figure A.2.2-28. Bias between the GMPEs and simulated ground motion computed as the ln(GMPE/SIM) RotD50 spectral acceleration ratio as a function of period, averaged over stations with same fault distance. The fault distance and the number of sites for each distance bin is indicated on each panel. Red squares and red vertical lines indicate the median value and +/- one standard deviation of the bias. The synthetics are computed for a rupture scenario with **rise time factor = 1.28**

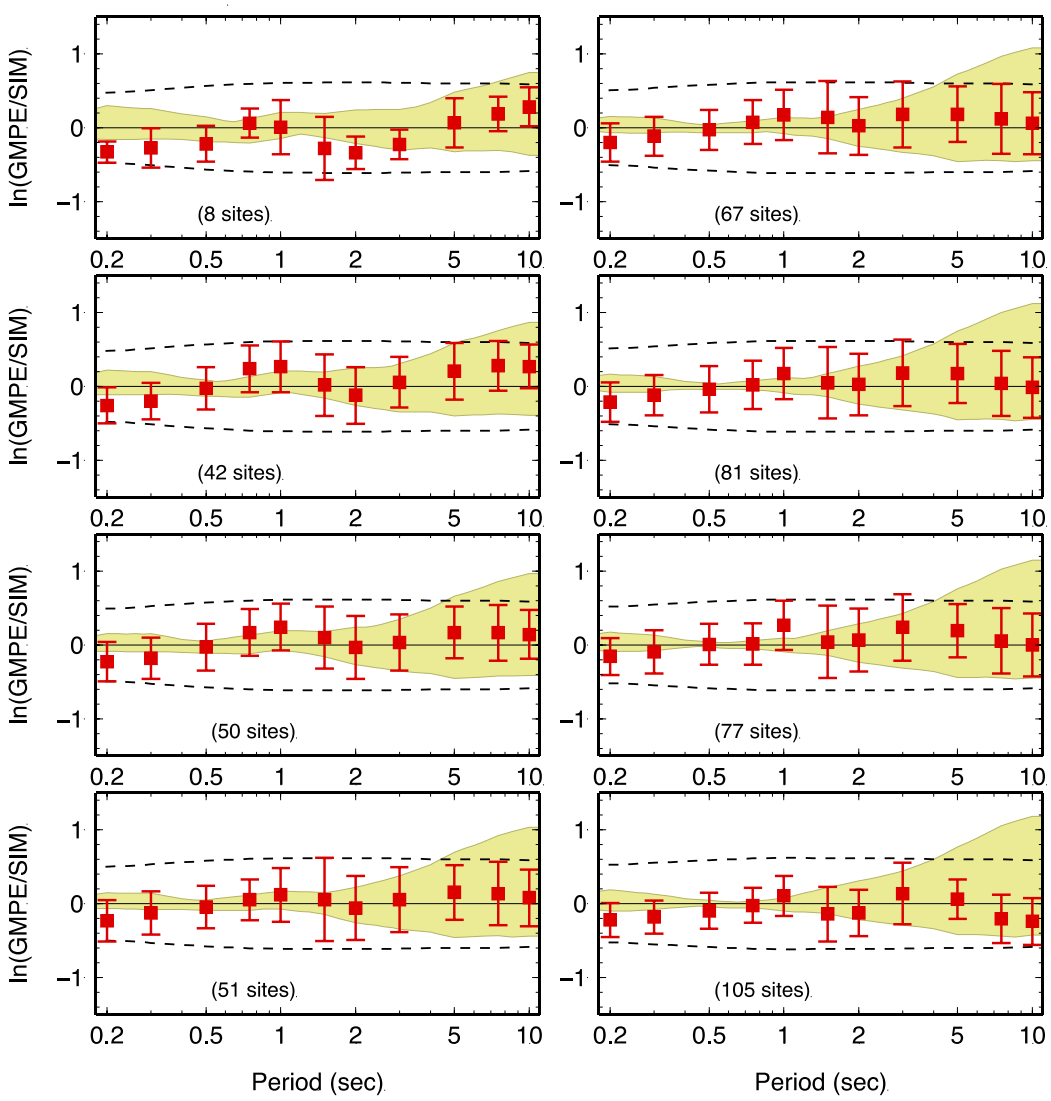

Figure A.2.2-29. Bias between the GMPEs and simulated ground motion computed as the ln(GMPE/SIM) RotD50 spectral acceleration ratio as a function of period, averaged over stations with same fault distance. The fault distance and the number of sites for each distance bin is indicated on each panel. Red squares and red vertical lines indicate the median value and +/- one standard deviation of the bias. The synthetics are computed for a rupture scenario with **rise time factor = 1.92**

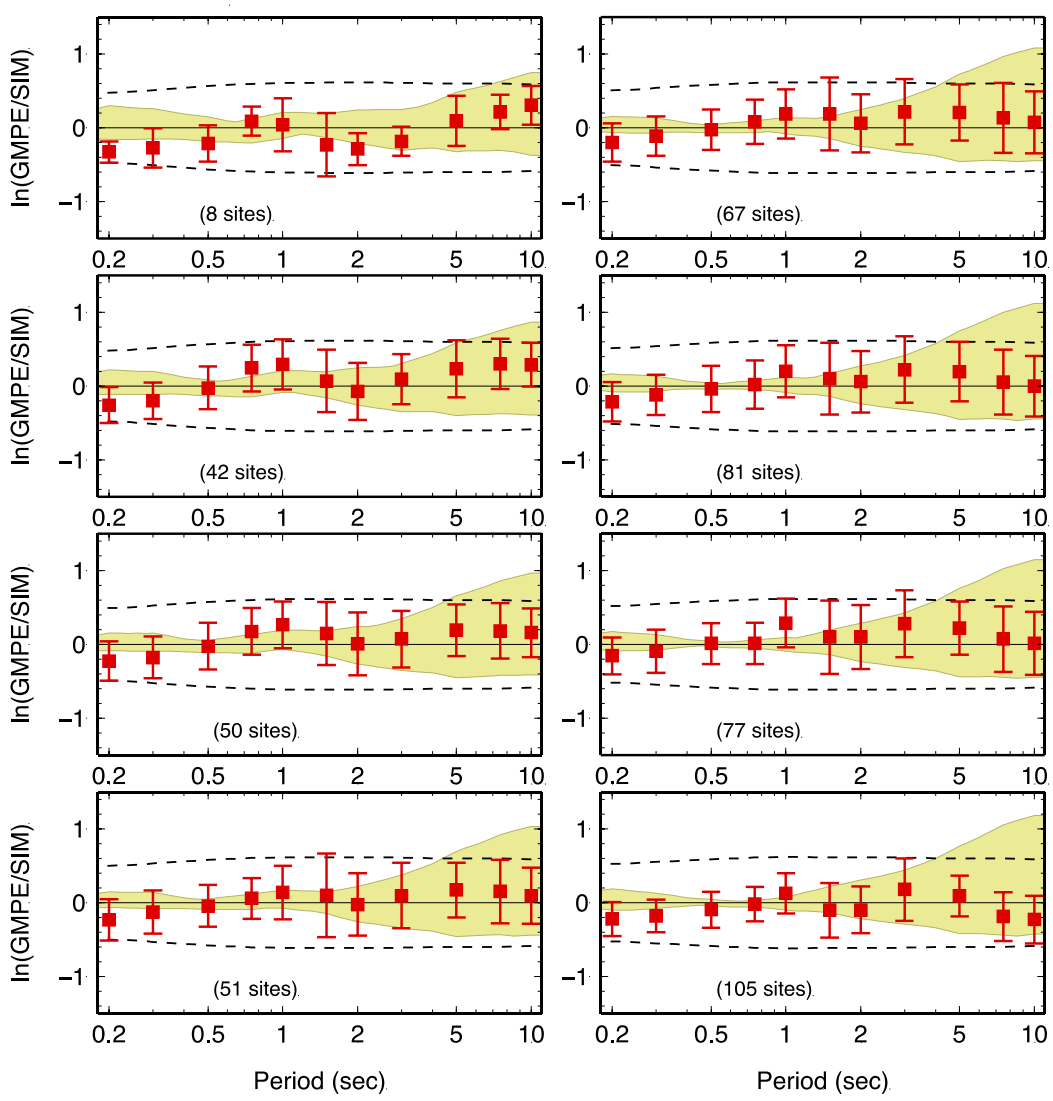

Figure A.2.2-30. Bias between the GMPEs and simulated ground motion computed as the ln(GMPE/SIM) RotD50 spectral acceleration ratio as a function of period, averaged over stations with same fault distance. The fault distance and the number of sites for each distance bin is indicated on each panel. Red squares and red vertical lines indicate the median value and +/- one standard deviation of the bias. The synthetics are computed for a rupture scenario with **rise time factor = 2.24**

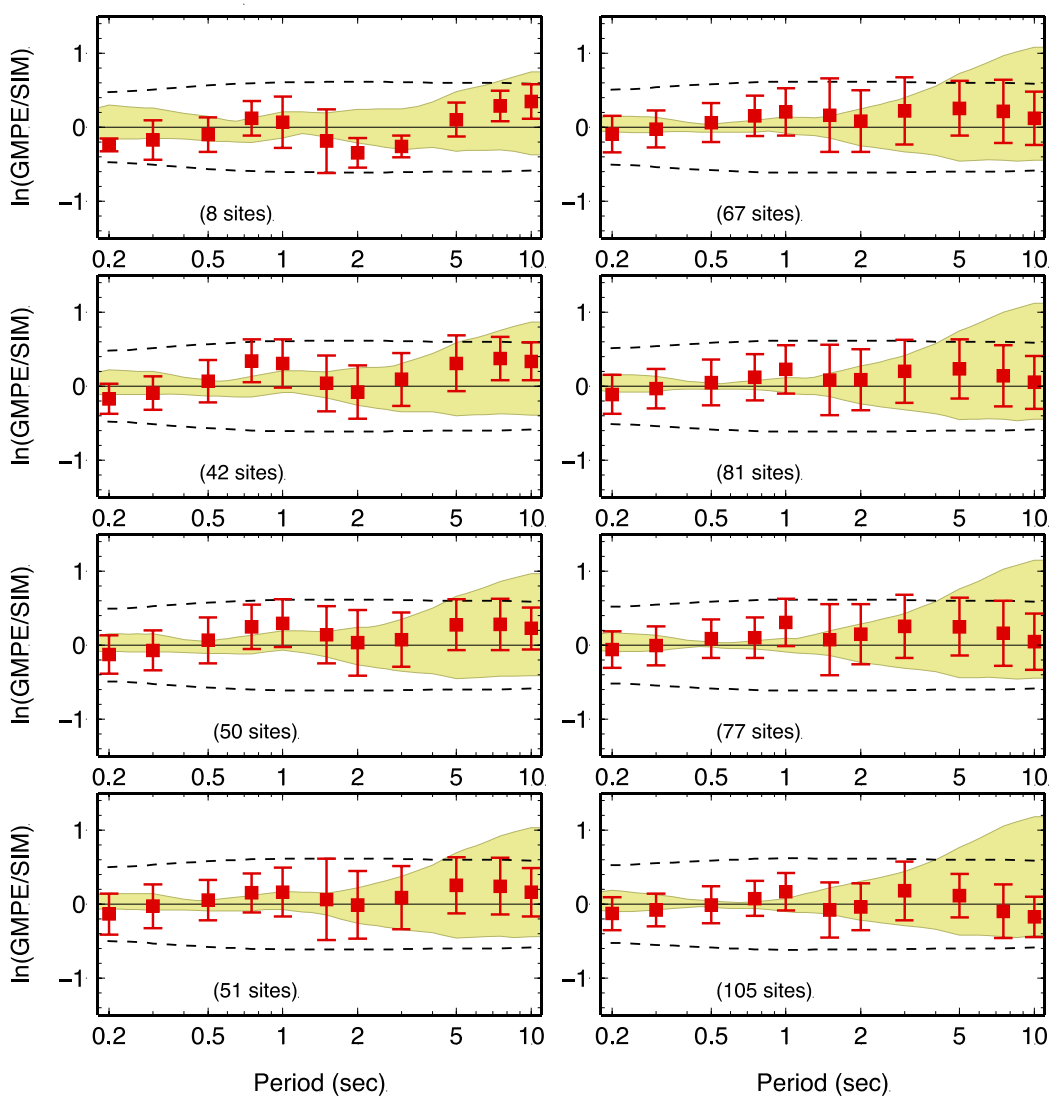

Figure A.2.2-31. Bias between the GMPEs and simulated ground motion computed as the ln(GMPE/SIM) RotD50 spectral acceleration ratio as a function of period, averaged over stations with same fault distance. The fault distance and the number of sites for each distance bin is indicated on each panel. Red squares and red vertical lines indicate the median value and +/- one standard deviation of the bias. The synthetics are computed for a rupture scenario with **slip roughness factor = 0.5**

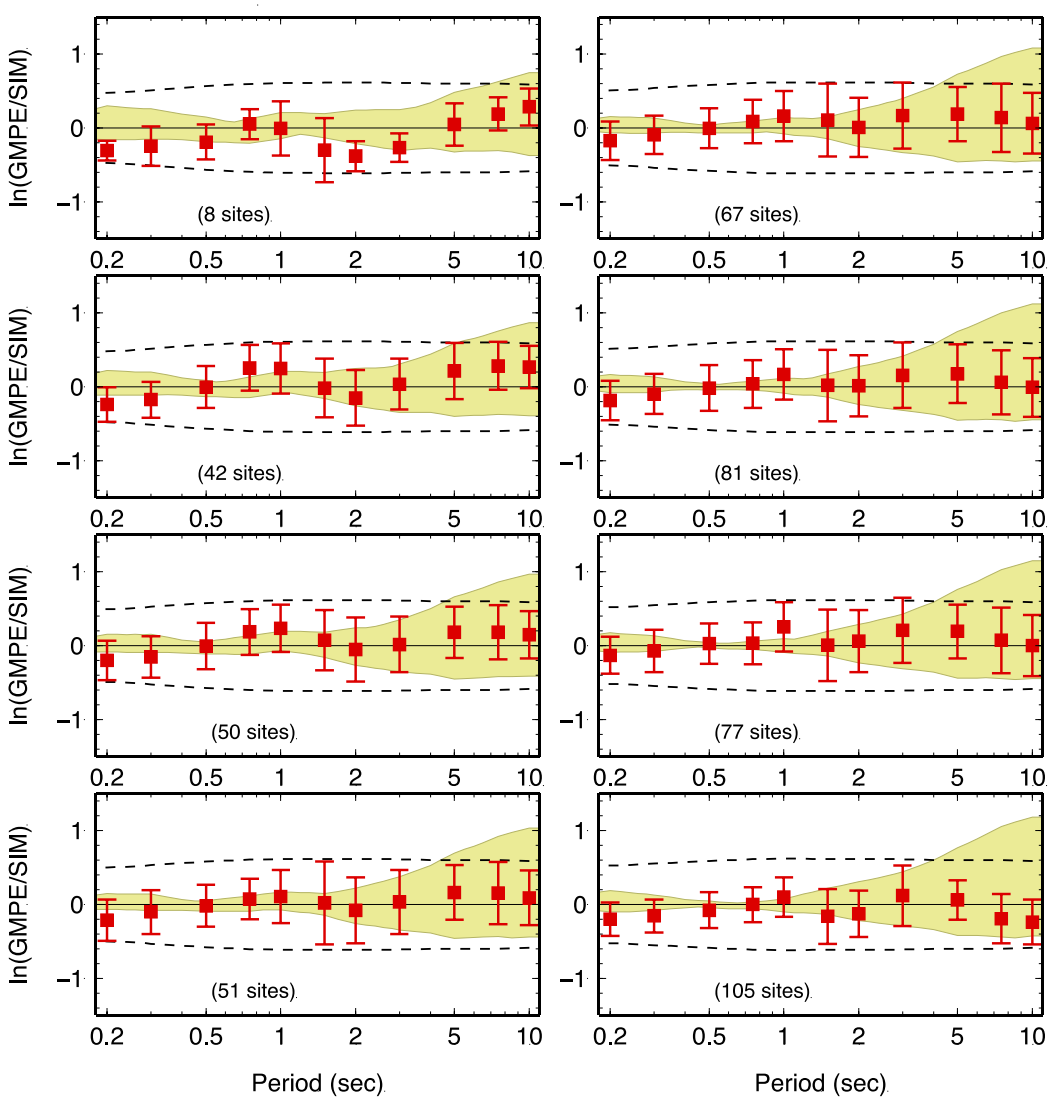

Figure A.2.2-32. Bias between the GMPEs and simulated ground motion computed as the ln(GMPE/SIM) RotD50 spectral acceleration ratio as a function of period, averaged over stations with same fault distance. The fault distance and the number of sites for each distance bin is indicated on each panel. Red squares and red vertical lines indicate the median value and +/- one standard deviation of the bias. The synthetics are computed for a rupture scenario with **slip roughness factor = 0.75**

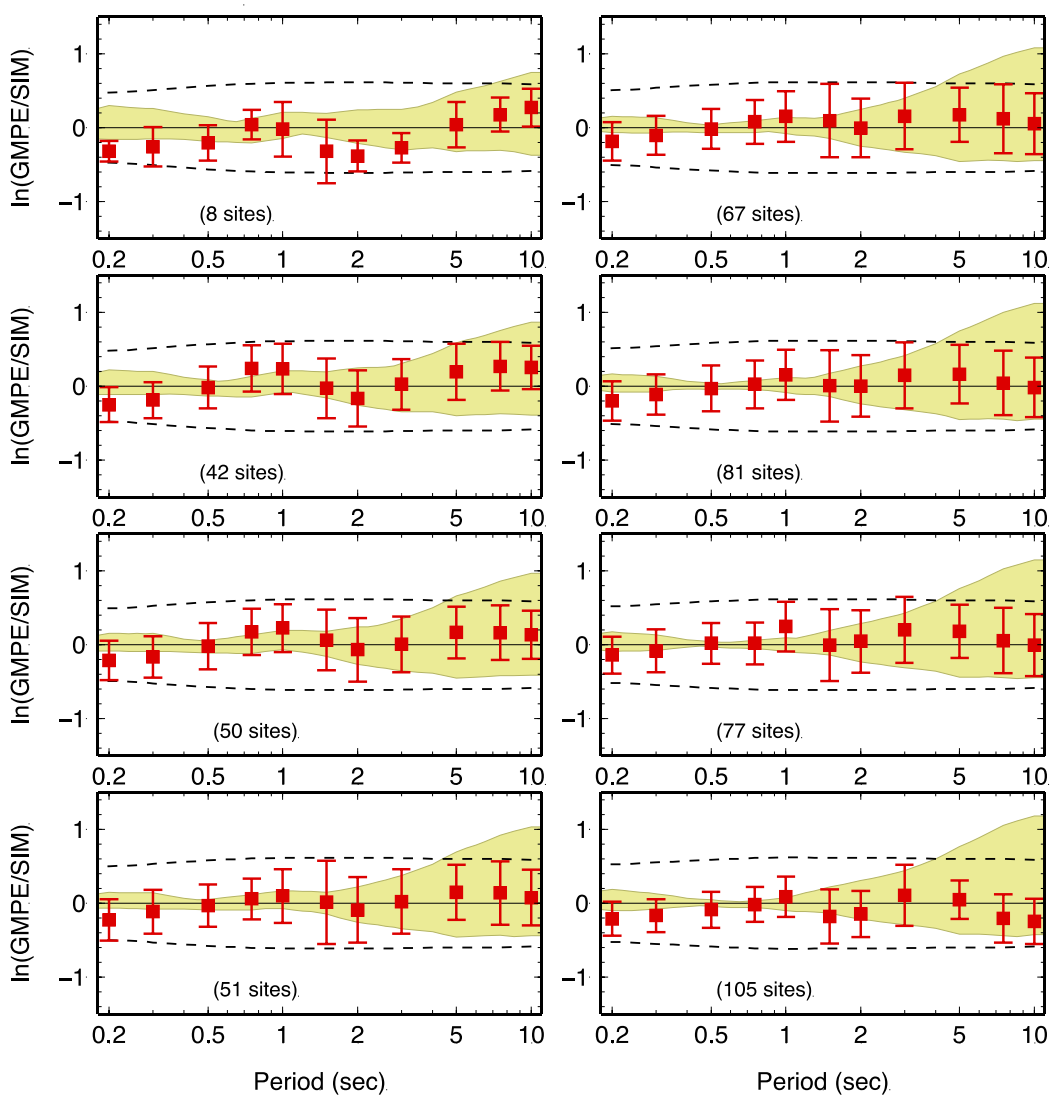

Figure A.2.2-33. Bias between the GMPEs and simulated ground motion computed as the ln(GMPE/SIM) RotD50 spectral acceleration ratio as a function of period, averaged over stations with same fault distance. The fault distance and the number of sites for each distance bin is indicated on each panel. Red squares and red vertical lines indicate the median value and +/- one standard deviation of the bias. The synthetics are computed for a rupture scenario with **slip roughness factor = 0.8**

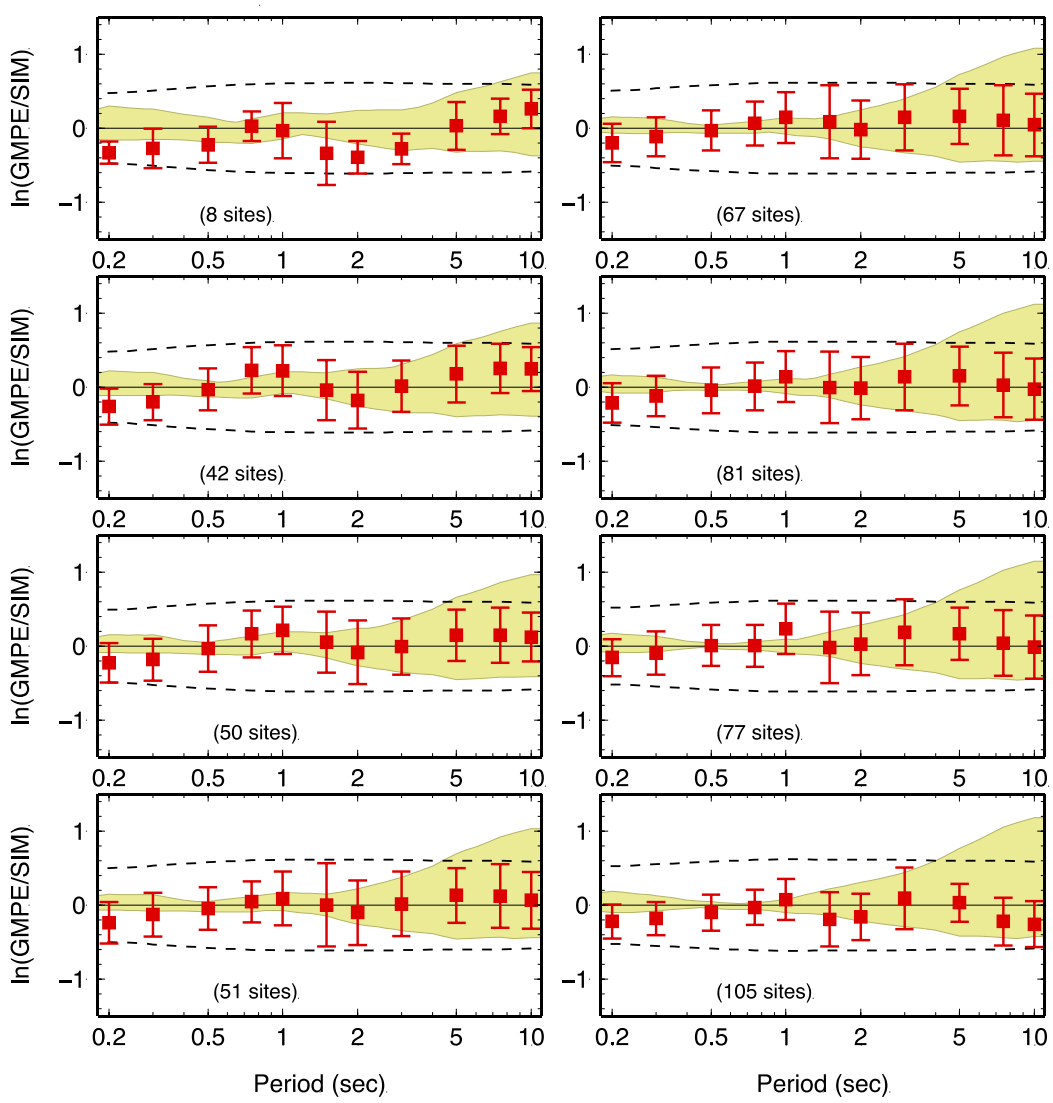

Figure A.2.2-34. Bias between the GMPEs and simulated ground motion computed as the ln(GMPE/SIM) RotD50 spectral acceleration ratio as a function of period, averaged over stations with same fault distance. The fault distance and the number of sites for each distance bin is indicated on each panel. Red squares and red vertical lines indicate the median value and +/- one standard deviation of the bias. The synthetics are computed for a rupture scenario with **slip roughness factor = 0.85**

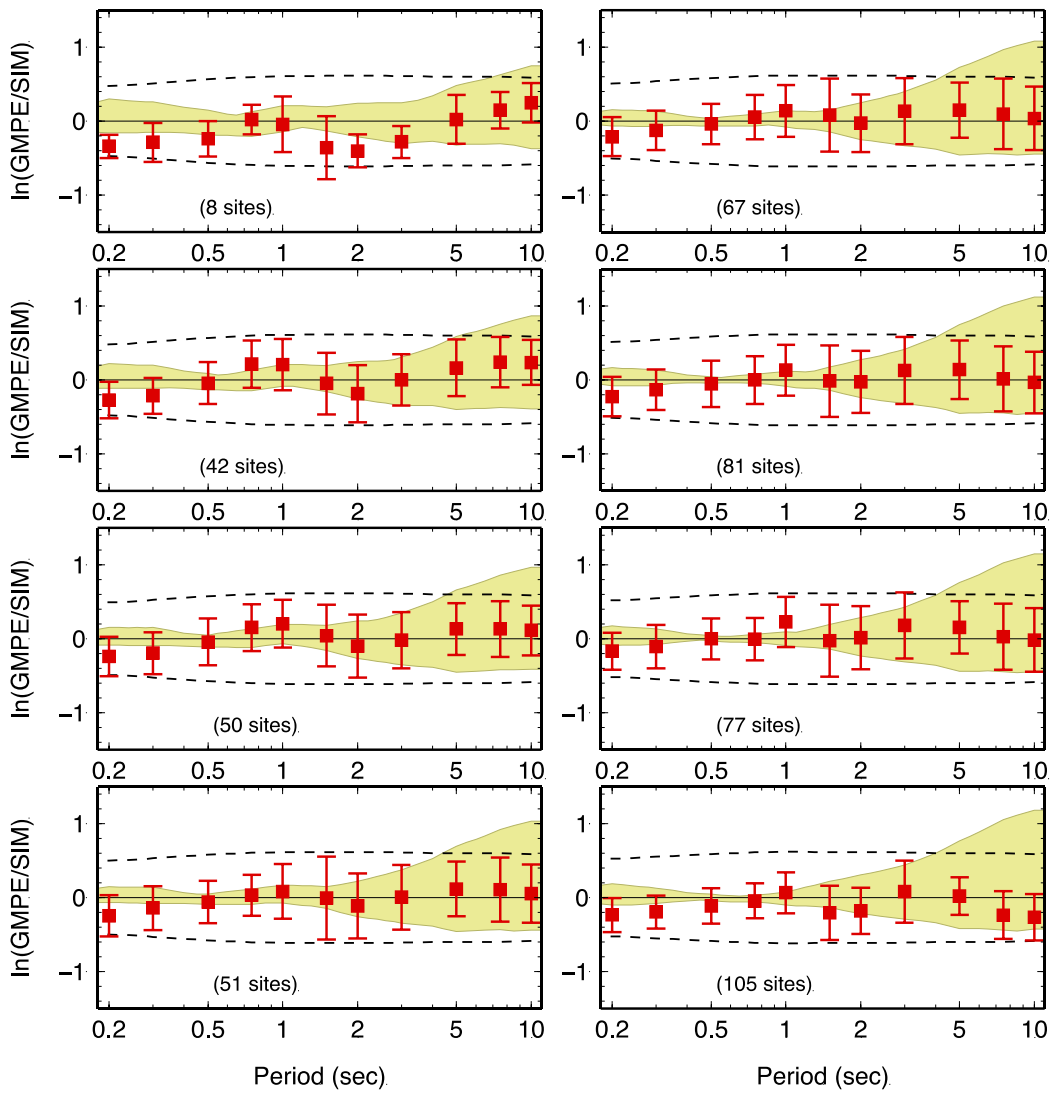

Figure A.2.2-35. Bias between the GMPEs and simulated ground motion computed as the ln(GMPE/SIM) RotD50 spectral acceleration ratio as a function of period, averaged over stations with same fault distance. The fault distance and the number of sites for each distance bin is indicated on each panel. Red squares and red vertical lines indicate the median value and +/- one standard deviation of the bias. The synthetics are computed for a rupture scenario with **slip roughness factor = 0.9**

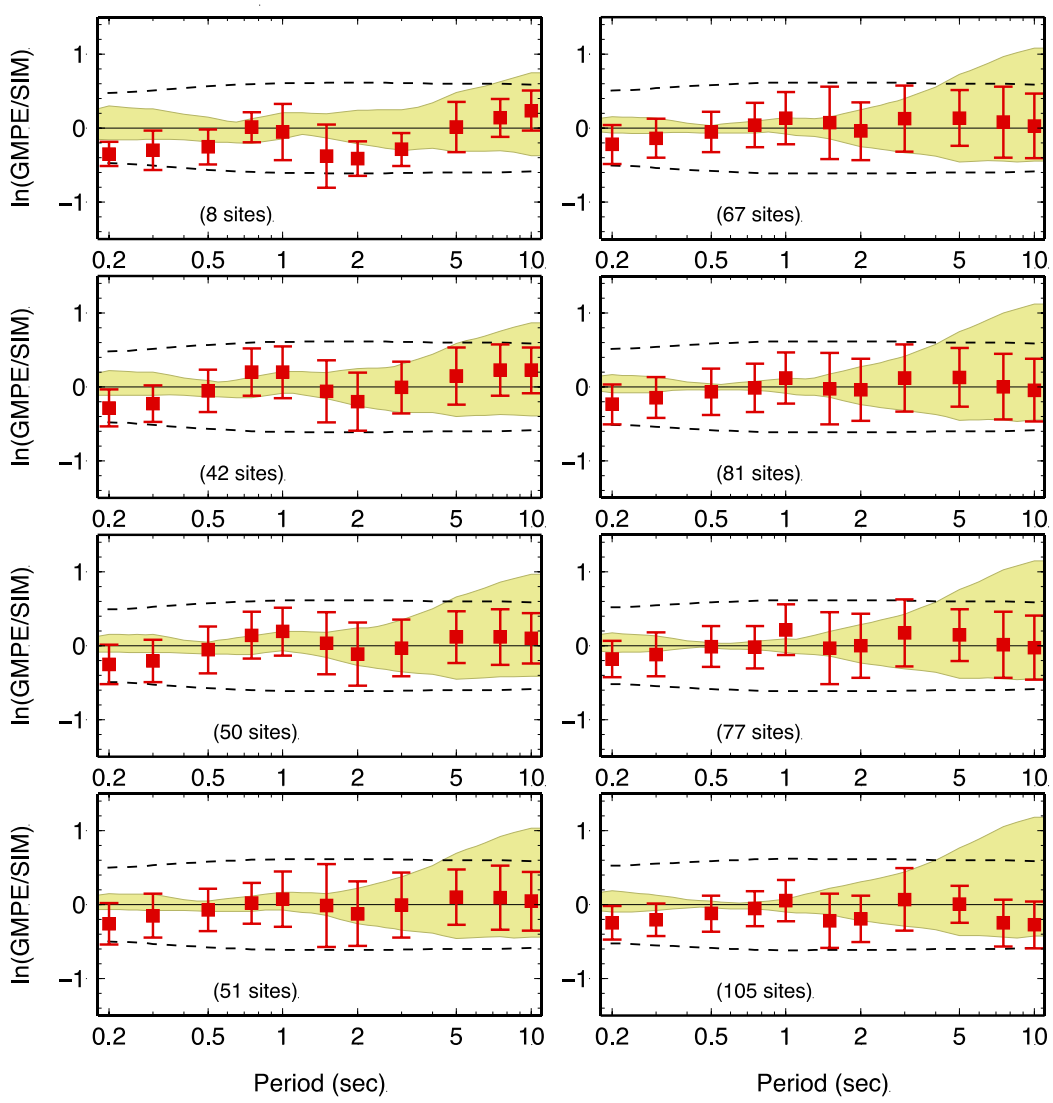

Figure A.2.2-36. Bias between the GMPEs and simulated ground motion computed as the ln(GMPE/SIM) RotD50 spectral acceleration ratio as a function of period, averaged over stations with same fault distance. The fault distance and the number of sites for each distance bin is indicated on each panel. Red squares and red vertical lines indicate the median value and +/- one standard deviation of the bias. The synthetics are computed for a rupture scenario with **slip roughness factor = 0.95**

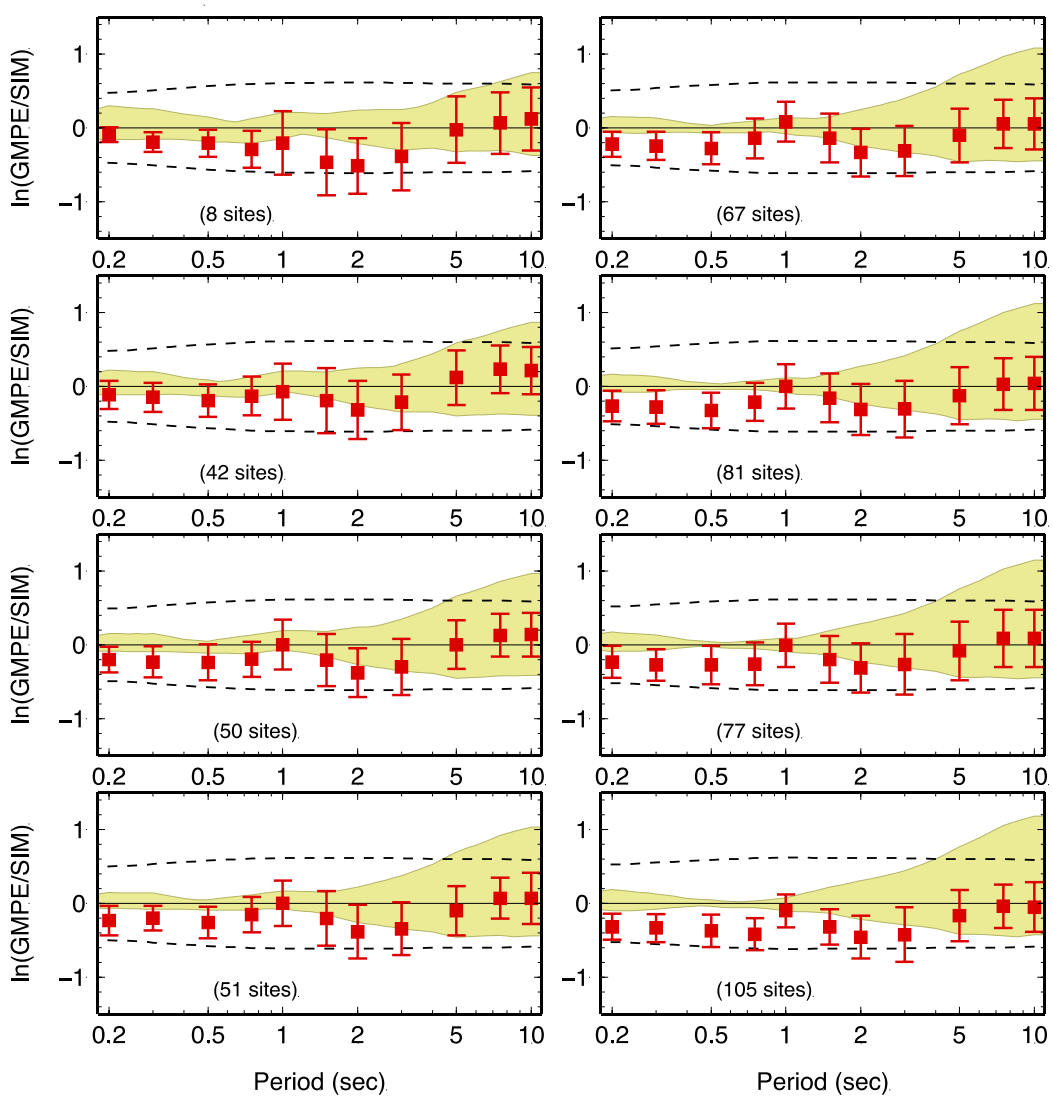

Figure A.2.2-37. Bias between the GMPEs and simulated ground motion computed as the ln(GMPE/SIM) RotD50 spectral acceleration ratio as a function of period, averaged over stations with same fault distance. The fault distance and the number of sites for each distance bin is indicated on each panel. Red squares and red vertical lines indicate the median value and +/- one standard deviation of the bias. The synthetics are computed for a rupture scenario with **slip generator seed = s1**

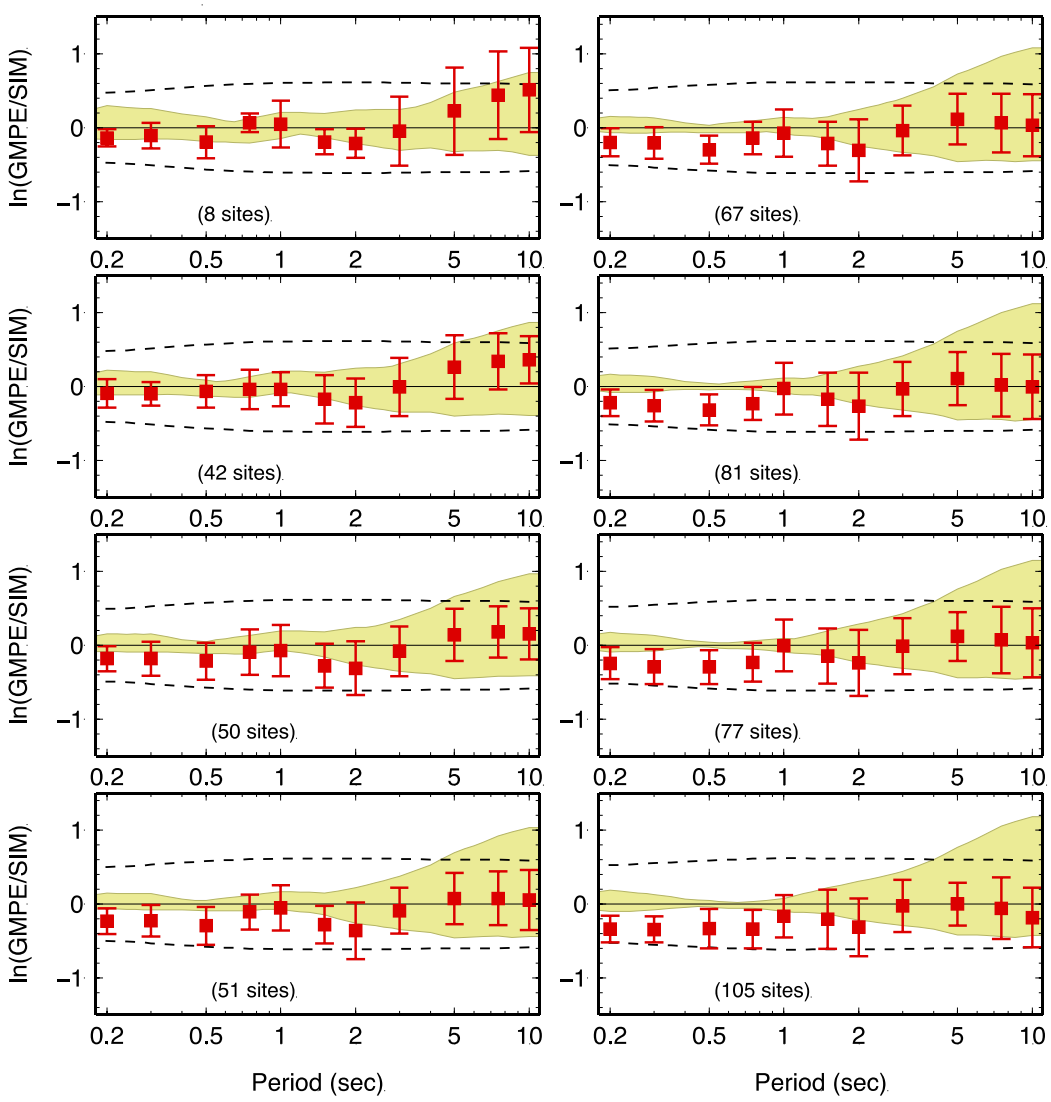

Figure A.2.2-38. Bias between the GMPEs and simulated ground motion computed as the ln(GMPE/SIM) RotD50 spectral acceleration ratio as a function of period, averaged over stations with same fault distance. The fault distance and the number of sites for each distance bin is indicated on each panel. Red squares and red vertical lines indicate the median value and +/- one standard deviation of the bias. The synthetics are computed for a rupture scenario with **slip generator seed = s2**

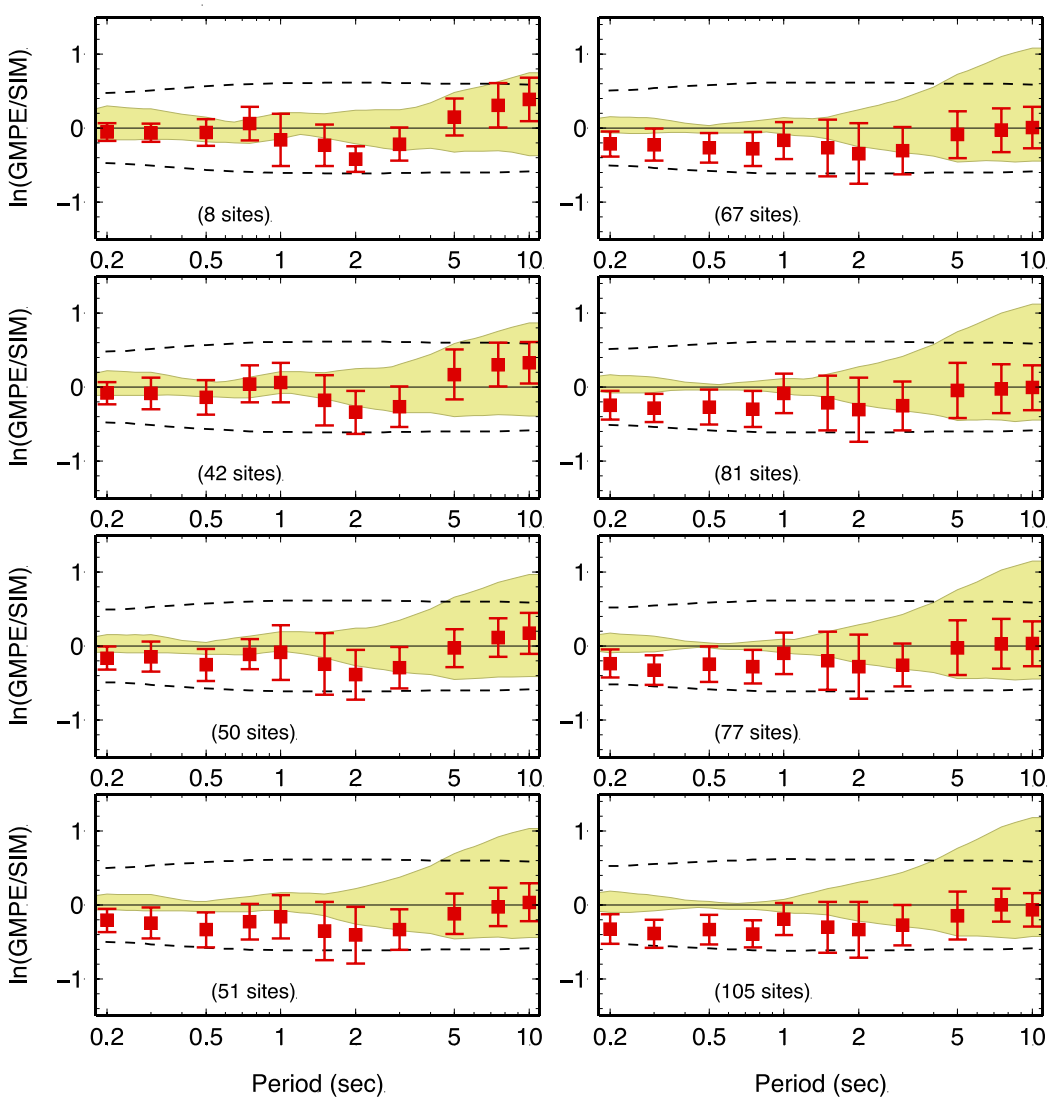

Figure A.2.2-39. Bias between the GMPEs and simulated ground motion computed as the ln(GMPE/SIM) RotD50 spectral acceleration ratio as a function of period, averaged over stations with same fault distance. The fault distance and the number of sites for each distance bin is indicated on each panel. Red squares and red vertical lines indicate the median value and +/- one standard deviation of the bias. The synthetics are computed for a rupture scenario with **slip generator seed = s3**

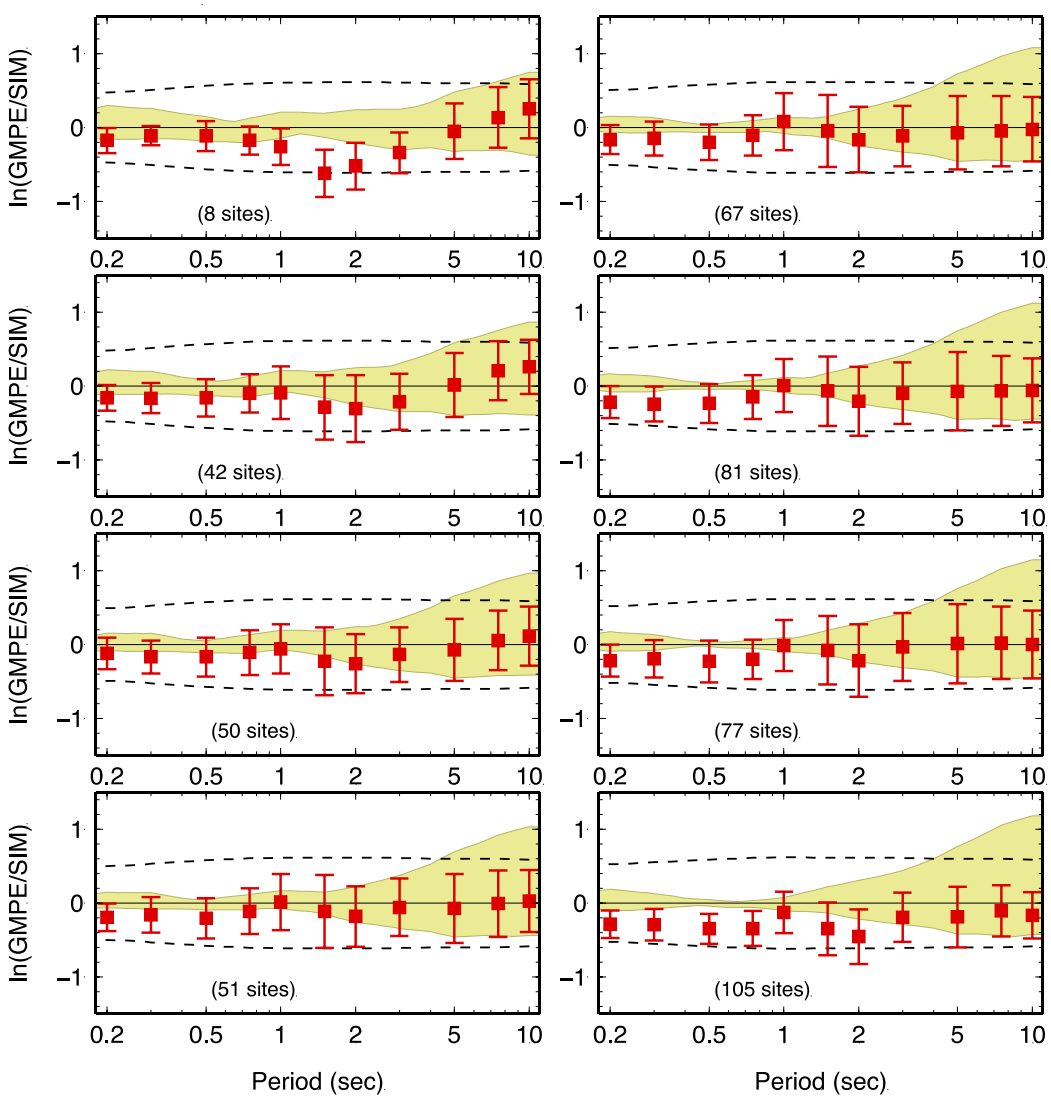

Figure A.2.2-40. Bias between the GMPEs and simulated ground motion computed as the ln(GMPE/SIM) RotD50 spectral acceleration ratio as a function of period, averaged over stations with same fault distance. The fault distance and the number of sites for each distance bin is indicated on each panel. Red squares and red vertical lines indicate the median value and +/- one standard deviation of the bias. The synthetics are computed for a rupture scenario with **slip generator seed = s4**

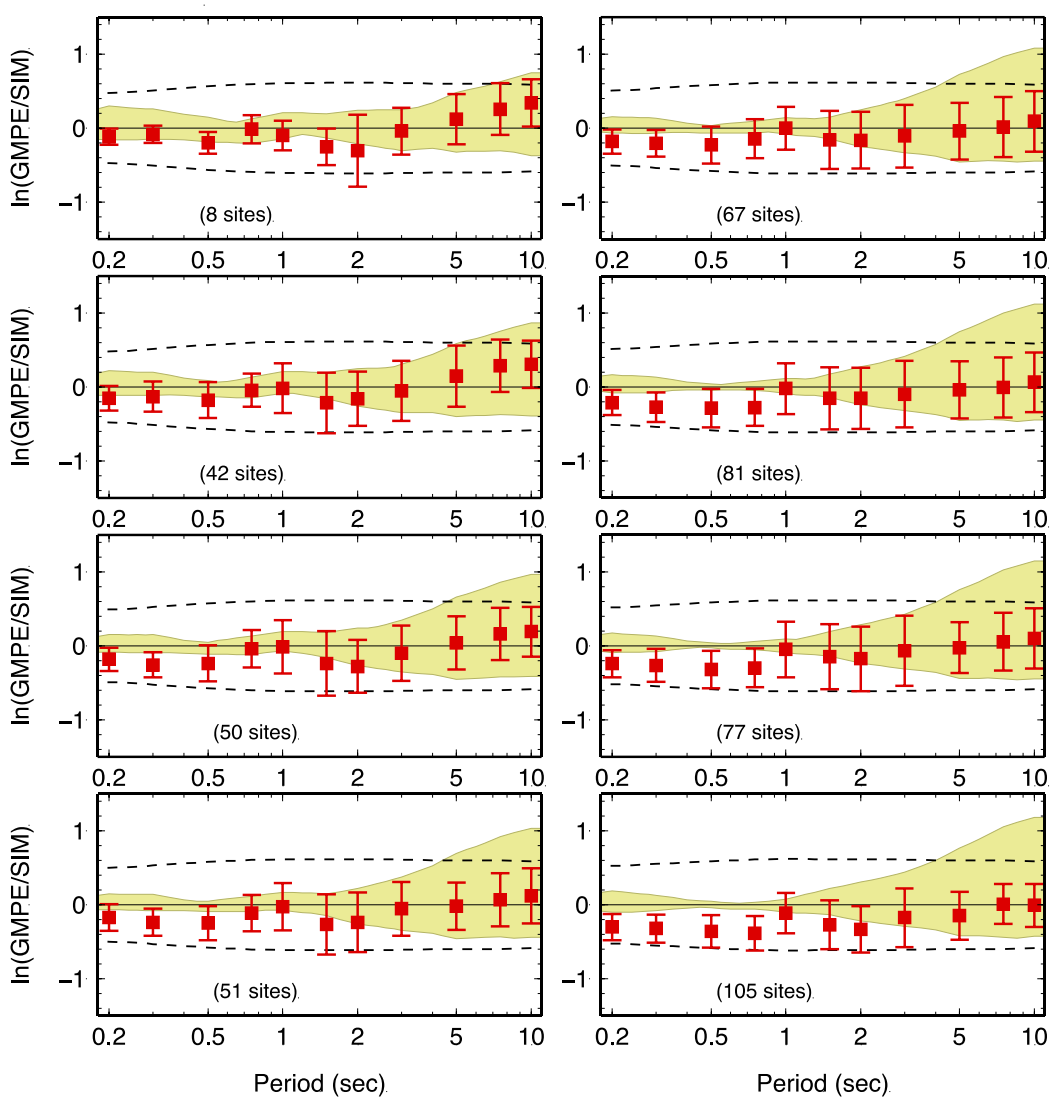

Figure A.2.2-41. Bias between the GMPEs and simulated ground motion computed as the ln(GMPE/SIM) RotD50 spectral acceleration ratio as a function of period, averaged over stations with same fault distance. The fault distance and the number of sites for each distance bin is indicated on each panel. Red squares and red vertical lines indicate the median value and +/- one standard deviation of the bias. The synthetics are computed for a rupture scenario with **slip generator seed = s5**

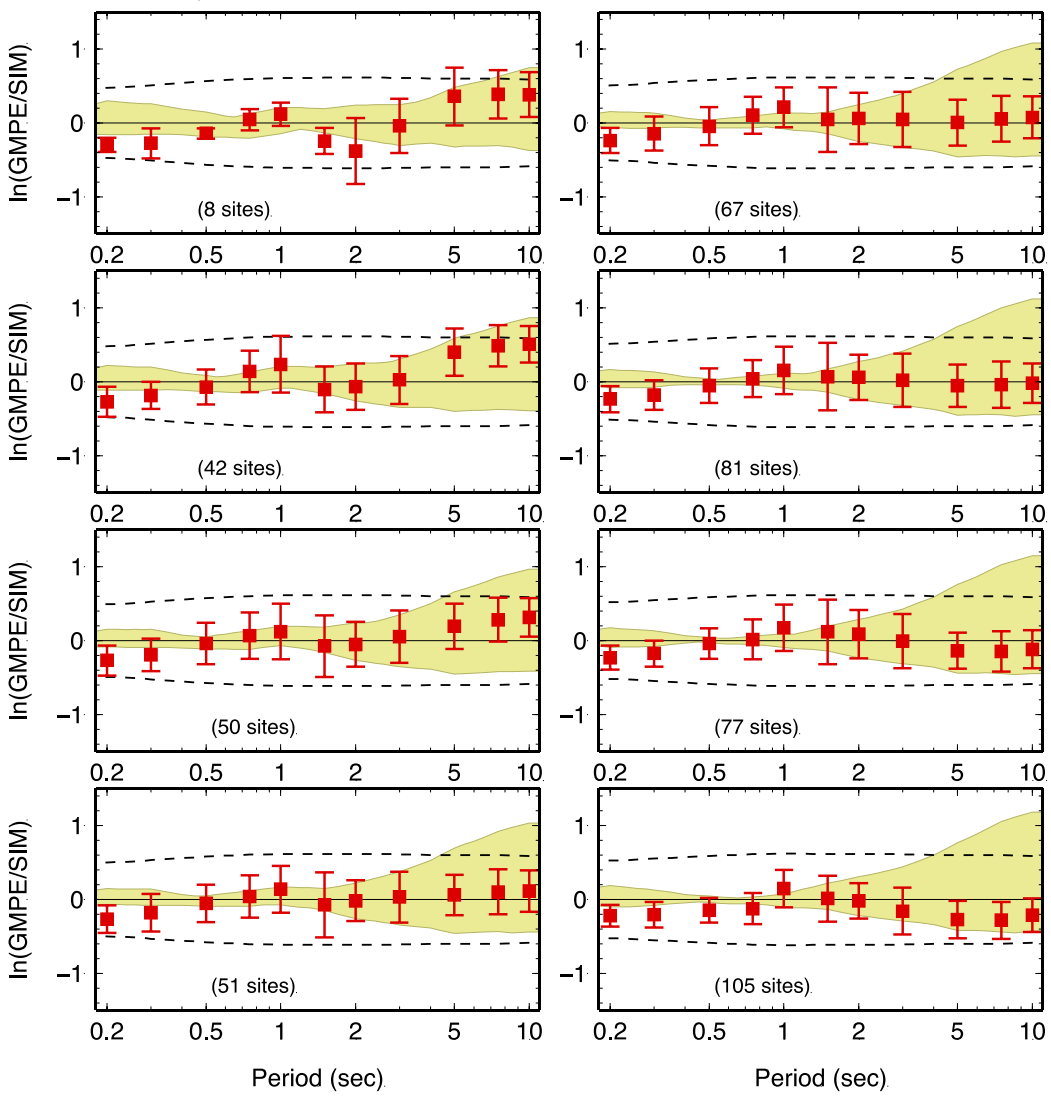

Figure A.2.2-42. Bias between the GMPEs and simulated ground motion computed as the ln(GMPE/SIM) RotD50 spectral acceleration ratio as a function of period, averaged over stations with same fault distance. The fault distance and the number of sites for each distance bin is indicated on each panel. Red squares and red vertical lines indicate the median value and +/- one standard deviation of the bias. The synthetics are computed for a rupture scenario with **rupture starting point = center**

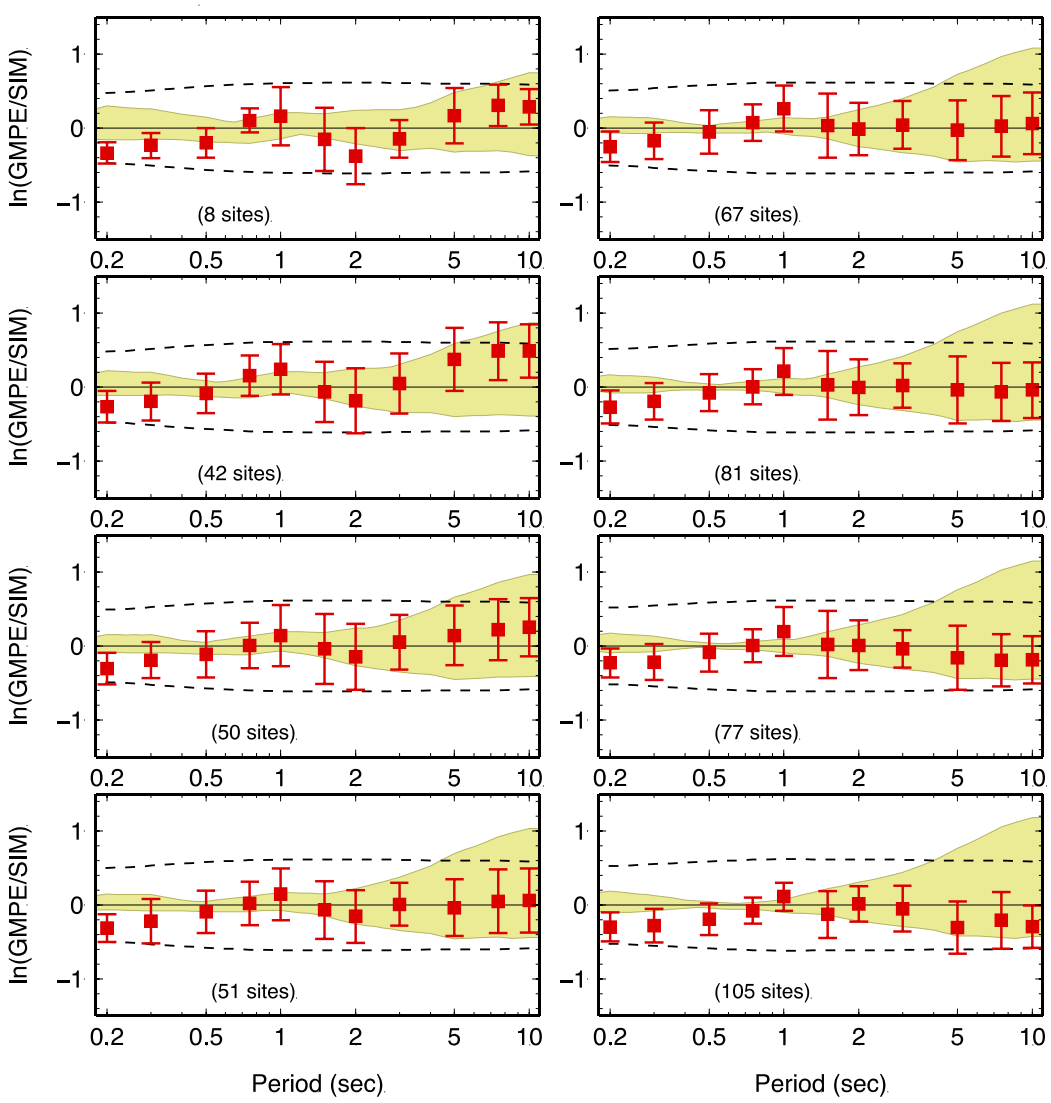

Figure A.2.2-43. Bias between the GMPEs and simulated ground motion computed as the ln(GMPE/SIM) RotD50 spectral acceleration ratio as a function of period, averaged over stations with same fault distance. The fault distance and the number of sites for each distance bin is indicated on each panel. Red squares and red vertical lines indicate the median value and +/- one standard deviation of the bias. The synthetics are computed for a rupture scenario with **rupture starting point = right**

A.2.3 Maps of simulated PGV

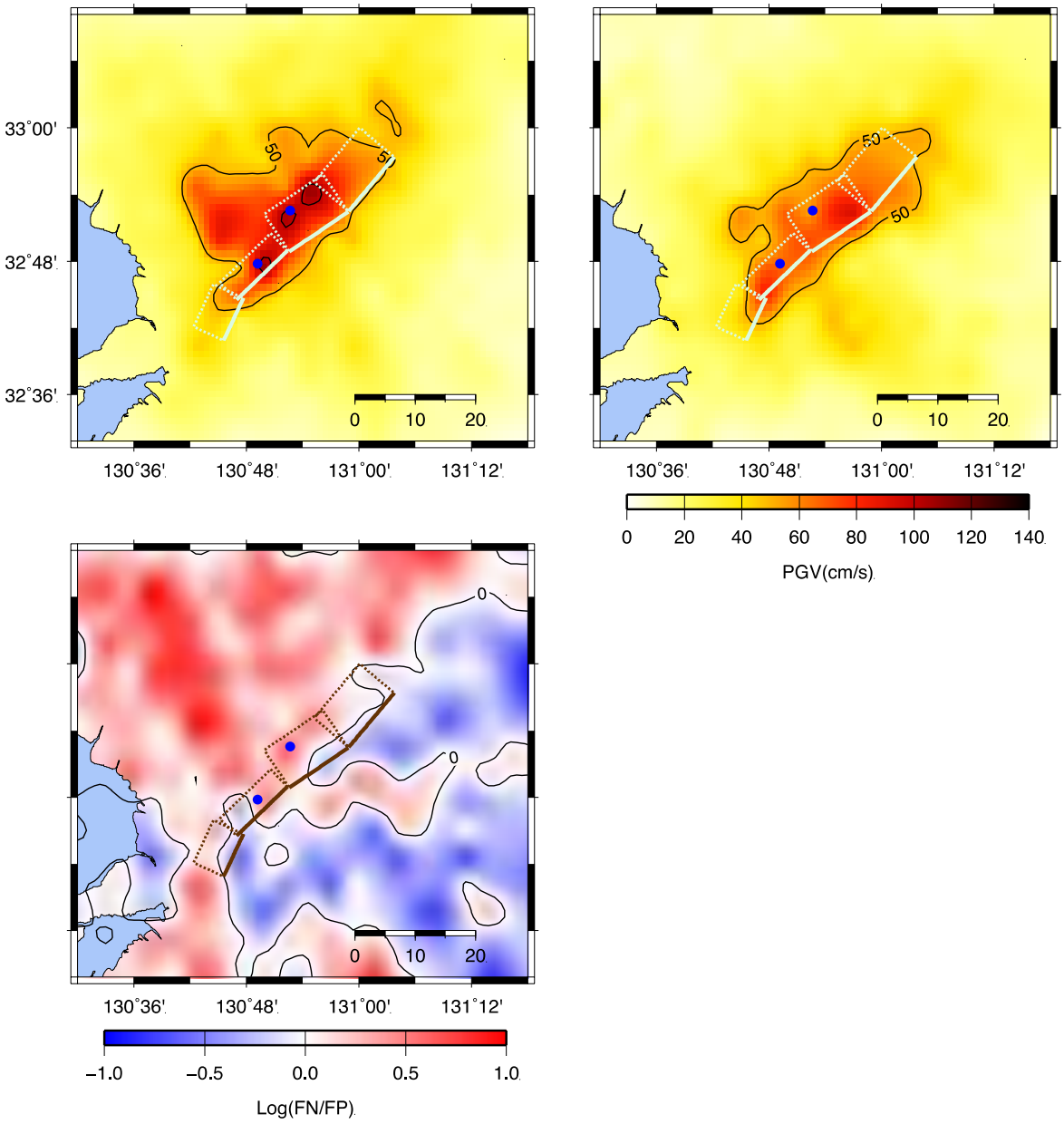

Figure A.2.3-1. Maps of FN (left panel) and FP (right panel) of simulated PGV using rupture scenario with **Vr/Vs=0.538**

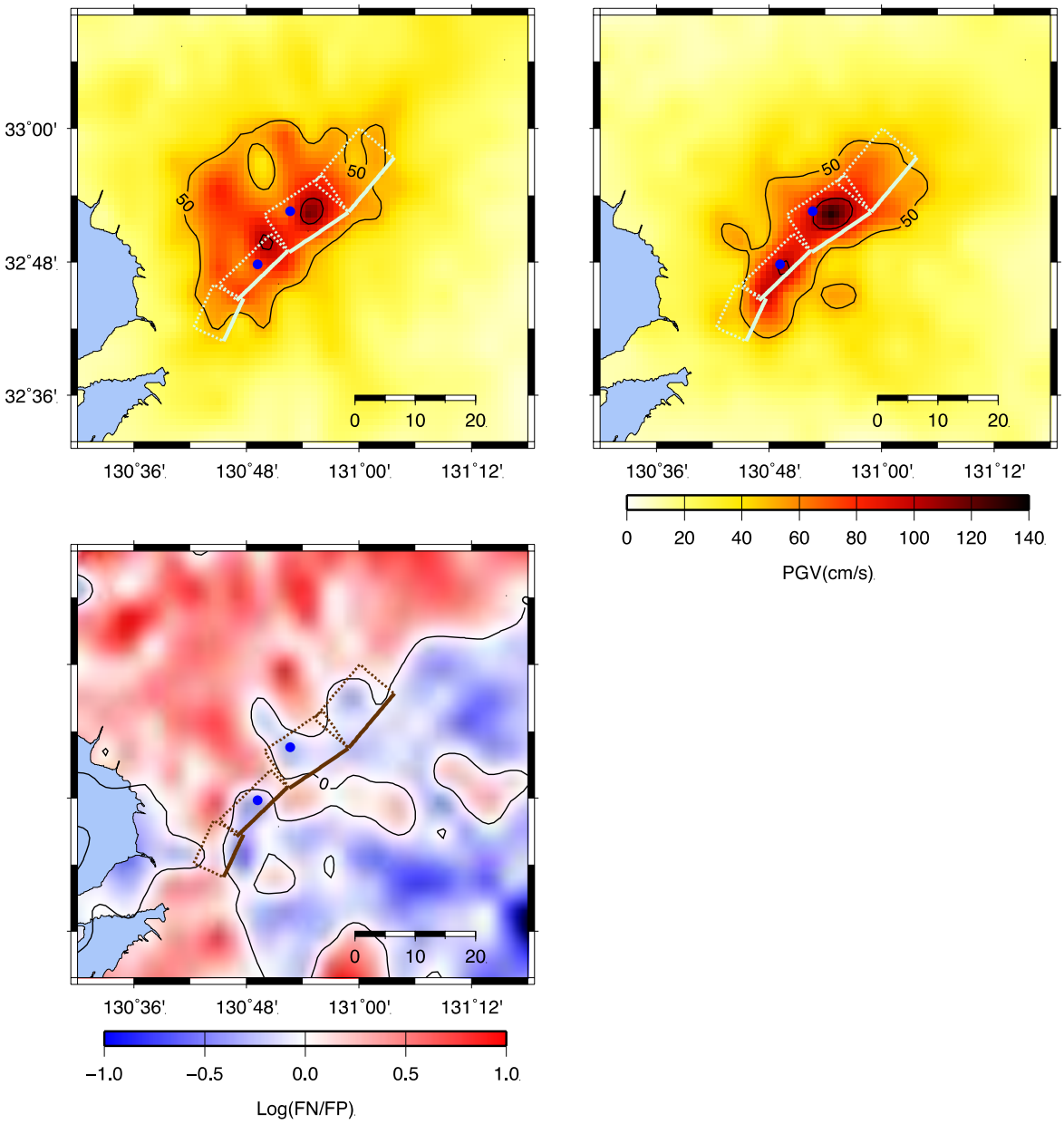

Figure A.2.3-2. Maps of FN (left panel) and FP (right panel) of simulated PGV using rupture scenario with **Vr/Vs=0.616**

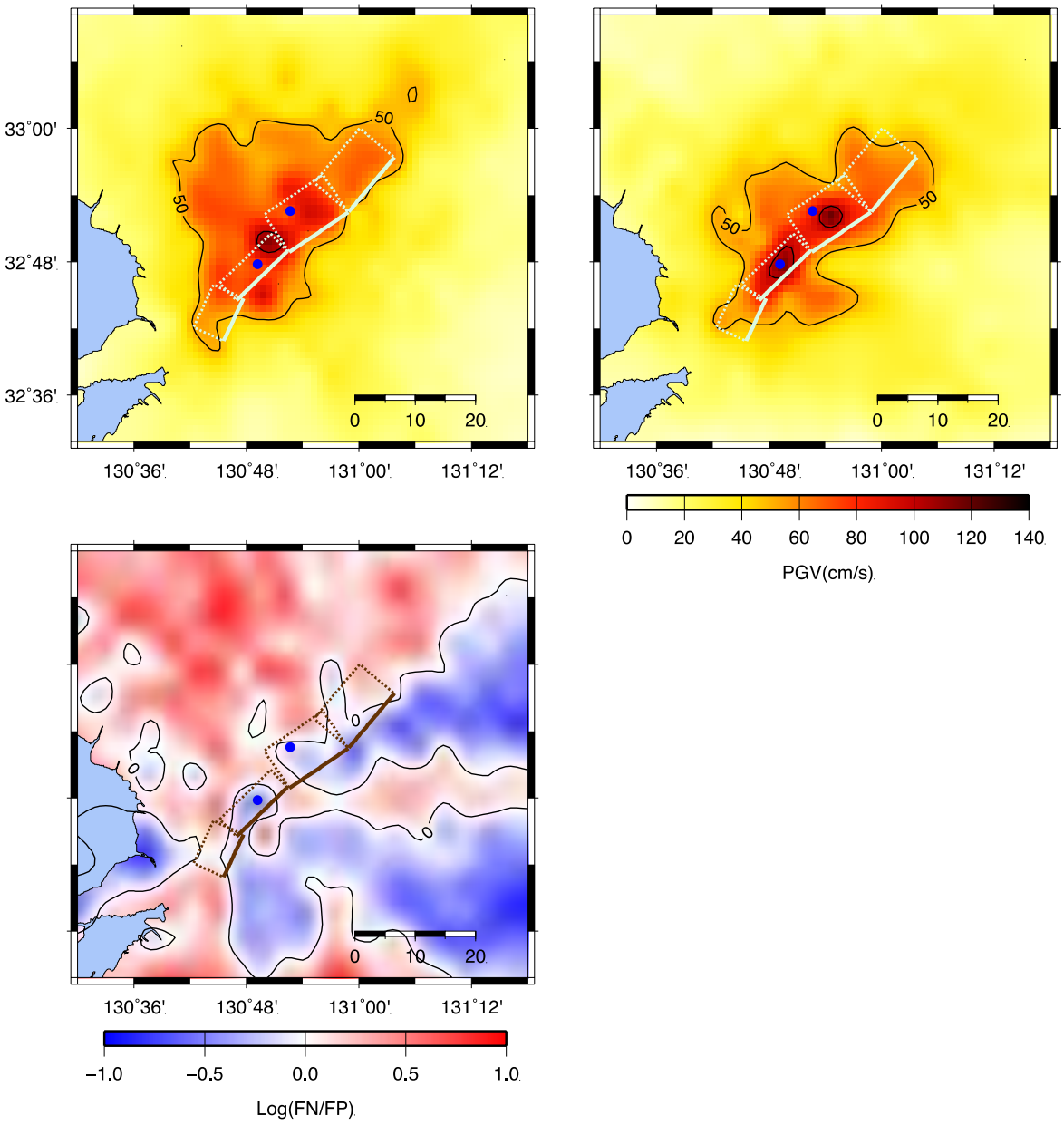

Figure A.2.3-3. Maps of FN (left panel) and FP (right panel) of simulated PGV using rupture scenario with **Vr/Vs=0.694**

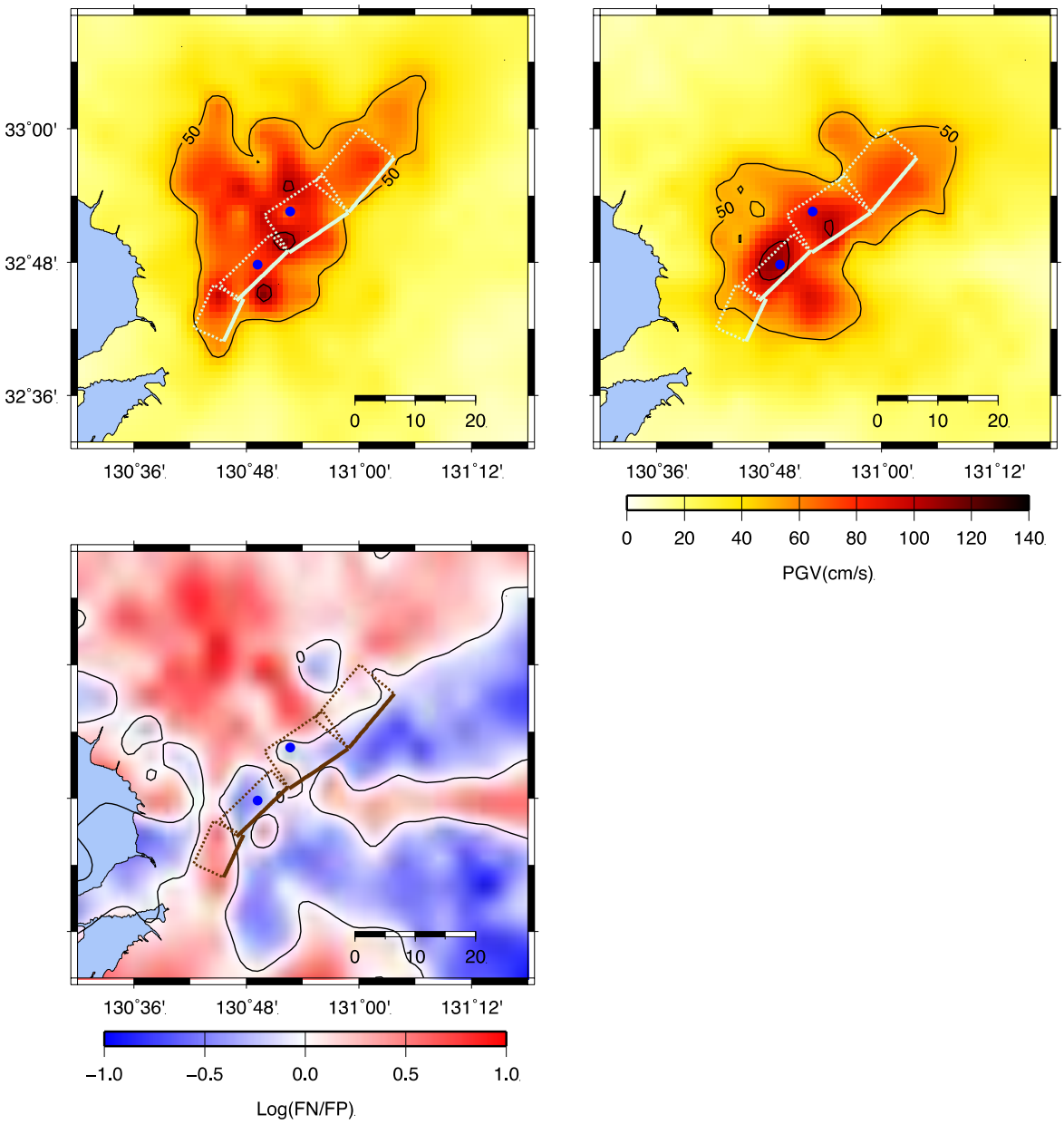

Figure A.2.3-4. Maps of FN (left panel) and FP (right panel) of simulated PGV using rupture

scenario with **Vr/Vs=0.772**

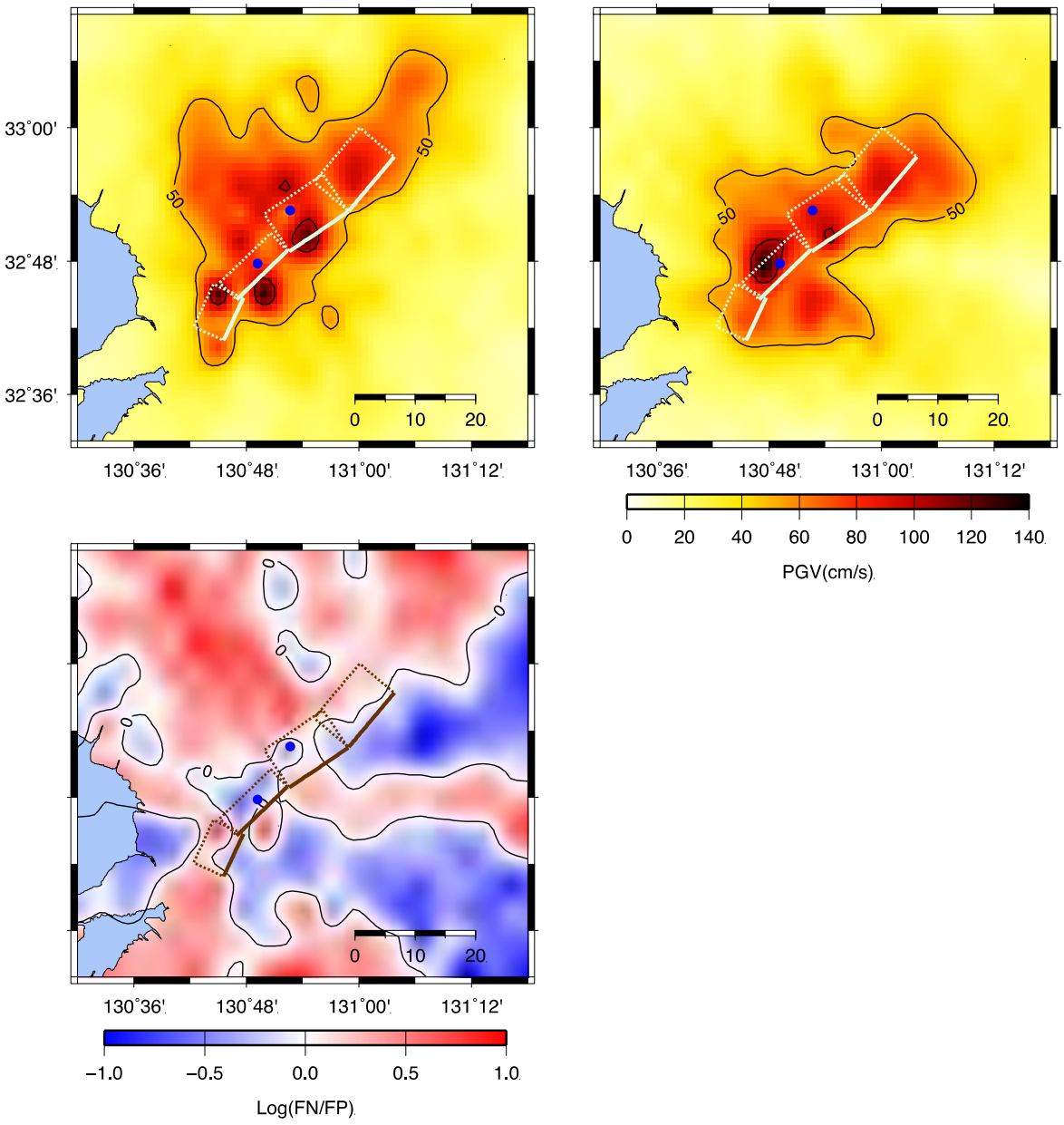

Figure A.2.3-5. Maps of FN (left panel) and FP (right panel) of simulated PGV using rupture scenario with **Vr/Vs=0.85**

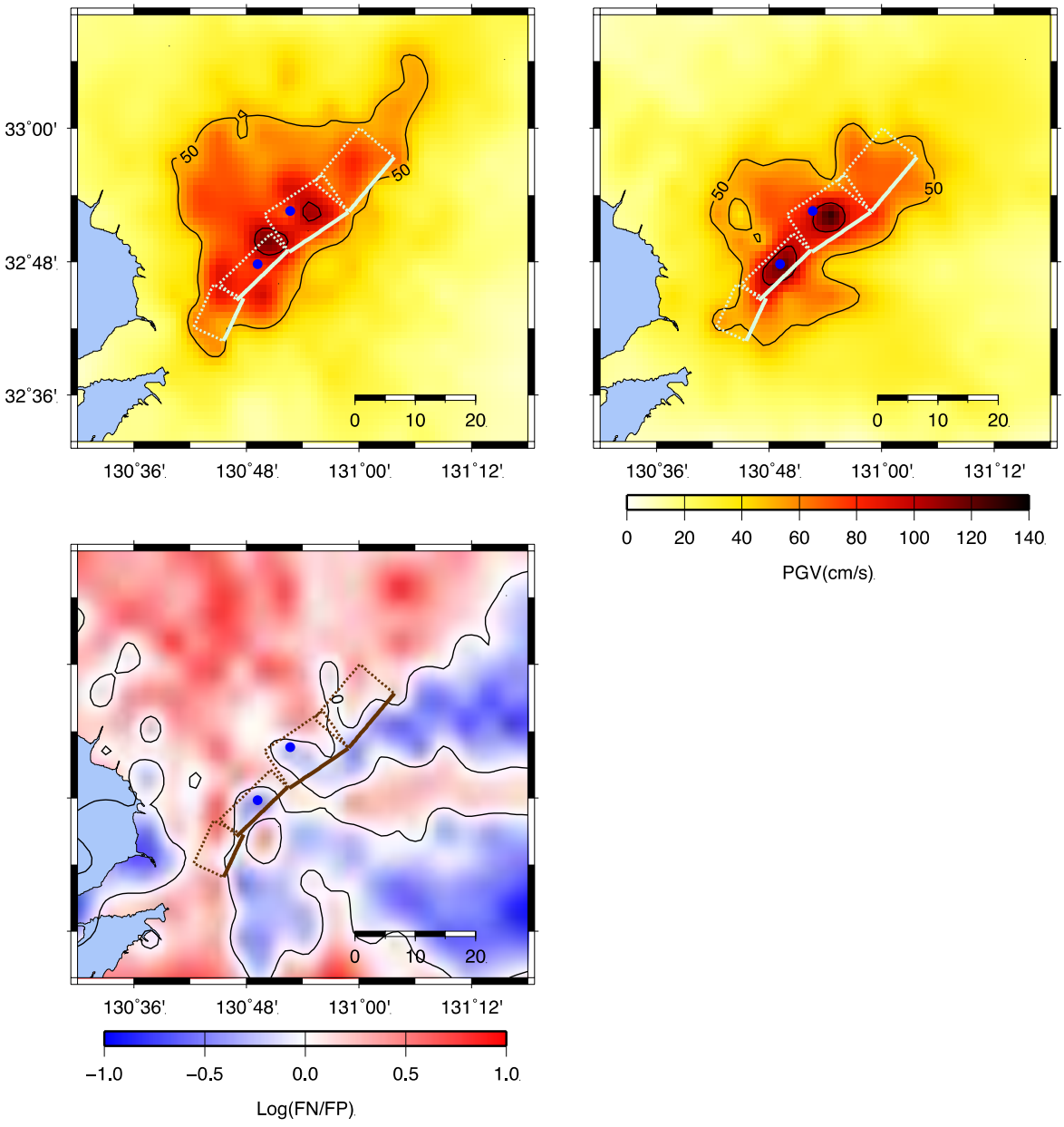

Figure A.2.3-6. Maps of FN (left panel) and FP (right panel) of simulated PGV using rupture scenario with **rise time parameter =0.96**

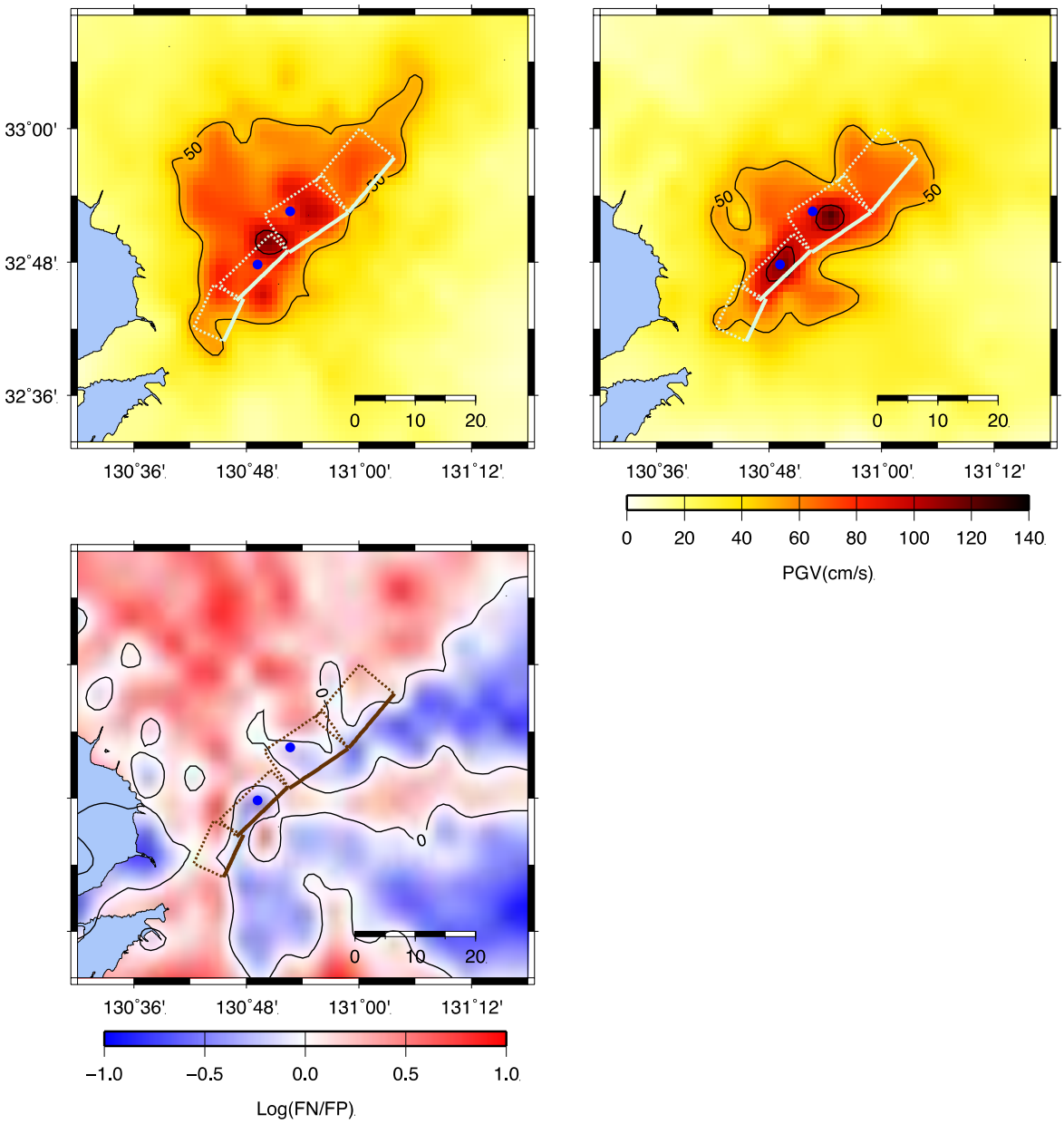

Figure A.2.3-7. Maps of FN (left panel) and FP (right panel) of simulated PGV using rupture scenario with **rise time parameter = 1.28**

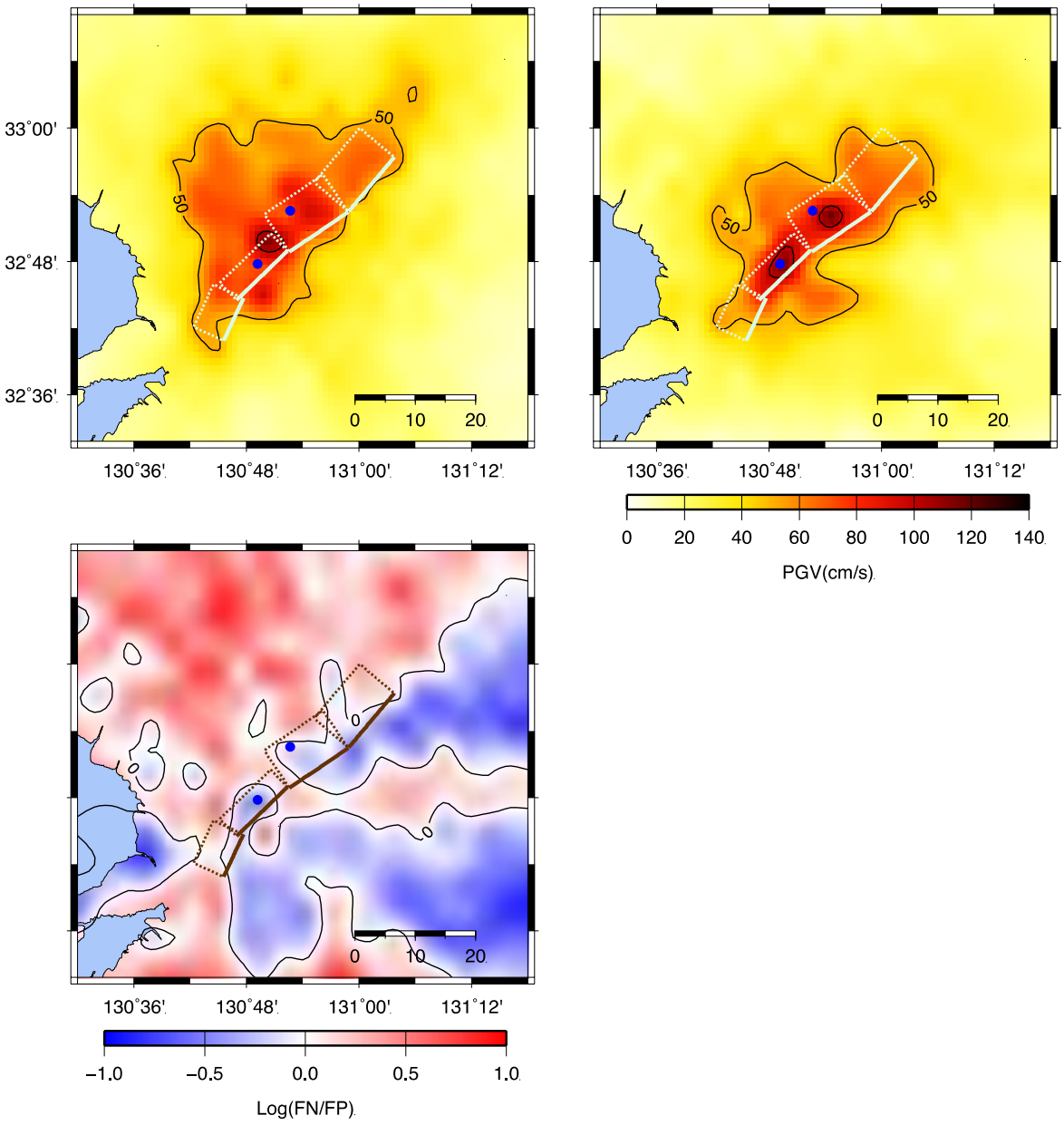

Figure A.2.3-8. Maps of FN (left panel) and FP (right panel) of simulated PGV using rupture scenario with **rise time parameter =1.6**

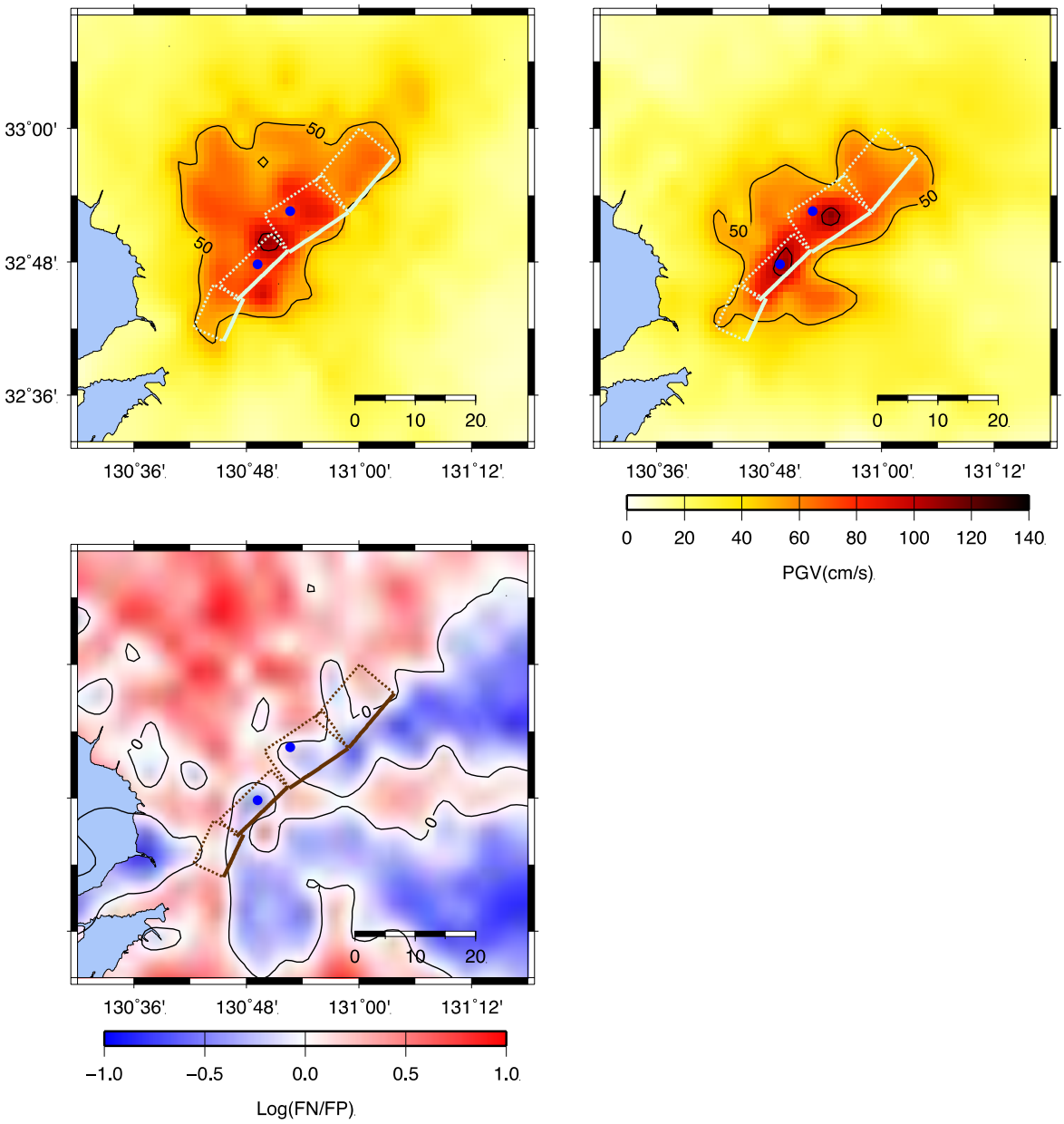

Figure A.2.3-9. Maps of FN (left panel) and FP (right panel) of simulated PGV using rupture scenario with **rise time parameter =1.92**

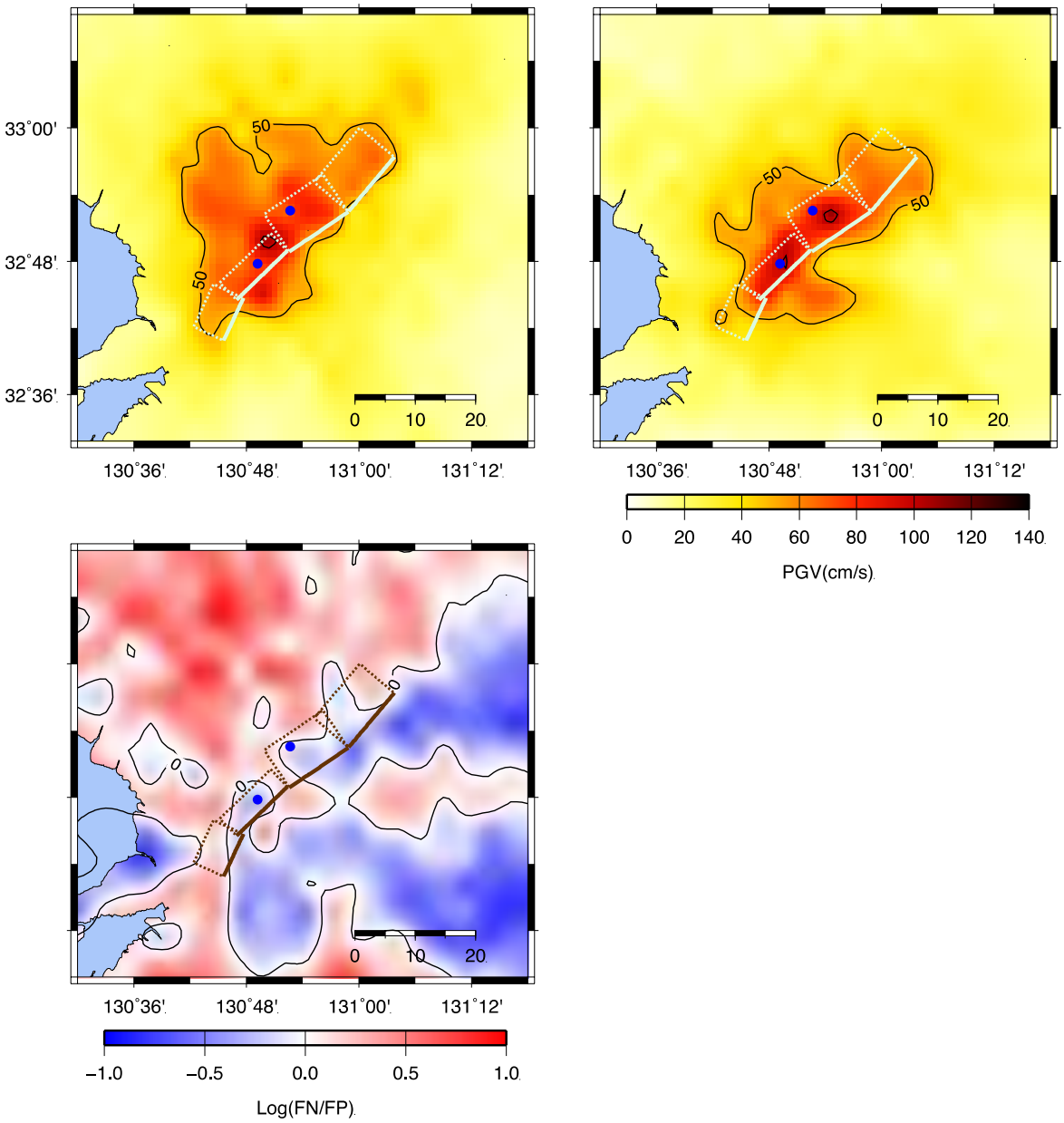

Figure A.2.3-10. Maps of FN (left panel) and FP (right panel) of simulated PGV using rupture scenario with **rise time parameter =2.24**

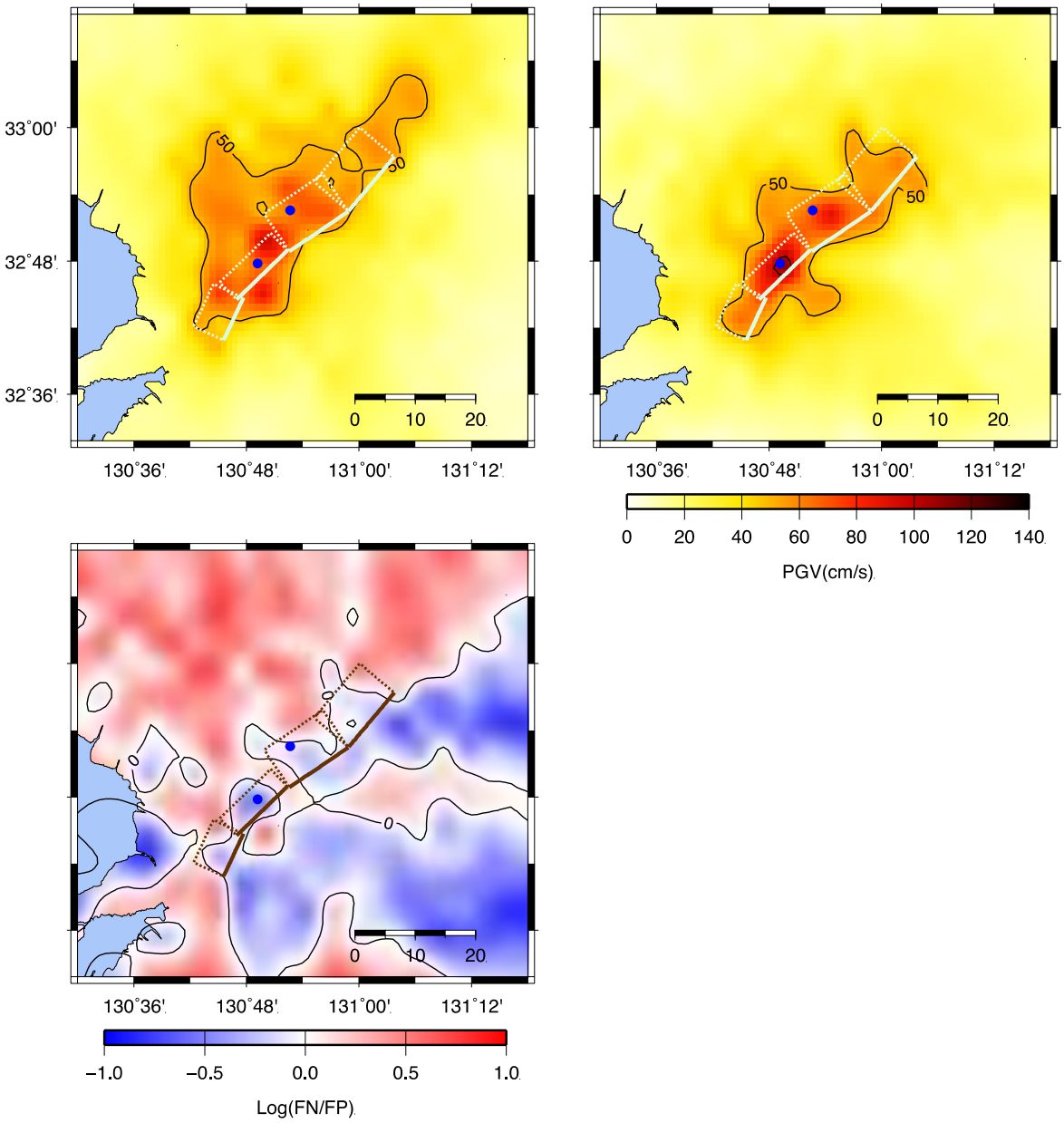

Figure A.2.3-11. Maps of FN (left panel) and FP (right panel) of simulated PGV using rupture scenario with **slip roughness =0.5**

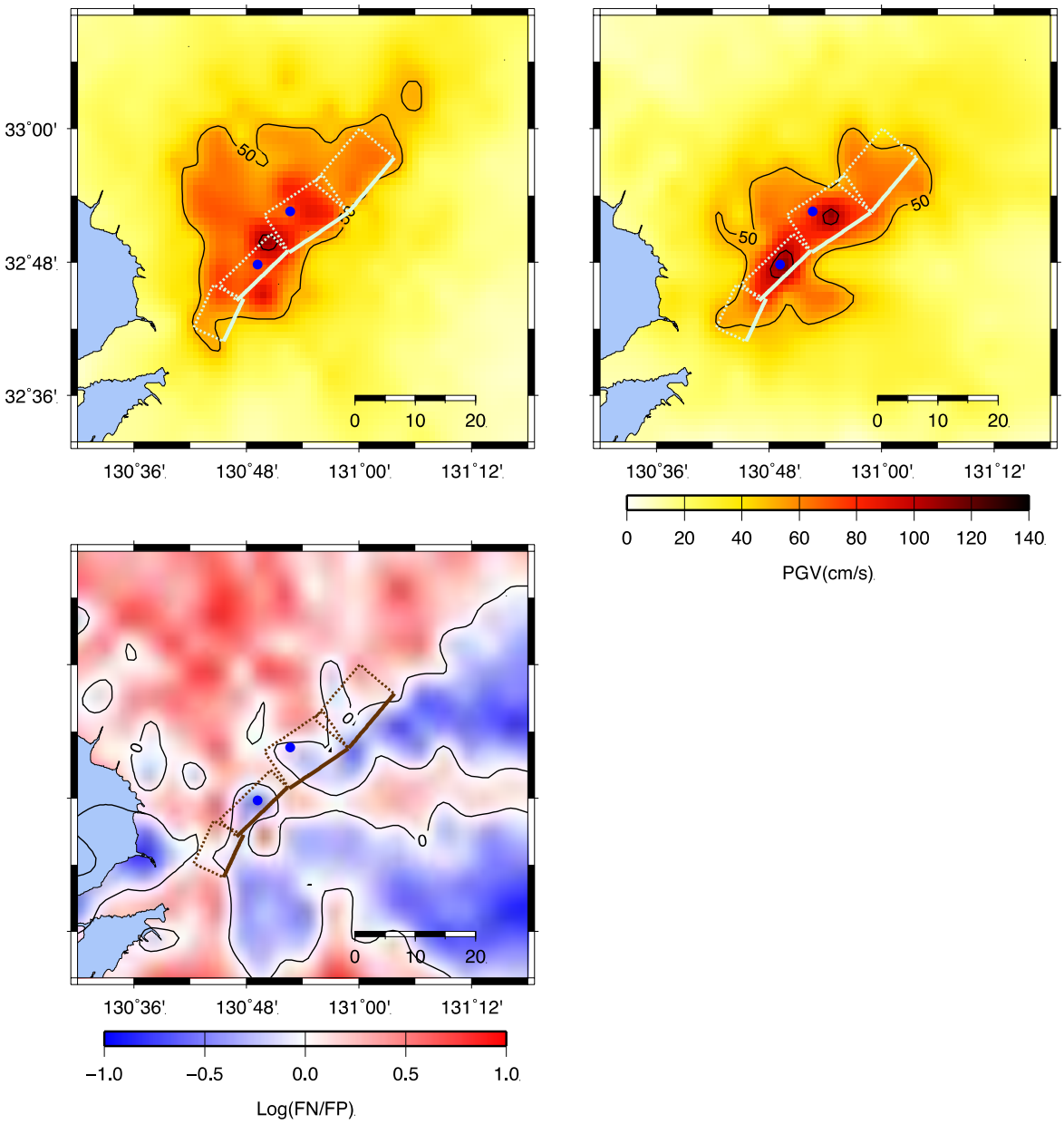

Figure A.2.3-12. Maps of FN (left panel) and FP (right panel) of simulated PGV using rupture scenario with **slip roughness =0.75**

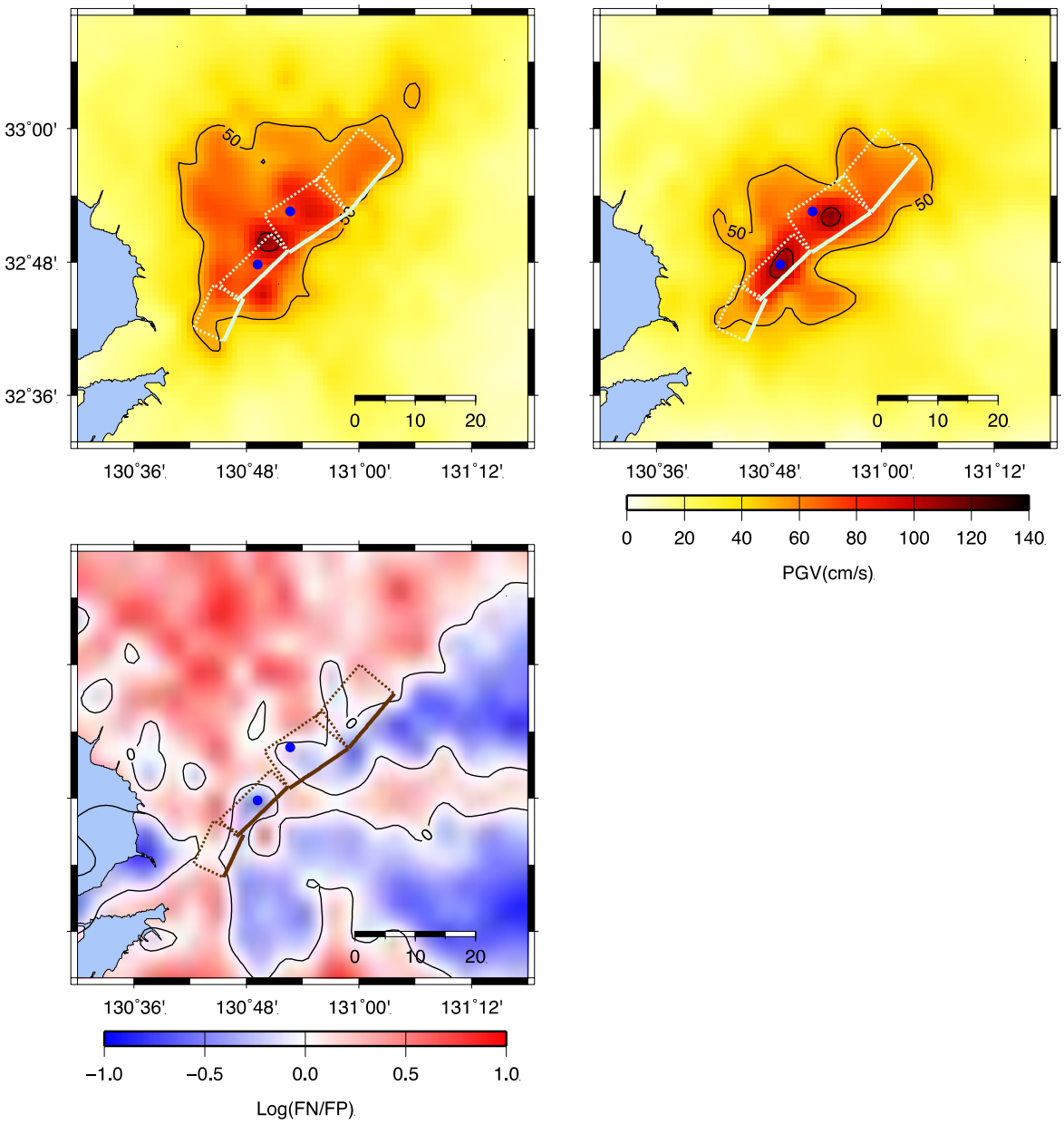

Figure A.2.3-13. Maps of FN (left panel) and FP (right panel) of simulated PGV using rupture scenario with **slip roughness =0.8**

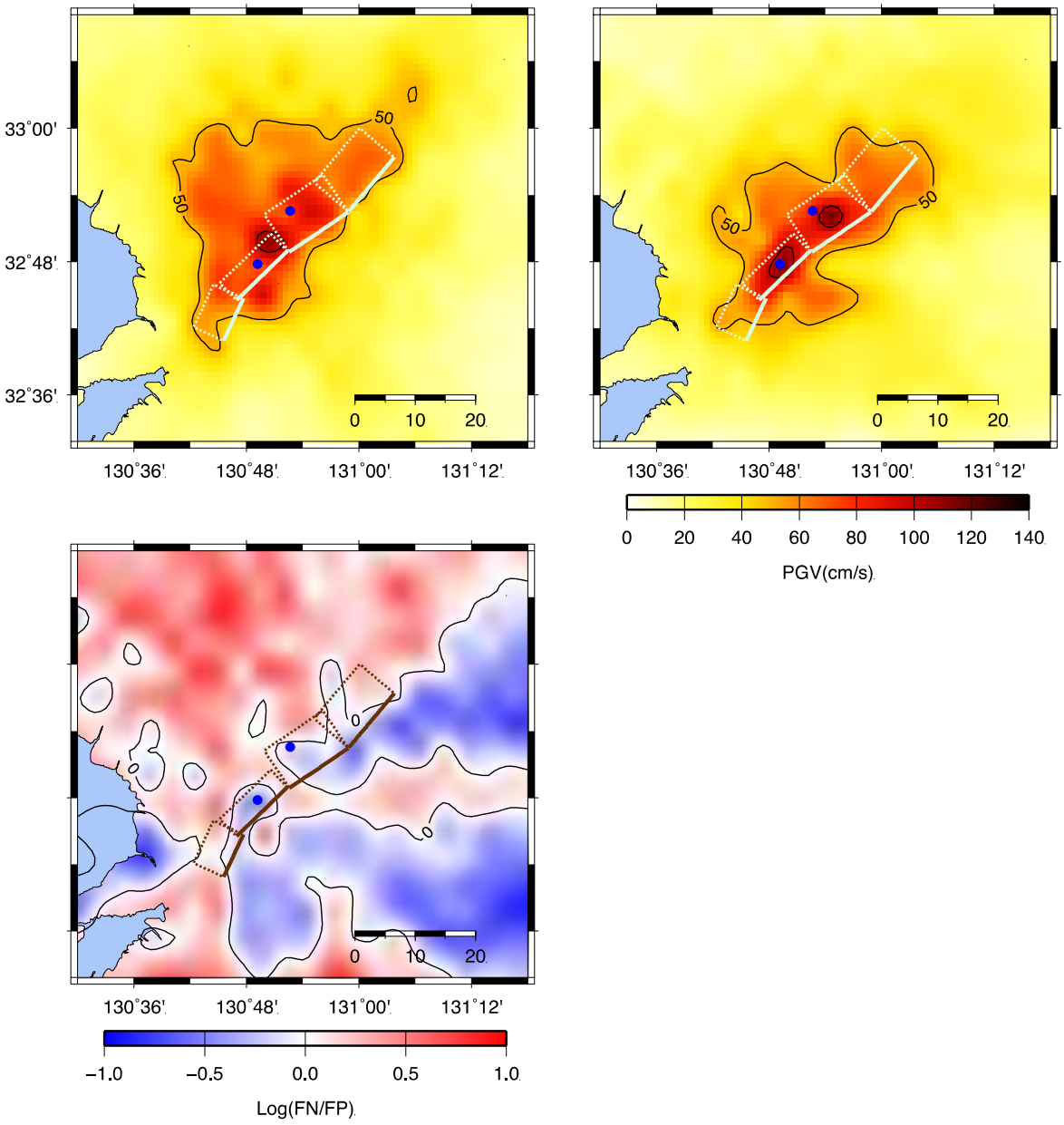

Figure A.2.3-14. Maps of FN (left panel) and FP (right panel) of simulated PGV using rupture scenario with **slip roughness =0.85**

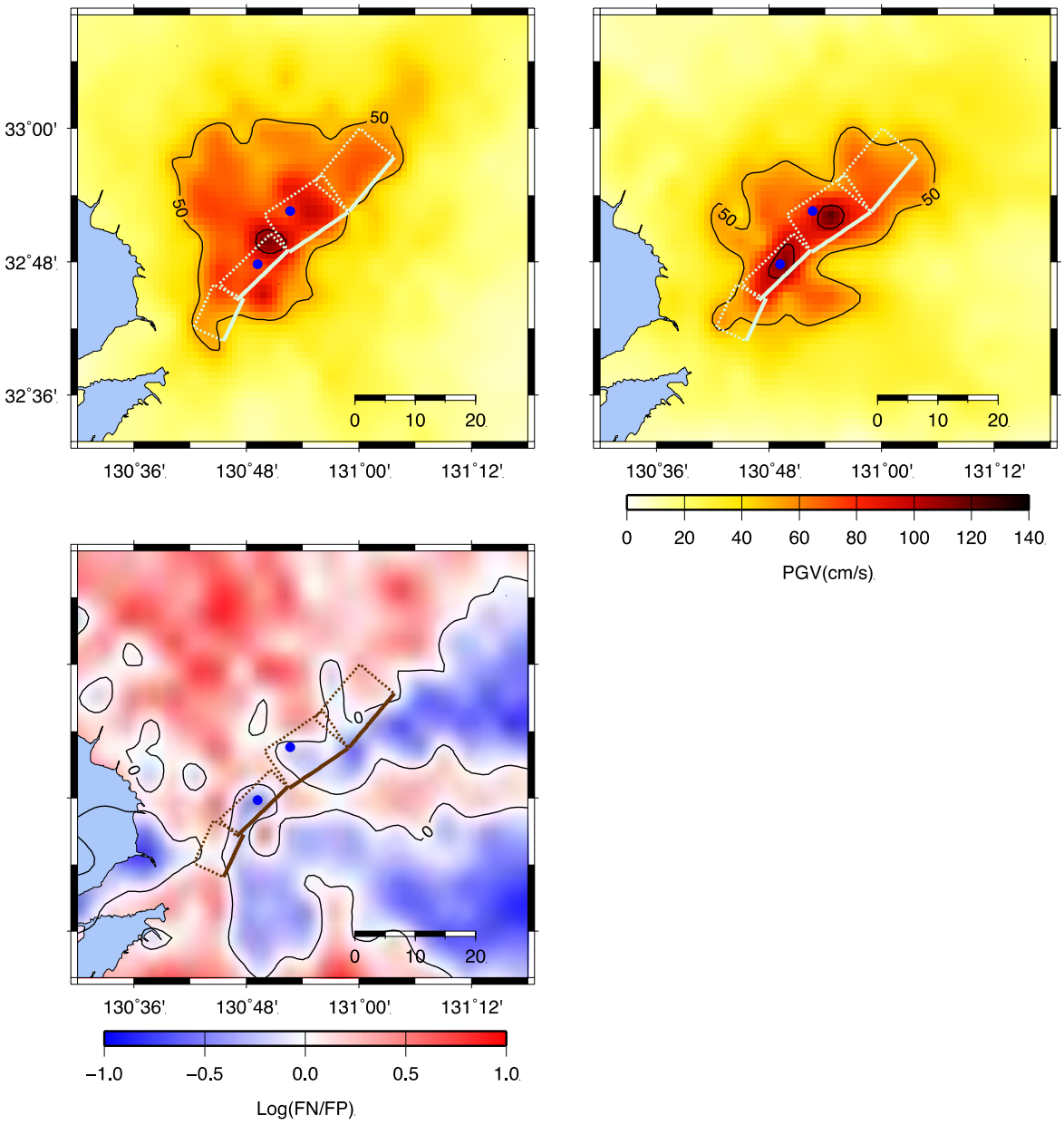

Figure A.2.3-15. Maps of FN (left panel) and FP (right panel) of simulated PGV using rupture scenario with **slip roughness =0.9**

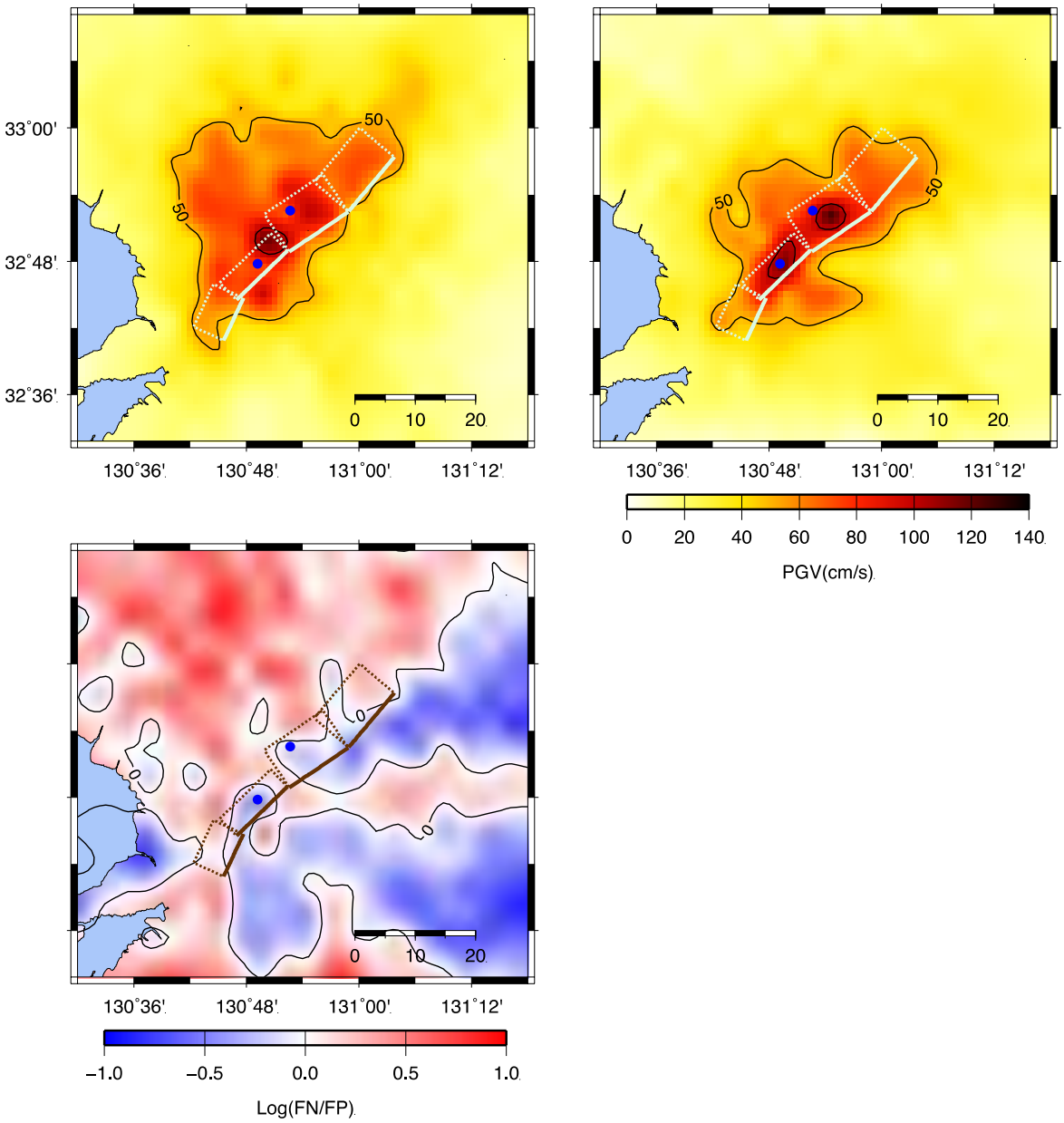

Figure A.2.3-16. Maps of FN (left panel) and FP (right panel) of simulated PGV using rupture scenario with **slip roughness =0.95**

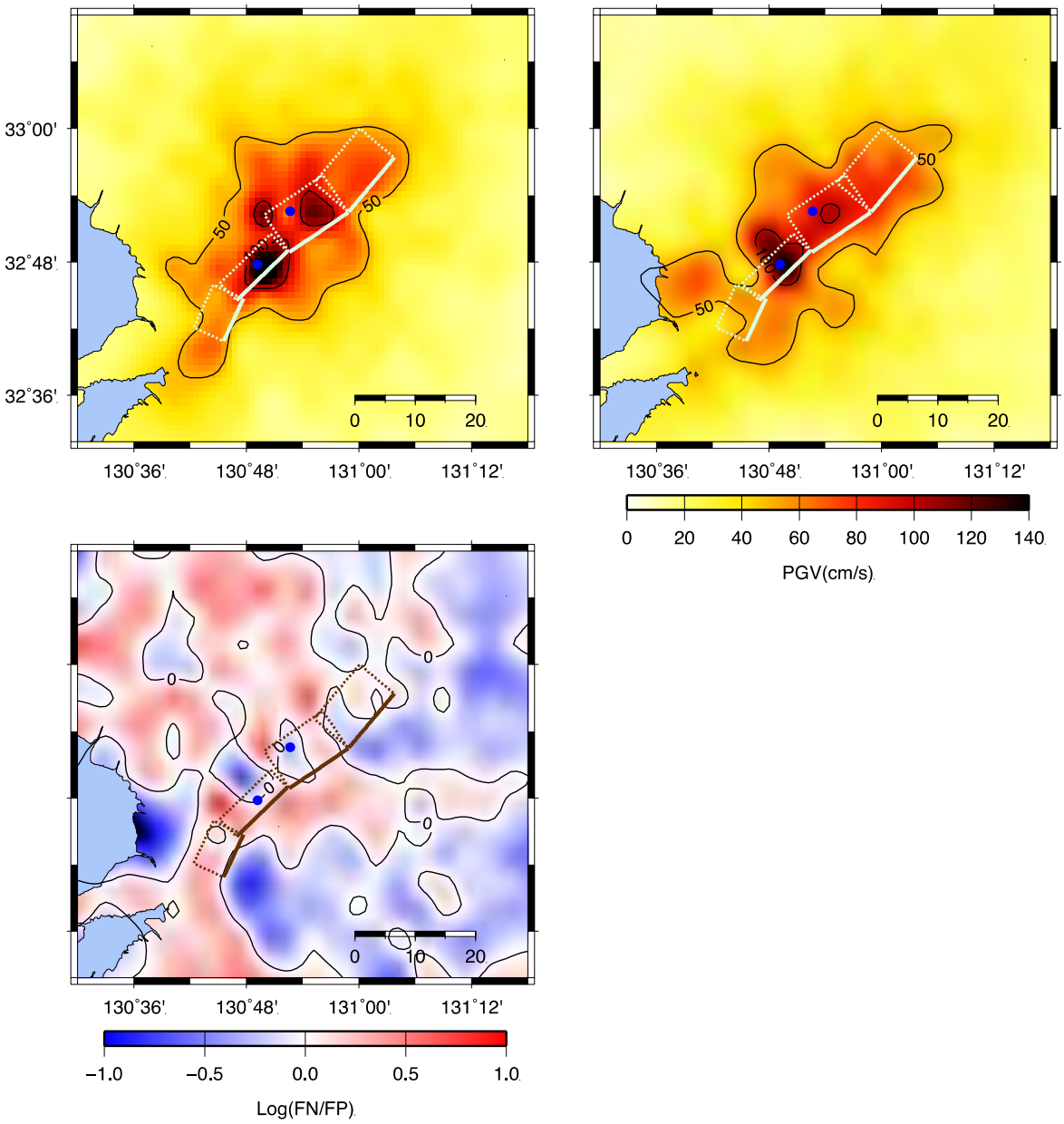

Figure A.2.3-17. Maps of FN (left panel) and FP (right panel) of simulated PGV using rupture scenario with **slip generator seed = s1**

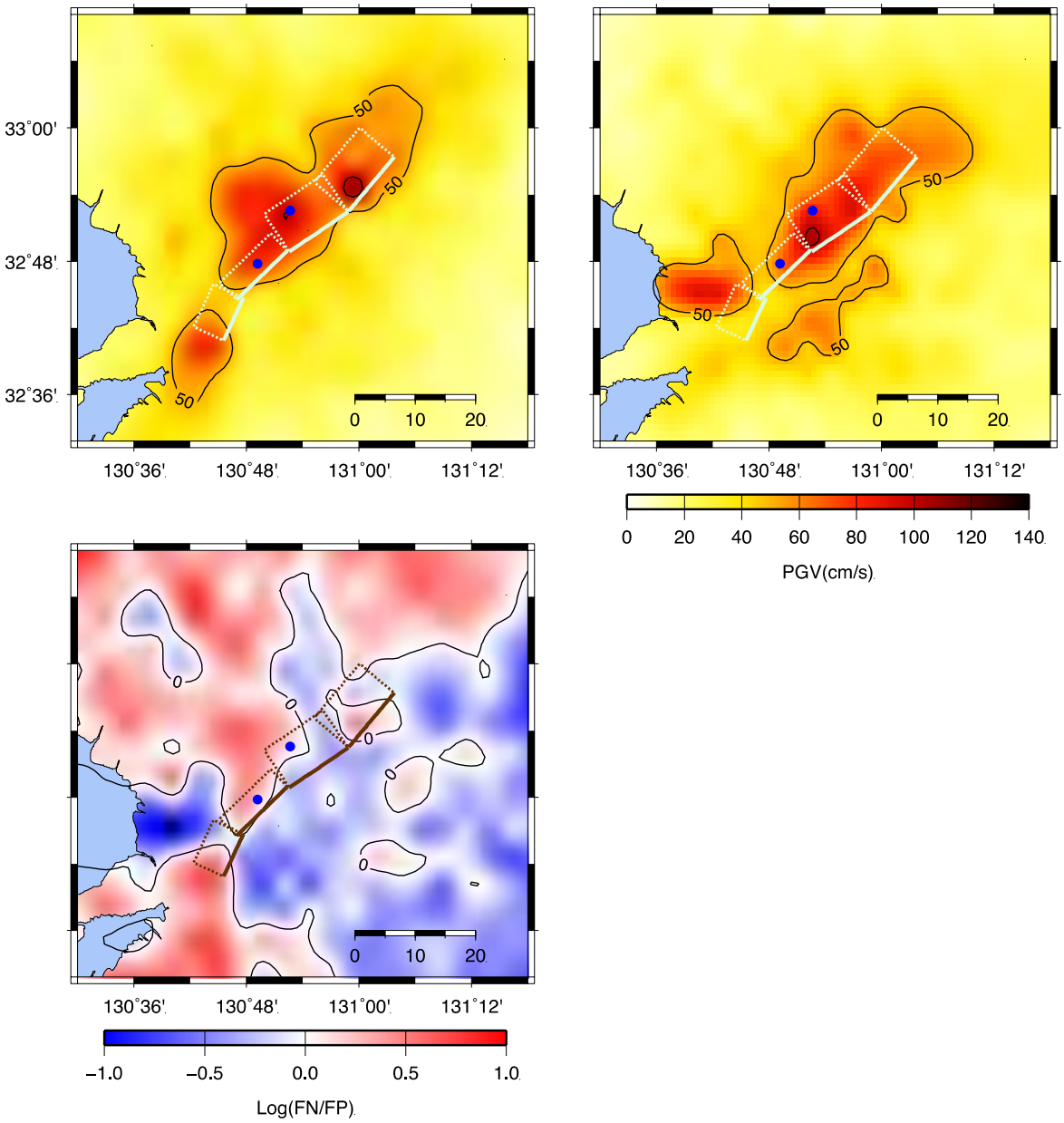

Figure A.2.3-18. Maps of FN (left panel) and FP (right panel) of simulated PGV using rupture scenario with **slip generator seed = s2**

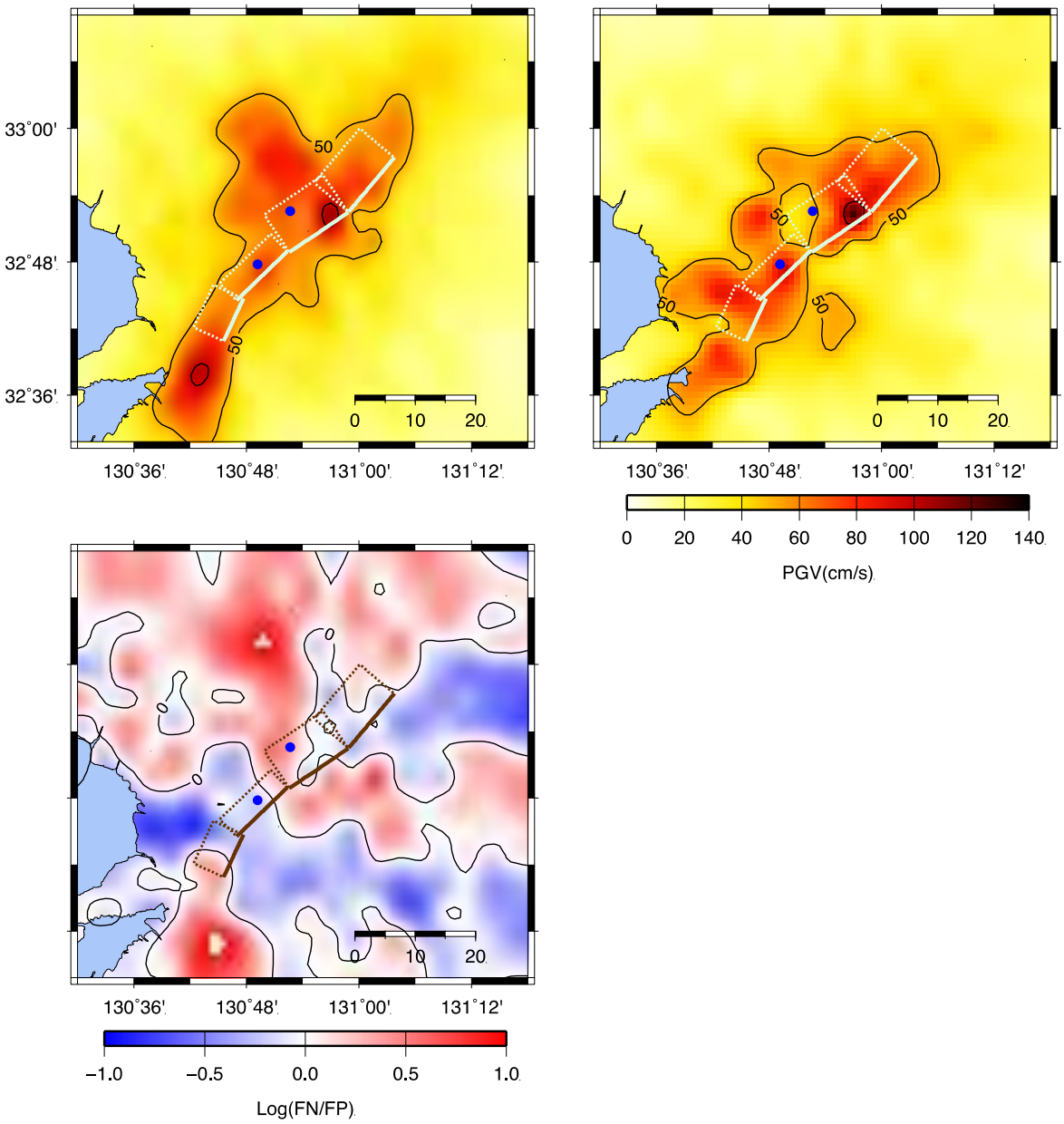

Figure A.2.3-19. Maps of FN (left panel) and FP (right panel) of simulated PGV using rupture scenario with **slip generator seed = s3**

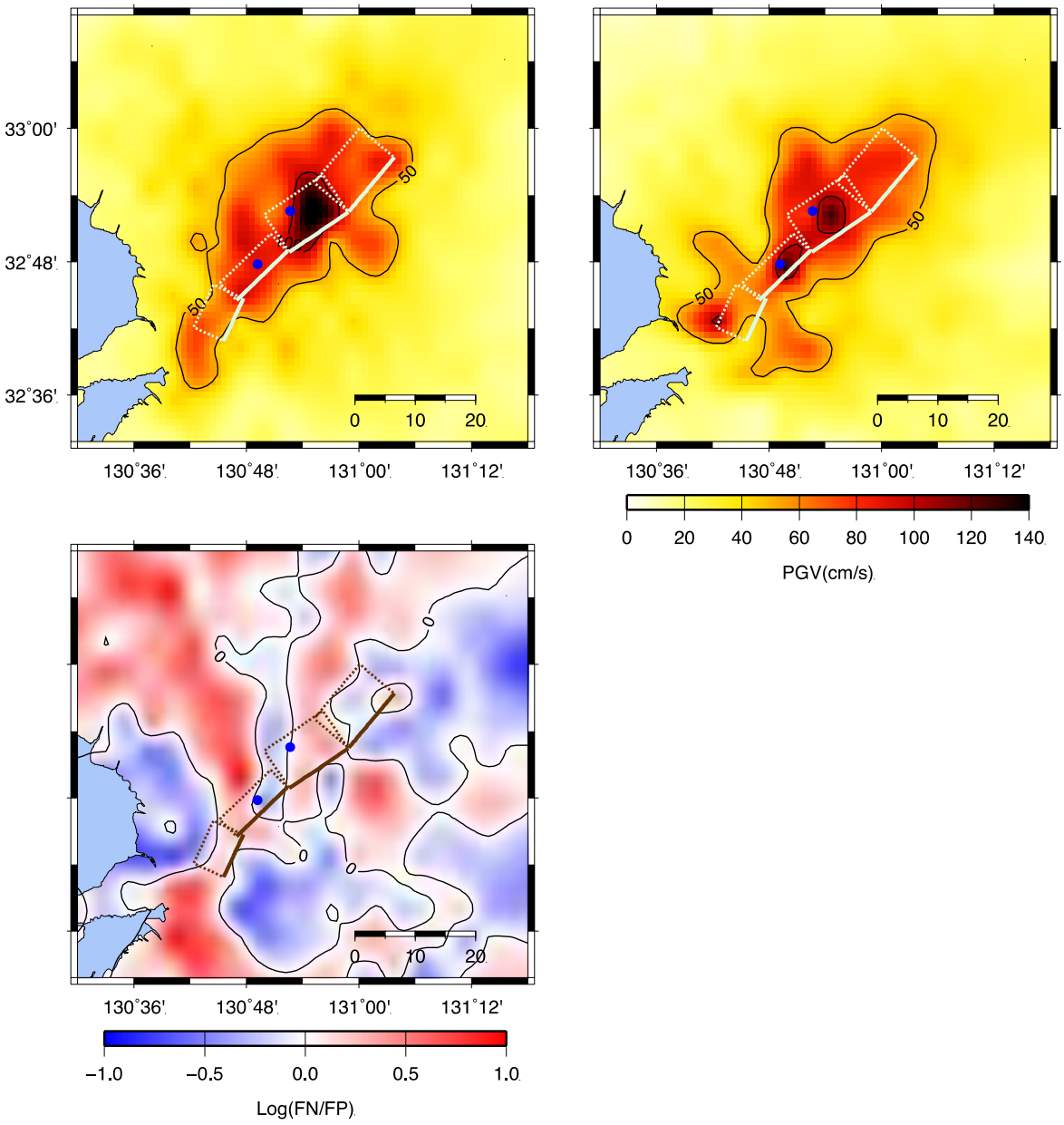

Figure A.2.3-20. Maps of FN (left panel) and FP (right panel) of simulated PGV using rupture scenario with **slip generator seed = s4**

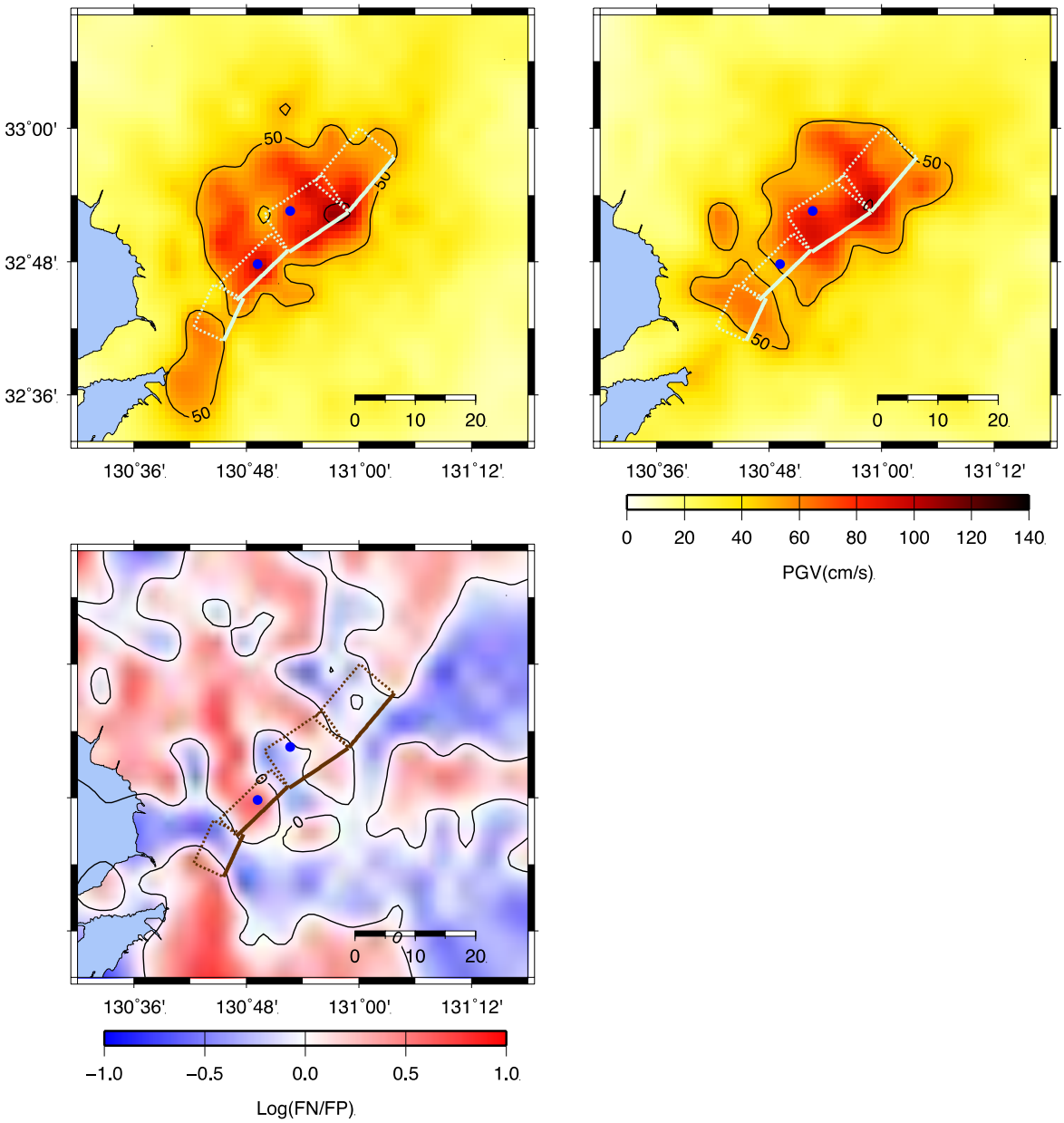

Figure A.2.3-21. Maps of FN (left panel) and FP (right panel) of simulated PGV using rupture scenario with **slip generator seed = s5**

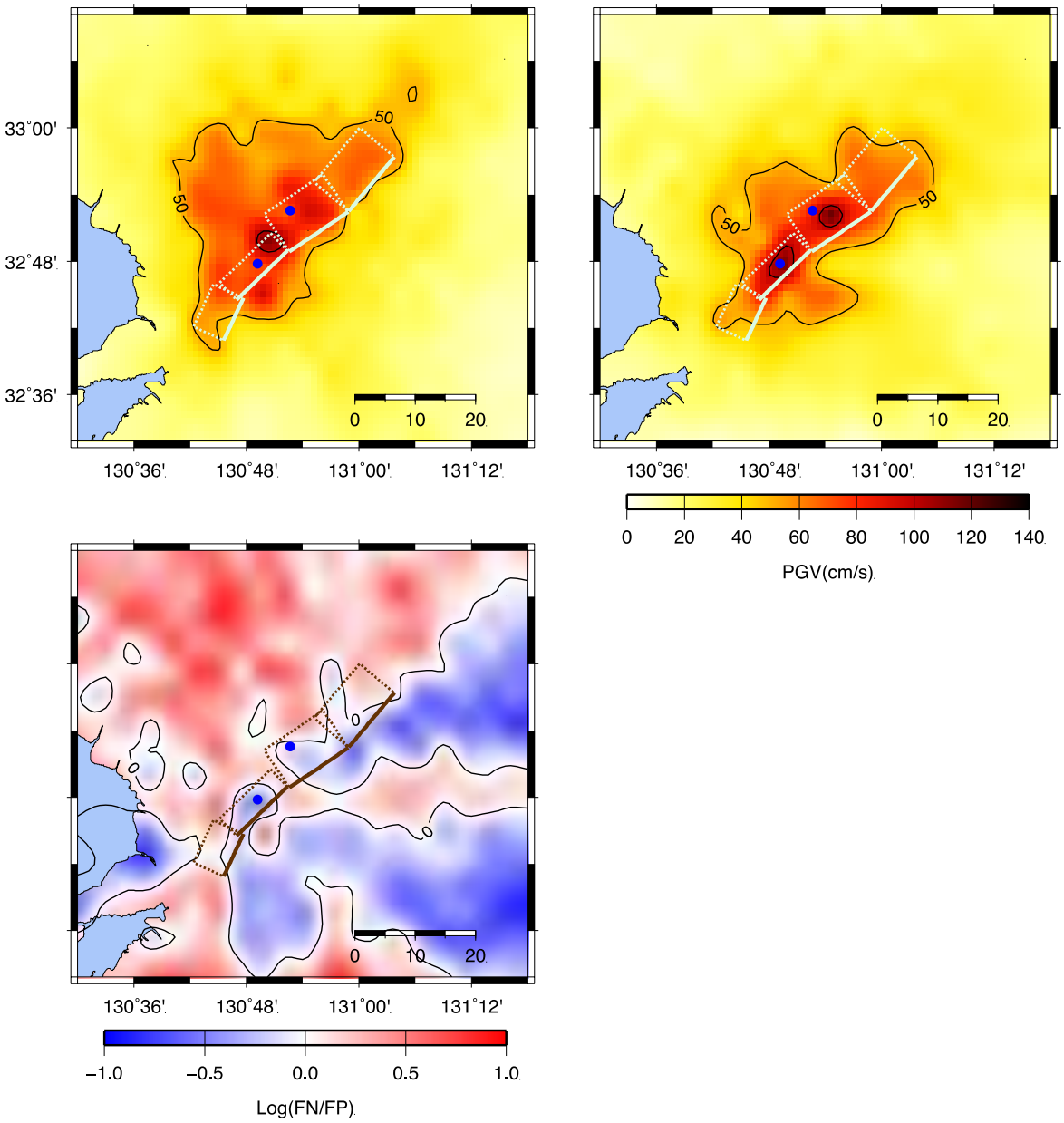

Figure A.2.3-22. Maps of FN (left panel) and FP (right panel) of simulated PGV using rupture scenario with **rupture starting point = left**

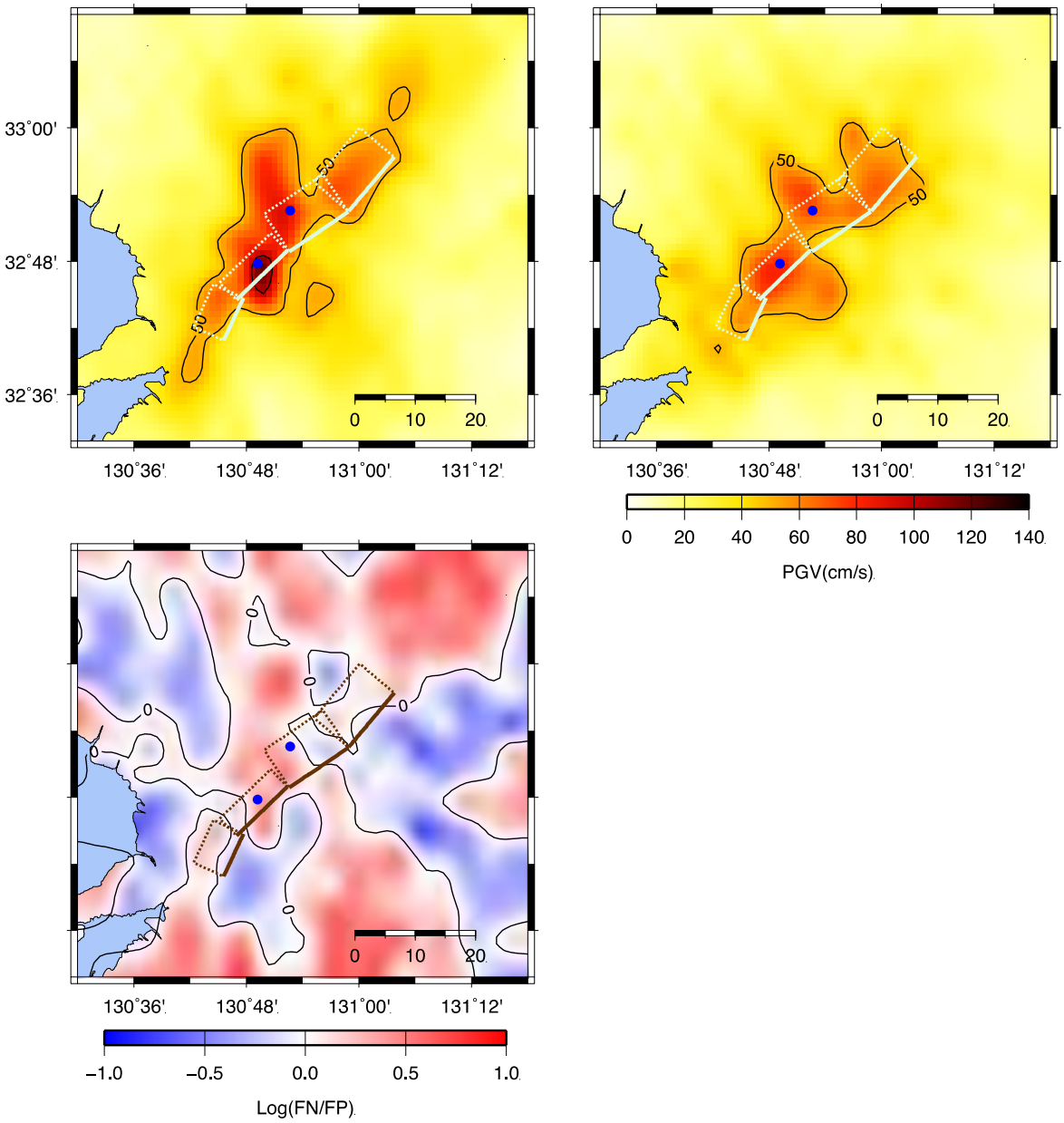

Figure A.2.3-23. Maps of FN (left panel) and FP (right panel) of simulated PGV using rupture scenario with **rupture starting point = center**

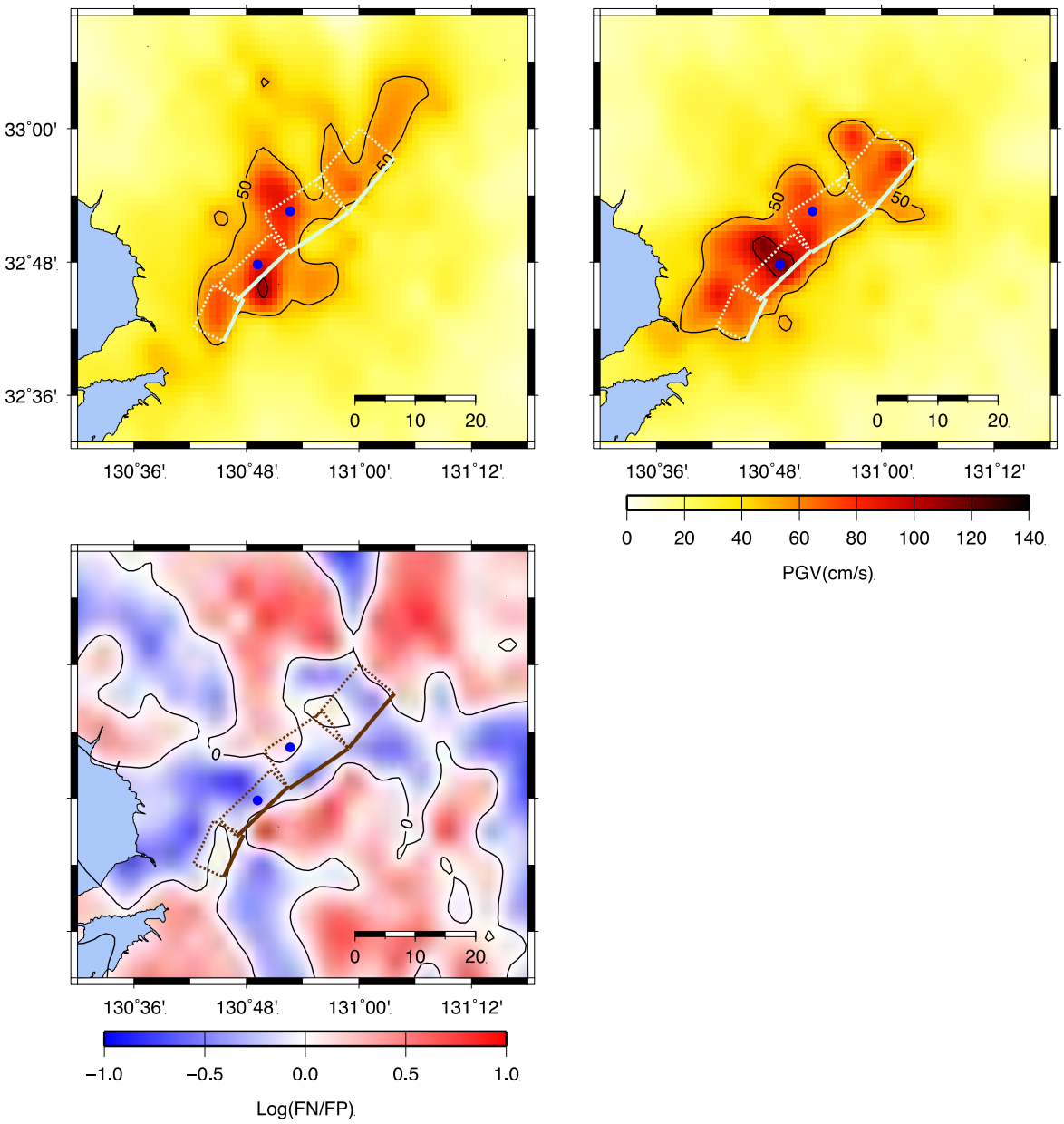

Figure A.2.3-24. Maps of FN (left panel) and FP (right panel) of simulated PGV using rupture scenario with **rupture starting point = right**

A.3　動力学シミュレーションによる震源スケーリング則の検討（付録資料）

A.3.1　2018 year working plan

Task 1. Improvement of the multi-cycle simulation methodology for the strike variable segmented fault.
We will improve the simulation methodology by introducing fault segmentation; applying an a-b taper to the edges of fault; decreasing seismogenic depth to 15 km, which is typical for Japan; and increasing fault length to 200km. In order to get better statistics, we will increase the number of simulated earthquakes, especially for the Stage 2-3 transition (Mw=7-7.5). We will adopt the multisegment fault model (80 km long) of the Landers earthquake that is being used on the SCEC Broadband Platform, extend it at both ends with segments based on the SCEC fault model so that it is 200 km long, apply an a-b taper, limit its depth to 15 km, and perform multi-cycle simulations with a focus on Mw 7 to 7.5 events.

Task 2. Validation of the source model by 1992 Landers earthquake.
We will validate simulated strong ground motions against recorded ground motions and ground motion prediction equations by comparing response spectra of a large inland earthquake, the 1992 Landers earthquake. For this validation, we will: (a) from fully dynamic multi-cycle simulations generated in Task 1, select appropriate events similar to the Landers earthquake); (b) calculate waveforms using the source time function (moment rate) on the fault, which is estimated from fully dynamic multi-cycle simulation; and (c) compare the response spectra of the simulated synthetic waveforms with the recorded spectra and with spectra calculated from ground motion prediction equations.

Task 3. Source parameters scaling check.
Check scaling of the rupture area, average slip and combined area of asperities, vs. Mo. Compare with observed 3-stage scaling. Tune Dc or consider 2-3 additional Dc cases, if necessary to adjust to the observed scaling and to the 1992 Landers eq.

A.3.2 Manuscript, submitted to the 2nd Best PSHA NI workshop

EARTHQUAKE CYCLE MODELING OF MULTI-SEGMENTED FAULTS: DYNAMIC RUPTURE AND GROUND MOTION SIMULATION OF THE 1992 MW 7.3 LANDERS EARTHQUAKE

P. GALVEZ [1,2], P. SOMERVILLE [2], A. PETUKHIN [3], J-P. AMPUERO [4,5]

[1] King Abdullah University of Science and Technology, Saudi Arabia

[2] AECOM, Los Angeles, USA

[3] Geo-Research Institute, Osaka, Japan

[4] California Institute of Technology, USA

[5] IRD, Université Côte d'Azur, CNRS, OCA, Géoazur, France

E-mail contacts of main authors: anatolyp@geor.or.jp; percy.galvez.barron@gmail.com

Abstract. We perform earthquake cycle simulations to study the characteristics of source scaling relations and strong ground motions in multi-segmented fault ruptures. For earthquake cycle modeling, a quasi-dynamic solver (QDYN, Luo et al, 2017a[1]) is used to nucleate events and the fully dynamic solver (SPECFEM3D, Galvez et al., 2014; 2016[2, 3]) is used to simulate earthquake ruptures. The Mw7.3 Landers earthquake was chosen as a target earthquake to validate our methodology. The fault geometry for the three-segmented Landers rupture from the SCEC community fault model is included and extended at both ends to a total length of 200 km. We used the 2D correlated spatial distributions of characteristic slip-weakening distance Dc based on Hillers et al., 2007[4] that associates the Dc distribution with different degrees of fault maturity. The fault maturity is related to the variability of Dc on a microscopic scale: large variations of Dc represent immature faults and smaller variations of Dc represent mature faults. Moreover, we limit the fault depth to 15 km. Using these settings, earthquake cycle simulations are performed to nucleate seismic events on different sections of the fault, and dynamic rupture modeling is used to propagate the ruptures. The quasi-dynamic simulations are substantially sped up by implementing a hierarchical matrix method. The model generates events similar to the Mw7.3 Landers earthquake. The simulated ground motions are validated by comparison of simulated response spectra with recorded response spectra.

Key Words: Full dynamic modelling, cycle simulation, 1992 Landers earthquake.

1. Introduction

Due to the lack of multiple, coherent, spatially properly distributed recordings of strong-ground motions in the vicinity of faults that can host potentially devastating, large earthquakes, numerical forward modeling is a necessary tool for the assessment of the variability of potential strong ground shaking. Ideally such modeling efforts include the current knowledge of earthquake source physics as well as sufficiently accurate simulation of the excited wave field, together with a spatially variable, realistic distribution of near-surface geologic conditions. It is relatively straightforward to generate kinematic rupture models with a certain level of earthquake slip heterogeneity, but this kinematic approach uses simplified assumptions about the temporal evolution of the rupture process and often fails to capture the essential physics of earthquake rupture. Spontaneous dynamic rupture modeling produces a physically self-consistent kinematic rupture model for a single event, given a set of dynamic

input parameters and a friction law. However, assigning initial conditions for each dynamic simulation is not trivial and often requires additional assumptions.

From the standpoint of earthquake physics, the potential complexity of the problem requires an initial approach based on a simplified yet versatile mechanical model. Some previous efforts have been focused on studying the effects of heterogeneities of fault strength and initial stress on dynamic rupture models, while keeping the assumed friction laws as simple as possible(e.g. Ripperger et al., 2007; 2008[5, 6]). An inherent difficulty in such efforts is that, from a mechanical point of view, stress and strength heterogeneities cannot be prescribed arbitrarily as was done in earlier work. Their inter-dependence must be consistent with a mechanical model of deformation and stress evolution over the longer time scale of the earthquake cycle. For instance, it is expected that stress concentrations can develop at the edges of asperities (defined as fault sub-regions delimited by frictional contrasts), introducing a correlation between stress and strength that enhances high frequency radiation at asperity edges. Failure to account for such mechanical correlations leaves the dynamic rupture modeling framework so unconstrained that virtually any outcome is possible with sufficient tuning.

In a simulation-based seismic hazard analysis, it is critical to be able to generate a large number of physically self-consistent source models whose rupture process captures the main physics of earthquake rupture and is consistent with the spatio-temporal heterogeneity of past earthquakes. Such a set of source models can be used for verification of assumptions underlying strong ground motion simulation schemes (e.g. Irikura and Miyake, 2011[7]) and for constraining seismic source inversion. The approach involves developing models based on idealized friction laws, slip-weakening or rate-and-state (RS) friction, to examine the impact of assumed statistical characteristics of heterogeneities (e.g., Hillers et al., 2006; 2007[4, 8]).

This study documents progress towards these objectives by performing quasi-dynamic multi-cycle simulation (Hillers et al., 2006; 2007[4, 8]) under the rate-and-state (RS) friction law (Dieterich, 1979; Ruina, 1983[9, 10]). Each simulation is controlled by a 2D distribution of the critical slip distance, Dc, and depth dependent frictional parameters a and b. Extending previous work, dynamic rupture parameters (stress drop, strength excess, critical distance) extracted from the multi-cycle simulations are used as input parameters in fully-dynamic single-event rupture modelling (Pitarka, 1999; Dalguer and Day, 2007; Galvez et al., 2014[11, 12, 2]) under the slip-weakening (SW) friction law (Ida, 1972; Andrews, 1976[13, 14]). A single RS simulation that spans about several thousand years can generate multiple scenario earthquakes with spatio-temporal complexity similar to past earthquakes. A limited number of RS cycle models can thereby provide a sufficiently large database of moderate-to-large earthquakes. This event dataset is used to investigate the dynamic rupture characteristics of each single event (which may be poorly resolved by source inversion, e.g. spatial correlation of high slip and high slip-rate areas, source time functions, rupture velocities, etc.) through spontaneous rupture modeling and their sensitivities to initial input models such as the critical distance, Dc. Most importantly, individual events are not the results of ad hoc tuning of stress and strength heterogeneities; they are the results of the spatio-temporal evolution of the governing parameters on the frictional interface in response to steady plate loading.

In order to validate the results of such simulations, we seek model events that reproduce the ground motions recorded in an earthquake: the Mw7.3 1992 Landers earthquake that occurred on the multi-segment Landers fault system. The strike variations of the faults involved lead to natural segmentation, which is necessary for the simulation of a broad magnitude range of earthquakes. The fault segmentation brings complexity into the rupture process. For instance, the change of strike between fault segments enhances strong variations of stress. In fact,

Oglesby and Mai, 2012[15] show that the normal stress varies from positive (clamping) to negative (unclamping) between fault segments, which leads to unfavorable or favorable conditions respectively for rupture growth. The spectral element method is used for dynamic simulations here. Earthquake cycle simulations for large earthquakes are computationally intensive and are probing the limits of the computational resources we have available in-house. We have been running simulations at the very edge of numerical resolution, hoping that they can be extended later if more resources become available.

2. Earthquake cycles

For earthquake cycle modelling we adopt the rate-and-state friction law of Dietrich and Kilgore, 1994[16] and solve the quasi-dynamic cycle problem with a boundary element method with adaptive time stepping (QDYN, Luo et al., 2017ab[1, 17]). Once an earthquake is nucleated and reaches seismic slip velocities (> 0.1 m/s), QDYN exports the stresses and friction parameters to a rupture dynamic solver based on the spectral element method with fixed time step (SPECFEM3D, Galvez et al., 2014; 2016[2, 3]) to properly resolve the rupture process.

An important feature is that in our simulations with adaptive time stepping we naturally nucleate the rupture, and the time step is decreased gradually to resolve the nucleation processes. In contrast to previous single-rupture fully-dynamic modelling (e.g. Song and Dalguer, 2013[18]) we do not apply any artificial procedure to accelerate the rupture initiation. QDYN is switched to SPECFEM once the slip rate reaches 0.1 m/s. The nucleation process starts before the slip rate reaches this threshold, but we do not expect that this affects aspects of the eventual rupture that are important for strong motion simulation.

With this new approach we obtained realistic final slip, slip velocities, rupture time and rupture velocities, similar to those observed during earthquakes. To allow for more efficient coupling of these two solvers, we implemented parallelization with the Message Passing Interface (MPI) both in SPECFEM and QDYN.

3. Landers Fault System

It is difficult to dynamically simulate small magnitude events if the rupture tends to propagate through the whole fault without stopping. In order to avoid this problem, we consider a naturally segmented fault system having segments of different strike. For this work it is also desirable to simulate large magnitude events up to Mw 7.8, which are probable on inland faults. With these two problems in mind, we focus this study on the Landers fault system (see FIG. 1 left), which hosted the Mw7.3 1992 Landers earthquake that is used here for validation.

3.1. Geometry and Mesh

The Landers fault model used in our study is composed of 5 segments. The 1992 Mw 7.3 Landers earthquake ruptured three fault segments: Johnson Valley Fault, Homestead Valley Fault and Camp Rock-Emerson fault. To extend these segments to a length of 200 km (Mw7.8), the Eureka-Peak fault and Graves Hills-Harper fault have been added at the ends, as shown in FIG.1 left. FIG.1right plots the corresponding fault corners. The upper right corner inset of FIG.1 right shows a 3D view of the fault model. The x,y,z coordinates are in

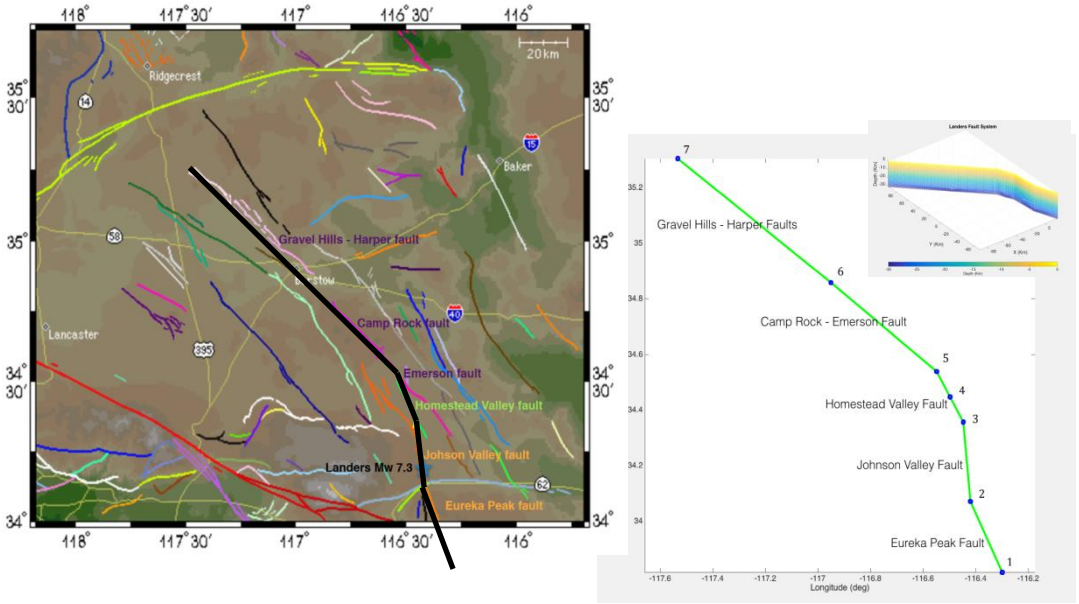

FIG. 1. Left: Southern California Fault system (source: http://scedc.caltech.edu/significant/Mojave.html). Bold black lines show the Landers rupture segments considered here. Right: Geometry of the Extended Landers Fault showing segments. Blue dots indicate the fault segment boundaries. We included the Eureka-Peak and Gravel Hills - Harper faults to reach 200 km fault length. The upper right corner inset is the 3D view in model coordinates.

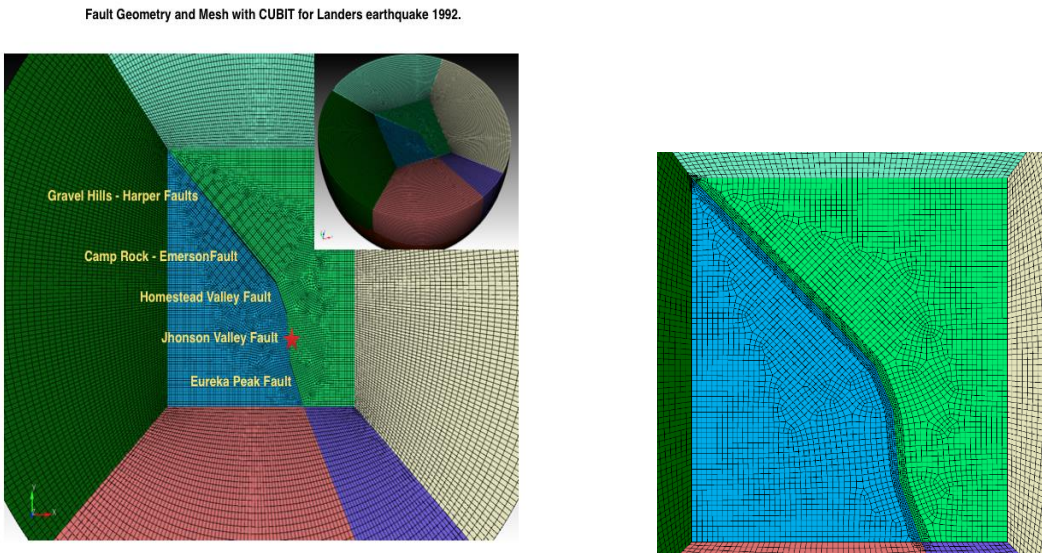

FIG. 2. Left: Mesh for the Extended Landers Fault. The red star represents the epicenter of the Landers earthquake. Right: Mesh refinement near the fault segments.

kilometres. The origin of the x,y coordinates correspond to point 4, whose latitude and longitude are 34.448 and -116.4980, respectively.

In order to mesh the complex fault system, we made use of CUBIT, a state-of-the-art hexaedral mesh generation software. The mesh and the faults used in this study are shown in FIG. 2. Minimal Dc values available for modeling depend on the minimum mesh size. In order to allow smaller Dc values, thus smaller nucleation area and event magnitude, we refine

the mesh size along the fault (see FIG. 2 right). This refinement allows accurate modeling of the rupture without strong increase of computer resources, while inducing only minor disturbance on the wave propagation modeling. The grid size of the refined fault elements is about 800 m. Each fault element contains 4 internal nodes, leading to an average 200 m spacing on the fault.

3.2. Friction Parameters

After testing several types of Dc distributions (random, hierarchical, lognormal) in quasi-dynamic cycle simulations, it was found that a lognormal Dc distribution is better at reproducing observed features of earthquake cycles, including their irregularity and magnitude distribution. In this study we prescribe the lognormal Dc distribution shown in FIG. 3. We consider a relatively small standard deviation typical of mature faults. The correlation length for the Dc distribution is 2.25 km (FIG. 3top). The mean and logarithmic standard deviation values of Dc are 0.025 m and 0.25, respectively (FIG. 3bottom). FIG. 4 shows the a-b and normal stress values as a function of depth. The region of (a-b) <0 defines the area of velocity weakening, where events nucleate. The seismogenic zone goes down to 15 km depth, as shown in FIG. 4.

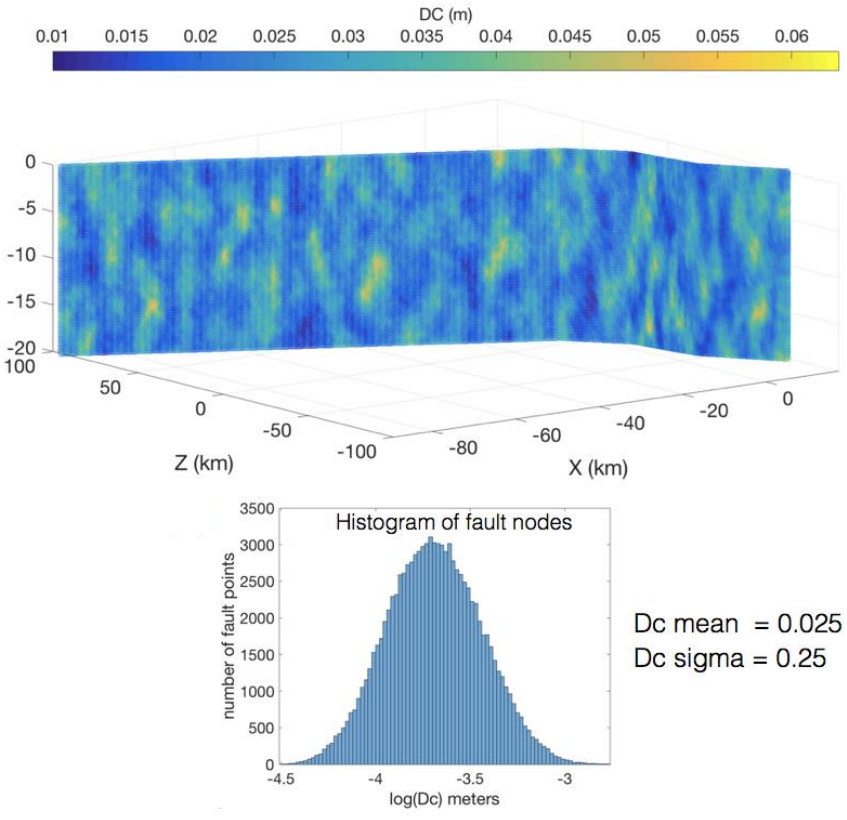

FIG. 3. Top: Assumed Dc distribution on the Landers fault system. Bottom: Histogram of the lognormal distribution of Dc.

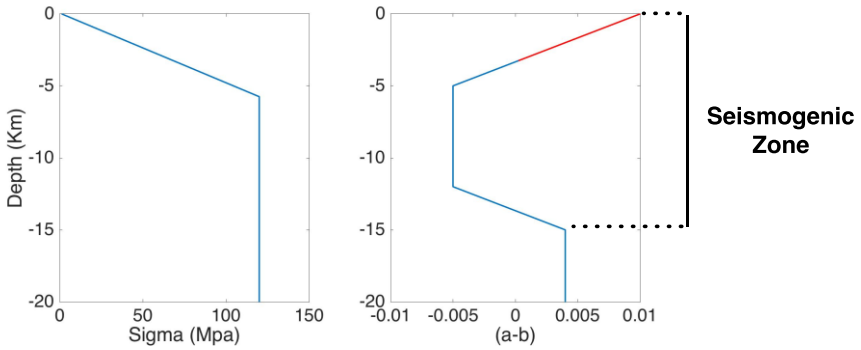

FIG. 4. Left: Normal stress vs. depth. Right: a-b vs. depth. The red line delineates the shallow velocity strengthening region where (a-b) > 0.

4. Hierarchical matrix method (H-matrix) for earthquake cycle simulations applied to the 1992 Landers, California earthquake

In this section, we implement the Hierarchical matrix multiplication (H-matrix) method, first proposed in earthquake cycle modelling by Ohtani et al., 2011[19], to perform earthquake cycle modelling for the Landers fault system. The most computationally intensive part of the quasi-dynamic simulations is the matrix-vector product (MVP) K*V required at each time step to update stress rates on the faults. K is a matrix whose (i,j) component is the stress on the i-th fault cell produced by unitary slip on the j-th fault cell. For N fault points the K matrix has size (N,N) if the slip rake is fixed and only the rake-parallel component of shear stress is considered. V is a vector that contains the slip velocity at each fault point and it has size N. In a trivial implementation, this MVP requires $O(N^2)$ operations and consumes most of the computing time. To speed up the MVP for planar faults, QDYN uses the FFT technique, but this method cannot deal with non-planar faults. For the non-planar Landers fault system we implement here the H-matrix method.

4.1.H-matrix method

The procedure to construct an H-matrix approximation of K has four parts. First, based on distance, cluster trees over mesh elements are formed. The cluster trees induce row and column permutations of K. Second, pairs of clusters are found that satisfy a criterion involving distance between the two clusters and their diameter. Third, the requested error tolerance ε is mapped to tolerances on each block K_i. The tolerance specifies the maximum error allowed. Fourth, each block is approximated by the low-rank approximation (LRA) that satisfies the block's tolerance. The K_i block requires $O(m \times n)$ storage, while its H-matrix approximation requires only $O(r(m+n))$ storage.

4.2.Implementation and validation of H-matrix method for QDYN

We make use of the H-matrix module "hmmvp" developed by Bradley et al., 2014[20]. This module makes use of the M approximation, which is a modification of LRA. The M approximation allows for greater compression of the K matrix making MVP less time consuming than the LRA approximation for large N values. The hmmvp module contains

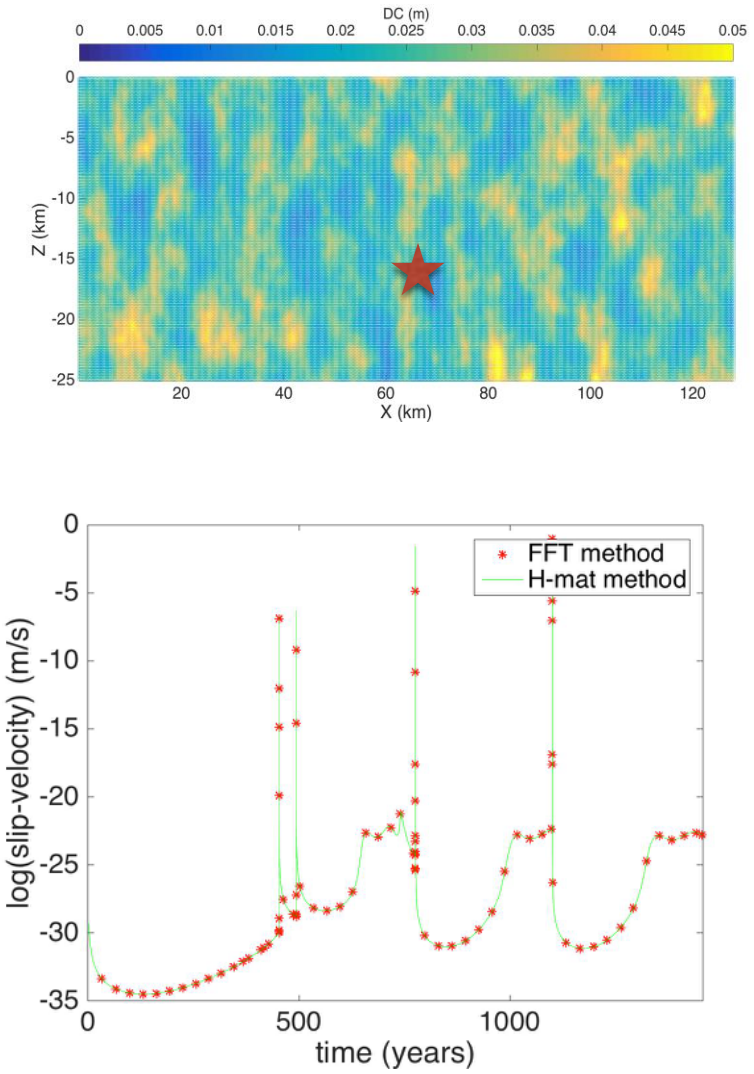

FIG. 5. Verification of the H-matrix method. Top: The Dc distribution on the fault. The red star is the reference point. Bottom: Log(slip-velocity) at the reference point. The solid green line and the red points are the log(slip-velocity) computed using the FFT and H-matrix methods, respectively. The tolerance error of the H-matrix method needed to reproduce satisfactorily the FFT results is 10^{-8}.

C++ routines that compress the K matrix and a library to compute MVP. More details on this module are presented in Bradley et al., 2014[20]. We implement the hmmvp routines into the QDYN solver for earthquake cycle modeling in complex fault systems. To validate the implementation, we perform earthquake cycle simulations for the planar fault shown at FIG.5top. This fault contains the Dc distribution for Case I (mature faults) of Galvez et al., 2017a[21]. The model runs for a duration of about 1400 years using the FFT method and our new implementation of the H-matrix method. The red star in FIG. 5top represents the fault point taken as reference. As can be seen in FIG. 5bottom, the slip velocities at the reference point obtained using the FFT and H-matrix are the same, validating our implementation.

5. Ruptures from earthquake cycle simulations of the Landers system

Using the implementation of the H-matrix method on QDYN, we were able to nucleate events along the Landers fault system. We generate about 30 events (FIG.6). The simulated events span a magnitude range of Mw 7.0-7.8, and nucleate on different sections of the Landers fault system.

6. Validation of earthquake cycle modelling by ground motion simulation

To validate earthquake source models and strong ground motion prediction methodologies, validation "in average" by comparison with GMPEs is used widely (e.g. Dreger et al., 2015[22]). However, data sets that are used for construction of GMPEs frequently have a shortage of near faults records, which in turn are important for hazard assessment of nuclear installations. In this study we will validate earthquake cycle models by comparison of observed and simulated records and response spectra for the Mw7.3 1992 Landers earthquake, for which many near-field strong motion records are available.

6.1.Method of validation

Among our 30 simulated events we selected events that satisfy the following criteria. (1) Magnitude should be nearly equal to that of the 1992 Landers earthquake, Mw 7.3. (2) The event should break the same 3 fault segments as the 1992 Landers earthquake, i.e. Johnson Valley, Homestead Valley and Camp Rock-Emerson faults. (3) Rupture initiation should be close to the hypocentre of 1992 Landers earthquake. Using these criteria, we selected two simulated events, a Mw 7.3 event at time 1245.2 yr and Mw 7.31 event at time 1831.3 yr. The slip distributions of the selected events are shown in FIG. 7 and compared to the multi-time-window source inversion result of Wald and Heaton, 1994[23]. Other inversion results (e.g. Cohee and Beroza, 1994; Cotton and Campillo, 1995; Hernandez et al., 1999[24, 25, 26]) have roughly similar slip distributions.

Recordings of the 1992 Landers earthquakes were downloaded from the Center for Engineering Strong Motion Data (https://www.strongmotioncenter.org/). Only processed records were used. A map of the selected stations is shown in FIG. 8. The sites are divided into basin and non-basin sites using the SCEC community velocity model (version 4, Lee and

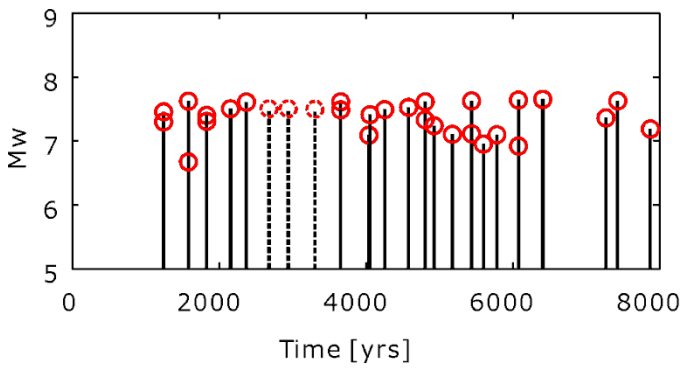

FIG. 6. Distribution of simulated events with time. Cycles in the first 1000 years are ignored. Events shown by dashed lines were not processed in this work.

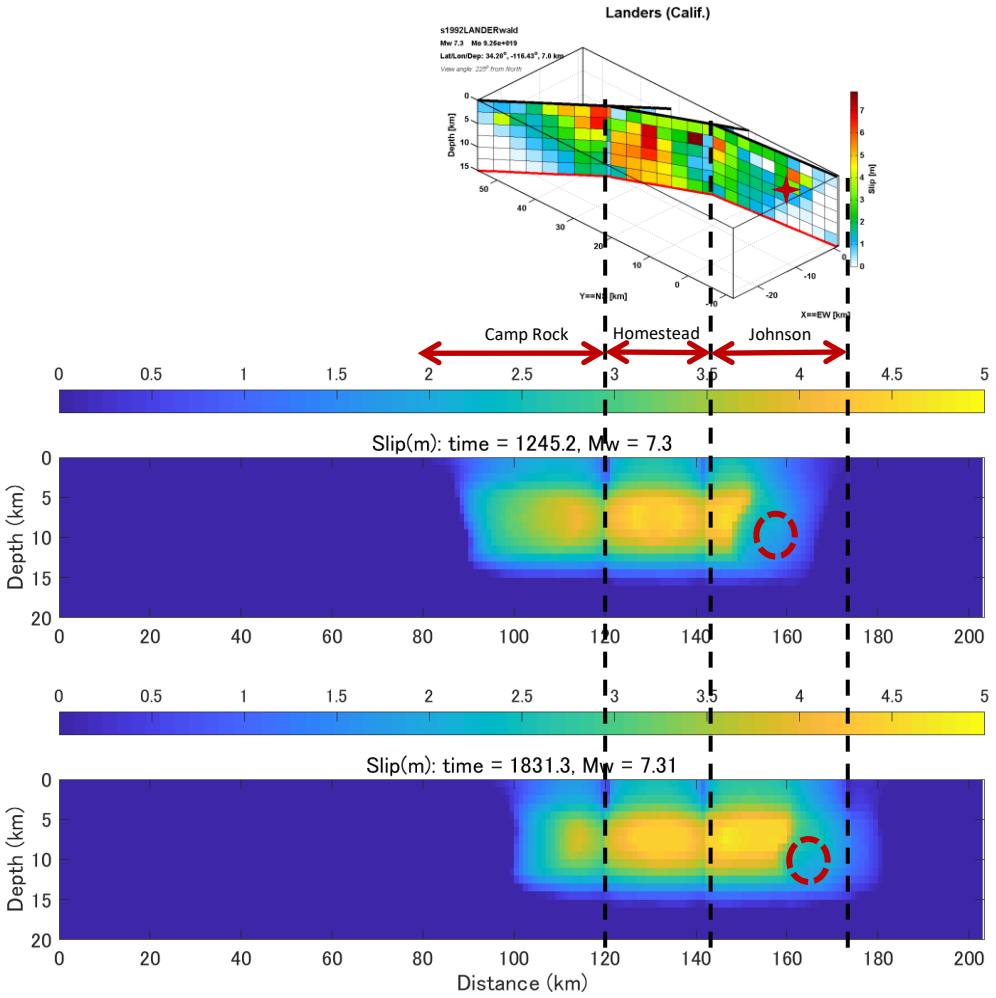

FIG. 7. Procedure for selection of events for the validation. Top: slip of the source inversion by Wald and Heaton, 1994[23] (courtesy of the Finite-Source Rupture Model Database: http://equake-rc.info/SRCMOD/). Middle and bottom: slip models of two selected simulated events with similar Mw, rupture nucleation and ruptured segments as the 1992 Landers earthquake. Dashed circles are rupture initiation areas.

Chen, 2016; Small et al., 2017[27, 28]). In order to avoid additional uncertainties related to uncertainties in the velocity model, only non-basin sites are used for validation.

We simulated ground motion waveforms for the two selected events without making any modifications to their source characteristics. We use the sources generated by the dynamic models and simulate waveforms using separate wave propagation software. We consider only the slip rate functions in cells of the dynamic source that have slip rate larger than 0.02 m/s. Due to the large number of cells (up to 2 million for a Mw 7.8 event) we used the staggered grid 3D-FDM method of Graves, 1996[29] instead of the discrete wavenumber method (Bouchon, 1981 [30]) widely used for 1D velocity structures. The velocity model is the 1D model used for source inversion by Wald and Heaton, 1994[23] (see TABLE 1). They used a regional velocity model with an additional shallow low-velocity layer that mimics thin alluvial layers at non-basin sites. The presence of such a layer is the reason why we prefer the 1D model of Wald and Heaton, 1994[23], to the more detailed 3D model of the SCEC

community, which employs seismic tomography results without waveform tuning and leaves optional shallow low-velocity layers (geotechnical layer).

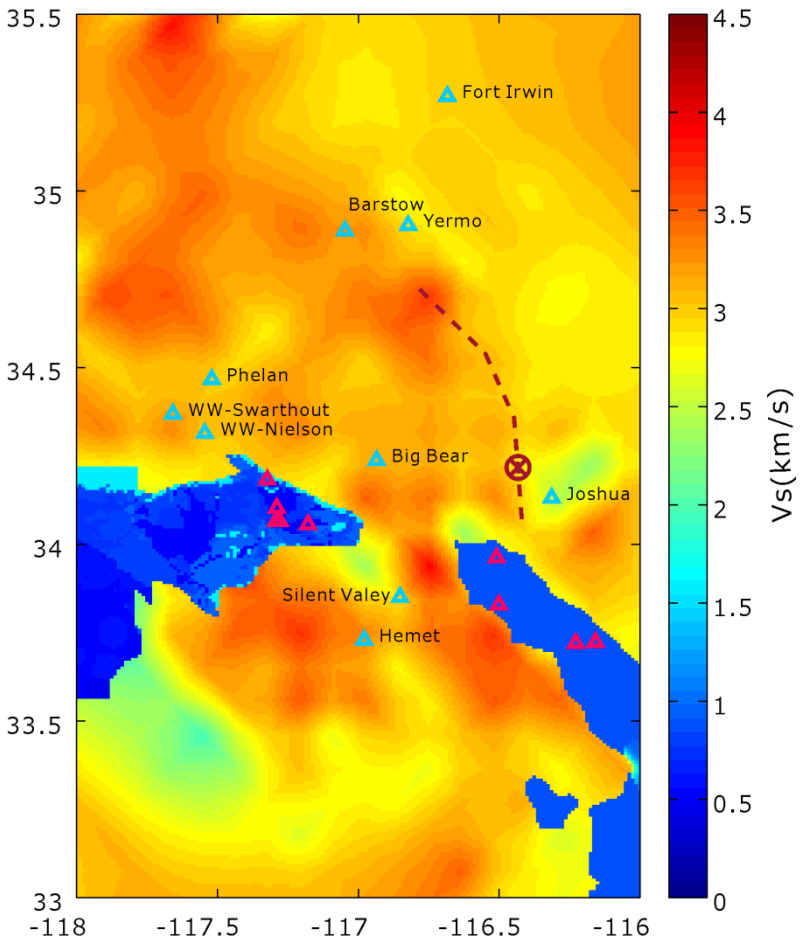

FIG. 8. Strong motion sites that recorded 1992 Landers earthquake (triangles). Color map is the surface shear wave velocity (Vs) distribution according to the SCEC community velocity model (see Lee and Chen, 2016 [27]). Dark blue areas are basins. Non-basin sites (light blue triangles) are used for validation.

TABLE 1: VELOCITY STRUCTURE MODEL FOR WAVEFORMS SIMULATION (WALD AND HEATON, 1994[23]).

Layer	**Thickness (km)**	**Vp (km/s)**	**Vs (km/s)**	**Density (kg/m3)**	**Qs**
Surface low-velocity	1.5	3.80	1.98	2300	30
Crustal low-velocity	2.5	5.50	3.15	2600	300
Upper crust	22.0	6.20	3.52	2700	300
Lower crust	6.0	6.80	3.83	2870	300

Upper Mantle	inf	8.00	4.64	3500	300

6.2.Validation results

The shortest period resolved by our FDM simulations was 1.0 sec. The longest usable period of the observed records is 10 sec. For waveform comparisons both observed and simulated waveforms are bandpass filtered in the 1-10 sec period range. Then velocity response spectra Sv are calculated. The valid period range of response spectra is 2-10 sec. FIG. 9 shows examples of simulated waveforms and Sv spectra and comparison with observations.

Among 10 non-basin sites, 6 sites had good waveform fit: amplitude, duration and predominant periods are well reproduced in the simulated waveforms. These sites are Fort Irwin, Barstow, Yermo, WW-Swarthout, WW-Nielson and Big Bear (see FIG. 8; official site names are simplified for clarity of FIG. 8). Most of these sites are in the forward direction of rupture propagation, so the directivity effect is strong. At the remaining four sites there is limited agreement between modeled and observed waveforms; only peak amplitudes are reproduced. These sites are Joshua, Silent Valley, Hemet and Phelan, and most of them are located in the backward rupture direction. The recorded waveforms at these sites have a prominent long-period wave-packet, e.g. a wave after 40 sec at Silent Valley in FIG. 9. This wave may be the result of a smaller basin amplification that was not considered in the simulations.

However, response spectra Sv have good fit for most of sites, even for sites that have limited waveform fit. Average observed/synthetic spectral ratios and their standard deviations are shown in FIG. 10 for both selected events. There are no systematic discrepancies of average spectral ratios in the valid period range 2-10 sec.

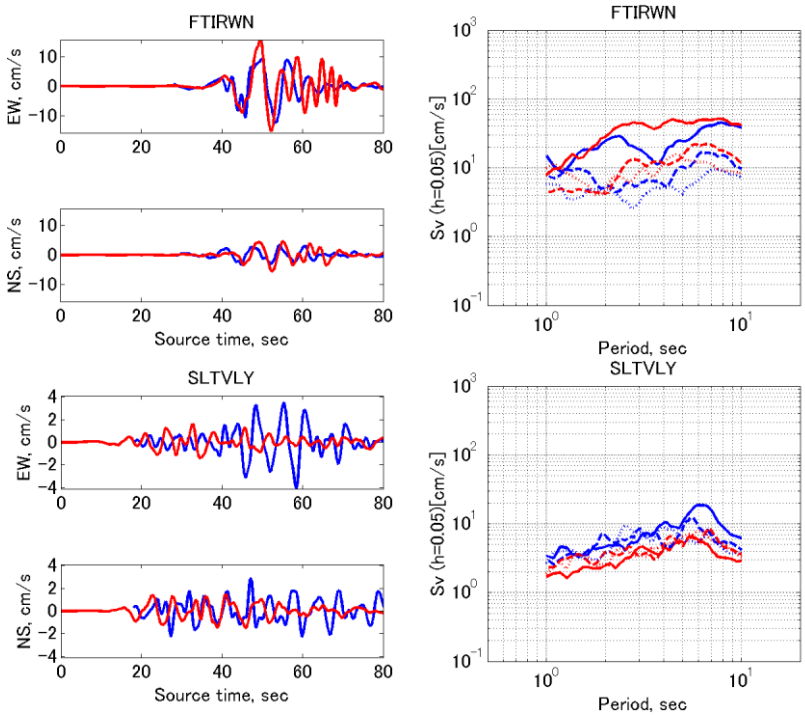

FIG. 9. Ground motion simulation examples: waveforms (left) and velocity response spectra (right) for the second selected event. Blue – observed, red – simulated; response spectra: solid – EW, dashed – NS, dotted – UD components. Top plots: example of good fit at site Fort Irwin. Bottom plots: example of limited fit at site Silent Valley.

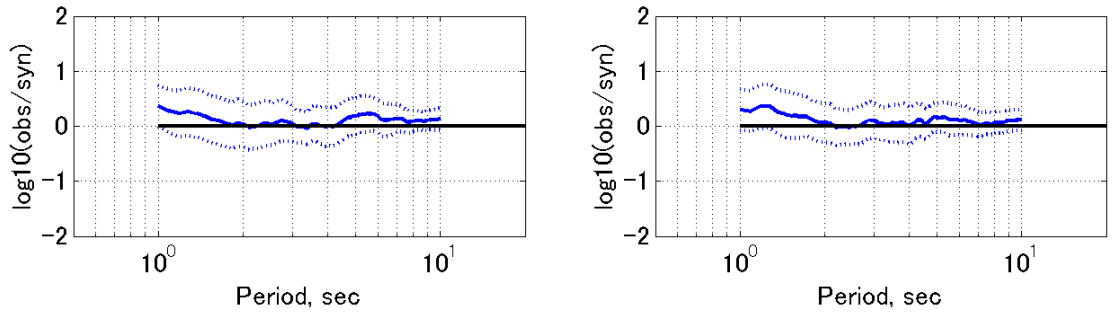

FIG. 10. Comparison of observed and synthetic Sv spectra for horizontal components of non-basin sites. Average+/-std value; left: first selected event, right: second selected event.

7. Discussion

In this study we validated multi-cycle earthquake simulations by waveform simulation for particular models. For more comprehensive validation, comparison of the ground motion attributes for all simulated events with GMPEs is necessary. We will do this in the near future, and anticipate some tuning of parameter settings (fault width, normal stress, etc.) may be necessary to achieve that.

Simulated events are a valuable data set for the study of detailed features of rupture models. Our preliminary studies (Galvez et al., 2017ab [21, 31]) indicate that there may be significant correlations between slip rate, rise time, rupture velocity and Dc distribution. There are also indications that the locations of high-rate areas are correlated with locations of high-slip areas, having the following order in space: rupture initiation – high-slip area – high-rate area. If confirmed, these features may improve strong ground motion predictions.

In our simulations Dc is the only heterogeneous model parameter. Heterogeneity of stress drop and strength excess is the spontaneous result of earthquake cycles. For this reason, correlations with Dc, the only parameter that remains unchanged throughout multiple cycles, are most important. They may allow us to extrapolate features observed in past earthquakes into future earthquakes on the same fault.

Finally, analysis of the discrepancy of short-period and long-period generation areas is also important. We will examine the scaling properties of the simulated earthquakes, with a particular focus on quantifying the distinct locations of areas of large slip and large slip velocity as a function of magnitude. The analysis will be supported by insight from the analysis of other dynamic quantities, including rupture speed, dynamic stress drop, rise time and general attributes of band-pass filtered slip velocity time histories. Our goal will be to understand the mechanical origin of the phenomenon at a sufficient level to provide a physical basis for the formulation of simplified methods to account for distinct short- and long-period slip in kinematic or pseudo-dynamic earthquake source generation algorithms for engineering ground motion prediction.

8. Conclusions

A large number of events with Mw 7.0~7.8 were successfully simulated by physics-based fully-dynamic multi-cycle earthquake simulations. Among the large number of simulated source models, two events have Mw and slip distribution similar to the 1992 Landers earthquake, and are suitable for validation. We ran waveform simulations for these two models. We find that the simulated average response spectra and waveforms for some sites are in good agreement with the recordings of the 1992 Landers earthquake.

Acknowledgements: This study was based on the 2017 research project 'Examination for uncertainty of strong ground motion prediction for the inland crustal earthquakes' by the Nuclear Regulation Authority (NRA), Japan. We would like to thank Dr. Andrew Bradley for providing the H-matrix module and his valuable assistance in the usage of this library. The Super Computer Shaheen II at KAUST University has been used to run the models presented in this study. Shaheen II is a Cray XC40 delivering over 7.2 Pflop/s of theoretical peak performance. Overall the system has a total of 197,568 processor cores and 790TB of aggregate memory.

REFERENCES

[1] LUO, Y., et al., „QDYN: a Quasi-DYNamic earthquake simulator (v1.1)", Zenodo (2017a) doi:10.5281/zenodo.322459.

[2] GALVEZ, P., et al., "Dynamic earthquake rupture modelled with an unstructured 3D spectral element method applied to the 2011 M9 Tohoku earthquake", Geophys. J. Int. **198** (2014) 1222.

[3] GALVEZ, P., et al., "Rupture reactivation during the 2011 Tohoku earthquake: Dynamic rupture and ground motion simulations", Bull. Seismol. Soc. Am., **106** (2016) 819, doi:101785/0120150153.

[4] HILLERS, G., et al., "Statistical properties of seismicity of fault zones at different evolutionary stages", Geophys. J. Int. **169** (2007) 515.

[5] RIPPERGER, J., et al., "Earthquake source characteristics from dynamic rupture with constrained stochastic fault stress", J. Geophys. Res. **112** (2007) B04311, doi:10.1029/2006JB004515.

[6] RIPPERGER, J., et al., "Variability of near-field ground motion from dynamic earthquake rupture simulations", Bull. Seism. Soc. Am. **98** (2008) 1207, doi:10.1785/0120070076.

[7] IRIKURA, K., MIYAKE, H., „Recipe for predicting strong ground motion from crustal earthquake scenarios", Pure Appl. Geophys. **168** (2011) 85, doi:10.1007/s00024-010-0150-9.

[8] HILLERS, G., et al., "Seismicity on a fault with rate- and state-dependent friction and spatial variations of the critical slip distance", J. Geophy. Res. **111** (2006) 2156, doi: 10.1029/2005JB003859.

[9] DIETERICH, J.H., "Modeling of Rock Friction, 1. Experimental results and constitutive equations", J. Geophy. Res. **84** (1979) 2161.

[10] RUINA, A., "Slip Instability and State Variable Friction Laws", J. Geophy. Res., **88** (1983) 10359.

[11] PITARKA, A., "3D elastic finite-difference modeling of seismic motion using staggered grids with nonuniform spacing", Bull. Seismol. Soc. Am. **89** (1999) 54.

[12] DALGUER, L.A., DAY, S.M., "Staggered-grid split-node method for spontaneous rupture simulation", J. Geophys. Res. **112** (2007) B02302, doi:10.1029/2006JB004467.

[13] IDA, Y., "Cohesive force across the tip of a longitudinal shear crack and Griffith's specific surface energy", J. Geophys. Res. **77** (1972) 3796.

[14] ANDREWS, D.J., "Rupture propagation with finite stress in antiplane strain", J. Geophys. Res. **81** (1976) 3575.

[15] OGLESBY, D., MAI, P.M., "Fault geometry, rupture dynamics and ground motion from potential earthquakes on the North Anatolian Fault under the Sea of Marmara", Geophys. J. Int. (2012) 188 1071, DOI: 10.1111/j.1365-246X.2011.05289.x

[16] DIETERICH, J.H., KILGORE, B.D., „Direct observation of frictional contacts: New insights for state-dependent properties", Pure Appl. Geophys. **143** (1994) 283, doi:10.1007/BF00874332.

[17] LUO, Y., et al., "Source rupture effects on earthquake moment-area scaling relations", Pure Appl. Geophys. **174** (2017b) 3331, doi: 10.1007/s00024-017-1467-4.

[18] SONG, S.G., DALGUER, L.A., "Importance of 1-point statistics in earthquake source modeling for ground motion simulation", Geophys. J. Int. 192 (2013) 1255, doi: 10.1093/gji/ggs089.

[19] OHTANI, M., et al., "Fast computation of quasidynamic earthquake cycle simulation with hierarchical matrices", Procedia Comput. Sci. 4 (2011) 1456.

[20] BRADLEY, A.M., "Software for efficient static dislocation-traction calculations in fault simulators", Seism. Res. Lett. **85** (2014) 1358, doi: 10.1785/0220140092.

[21] GALVEZ, P., et al., "Characteristics of strong ground motion generation areas inferred from fully dynamic multicycle earthquake simulations", 2017 Joint Meeting of Earth and Planetary Science, Chiba, Japan (2017a) SCG70-02, https://confit.atlas.jp/guide/event/jpguagu2017/subject/SCG70-02/tables?cryptoId=

[22] DREGER, D.S., JORDAN, T.H., "Introduction to the Focus Section on Validation of the SCEC Broadband Platform V14.3 Simulation Methods", Seism. Res. Lett. **86** (2014) 15, doi: https://doi.org/10.1785/0220140233.

[23] WALD, D. J., HEATON, T.H., "Spatial and Temporal Distribution of Slip for the 1992 Landers, California, Earthquake", Bull. Seismol. Soc. Am. **84** (1994) 668.

[24] COHEE, B.P., BEROZA, G.C, "Slip distribution of the 1992 Landers earthquake and its implications for earthquake source mechanics", Bull. Seismol. Soc. Am **84** (1994) 692.

[25] COTTON, F., CAMPILLO, M., "Frequency-Domain Inversion of Strong Motions - Application to the 1992 Landers Earthquake", J. Geophys. Res.**100** (1995) 3961.

[26] HERNANDEZ, B., et al., "Contribution of radar interferometry to a two-step inversion of the kinematic process of the 1992 Landers earthquake", J. Geophys. Res. **104** (1999) 13083.

[27] LEE, E.-J., CHEN, P., "Improved Basin Structures in Southern California Obtained Through Full-3D Seismic Waveform Tomography (F3DT)", Seism. Res. Lett. **87** (2016) 874, doi: 10.1785/0220160013.

[28] SMALL, P., et al., The SCEC Unified Community Velocity Model Software Framework, Seism. Res. Lett. **88** (2017) 1539, doi: 10.1785/0220170082.

[29] GRAVES, R.W., "Simulating seismic wave propagation in 3D elastic media using staggered-grid finite differences", Bull. Seismol. Soc. Am. **86** (1996) 1091.

[30] BOUCHON, M., "A Simple Method to Calculate Green's Function for Elastic Layered Media", Bull. Seismol. Soc. Am. **71** (1981) 959.

[31] GALVEZ, P., et al., "Multicycle Dynamic simulations of Inner Fault Parameters of Inland Faults", PSHA Workshop: Future Directions for Probabilistic Seismic Hazard Assessment at a Local, National and Transnational Scale, Lenzburg, Switzerland (2017b) poster B3, http://www.seismo.ethz.ch/export/sites/sedsite/research-and-teaching/.galleries/pdf_psha/Poster_Galvez.pdf

A.3.3 Effect of the shallow (a-b) velocity strengthening region

In attempt to reproduce large near surface slip on the Camp Rock segment of the 1992 Landers earthquake, we analyzed the possible effect of the shallow velocity strengthening (a-b)>0 (VS) regions on the rupture area and seismic moment. We gradually decreased the VS region and found that by decreasing the thickness of VS the rupture propagates larger distances and produces more elongated ruptures. Figure A.3.3-1 shows the three VS models chosen. All three models have the same parameters, the only difference is in the VS thickness. As shown in Figure A.3.3-2, decreasing the thickness of VS from 3.2 to 1.25 increases the seismic moment from 7.3 to 7.6. This is because by decreasing the width of VS the rupture absorbs less rupture energy, hence the rupture has more energy left to propagate larger distances.

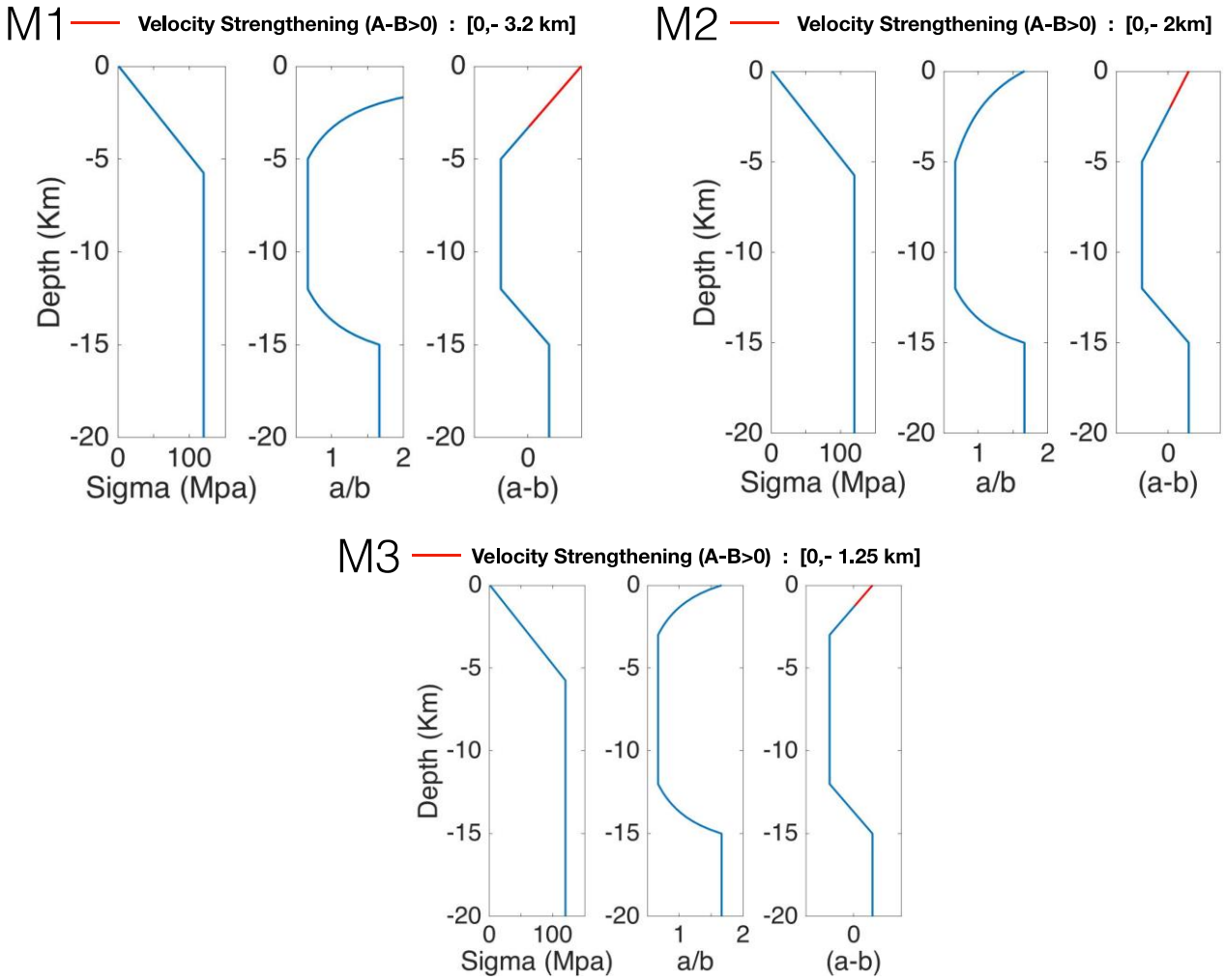

Figure A.3.3-1. Profiles of normal stress (Sigma), A/B ratio and (A-B) parameters along depth for three different models. The red line in the (A-B) profile shows the region of (A-B)>0, velocity strengthening thickness.

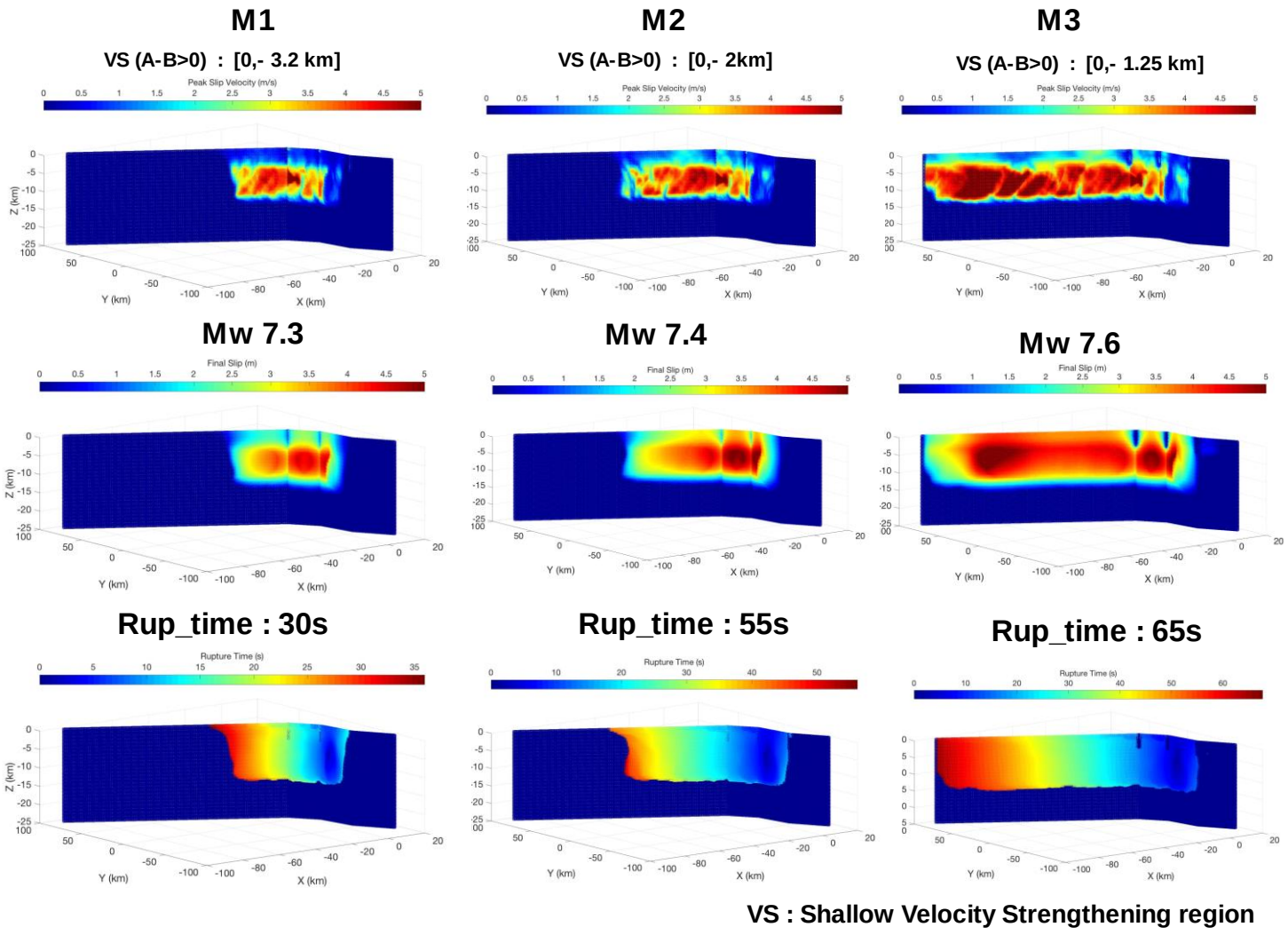

Figure A.3.3-2. Each column shows the peak slip velocity, final slip and rupture time of the three models (M1, M2 and M3) shown in Figure A.3.3-1. By decreasing the thickness of the VS region (A-B>0), the rupture travels larger distances and has larger moment magnitude Mw increasing from 7.3 to 7.6.

A.3.4 Distribution of event parameters

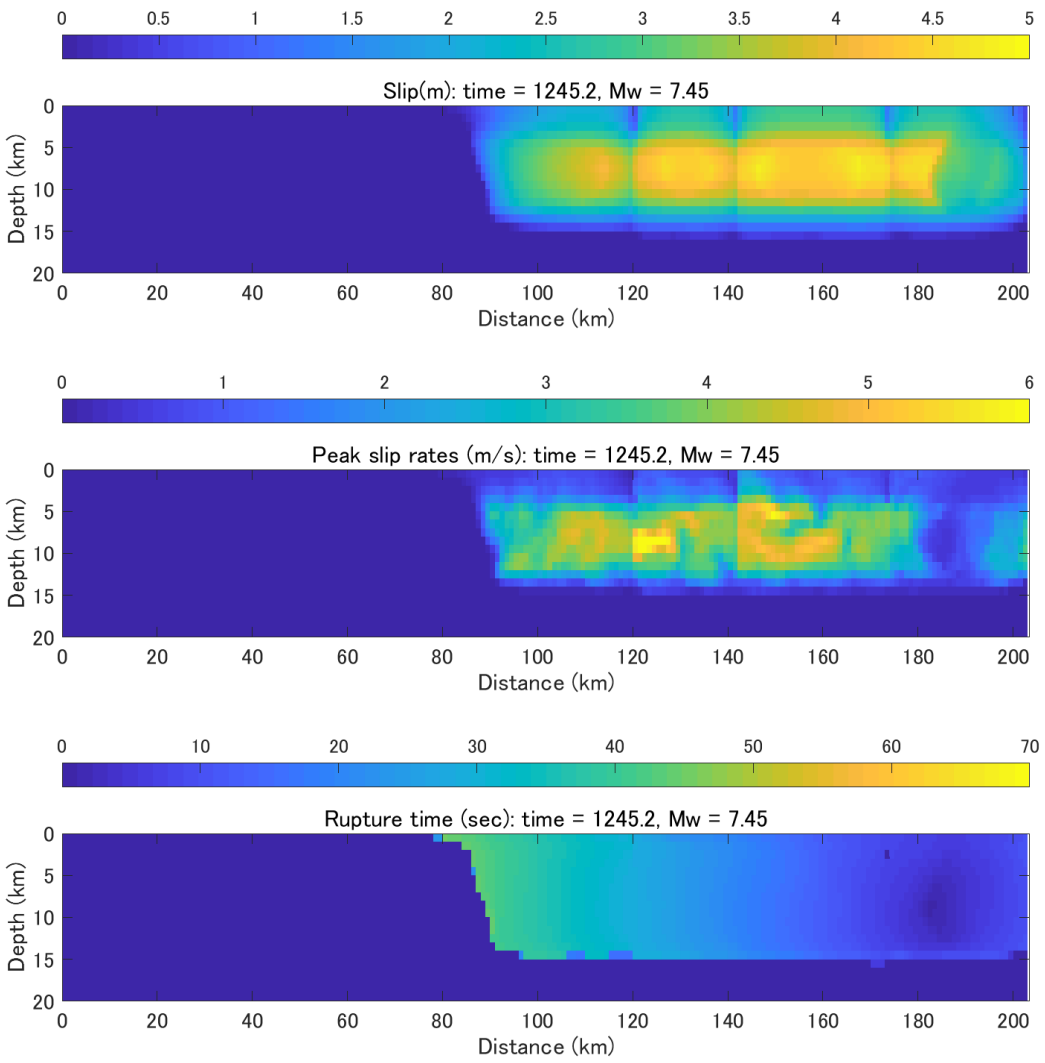

Figure A.3.4-1. Peak slip, peak slip rate and rupture time distributions for Event 1, 1245.2 year, *Mw*7.45

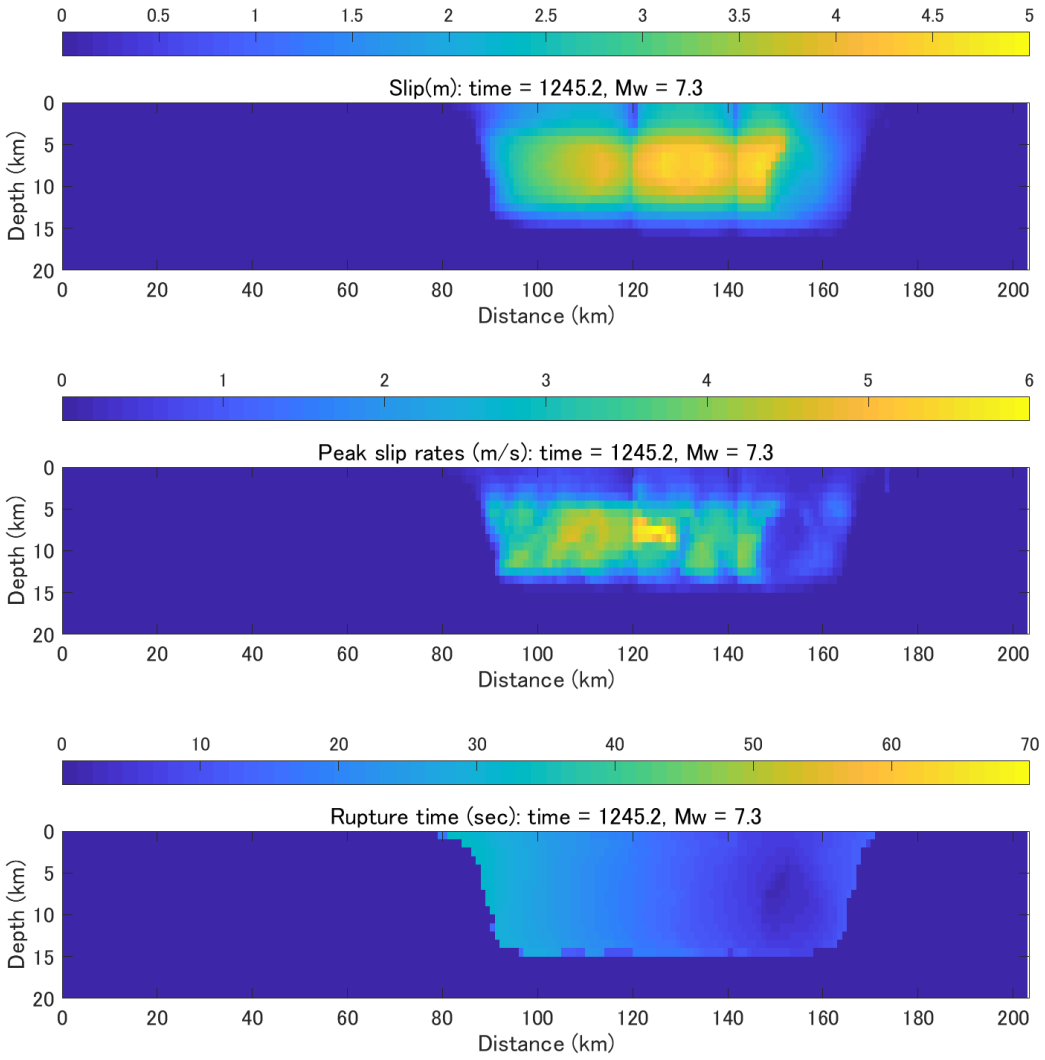

Figure A.3.4-2. Peak slip, peak slip rate and rupture time distributions for Event 2, 1245.2 year, *Mw*7.3

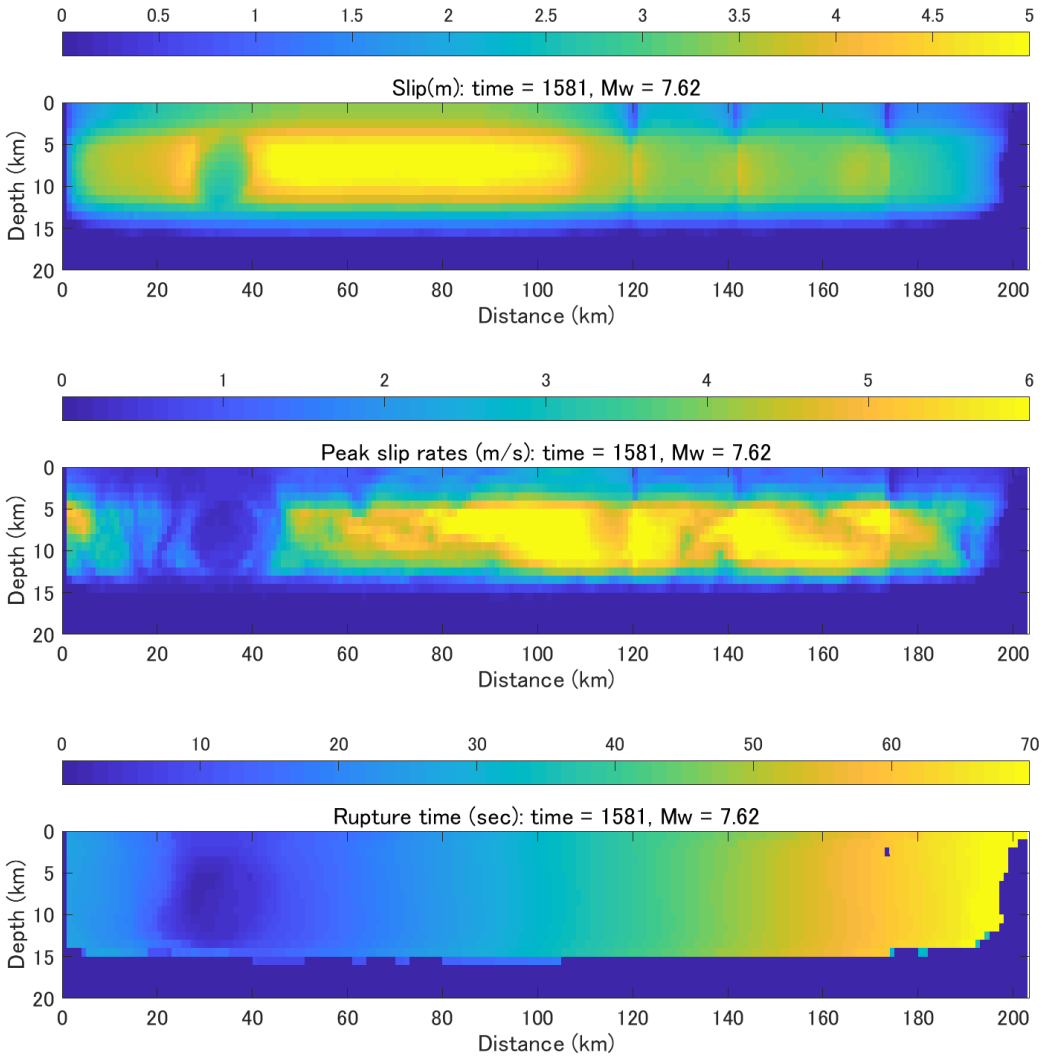

Figure A.3.4-3. Peak slip, peak slip rate and rupture time distributions for Event 3, 1581.0 year, *Mw*7.62

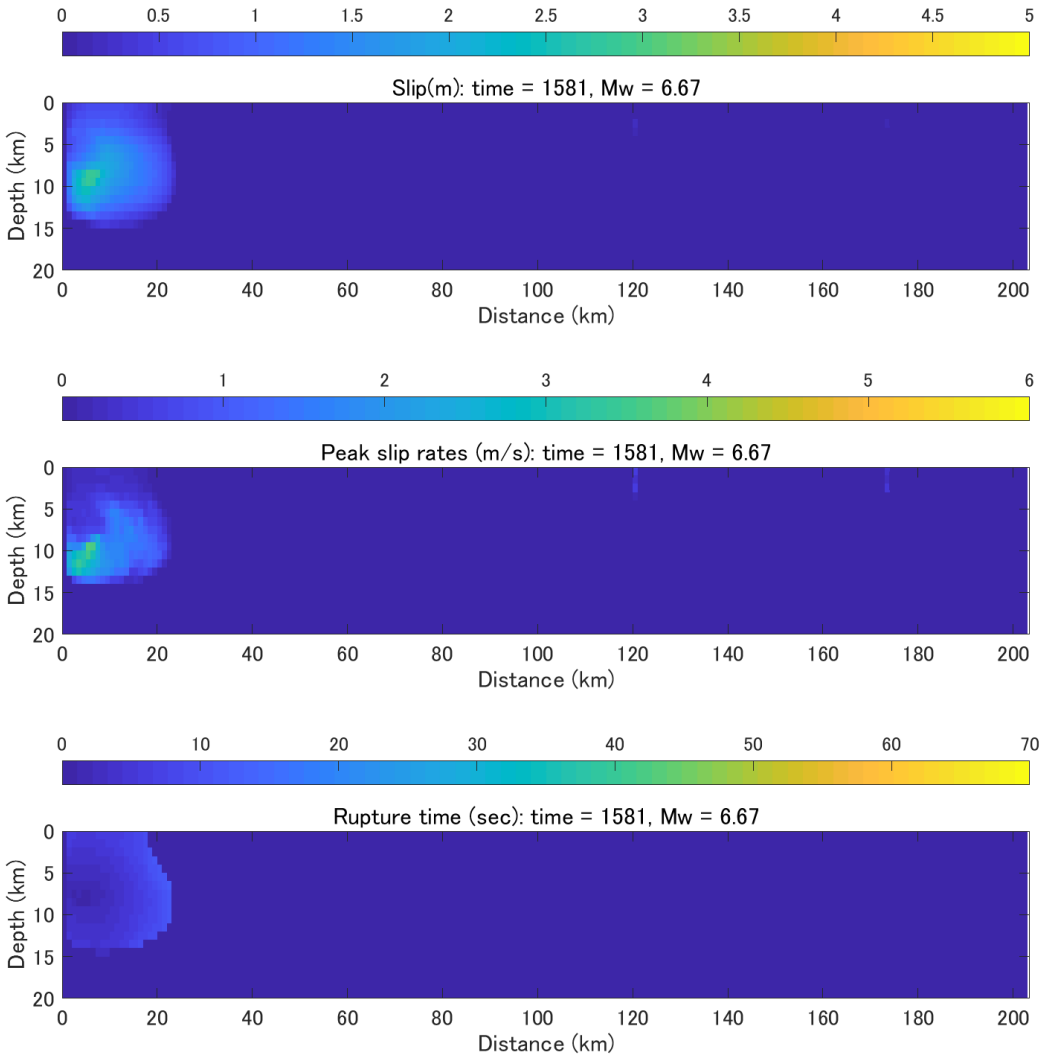

Figure A.3.4-4. Peak slip, peak slip rate and rupture time distributions for Event 4, 1581.0 year, *Mw*6.67

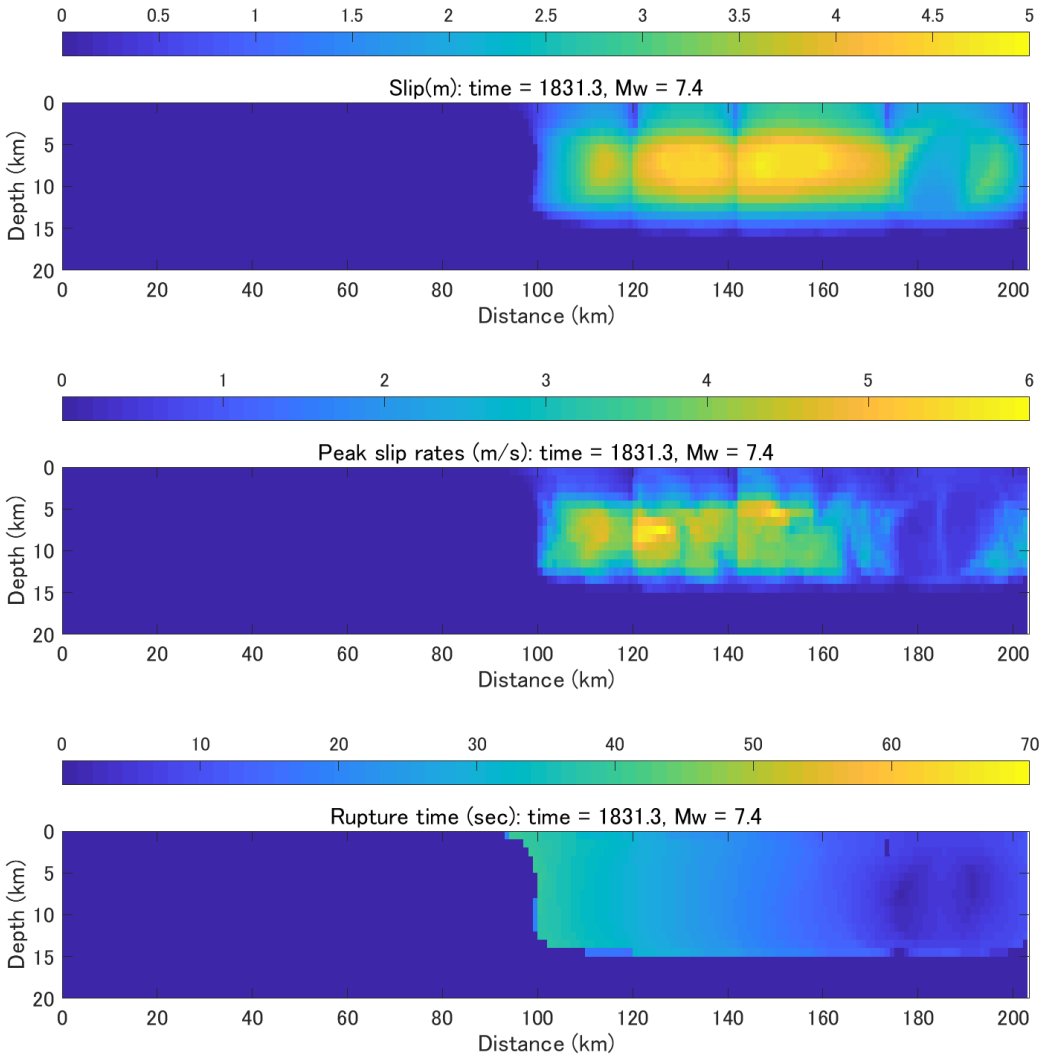

Figure A.3.4-5. Peak slip, peak slip rate and rupture time distributions for Event 5, 1831.3 year, *Mw*7.4

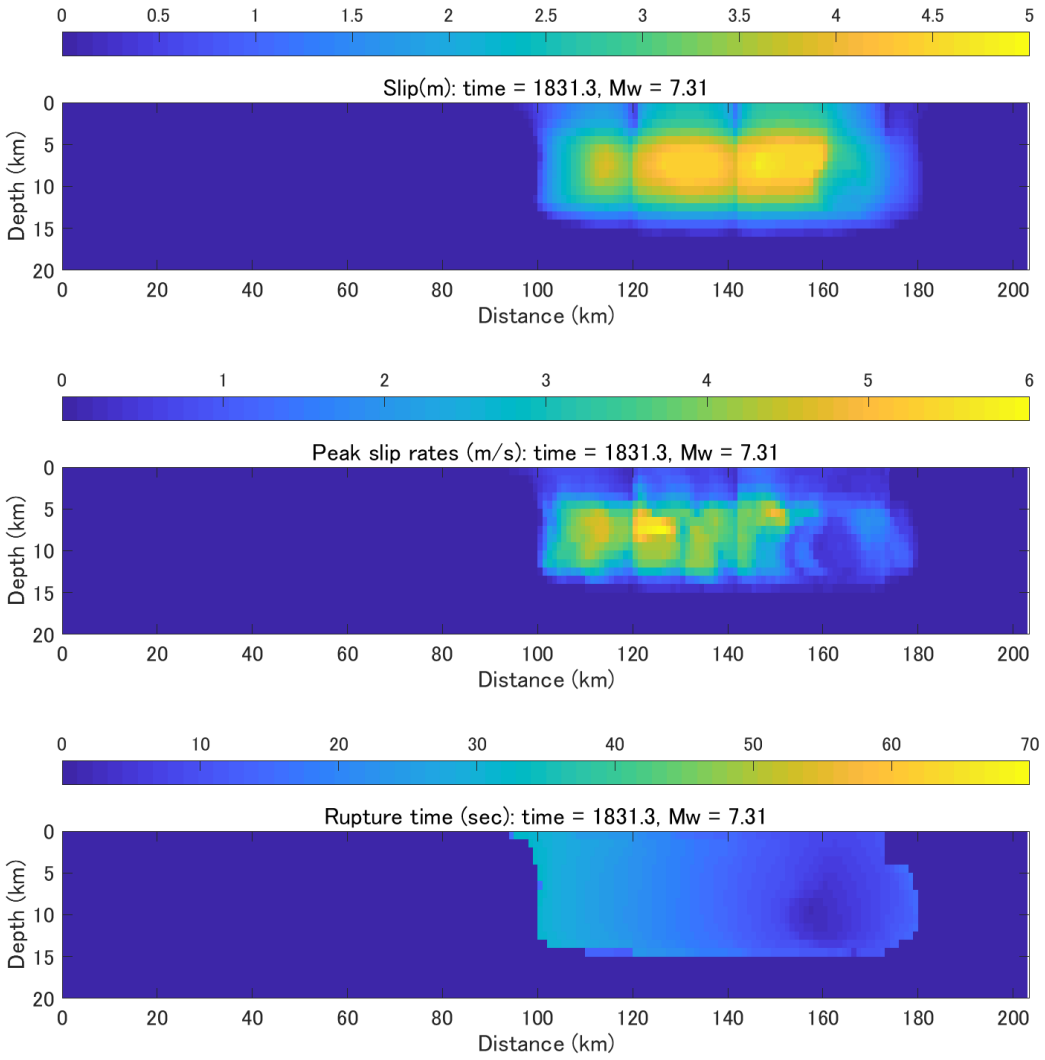

Figure A.3.4-6. Peak slip, peak slip rate and rupture time distributions for Event 6, 1831.3 year, *Mw*7.31

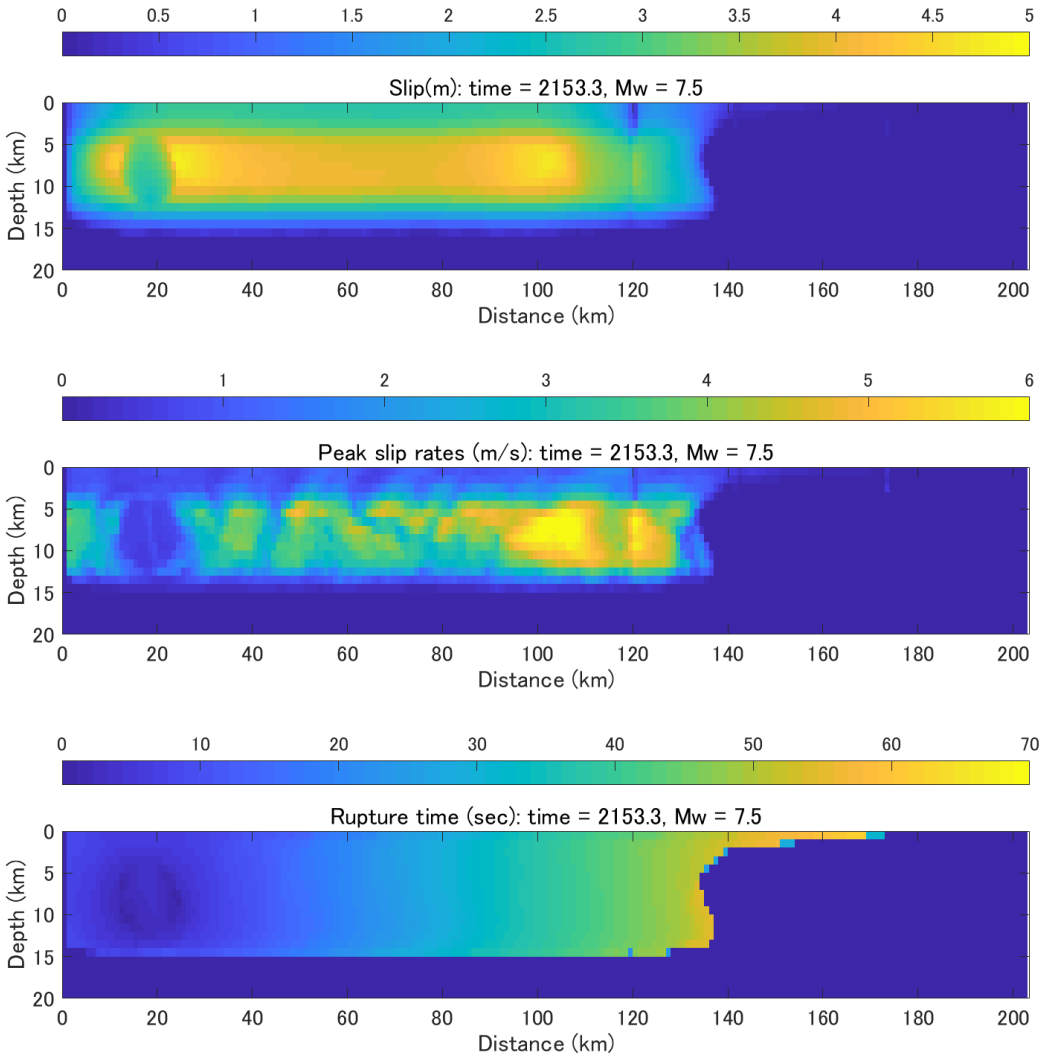

Figure A.3.4-7. Peak slip, peak slip rate and rupture time distributions for Event 7, 2153.3 year, *Mw*7.5

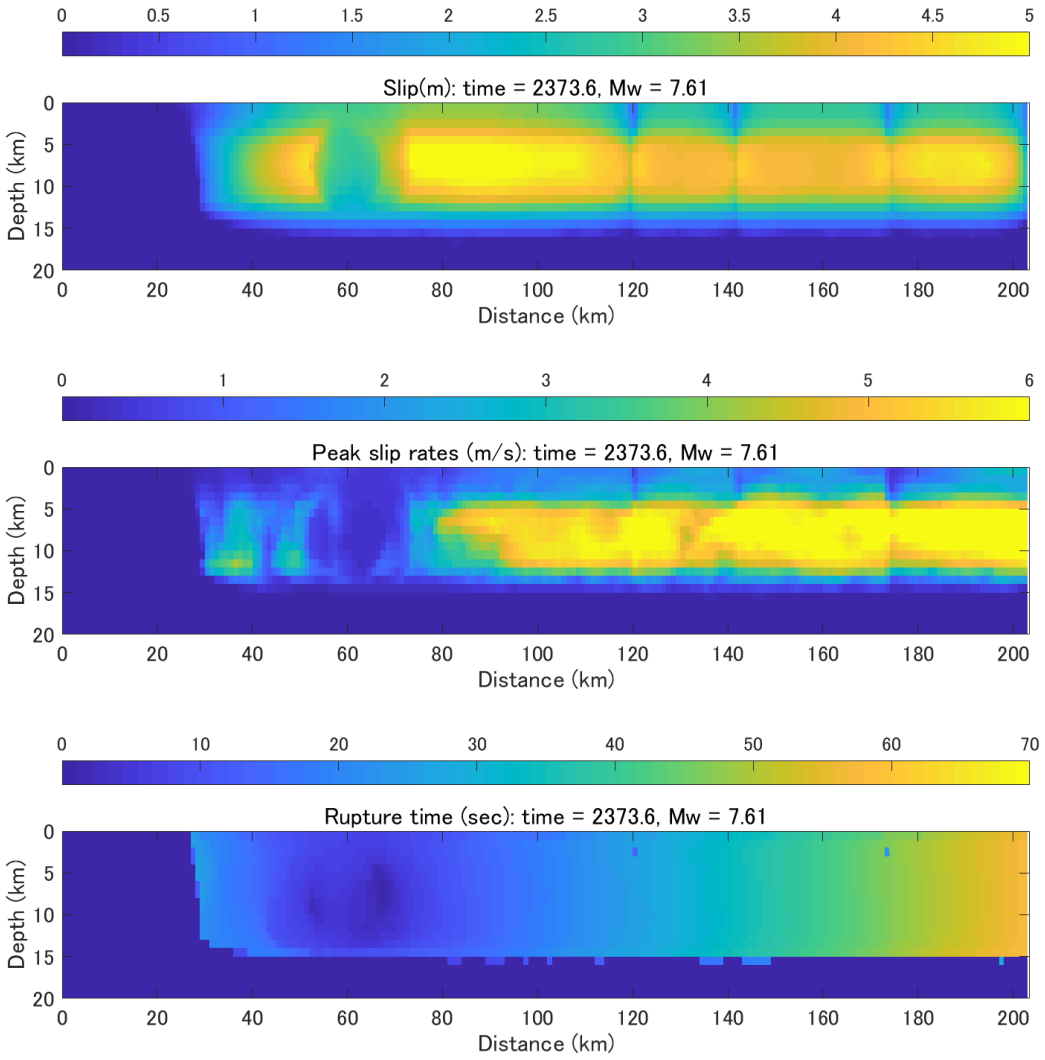

Figure A.3.4-8. Peak slip, peak slip rate and rupture time distributions for Event 8, 2373.6 year, *Mw*7.61

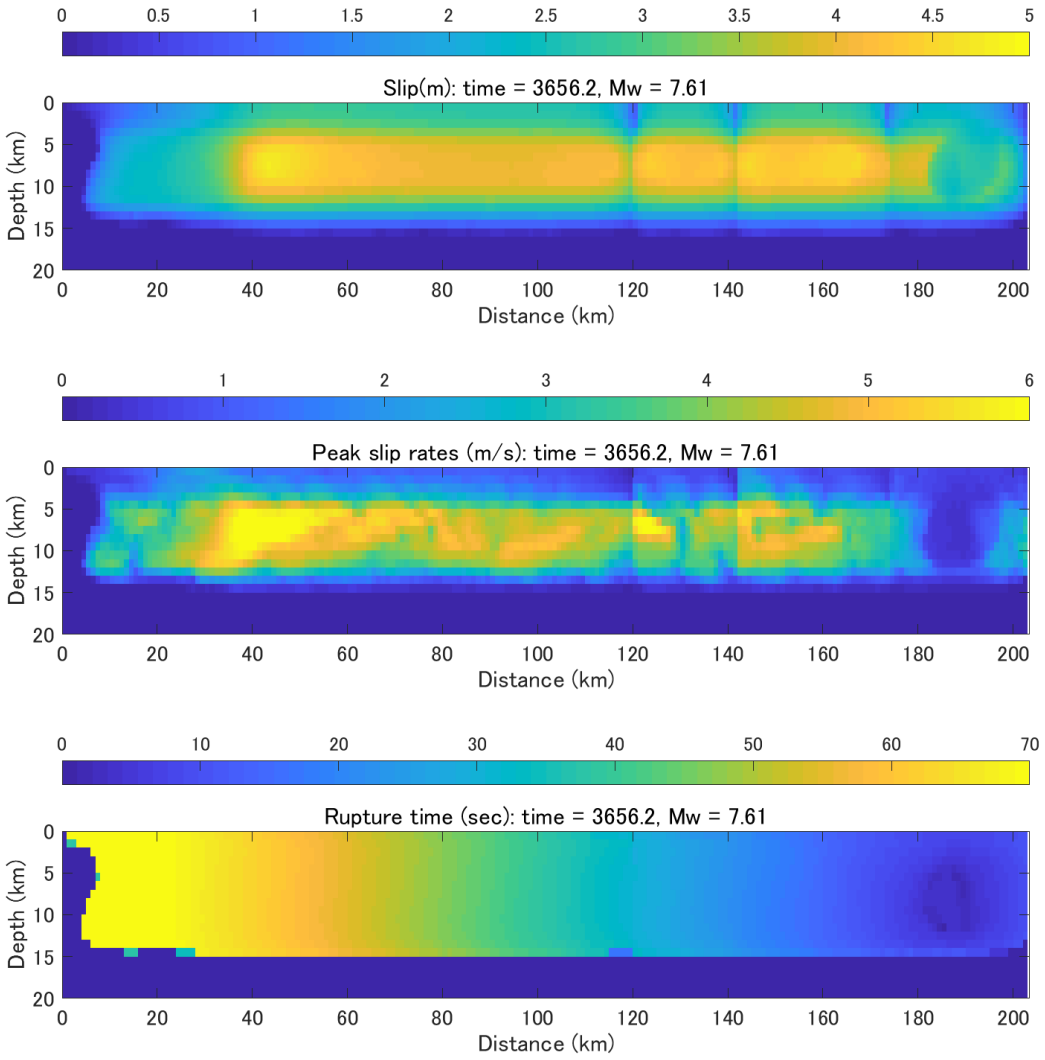

Figure A.3.4-9. Peak slip, peak slip rate and rupture time distributions for Event 12, 3656.2 year, *Mw*7.61

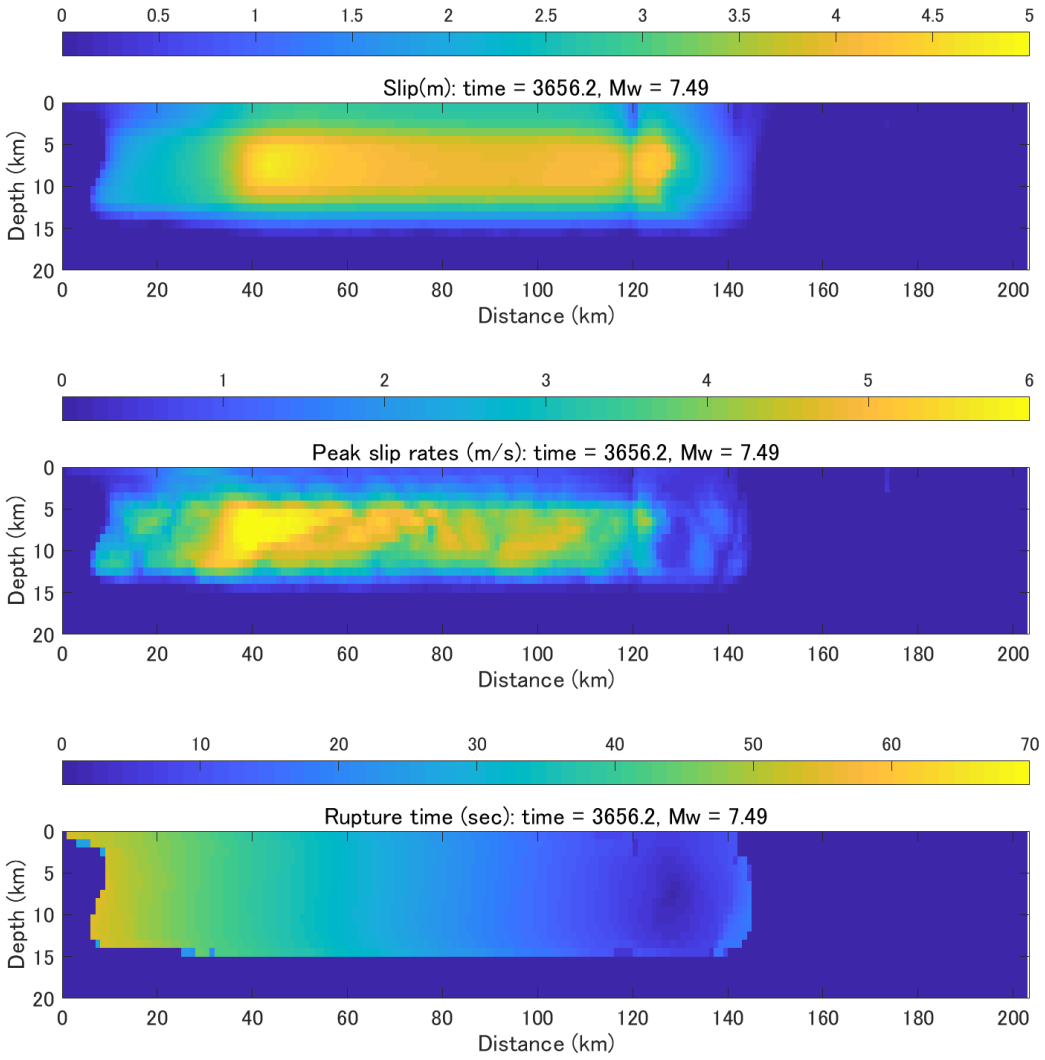

Figure A.3.4-10. Peak slip, peak slip rate and rupture time distributions for Event 13, 3656.2 year, *Mw*7.49

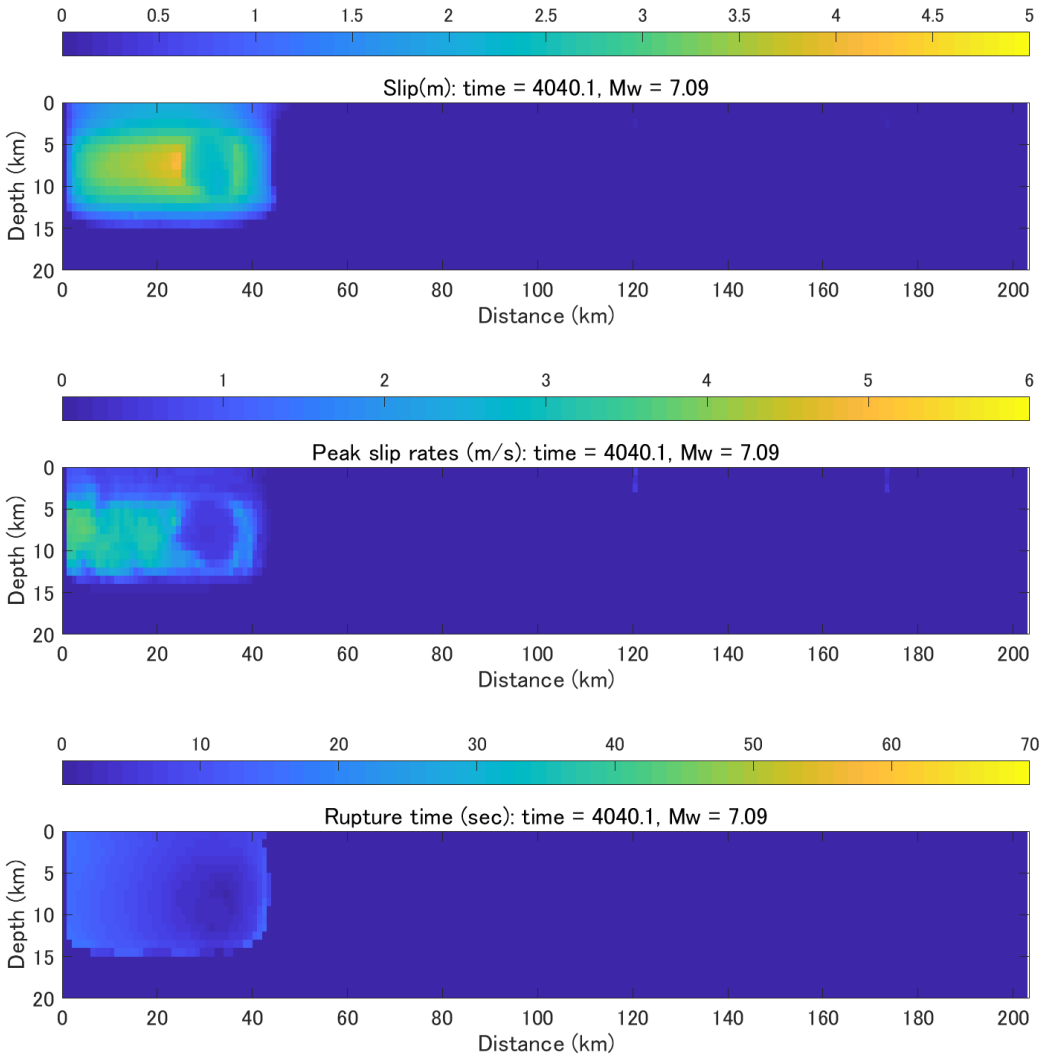

Figure A.3.4-11. Peak slip, peak slip rate and rupture time distributions for Event 14, 4040.1 year, *Mw*7.09

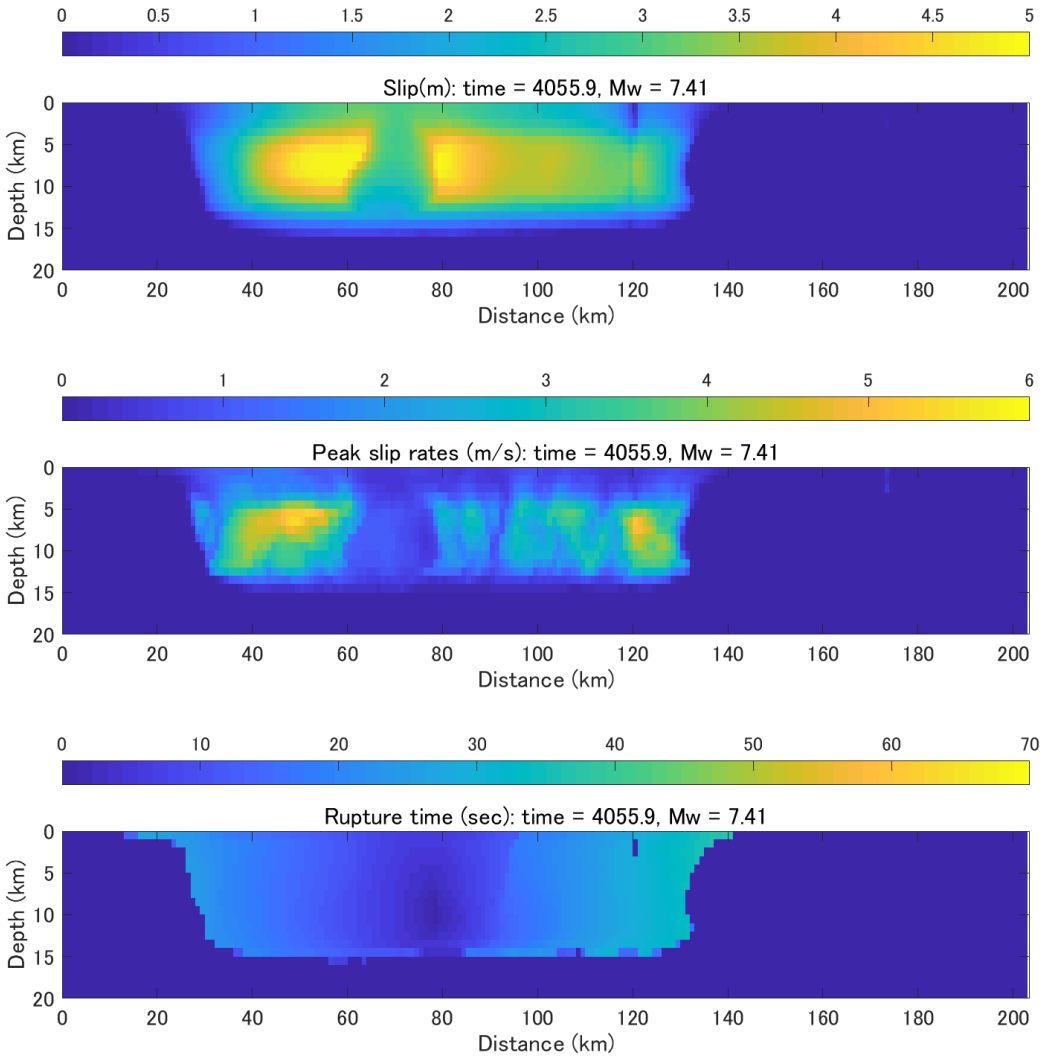

Figure A.3.4-12. Peak slip, peak slip rate and rupture time distributions for Event 15, 4055.9 year, *Mw*7.41

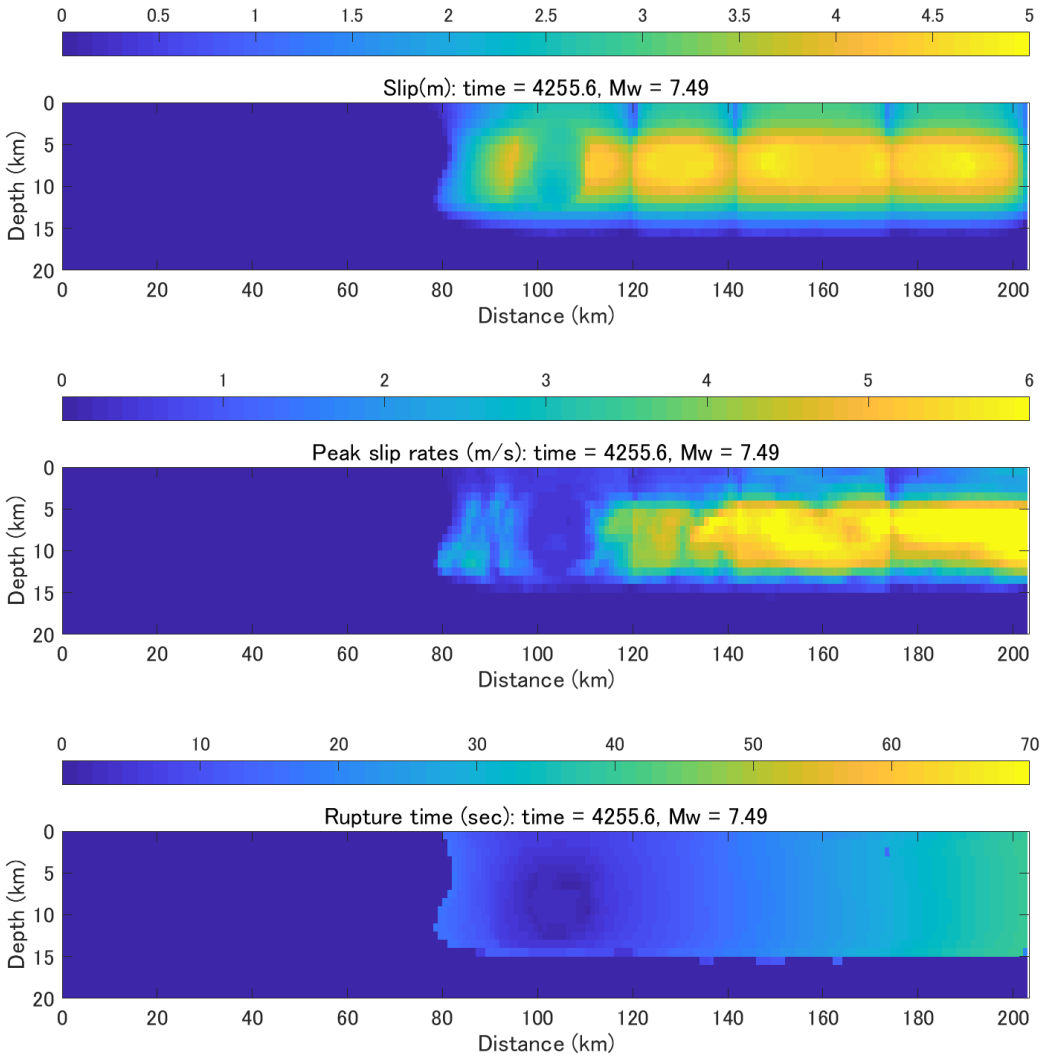

Figure A.3.4-13. Peak slip, peak slip rate and rupture time distributions for Event 16, 4255.6 year, *Mw*7.49

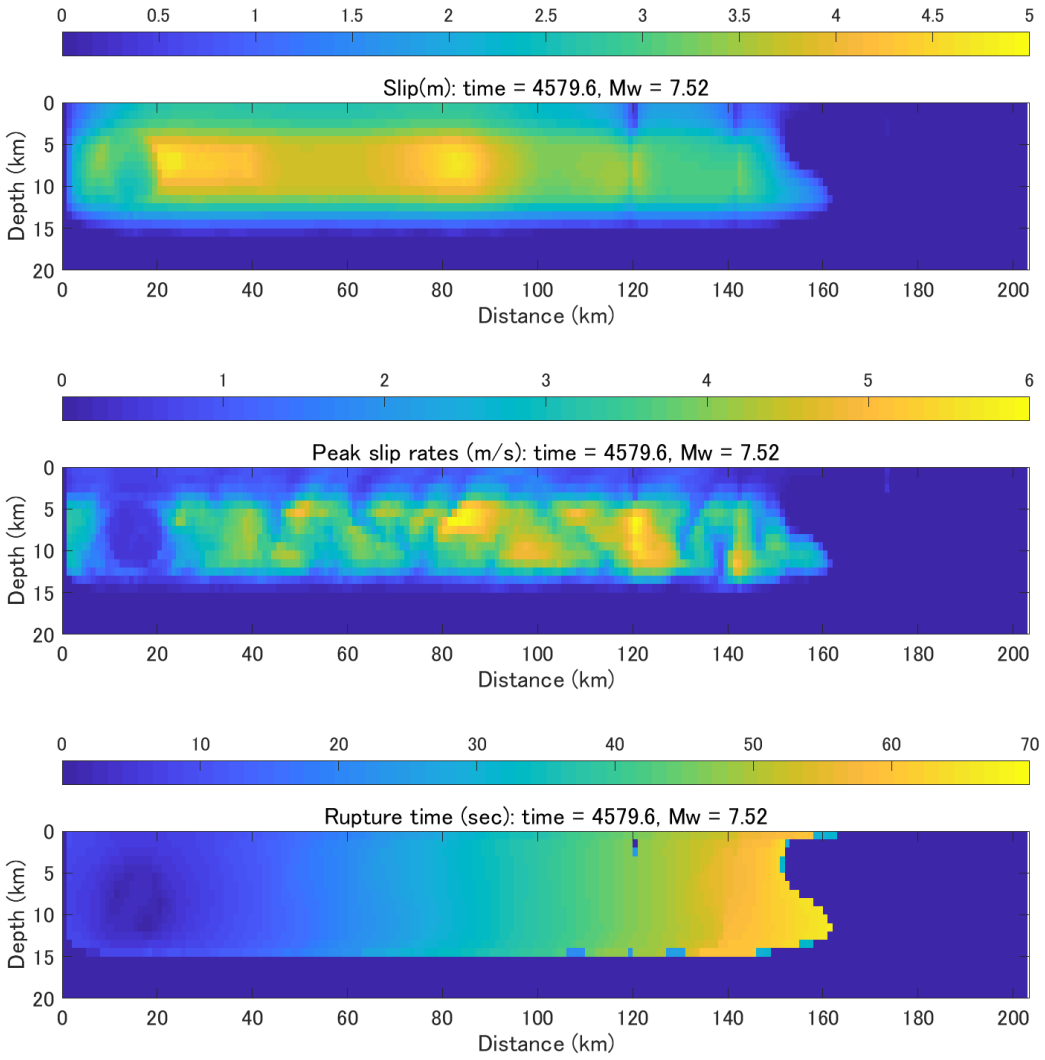

Figure A.3.4-14. Peak slip, peak slip rate and rupture time distributions for Event 17, 4579.6 year, *Mw*7.52

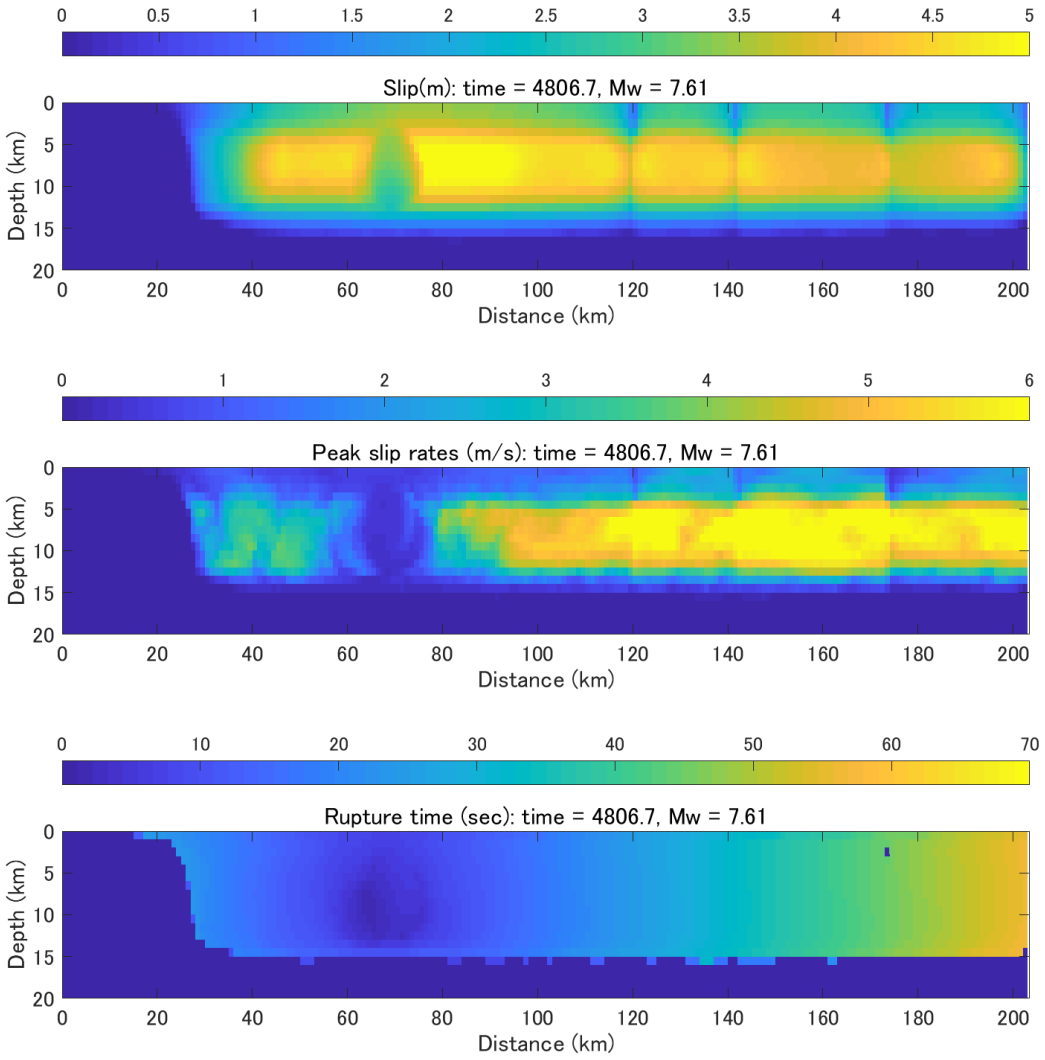

Figure A.3.4-15. Peak slip, peak slip rate and rupture time distributions for Event 18, 4806.7 year, *Mw*7.61

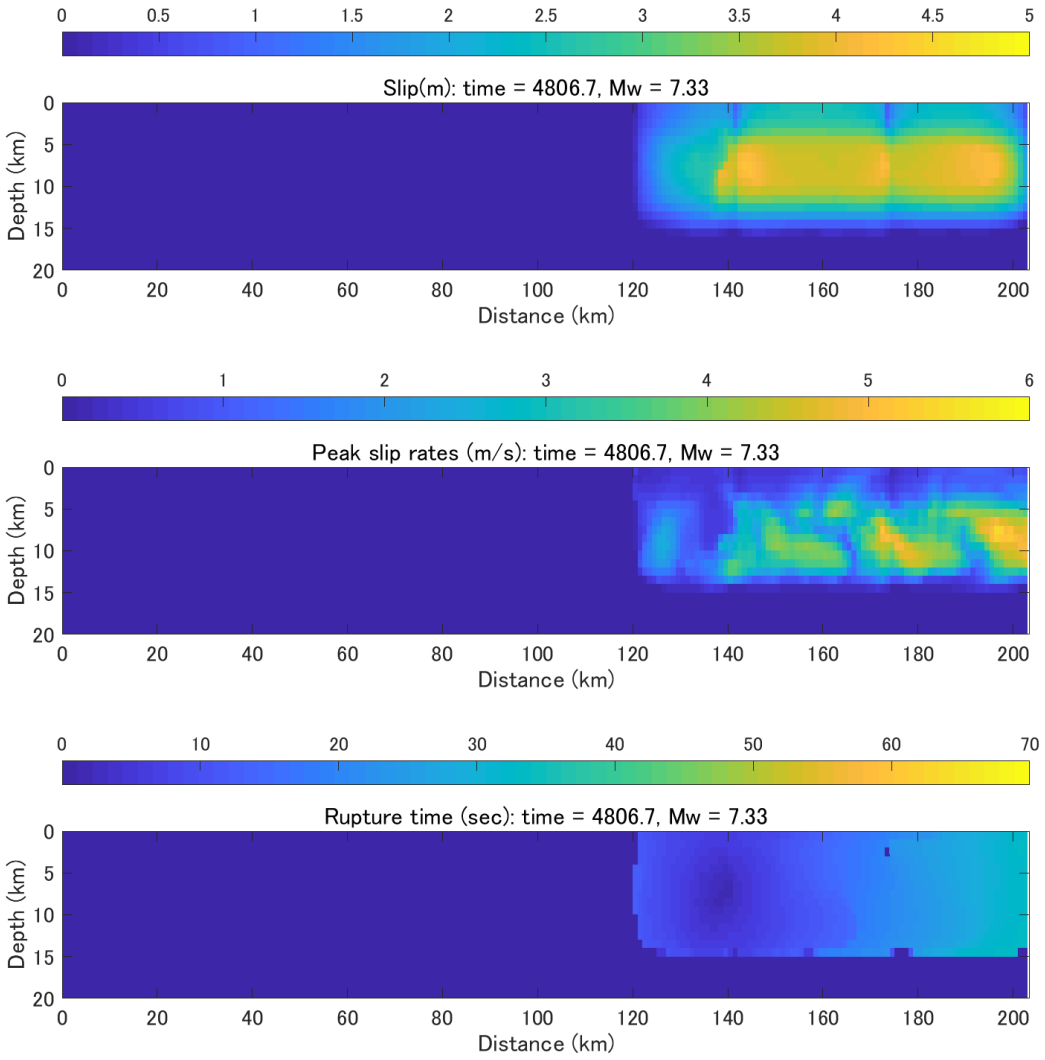

Figure A.3.4-16. Peak slip, peak slip rate and rupture time distributions for Event 19, 4806.7 year, *Mw*7.33

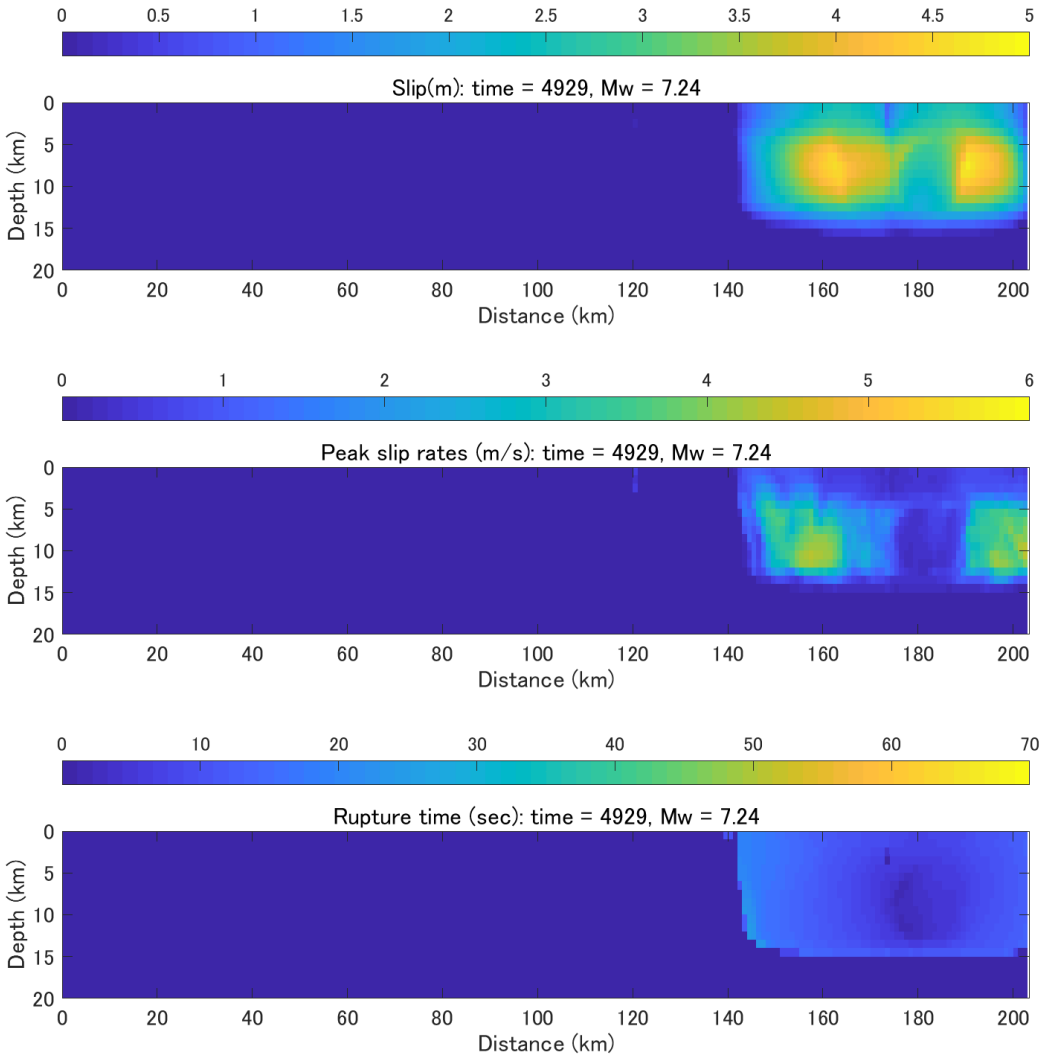

Figure A.3.4-17. Peak slip, peak slip rate and rupture time distributions for Event 20, 4929.0 year, *Mw*7.24

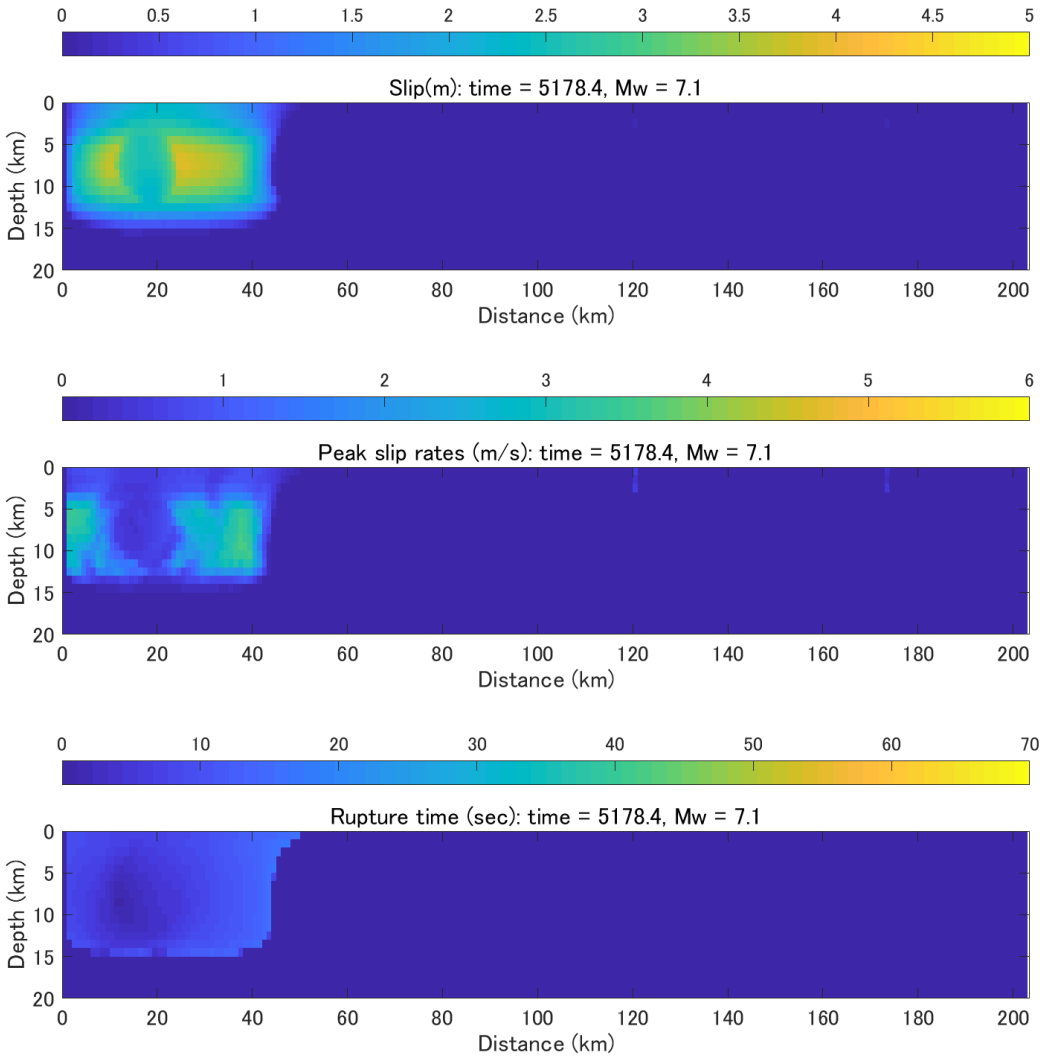

Figure A.3.4-18. Peak slip, peak slip rate and rupture time distributions for Event 21, 5178.4 year, *Mw*7.1

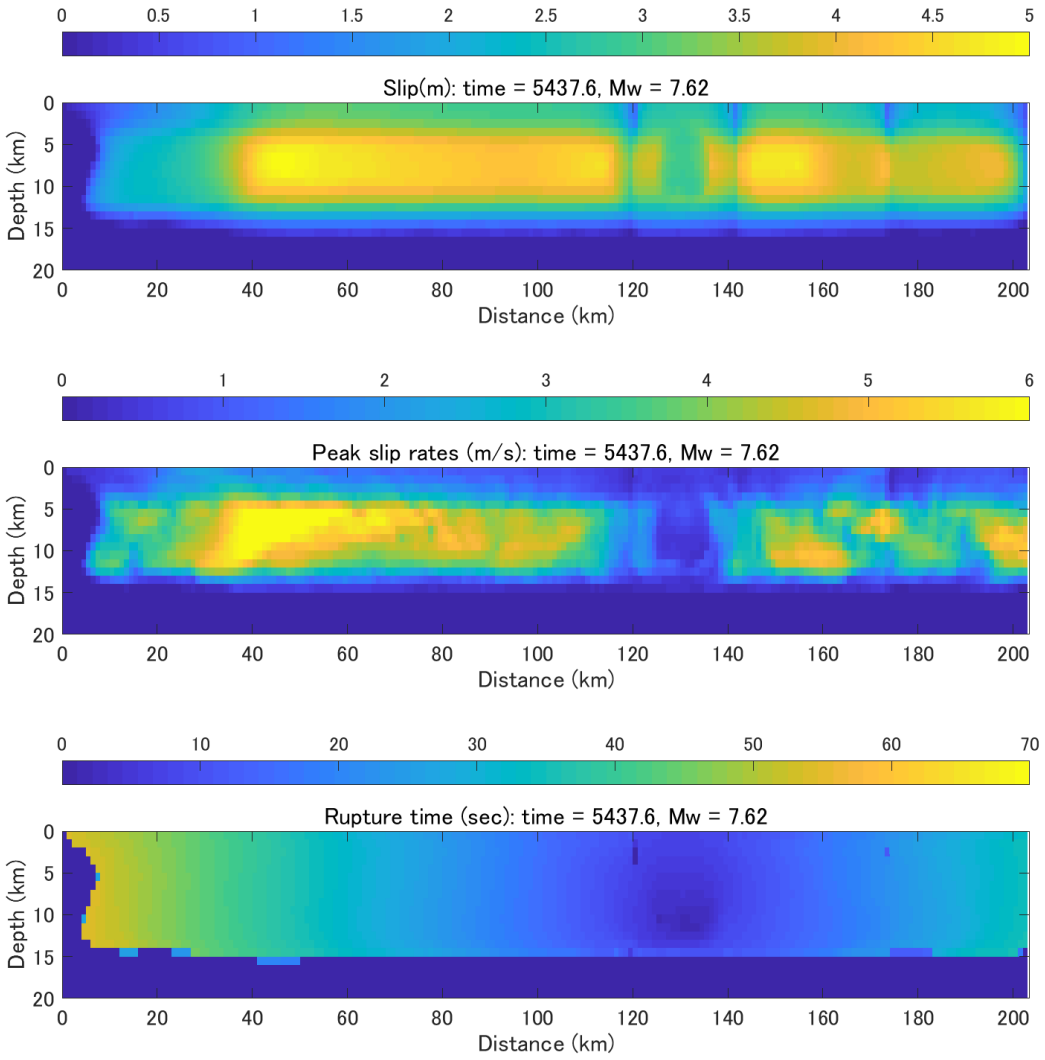

Figure A.3.4-19. Peak slip, peak slip rate and rupture time distributions for Event 22, 5437.6 year, *Mw*7.62

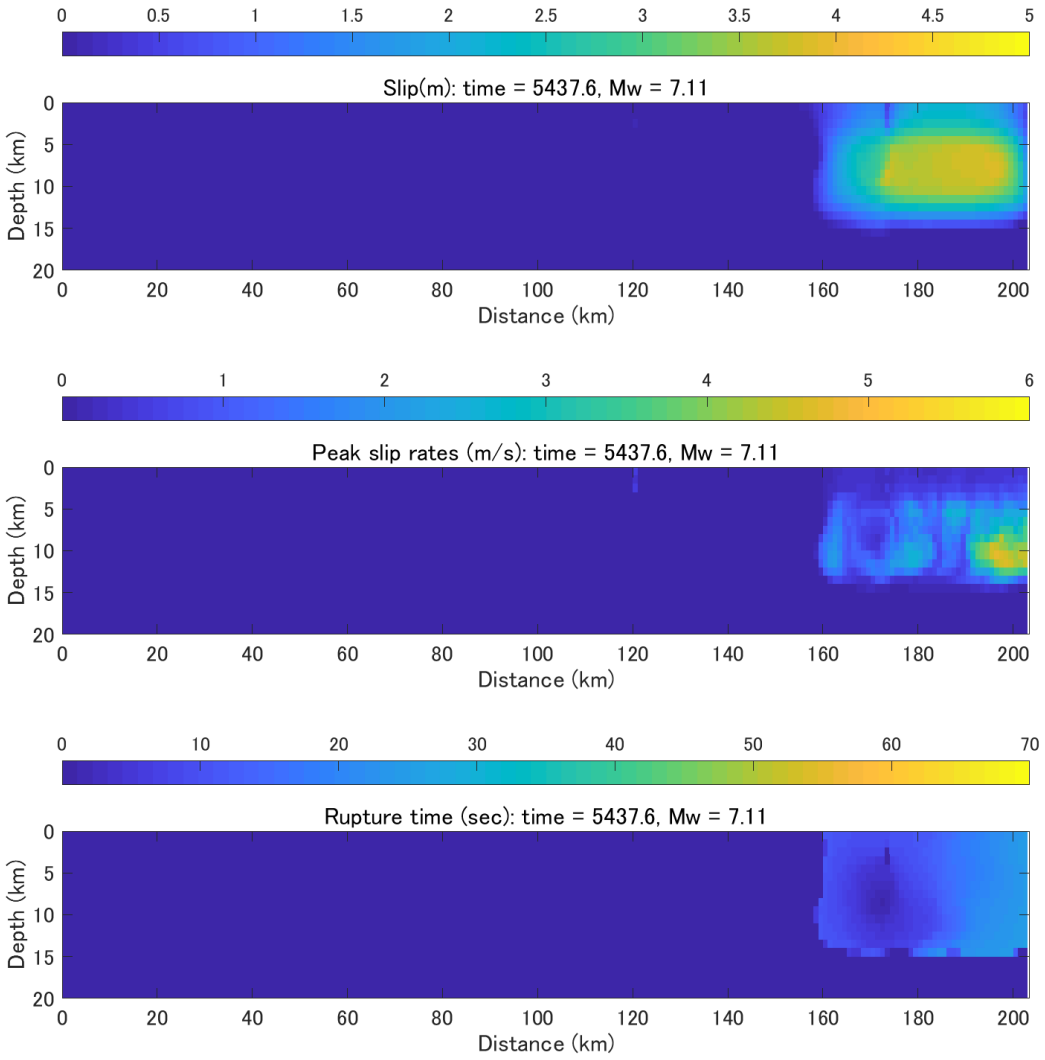

Figure A.3.4-20. Peak slip, peak slip rate and rupture time distributions for Event 23, 5437.6 year, *Mw*7.11

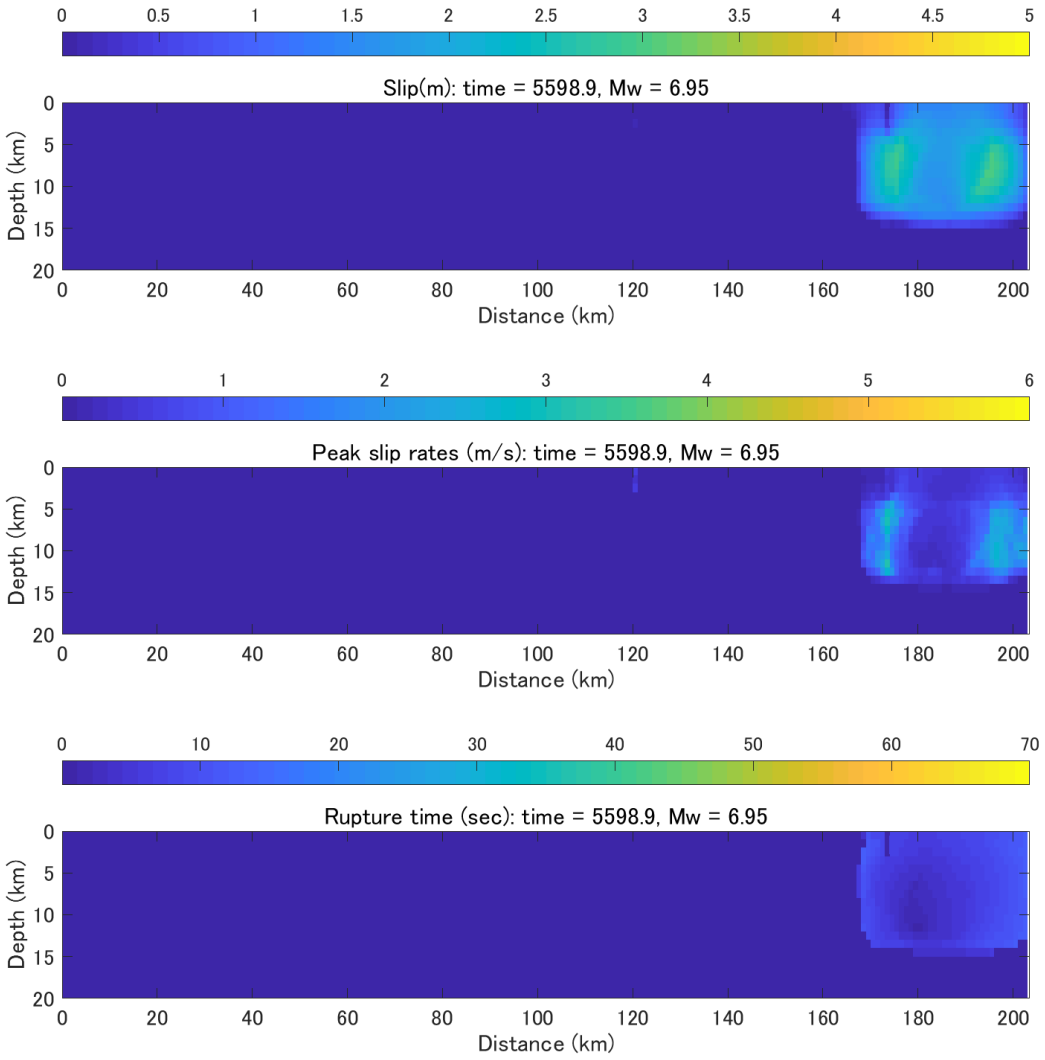

Figure A.3.4-21. Peak slip, peak slip rate and rupture time distributions for Event 24, 5598.9 year, *Mw*6.95

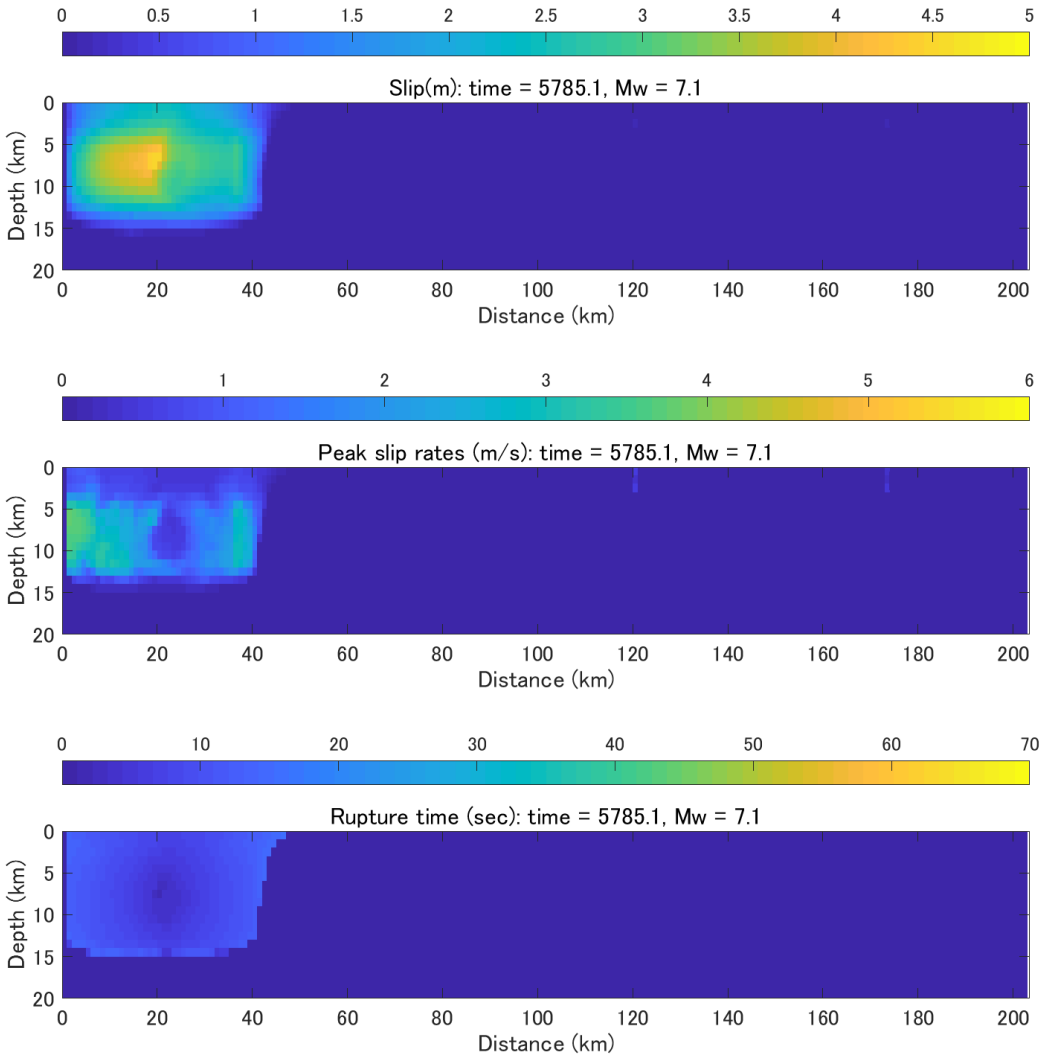

Figure A.3.4-22. Peak slip, peak slip rate and rupture time distributions for Event 25, 5785.1 year, *Mw*7.1

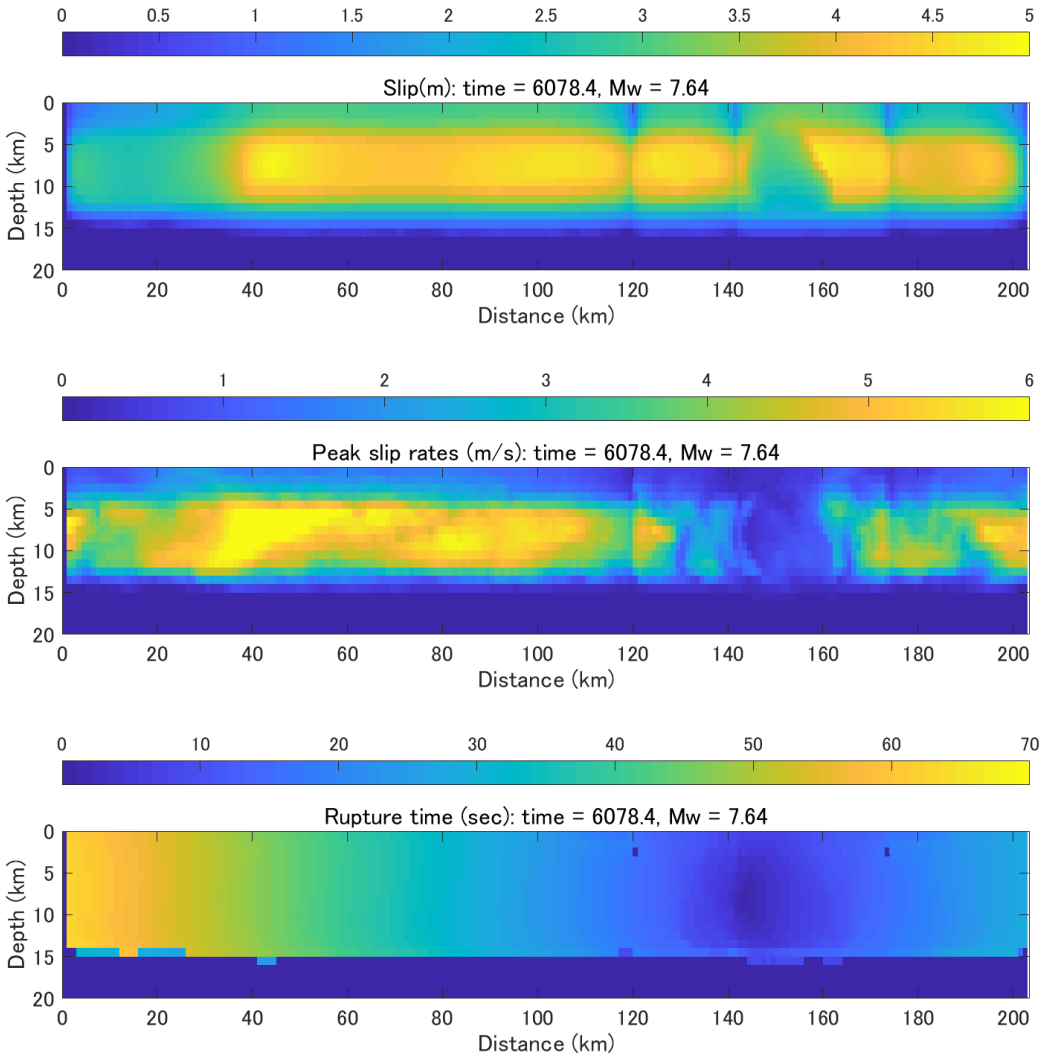

Figure A.3.4-23. Peak slip, peak slip rate and rupture time distributions for Event 26, 6078.4 year, *Mw*7.64

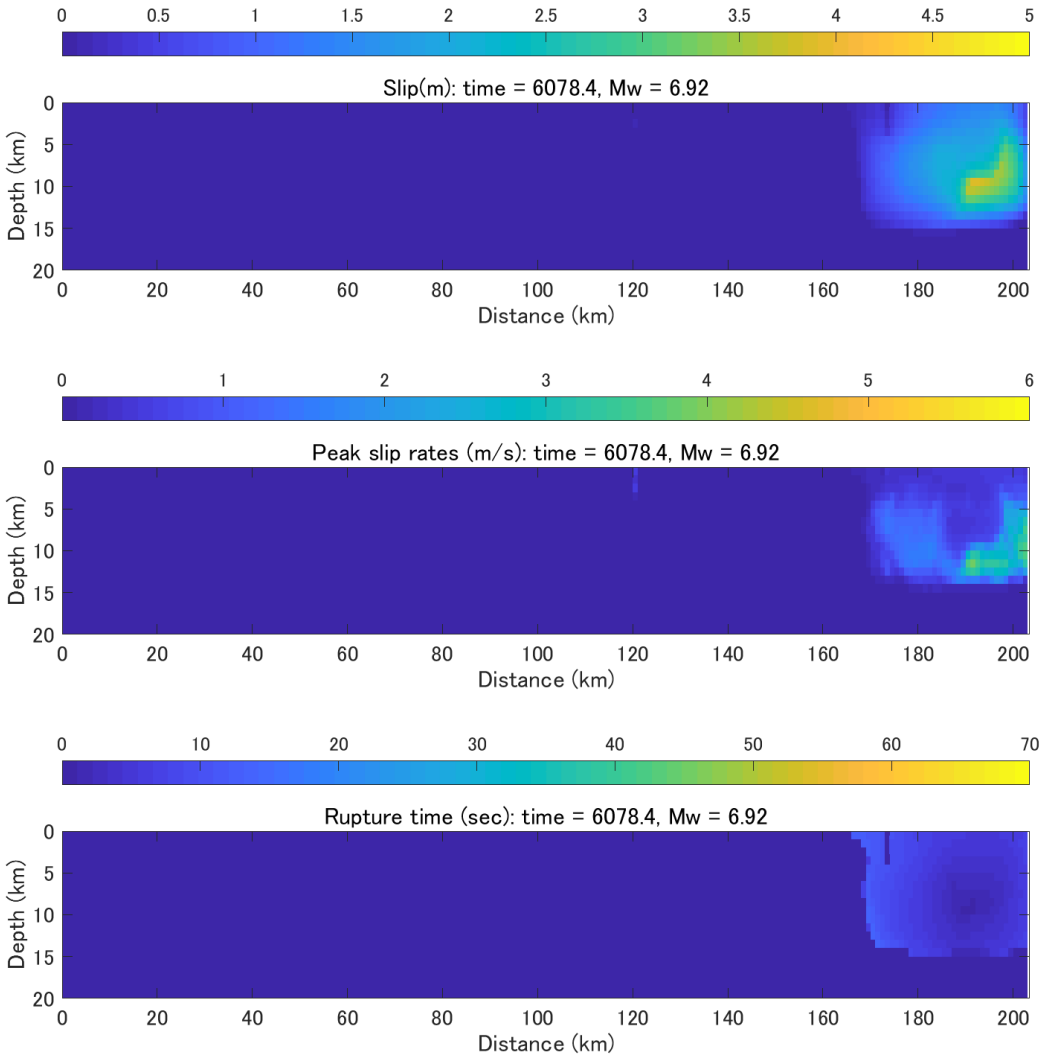

Figure A.3.4-24. Peak slip, peak slip rate and rupture time distributions for Event 27, 6078.4 year, *Mw*6.92

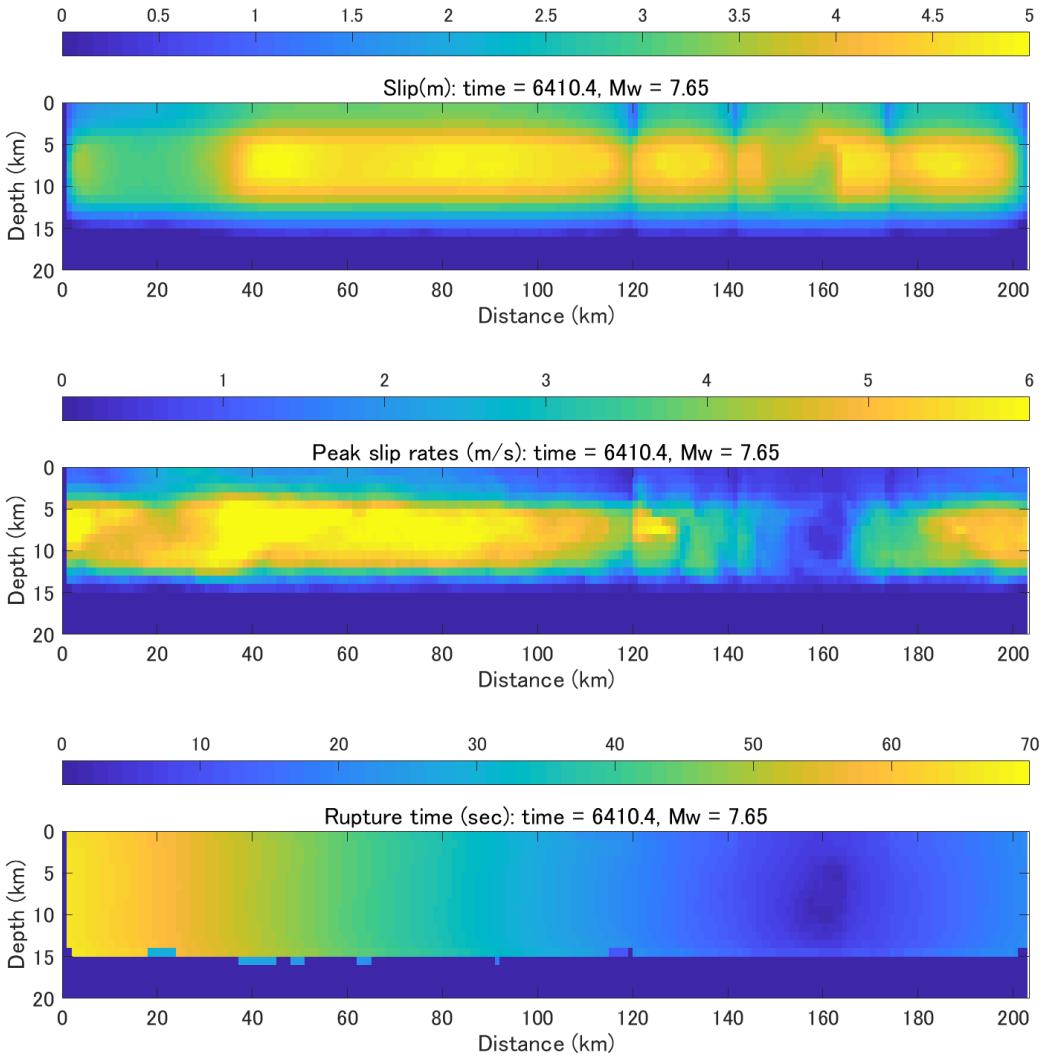

Figure A.3.4-25. Peak slip, peak slip rate and rupture time distributions for Event 28, 6410.4 year, *Mw*7.65

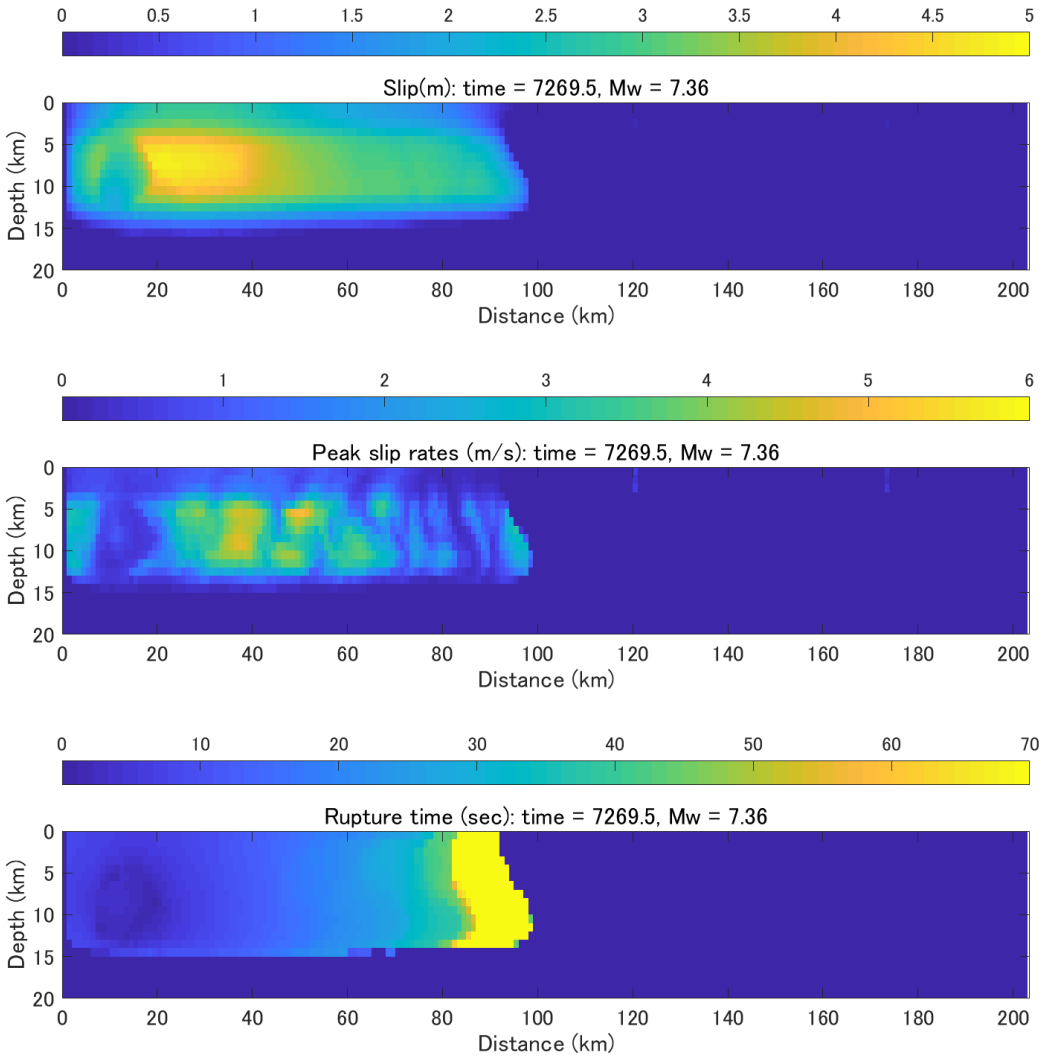

Figure A.3.4-26. Peak slip, peak slip rate and rupture time distributions for Event 29, 7269.5 year, *Mw*7.36

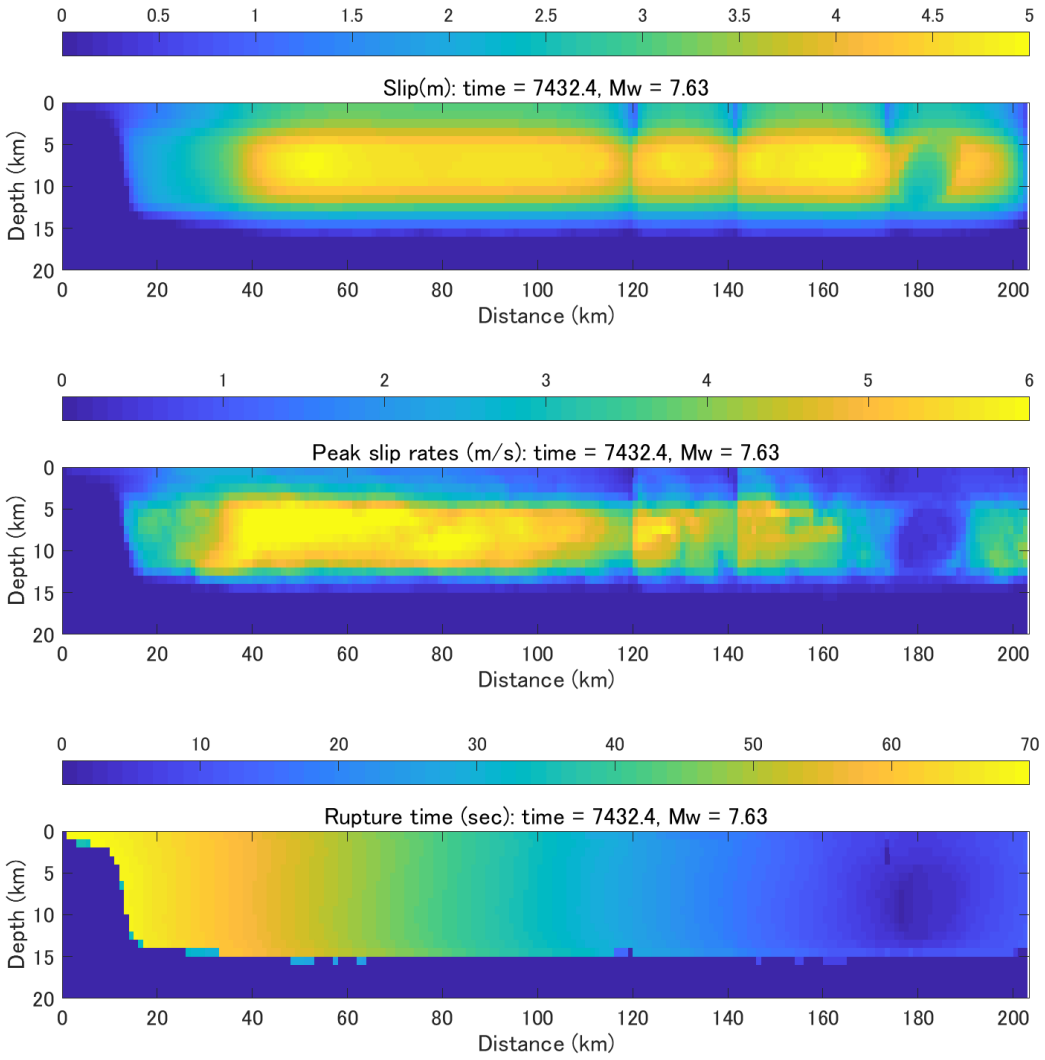

Figure A.3.4-27. Peak slip, peak slip rate and rupture time distributions for Event 30, 7432.4 year, *Mw*7.63

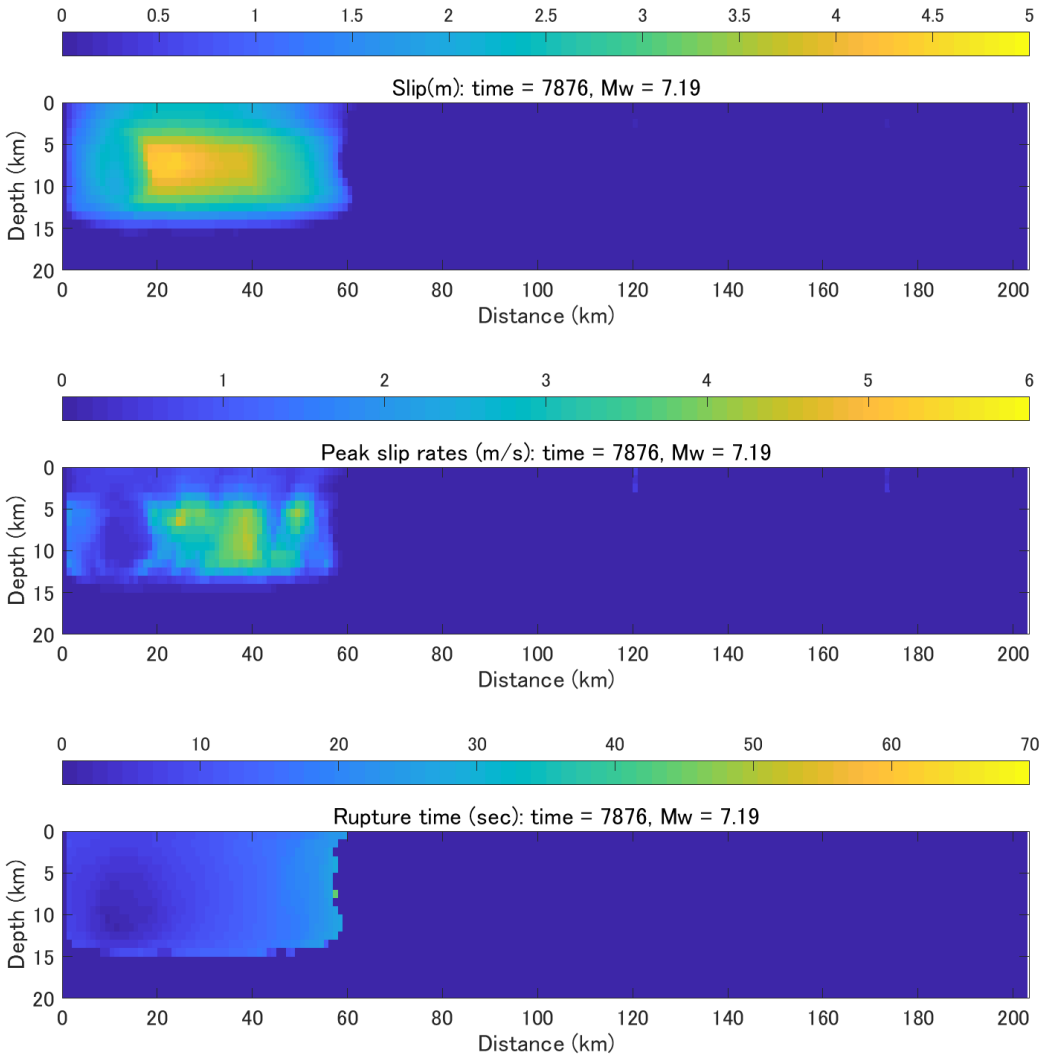

Figure A.3.4-28. Peak slip, peak slip rate and rupture time distributions for Event 31, 7876.0 year, *Mw*7.19

A.3.5 Simulated ground motions for 1992 Landers earthquake and comparison with observations

Figures below show ground motion simulation examples for target sites and comparison with observations. Notations: waveforms (left) and velocity response spectra (right); blue lines – observed, red – simulated; response spectra: solid – EW, dashed – NS, dotted – UD components.

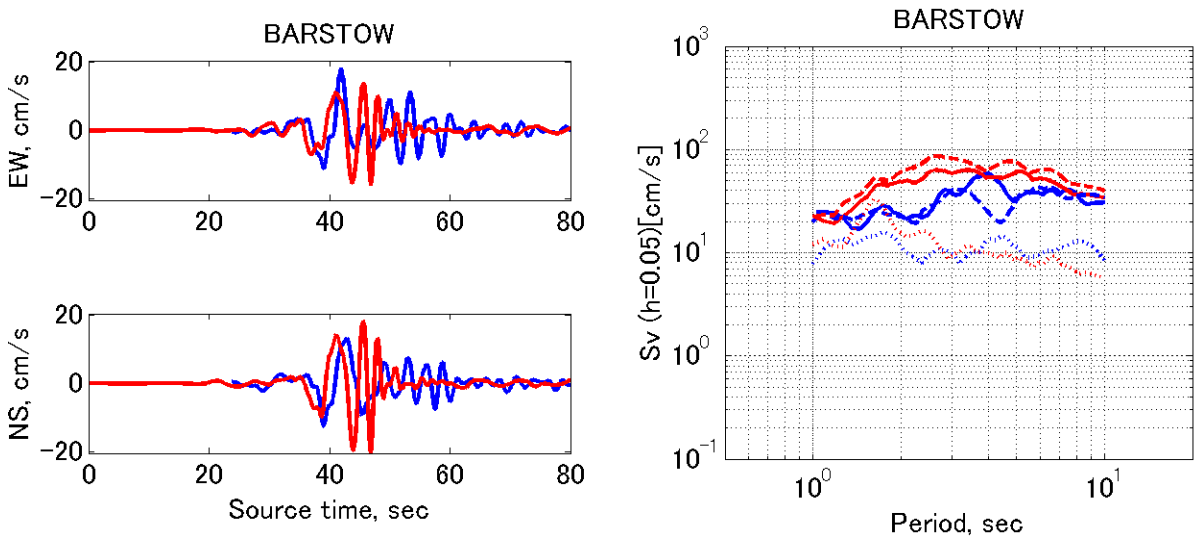

Figure A.3.5-1. Waveforms and *Sv* response spectra for the first Landers event (*Mw*7.3) occurred in year 1245.2. Site Barstow (non-basin).

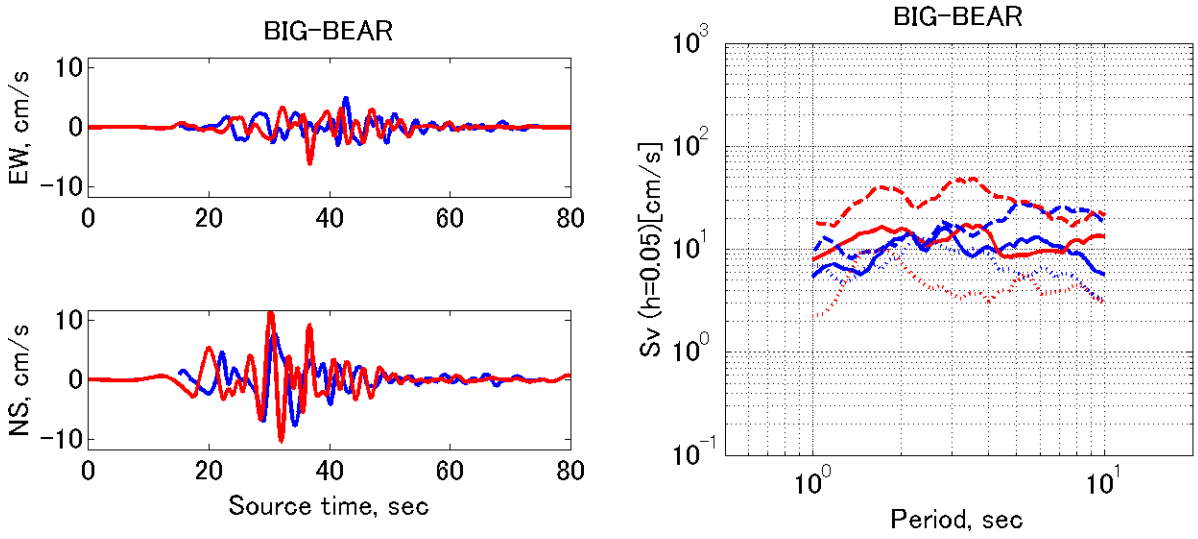

Figure A.3.5-2. Waveforms and *Sv* response spectra for the first Landers event (*Mw*7.3) occurred in year 1245.2. Site Big Bear (non-basin).

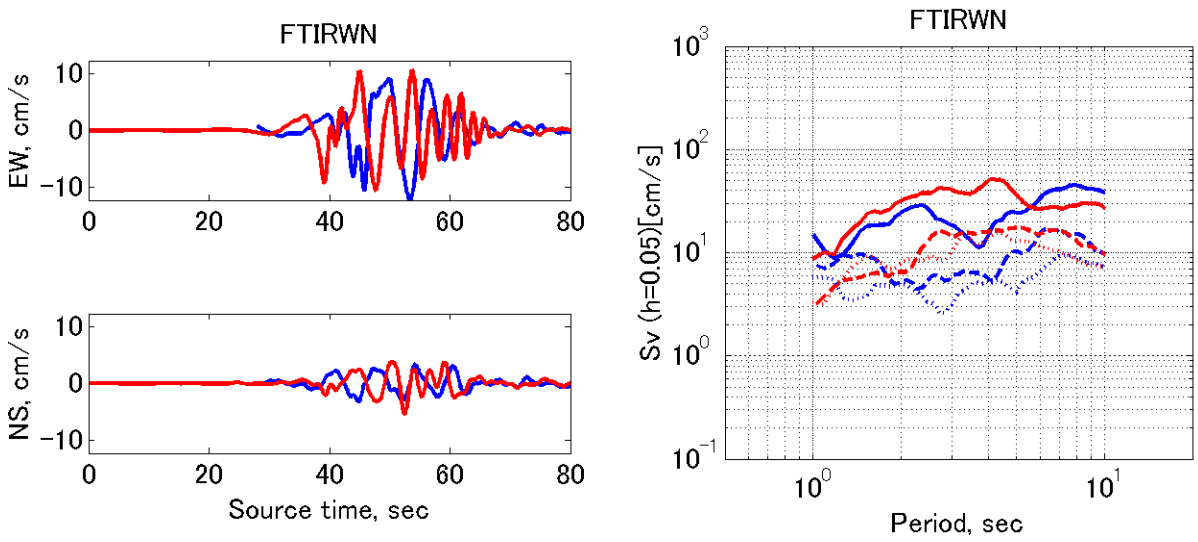

Figure A.3.5-3. Waveforms and *Sv* response spectra for the first Landers event (*Mw*7.3) occurred in year 1245.2. Site Fort Irwin (non-basin).

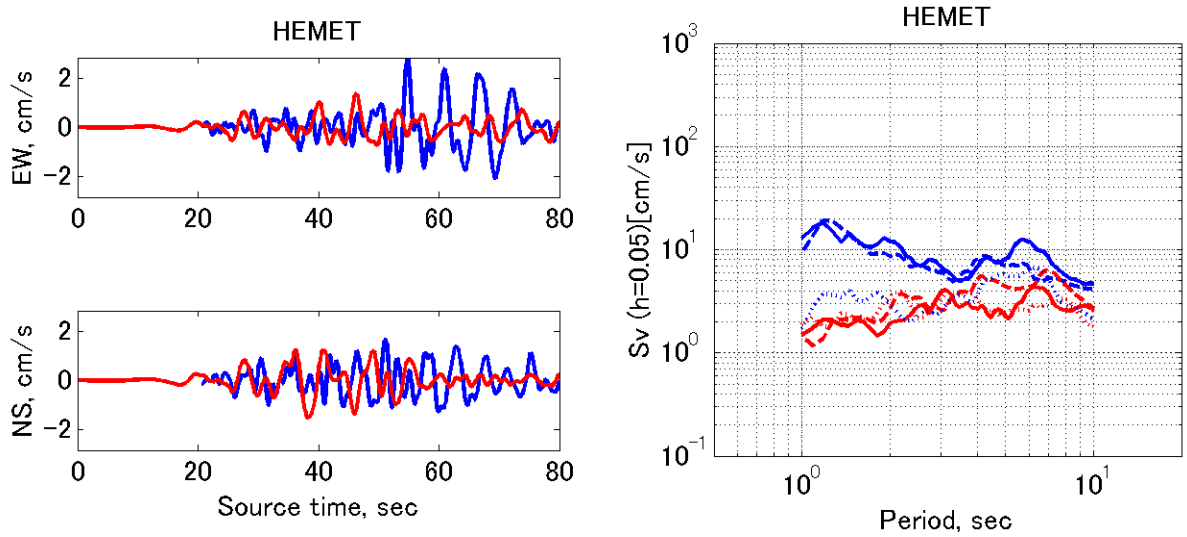

Figure A.3.5-4. Waveforms and *Sv* response spectra for the first Landers event (*Mw*7.3) occurred in year 1245.2. Site Hemet (non-basin).

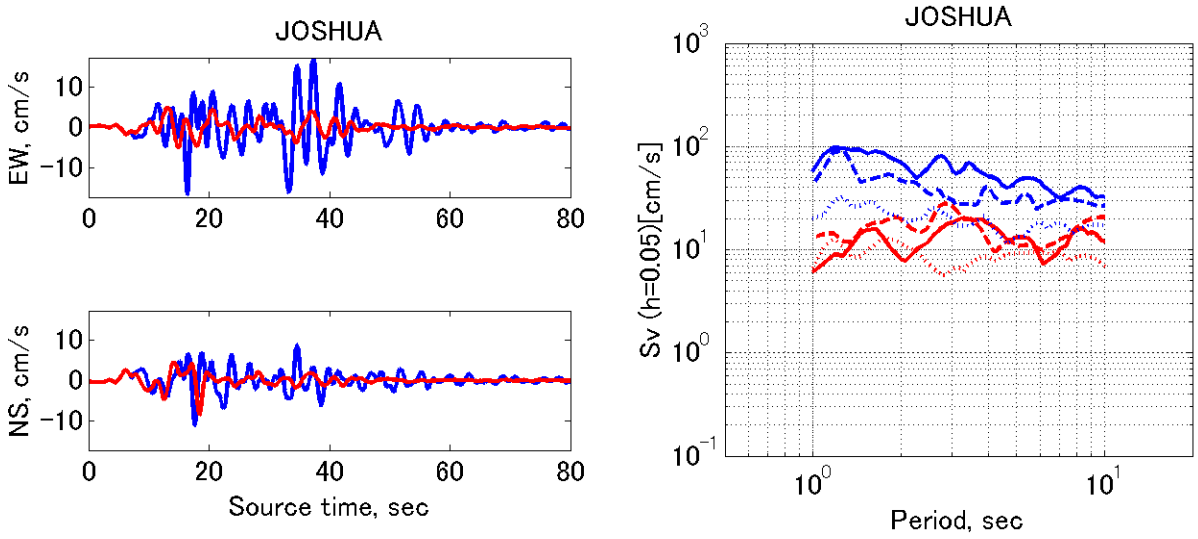

Figure A.3.5-5. Waveforms and *Sv* response spectra for the first Landers event (*Mw*7.3) occurred in year 1245.2. Site Joshua (non-basin).

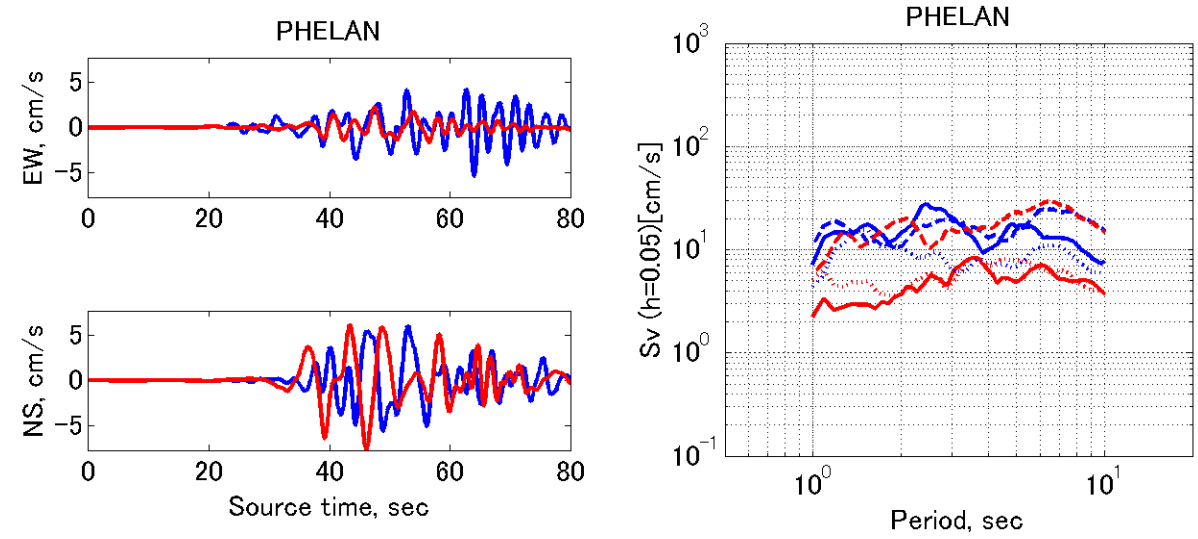

Figure A.3.5-6. Waveforms and *Sv* response spectra for the first Landers event (*Mw*7.3) occurred in year 1245.2. Site Phelan (non-basin).

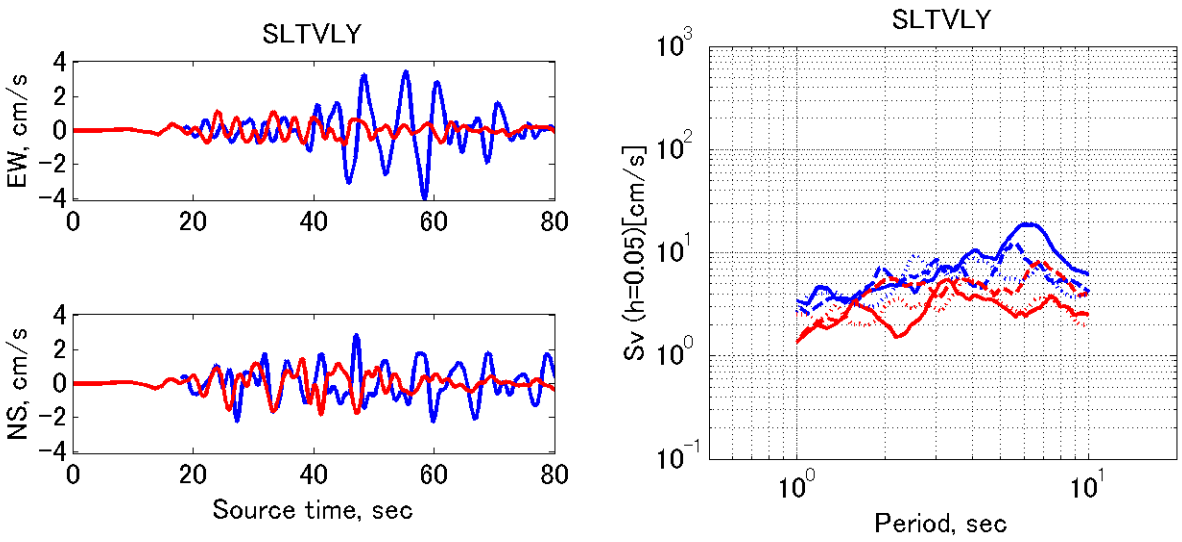

Figure A.3.5-7. Waveforms and *Sv* response spectra for the first Landers event (*Mw*7.3) occurred in year 1245.2. Site Silent Valley (non-basin).

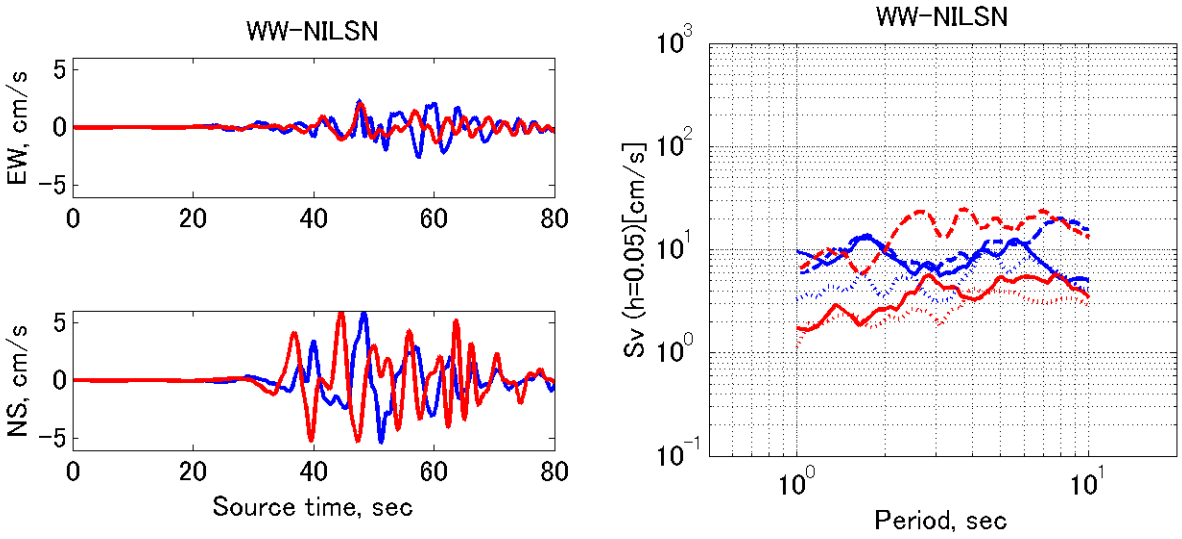

Figure A.3.5-8. Waveforms and *Sv* response spectra for the first Landers event (*Mw*7.3) occurred in year 1245.2. Site WW-Nielson (non-basin).

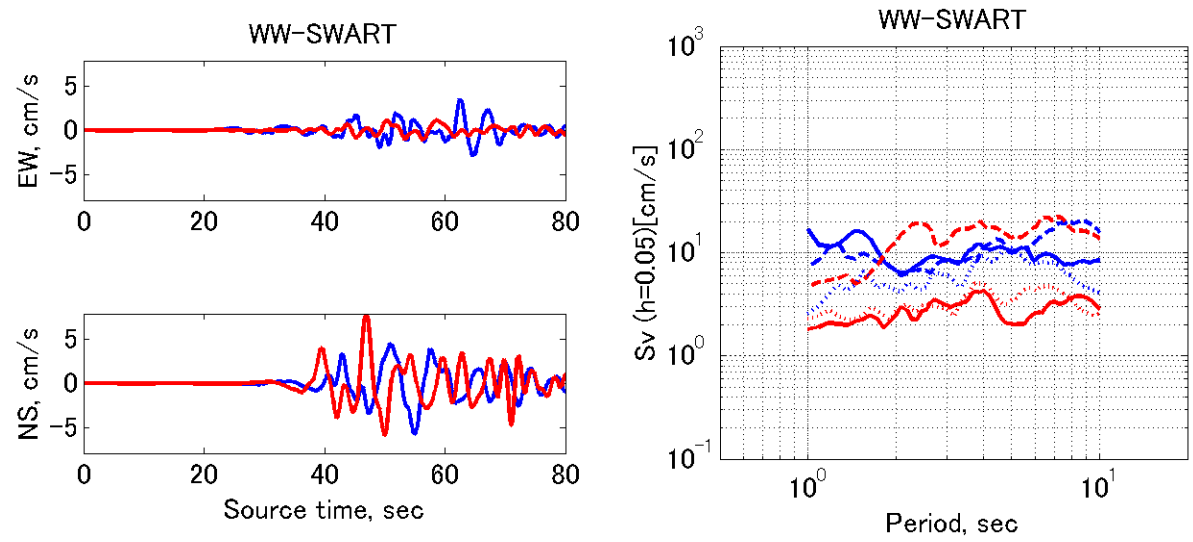

Figure A.3.5-9. Waveforms and *Sv* response spectra for the first Landers event (*Mw*7.3) occurred in year 1245.2. Site WW-Swarthout (non-basin).

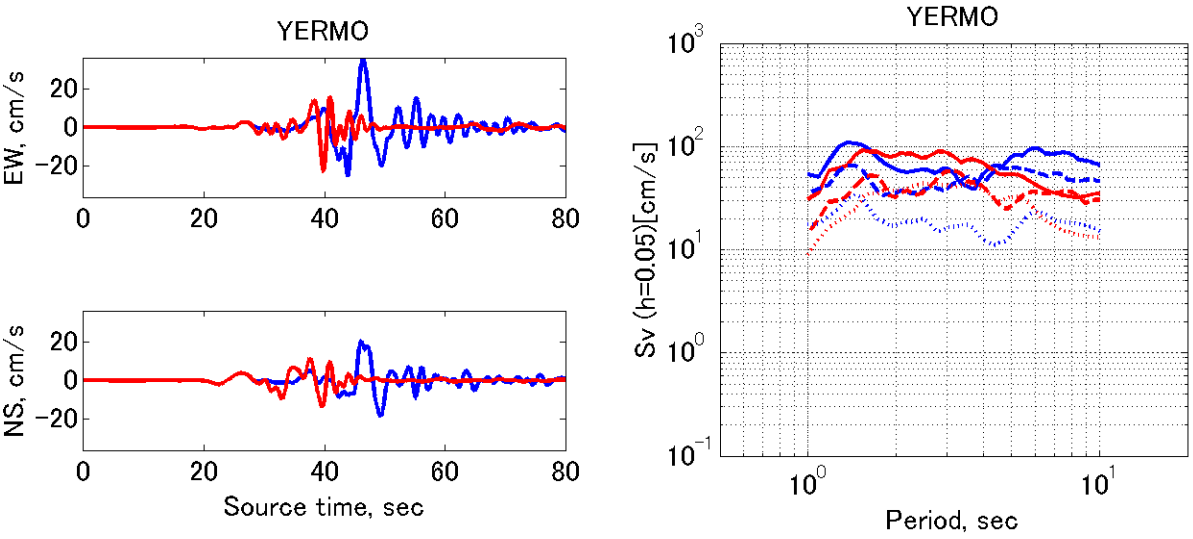

Figure A.3.5-10. Waveforms and *Sv* response spectra for the first Landers event (*Mw*7.3) occurred in year 1245.2. Site Yermo (non-basin).

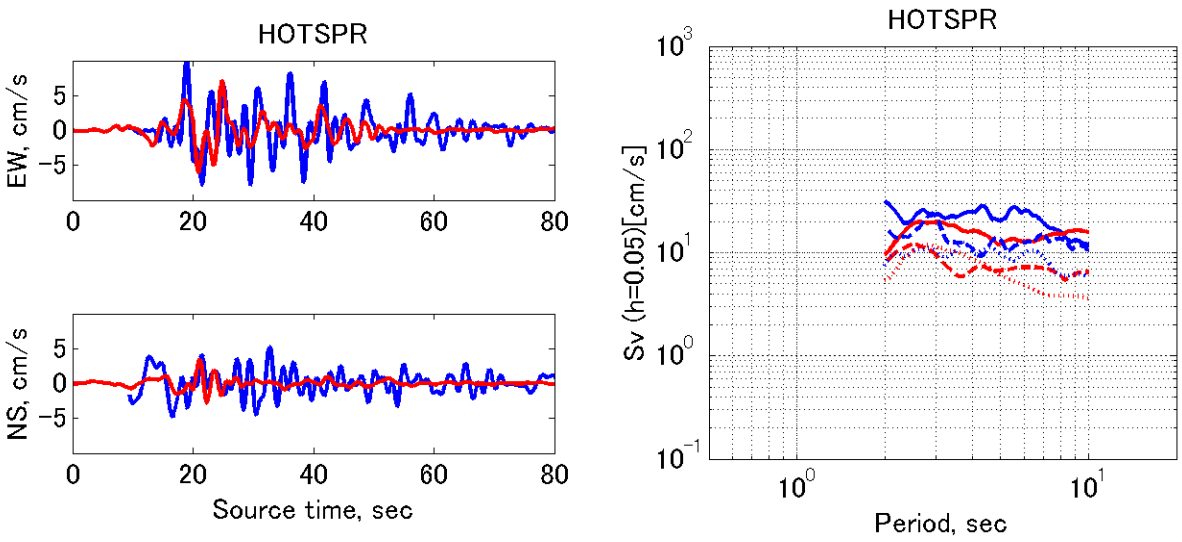

Figure A.3.5-11. Waveforms and *Sv* response spectra for the first Landers event (*Mw*7.3) occurred in year 1245.2. Site Desert Hot Spring (basin).

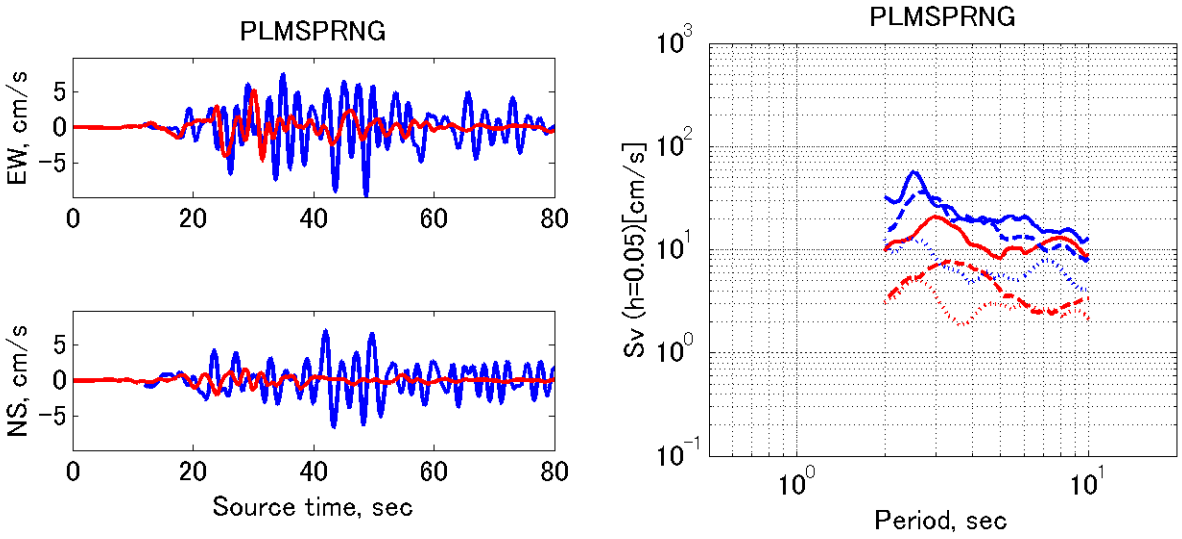

Figure A.3.5-12. Waveforms and *Sv* response spectra for the first Landers event (*Mw*7.3) occurred in year 1245.2. Site Palm Springs (basin).

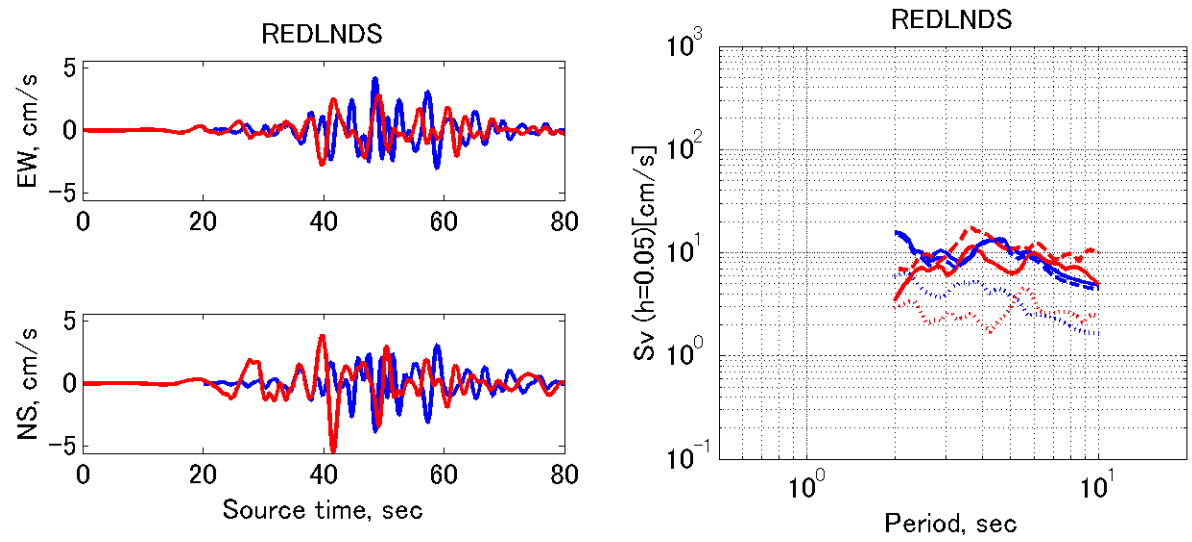

Figure A.3.5-13. Waveforms and *Sv* response spectra for the first Landers event (*Mw*7.3) occurred in year 1245.2. Site Redlands (basin).

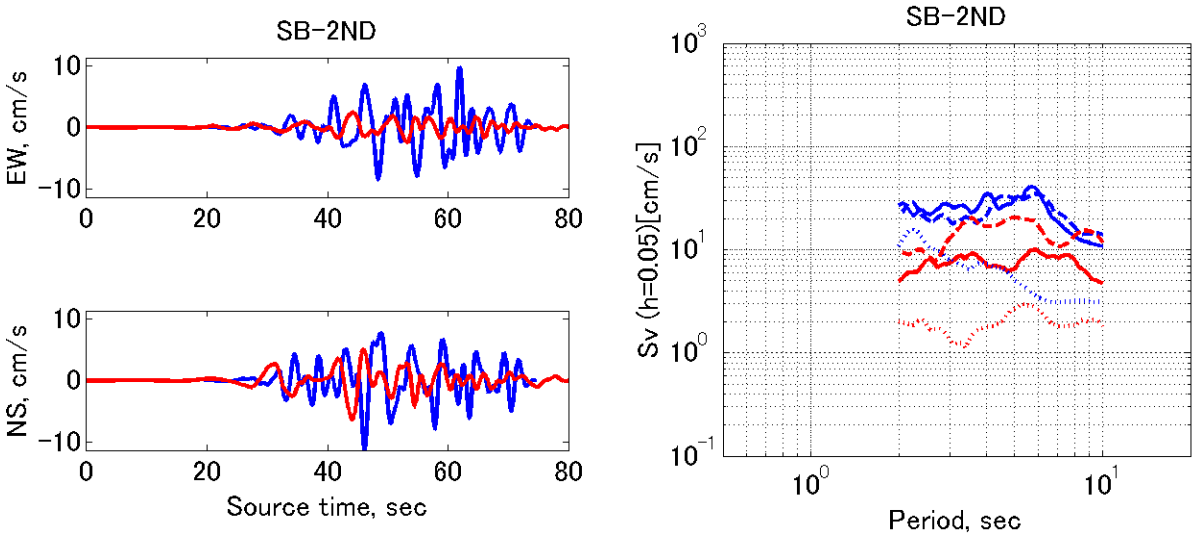

Figure A.3.5-14. Waveforms and *Sv* response spectra for the first Landers event (*Mw*7.3) occurred in year 1245.2. Site SB-2ndArrowhead (basin).

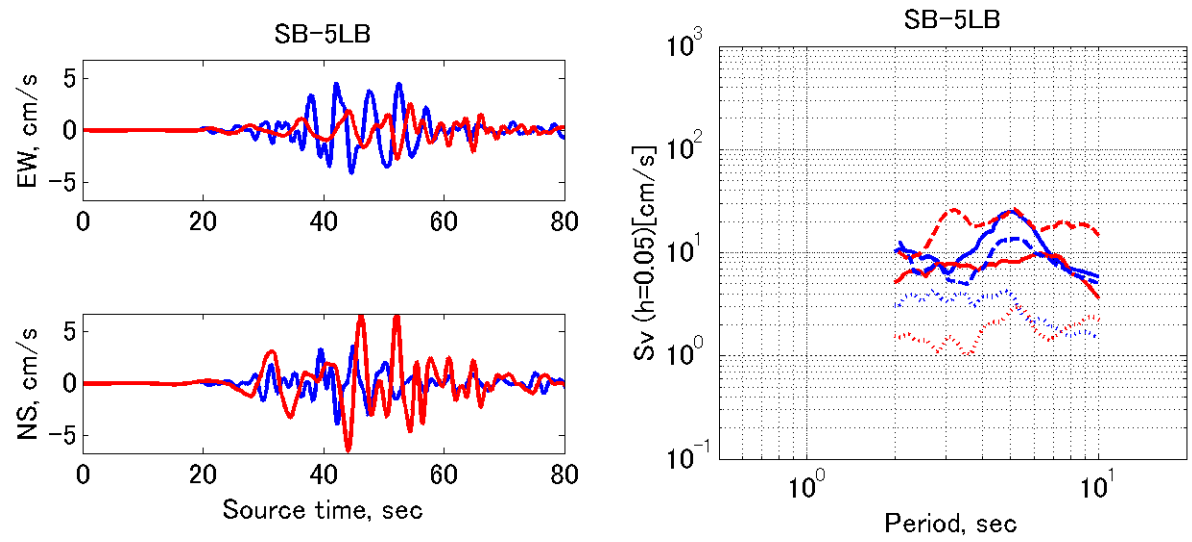

Figure A.3.5-15. Waveforms and *Sv* response spectra for the first Landers event (*Mw*7.3) occurred in year 1245.2. Site SB-Library (basin).

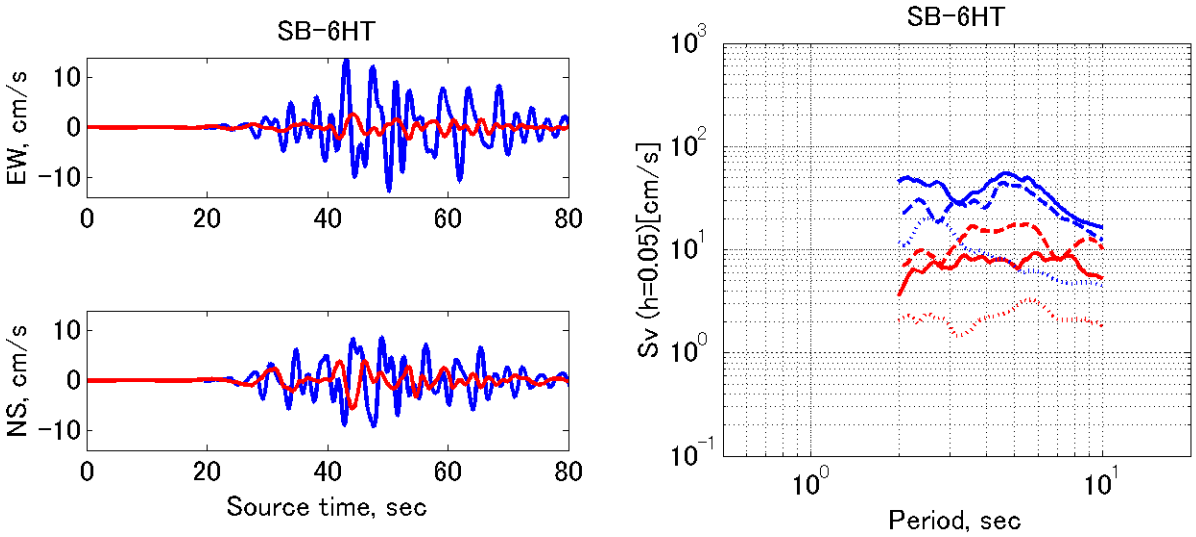

Figure A.3.5-16. Waveforms and *Sv* response spectra for the first Landers event (*Mw*7.3) occurred in year 1245.2. Site SB-Hotel (basin).

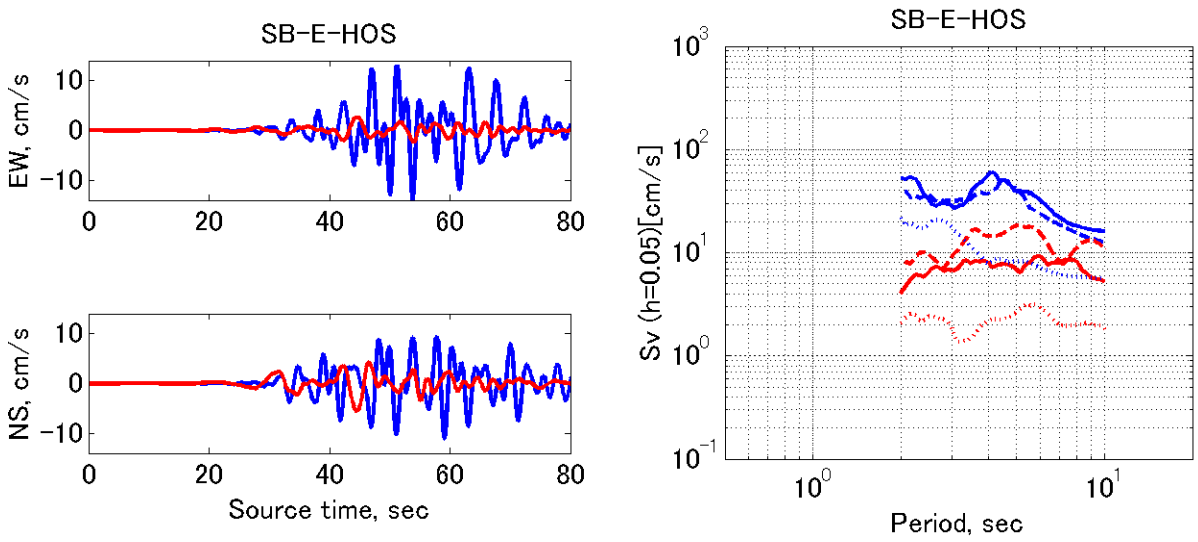

Figure A.3.5-17. Waveforms and *Sv* response spectra for the first Landers event (*Mw*7.3) occurred in year 1245.2. Site SB-E&Hospitality (basin).

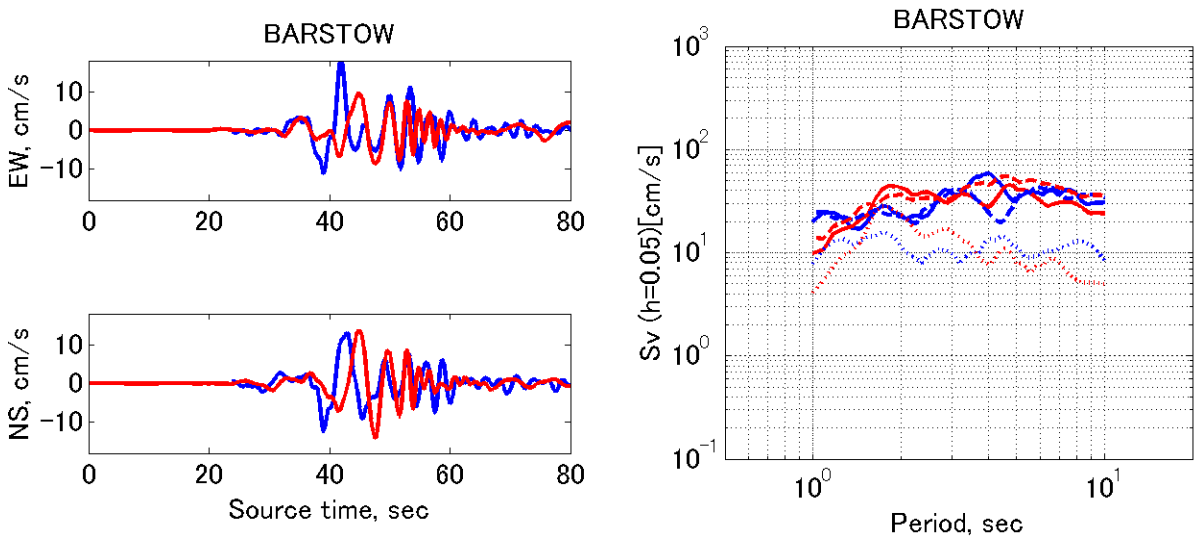

Figure A.3.5-18. Waveforms and *Sv* response spectra for the second Landers event (*Mw*7.31) occurred in year 1831.3. Site Barstow (non-basin).

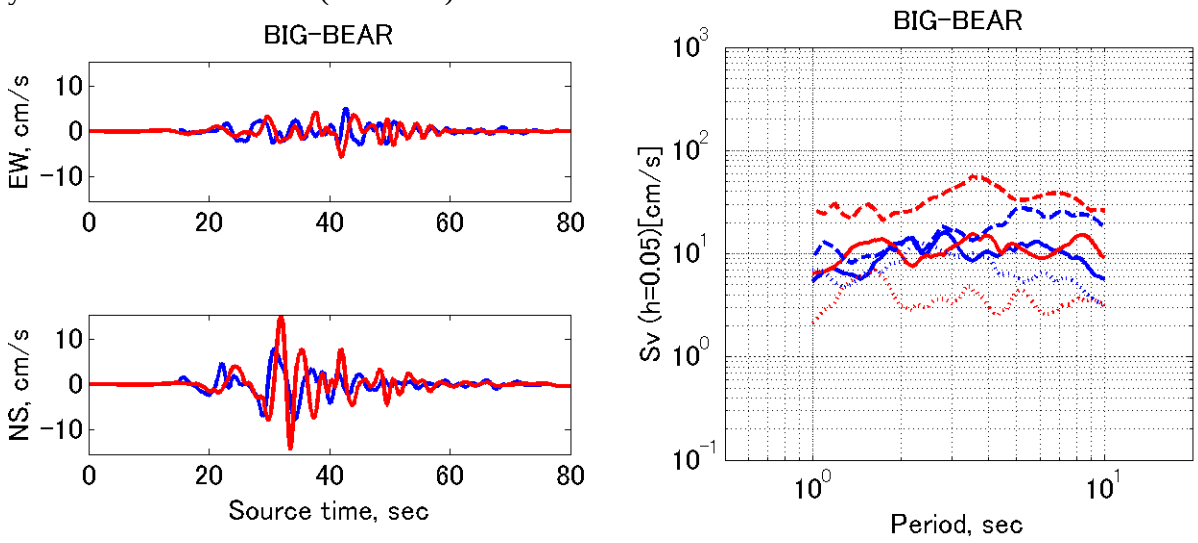

Figure A.3.5-19. Waveforms and *Sv* response spectra for the second Landers event (*Mw*7.31) occurred in year 1831.3. Site Big Bear (non-basin).

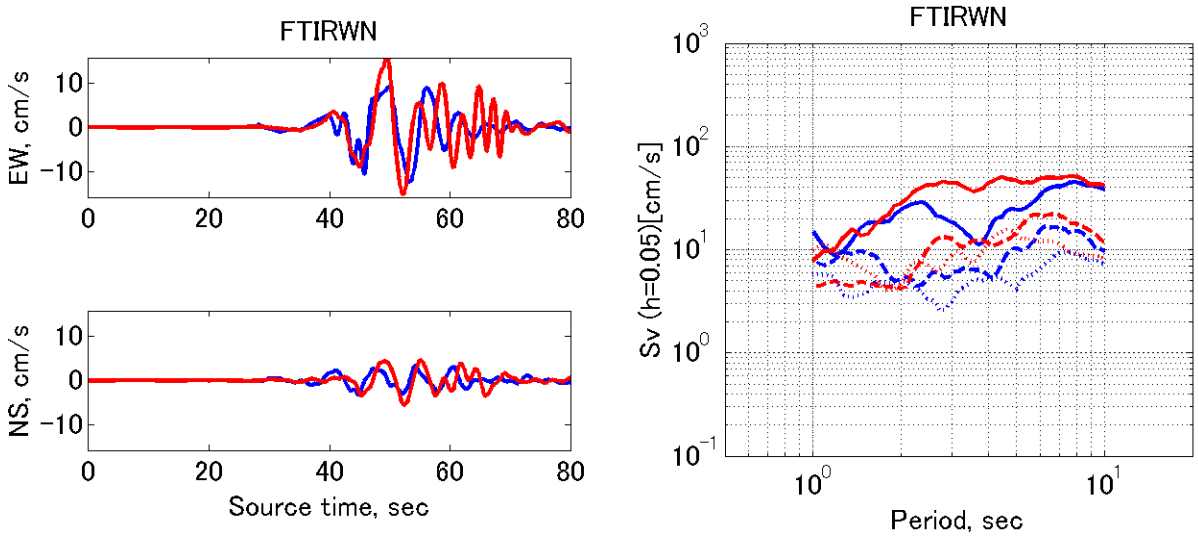

Figure A.3.5-20. Waveforms and *Sv* response spectra for the second Landers event (*Mw*7.31) occurred in year 1831.3. Site Fort Irwin (non-basin).

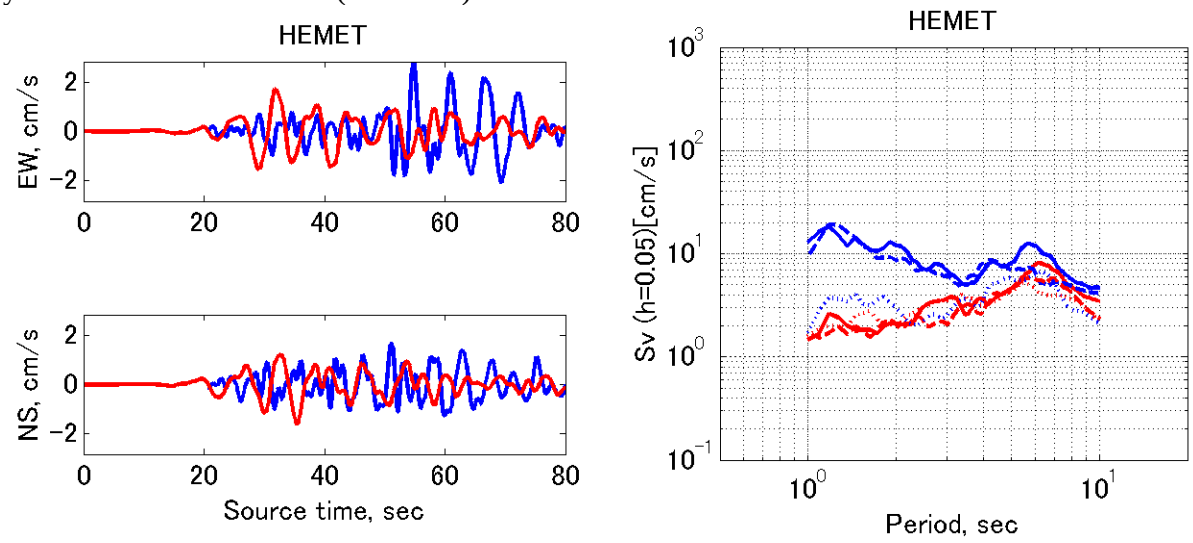

Figure A.3.5-21. Waveforms and *Sv* response spectra for the second Landers event (*Mw*7.31) occurred in year 1831.3. Site Hemet (non-basin).

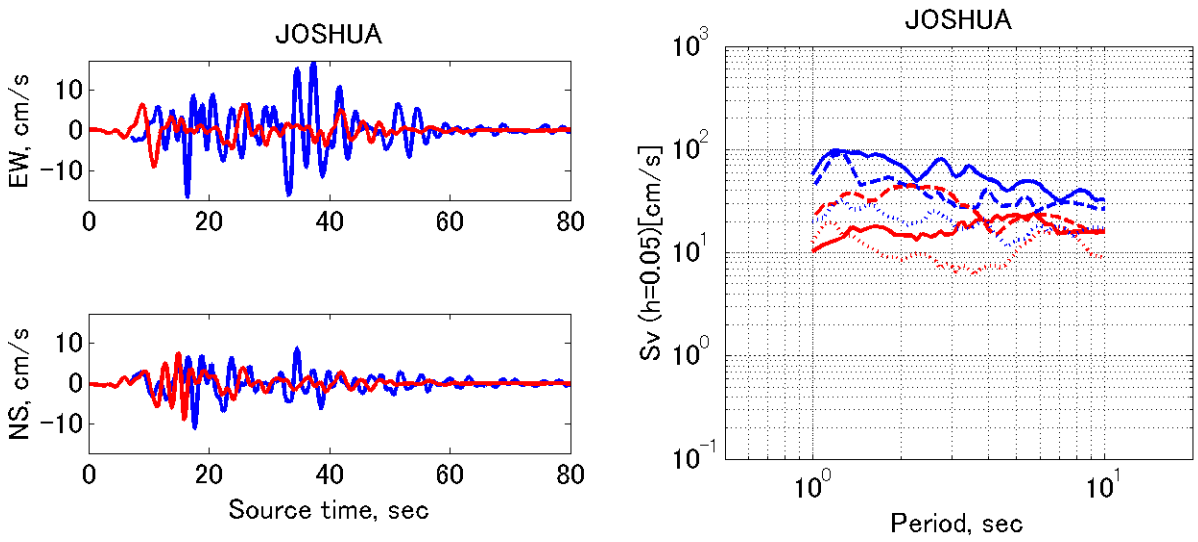

Figure A.3.5-22. Waveforms and *Sv* response spectra for the second Landers event (*Mw*7.31) occurred in year 1831.3. Site Joshua (non-basin).

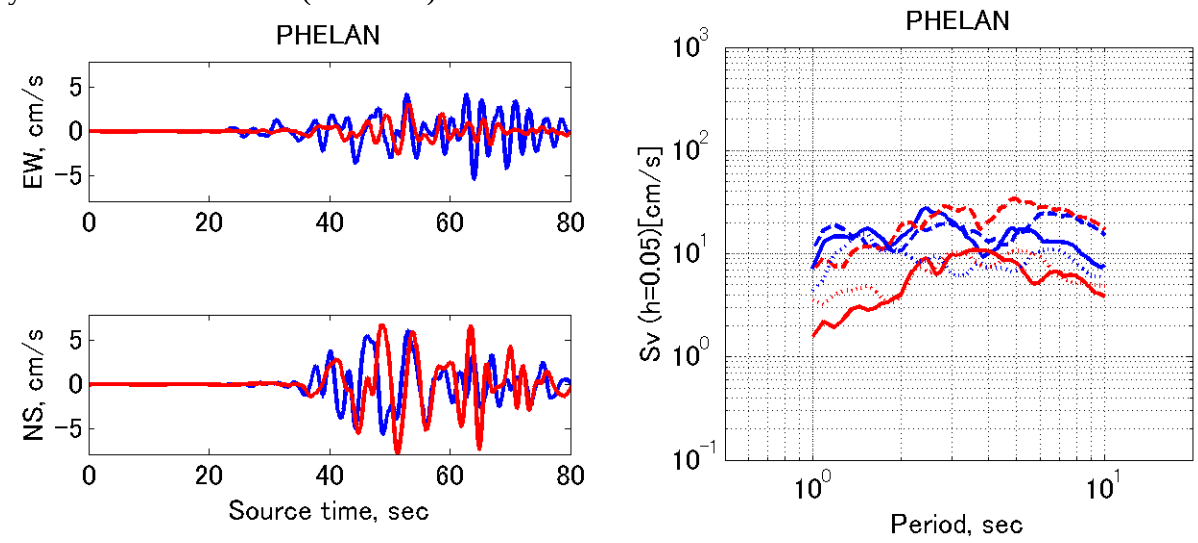

Figure A.3.5-23. Waveforms and *Sv* response spectra for the second Landers event (*Mw*7.31) occurred in year 1831.3. Site Phelan (non-basin).

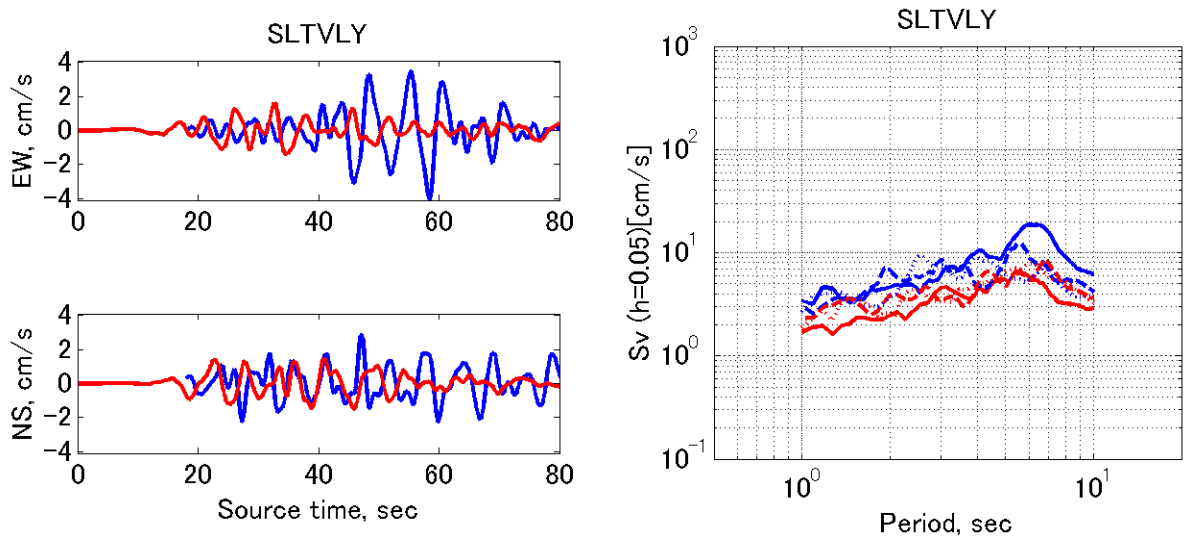

Figure A.3.5-24. Waveforms and *Sv* response spectra for the second Landers event (*Mw*7.31) occurred in year 1831.3. Site Silent Valley (non-basin).

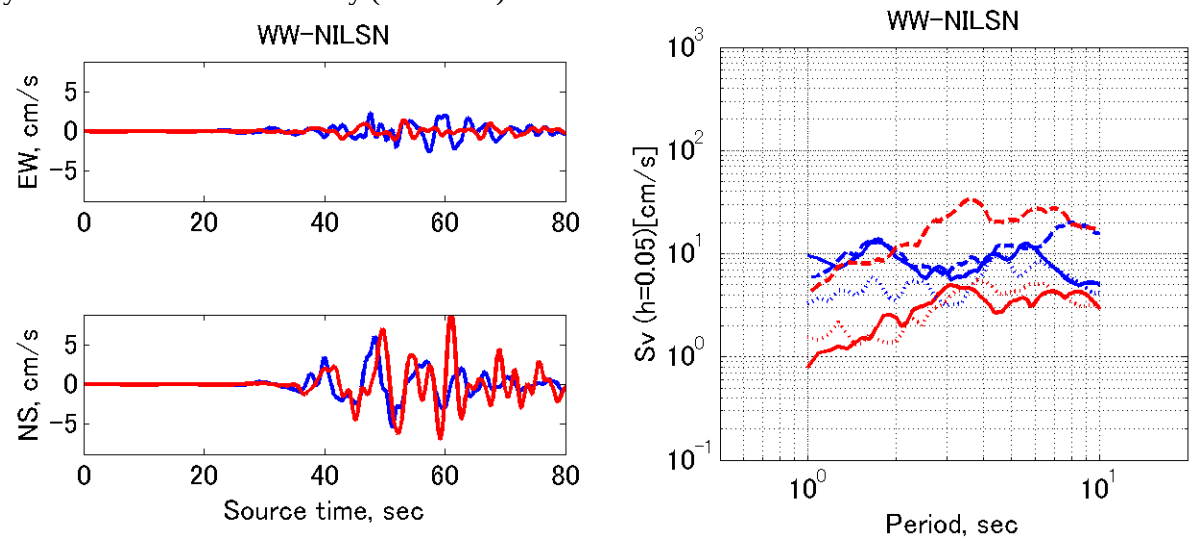

Figure A.3.5-25. Waveforms and *Sv* response spectra for the second Landers event (*Mw*7.31) occurred in year 1831.3. Site WW-Nielson (non-basin).

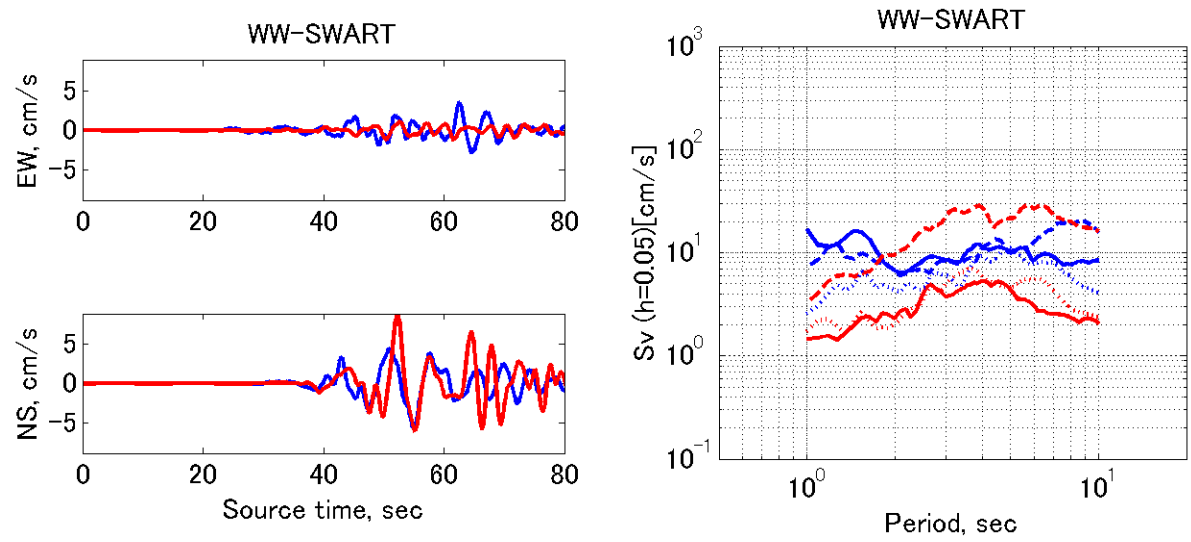

Figure A.3.5-26. Waveforms and *Sv* response spectra for the second Landers event (*Mw*7.31) occurred in year 1831.3. Site WW-Swarthout (non-basin).

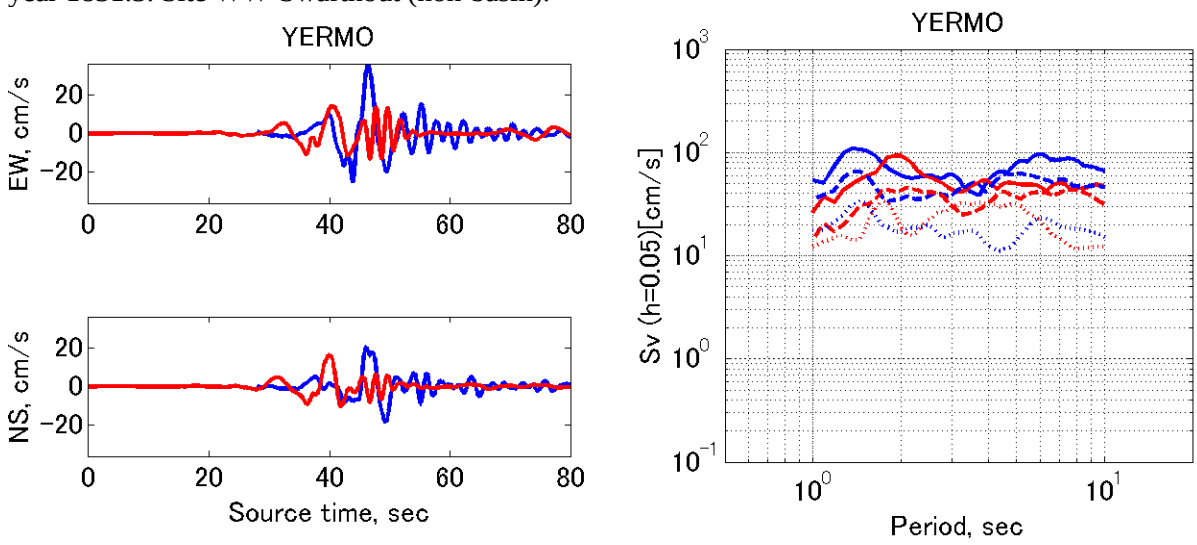

Figure A.3.5-27. Waveforms and *Sv* response spectra for the second Landers event (*Mw*7.31) occurred in year 1831.3. Site Yermo (non-basin).

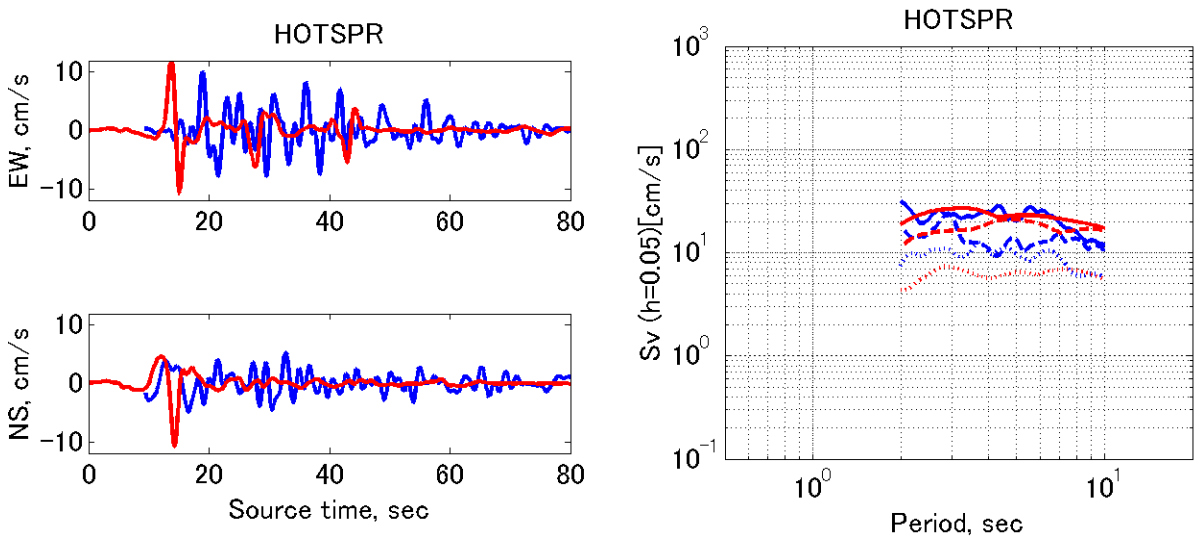

Figure A.3.5-28. Waveforms and *Sv* response spectra for the second Landers event (*Mw*7.31) occurred in year 1831.3. Site Desert Hot Spring (basin).

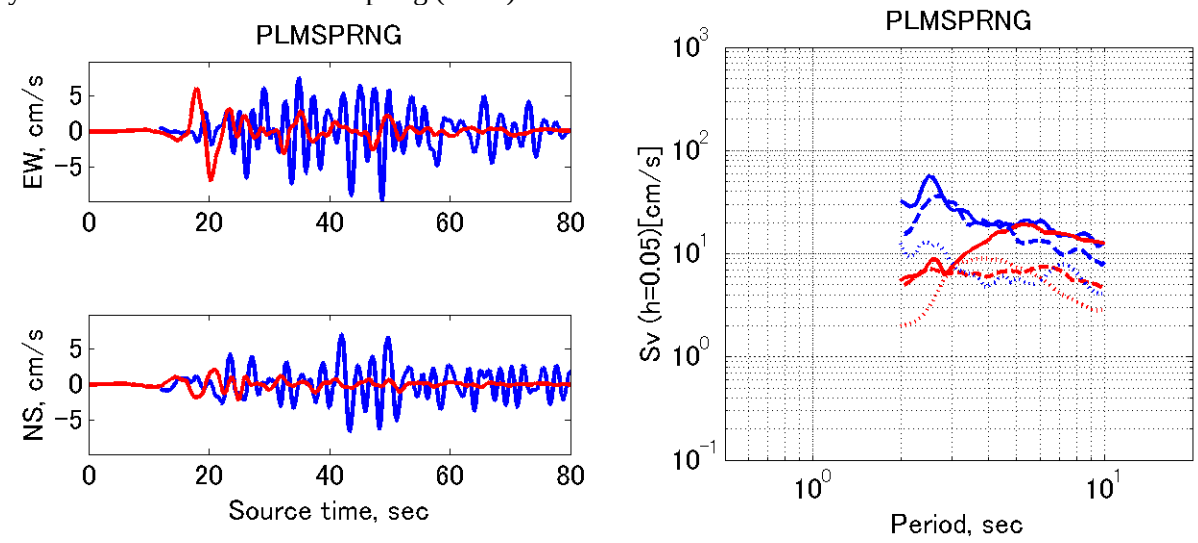

Figure A.3.5-29. Waveforms and *Sv* response spectra for the second Landers event (*Mw*7.31) occurred in year 1831.3. Site Palm Springs (basin).

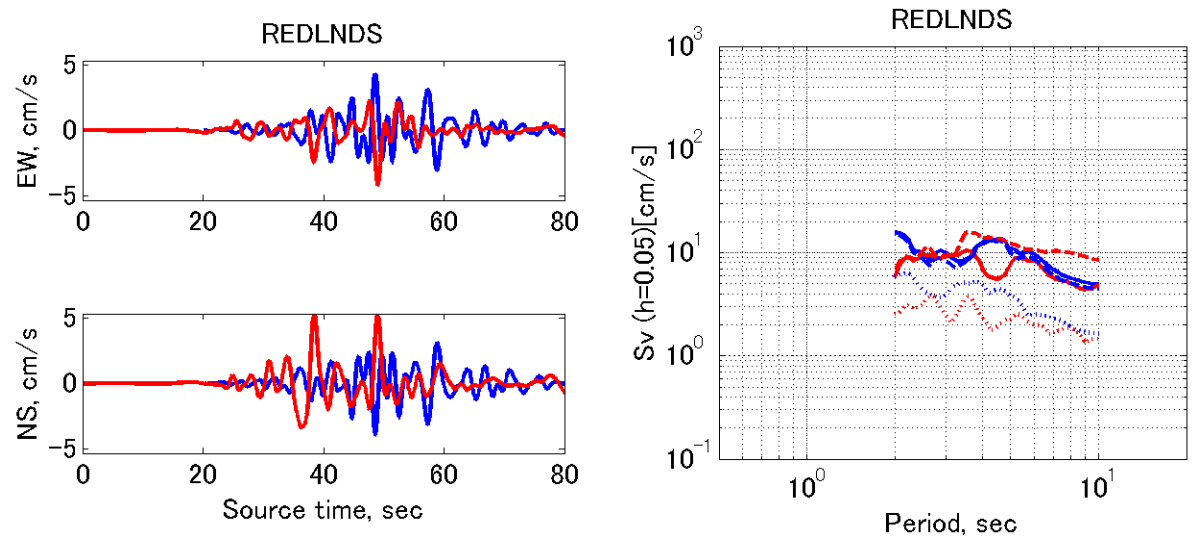

Figure A.3.5-30. Waveforms and *Sv* response spectra for the second Landers event (*Mw*7.31) occurred in year 1831.3. Site Redlands (basin).

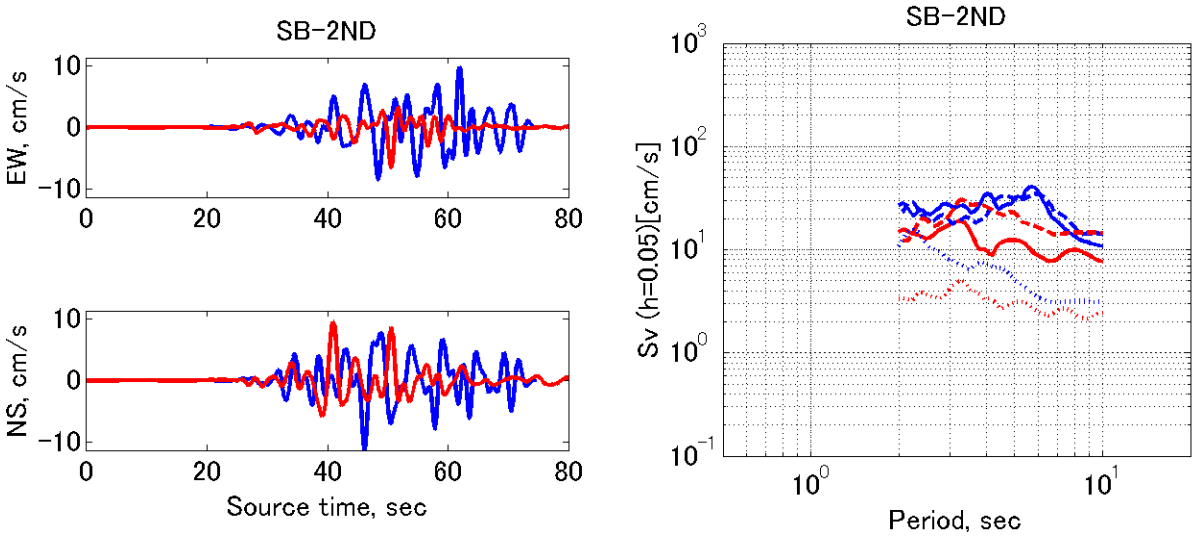

Figure A.3.5-31. Waveforms and *Sv* response spectra for the second Landers event (*Mw*7.31) occurred in year 1831.3. Site SB-2ndArrowhead (basin).

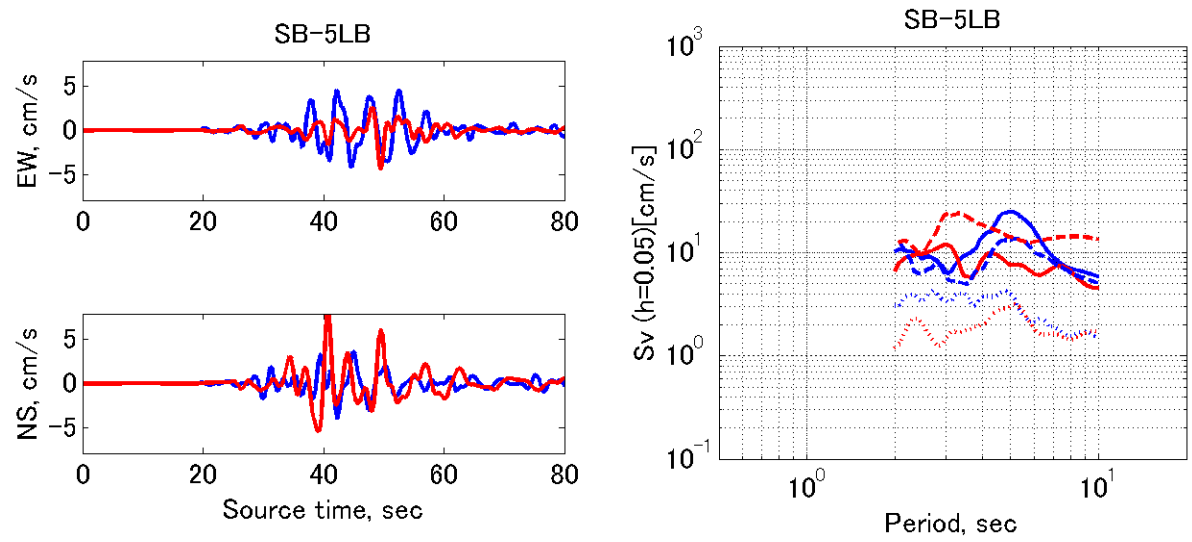

Figure A.3.5-32. Waveforms and *Sv* response spectra for the second Landers event (*Mw*7.31) occurred in year 1831.3. Site SB-Library (basin).

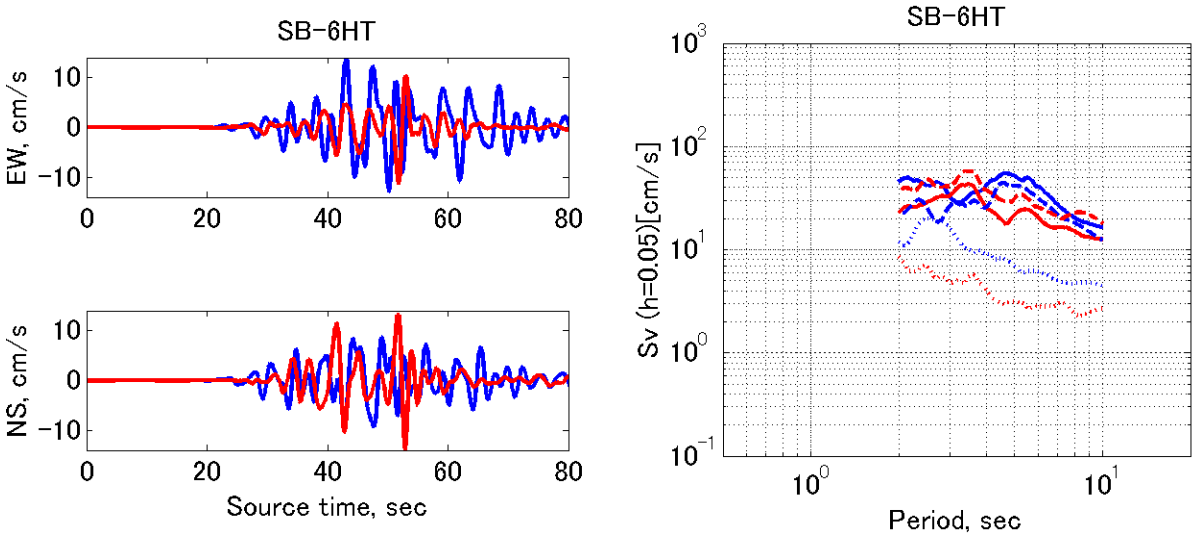

Figure A.3.5-33. Waveforms and *Sv* response spectra for the second Landers event (*Mw*7.31) occurred in year 1831.3. Site SB-Hotel (basin).

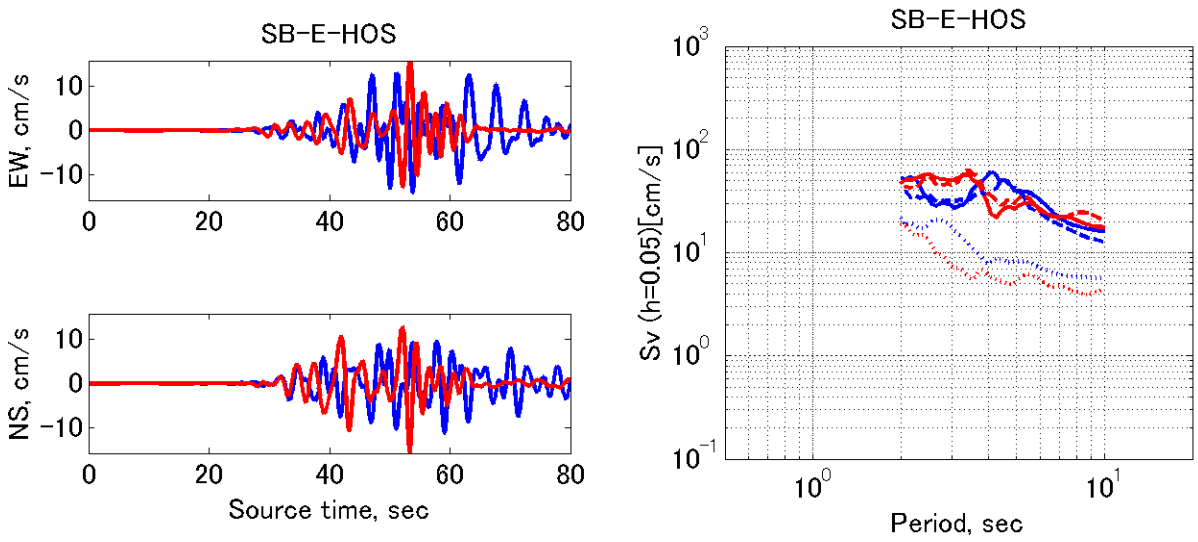

Figure A.3.5-34. Waveforms and *Sv* response spectra for the second Landers event (*Mw*7.31) occurred in year 1831.3. Site SB-E&Hospitality (basin).

A.3.6 Trimming results

Figures below show trimming for the LSAs and HRAs (slip asperities and slip rate asperities). Criteria of Somerville et al., 1999 is used. Dashed line – trimmed rupture area, solid line – trimmed LSA or HRA.

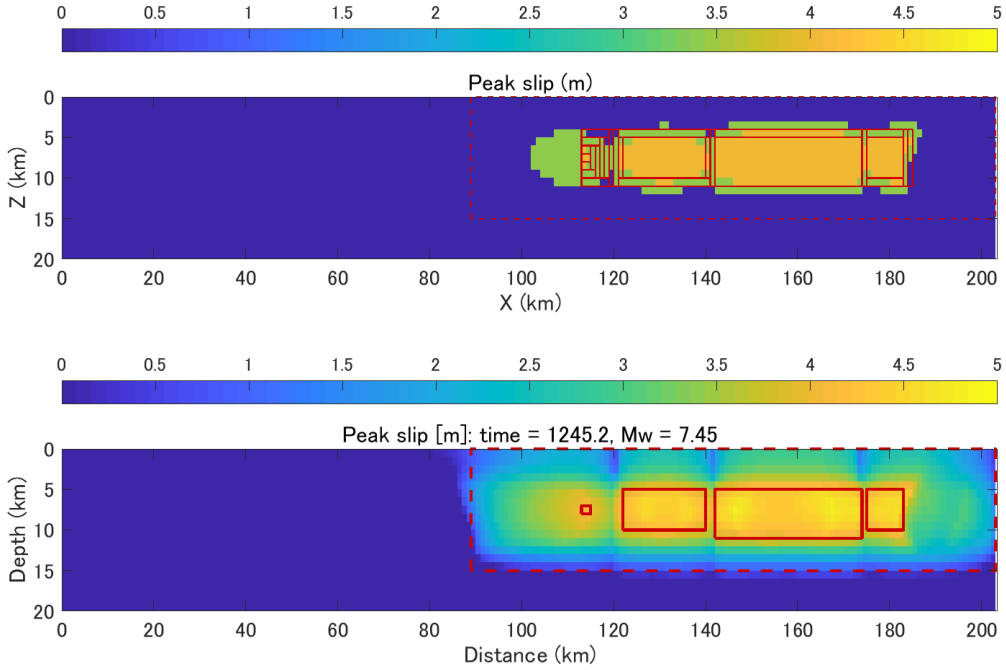

Figure A.3.6-1. Trimming for the slip asperity: procedure (top) and trimming result (bottom) for Event 1, 1245.2 year, *Mw*7.45

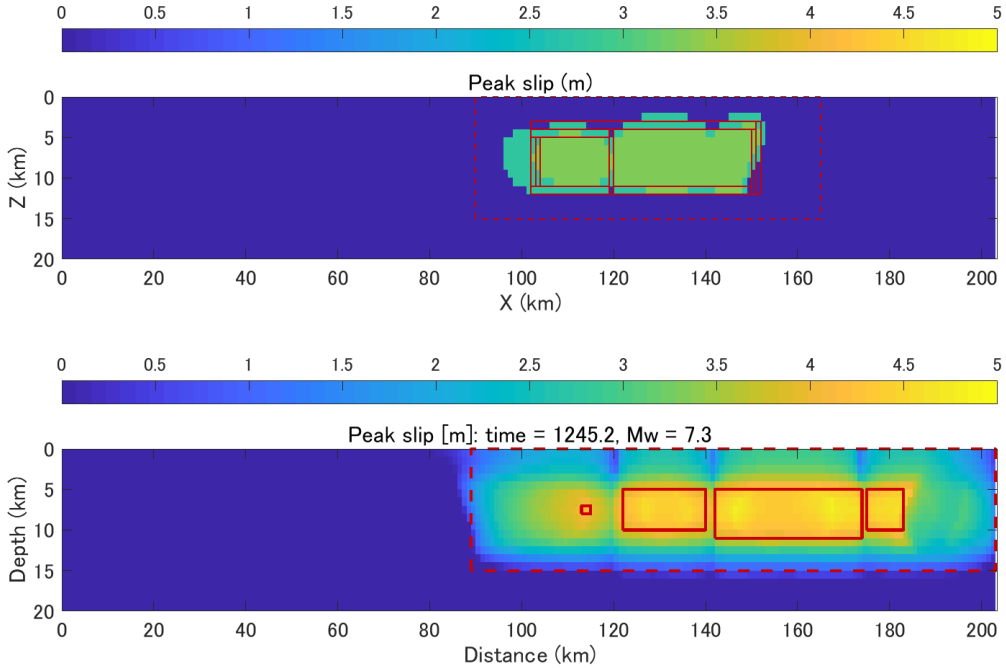

Figure A.3.6-2. Trimming for the slip asperity: procedure (top) and trimming result (bottom) for Event 2, 1245.2 year, *Mw*7.3

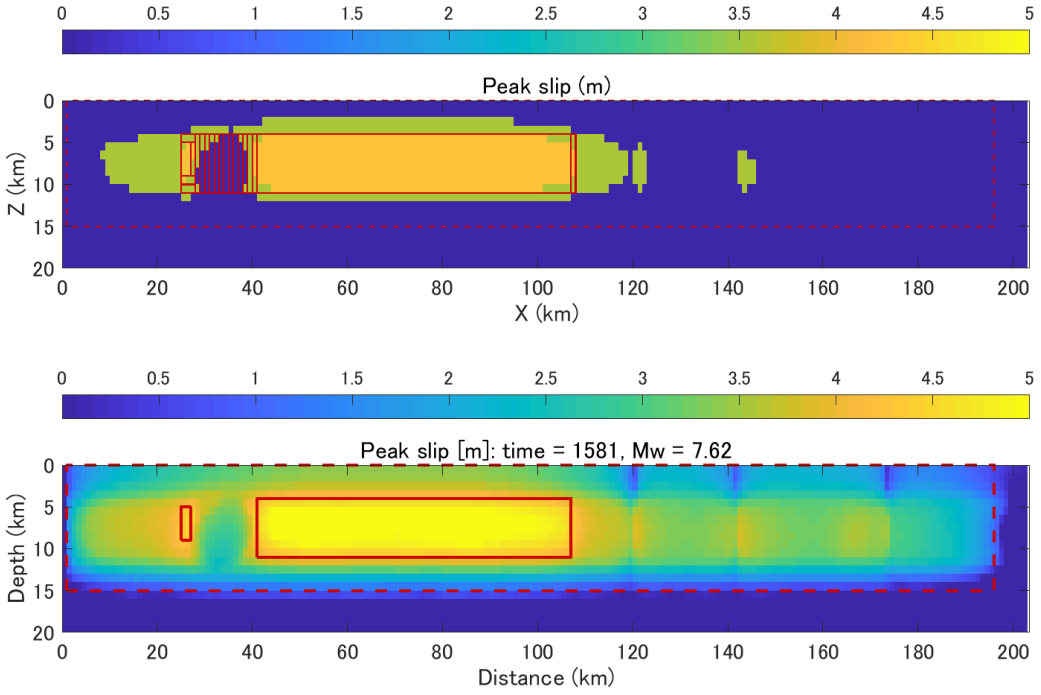

Figure A.3.6-3. Trimming for the slip asperity: procedure (top) and trimming result (bottom) for Event 3, 1581.0 year, *Mw*7.62

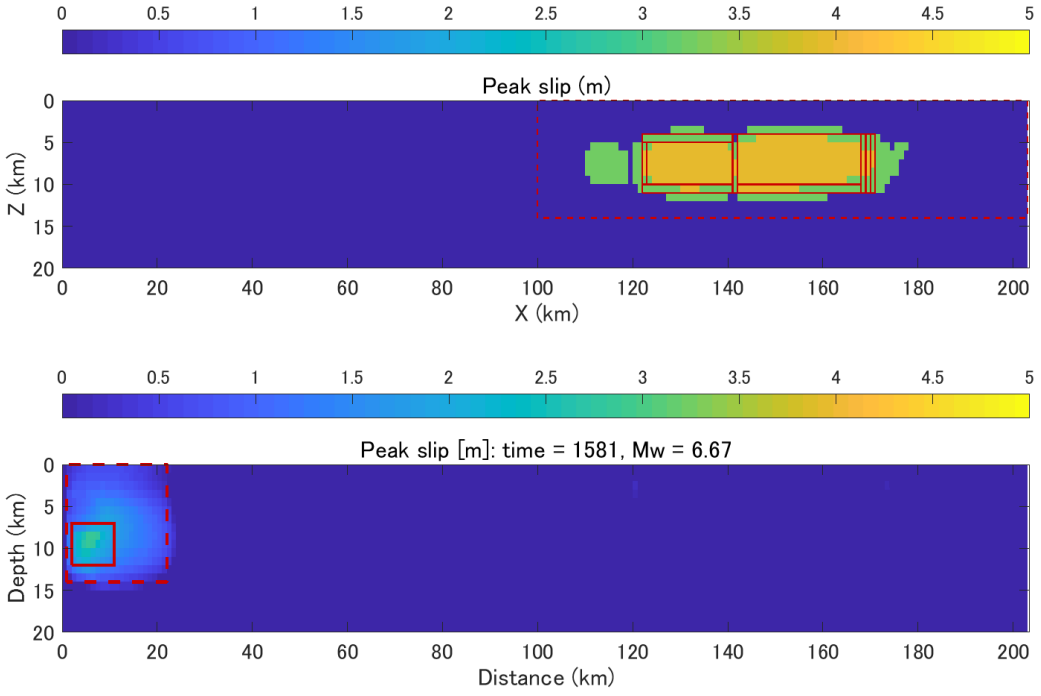

Figure A.3.6-4. Trimming for the slip asperity: procedure (top) and trimming result (bottom) for Event 4, 1581.0 year, *Mw*6.67

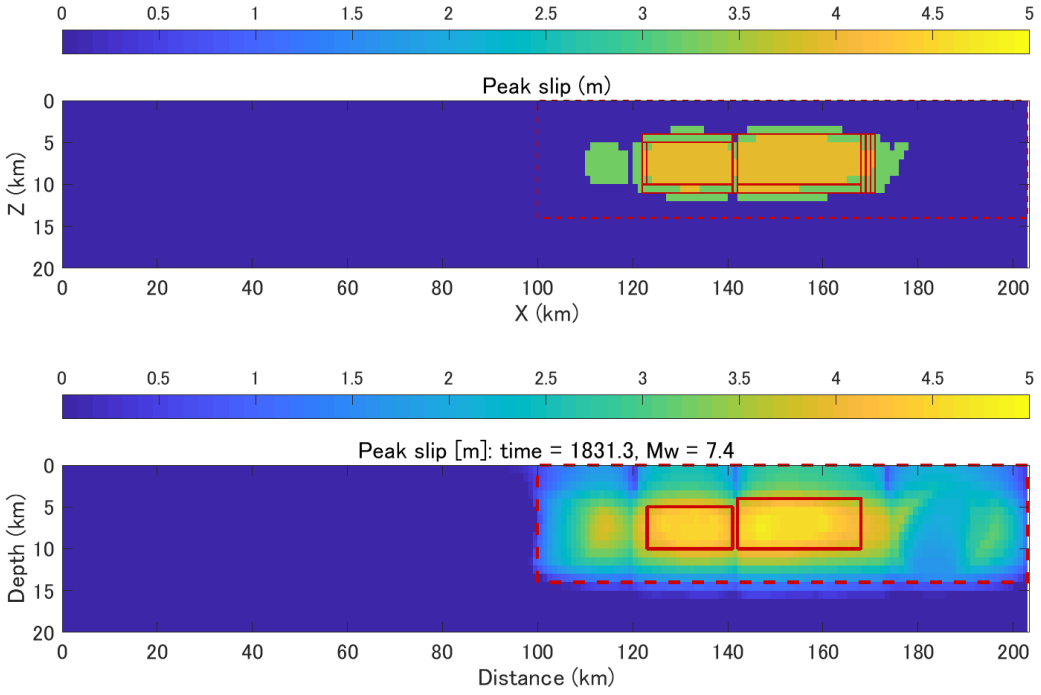

Figure A.3.6-5. Trimming for the slip asperity: procedure (top) and trimming result (bottom) for Event 5, 1831.3 year, *Mw*7.4

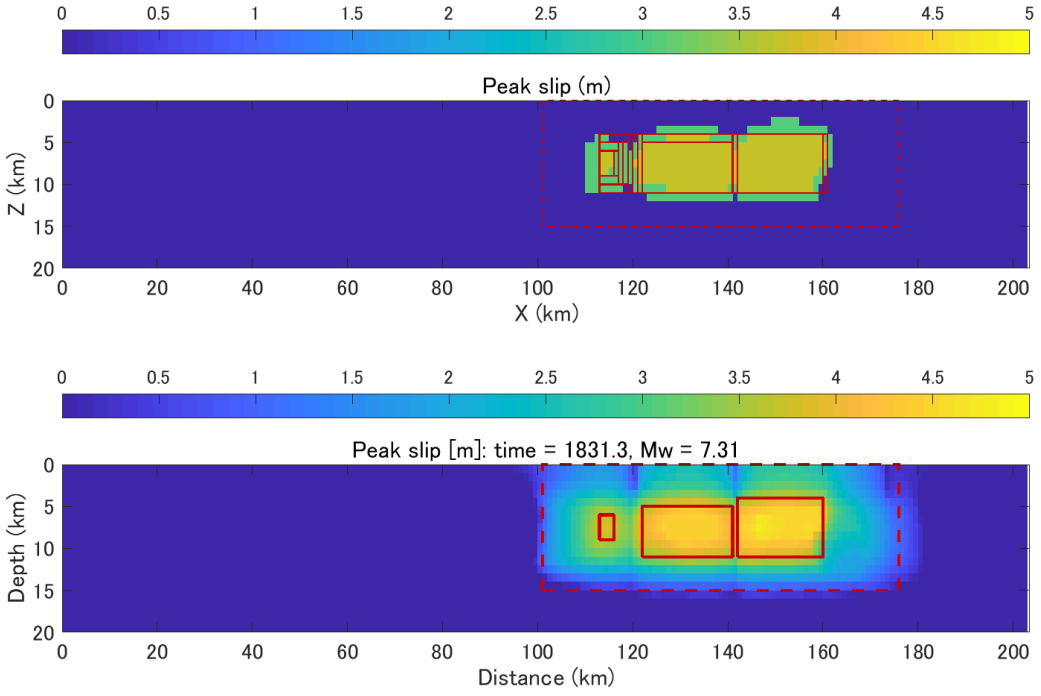

Figure A.3.6-6. Trimming for the slip asperity: procedure (top) and trimming result (bottom) for Event 6, 1831.3 year, *Mw*7.31

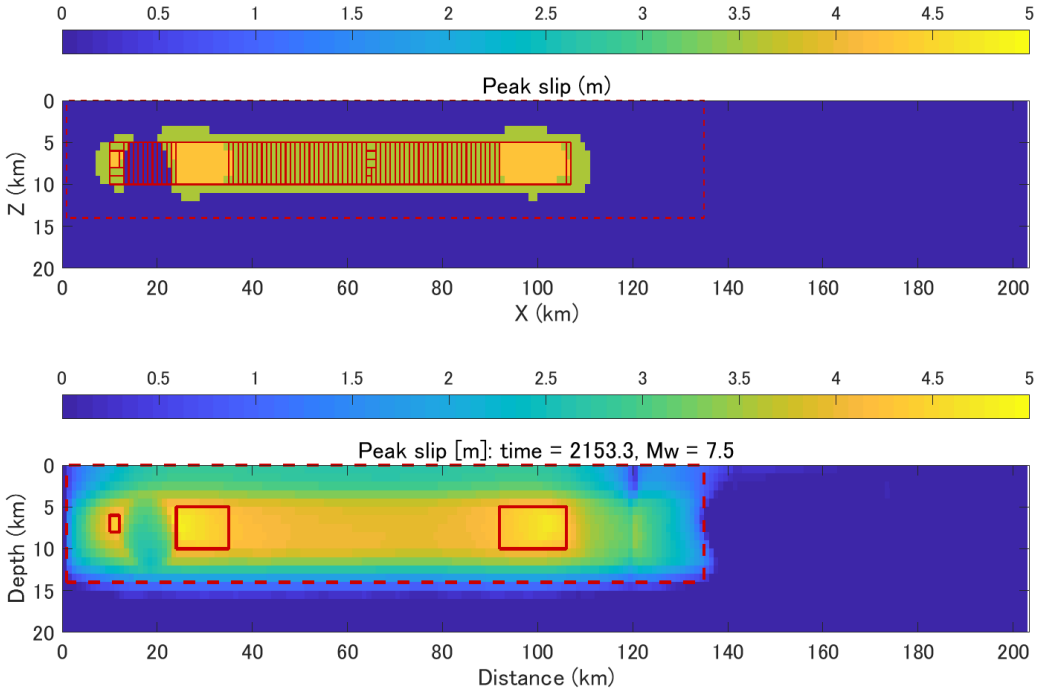

Figure A.3.6-7. Trimming for the slip asperity: procedure (top) and trimming result (bottom) for Event 7, 2153.3 year, *Mw*7.5

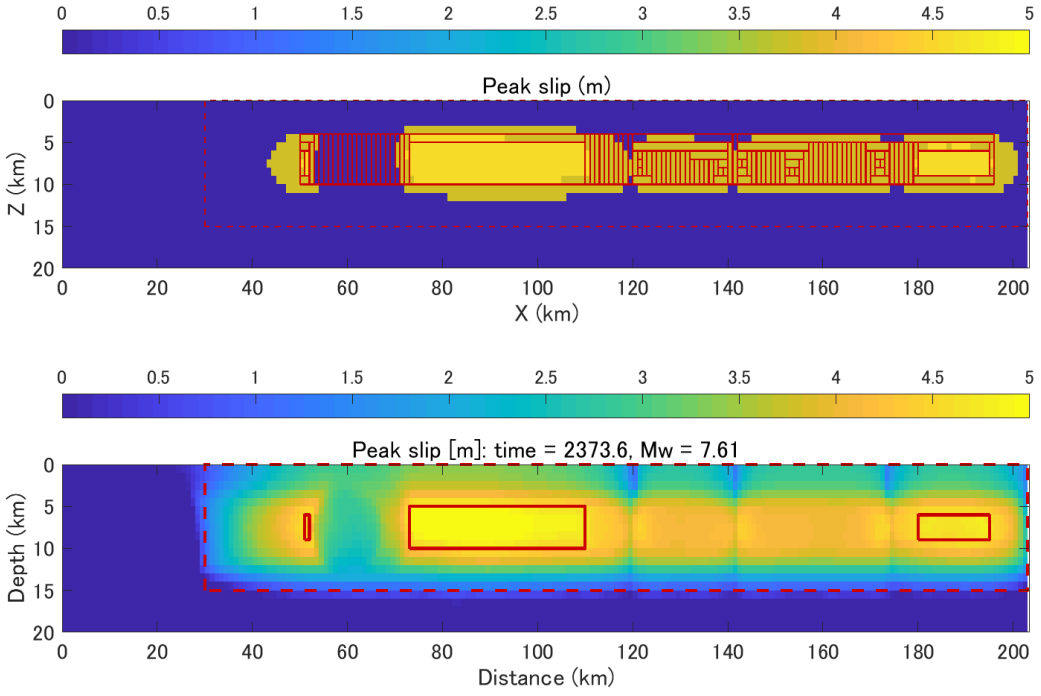

Figure A.3.6-8. Trimming for the slip asperity: procedure (top) and trimming result (bottom) for Event 8, 2373.6 year, *Mw*7.61

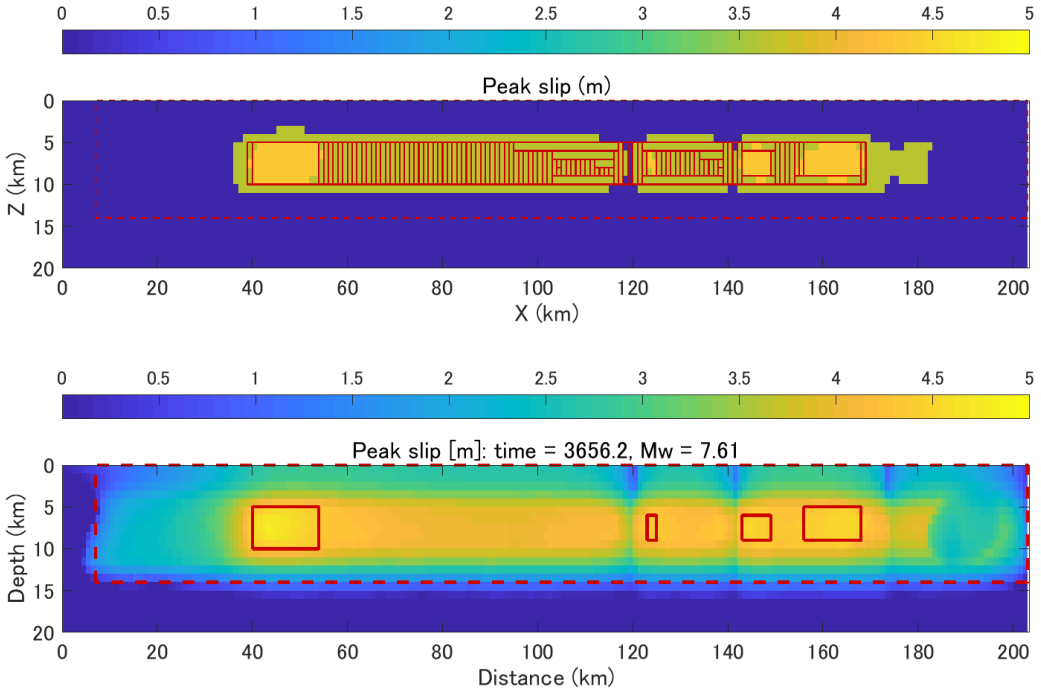

Figure A.3.6-9. Trimming for the slip asperity: procedure (top) and trimming result (bottom) for Event 12, 3656.2 year, *Mw*7.61

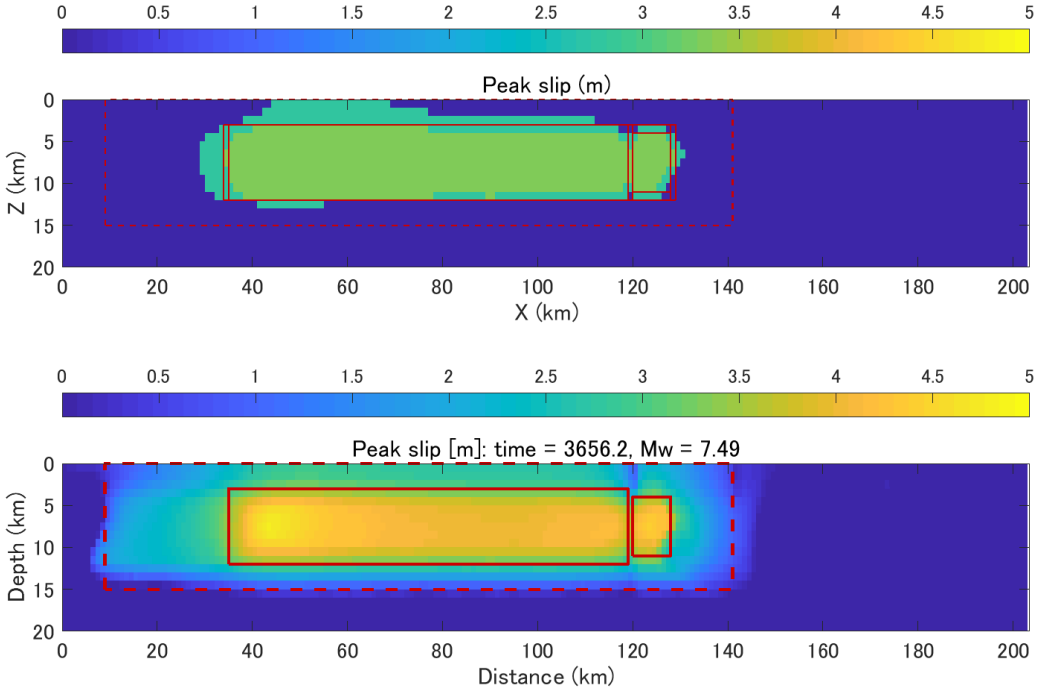

Figure A.3.6-10. Trimming for the slip asperity: procedure (top) and trimming result (bottom) for Event 13, 3656.2 year, *Mw*7.49

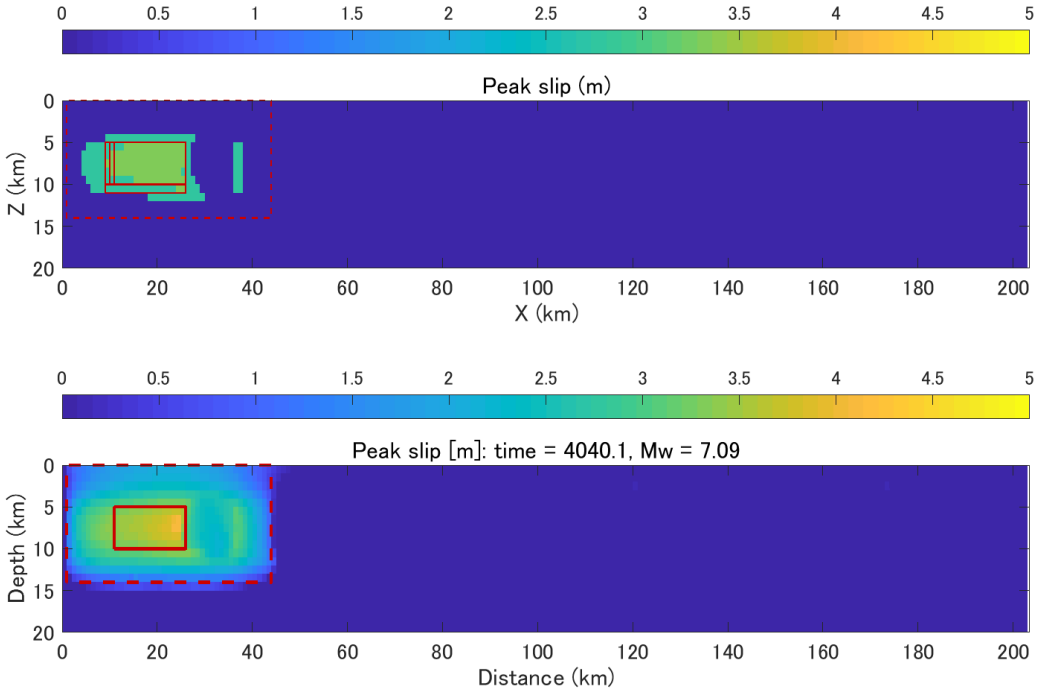

Figure A.3.6-11. Trimming for the slip asperity: procedure (top) and trimming result (bottom) for Event 14, 4040.1 year, *Mw*7.09

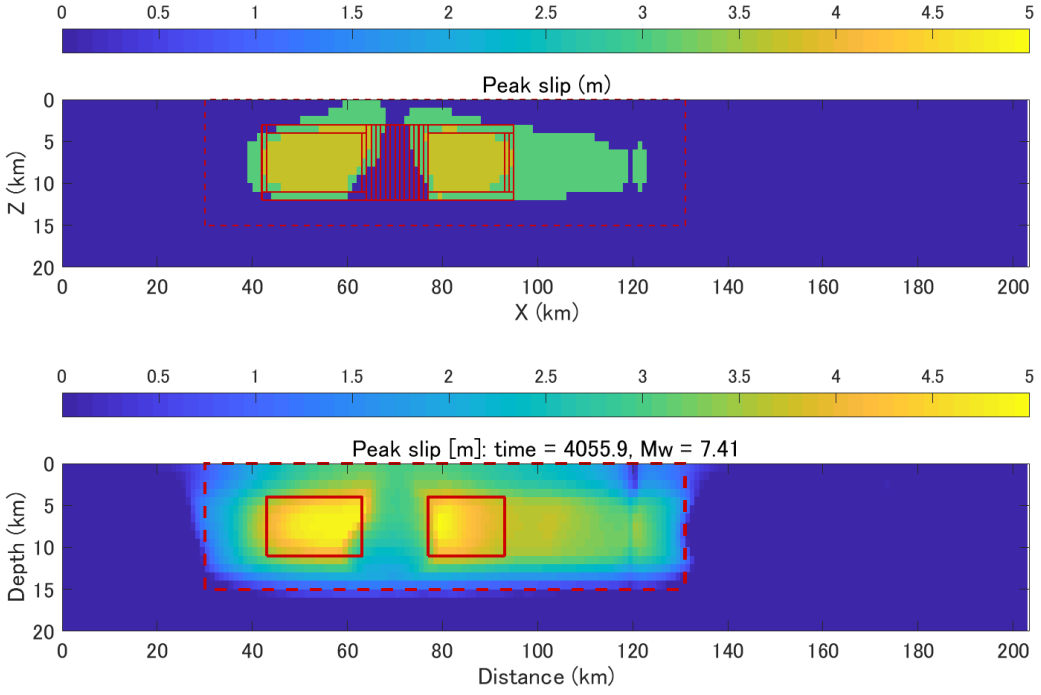

Figure A.3.6-12. Trimming for the slip asperity: procedure (top) and trimming result (bottom) for Event 15, 4055.9 year, *Mw*7.41

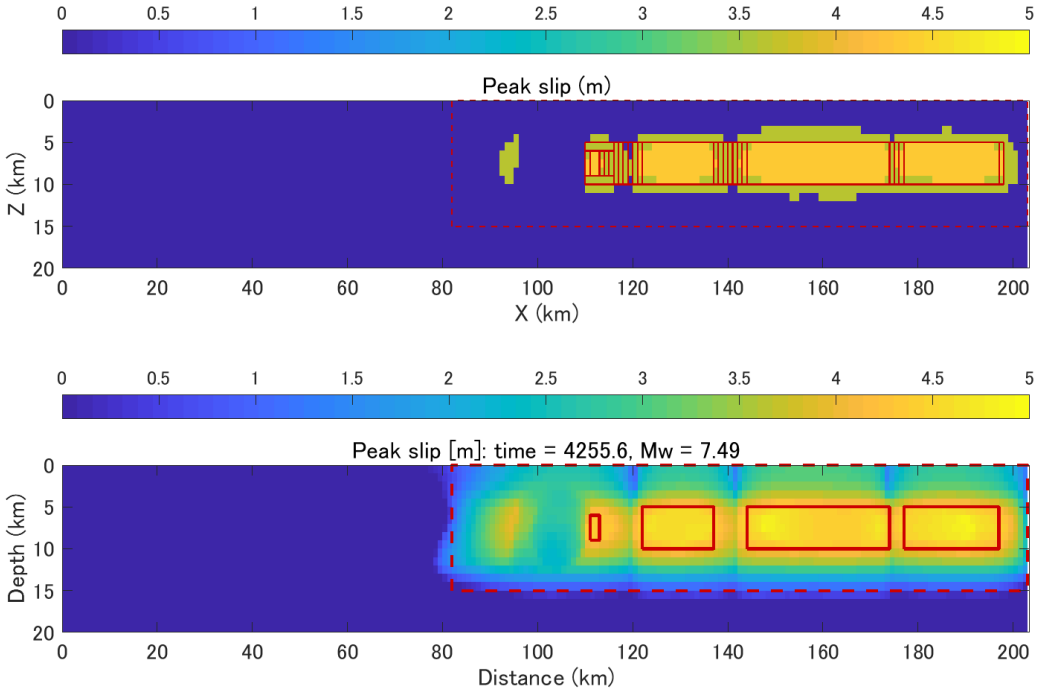

Figure A.3.6-13. Trimming for the slip asperity: procedure (top) and trimming result (bottom) for Event 16, 4255.6 year, *Mw*7.49

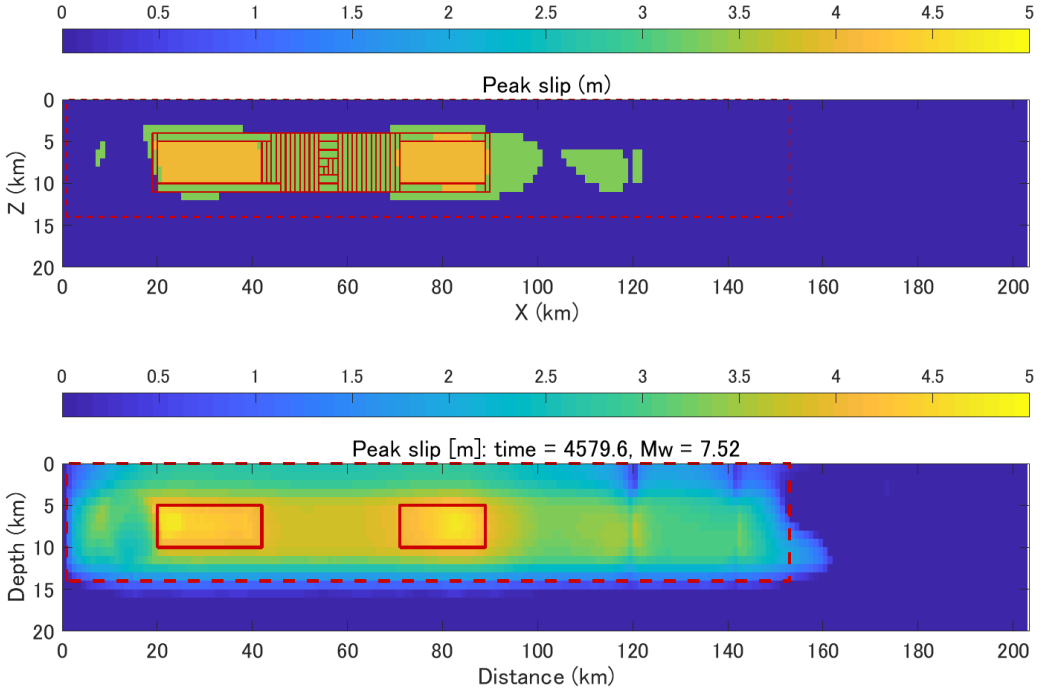

Figure A.3.6-14. Trimming for the slip asperity: procedure (top) and trimming result (bottom) for Event 17, 4579.6 year, *Mw*7.52

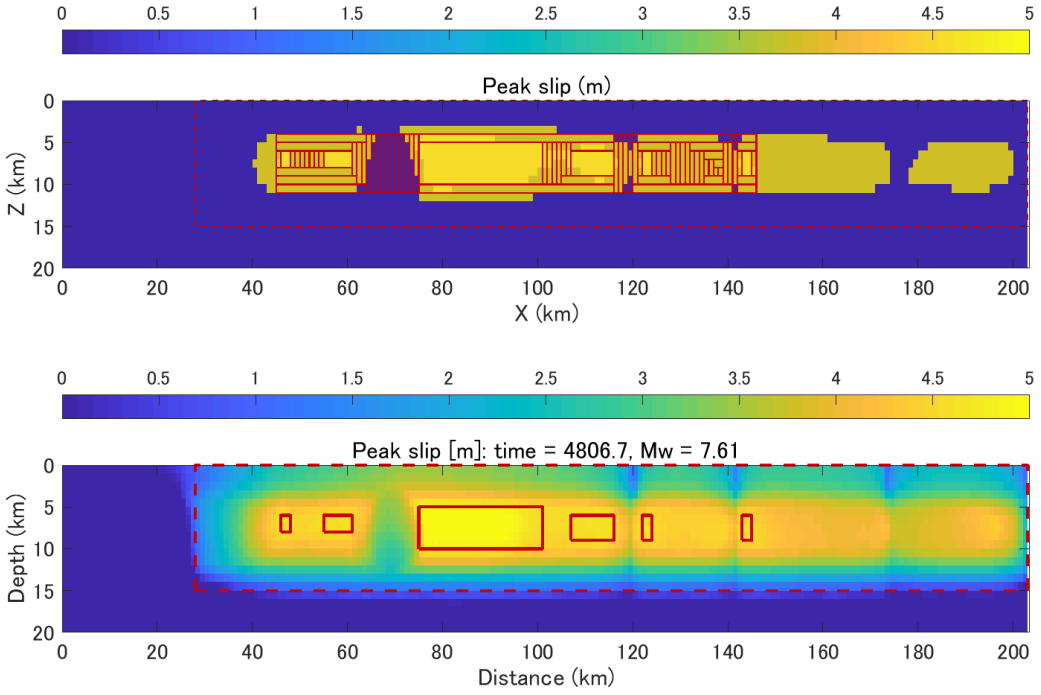

Figure A.3.6-15. Trimming for the slip asperity: procedure (top) and trimming result (bottom) for Event 18, 4806.7 year, *Mw*7.61

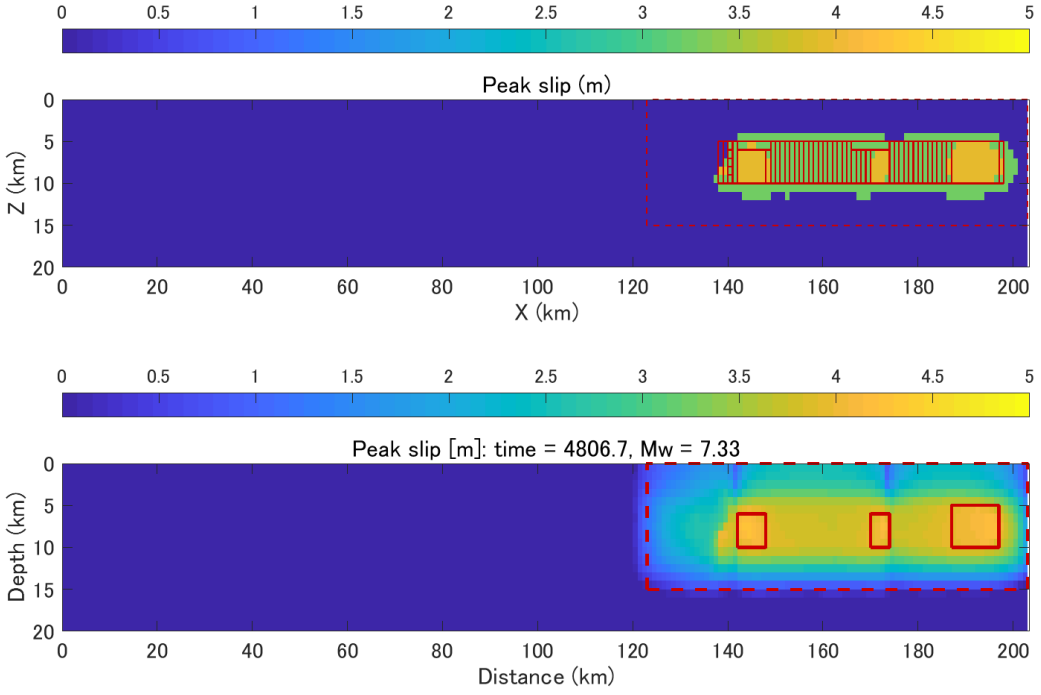

Figure A.3.6-16. Trimming for the slip asperity: procedure (top) and trimming result (bottom) for Event 19, 4806.7 year, *Mw*7.33

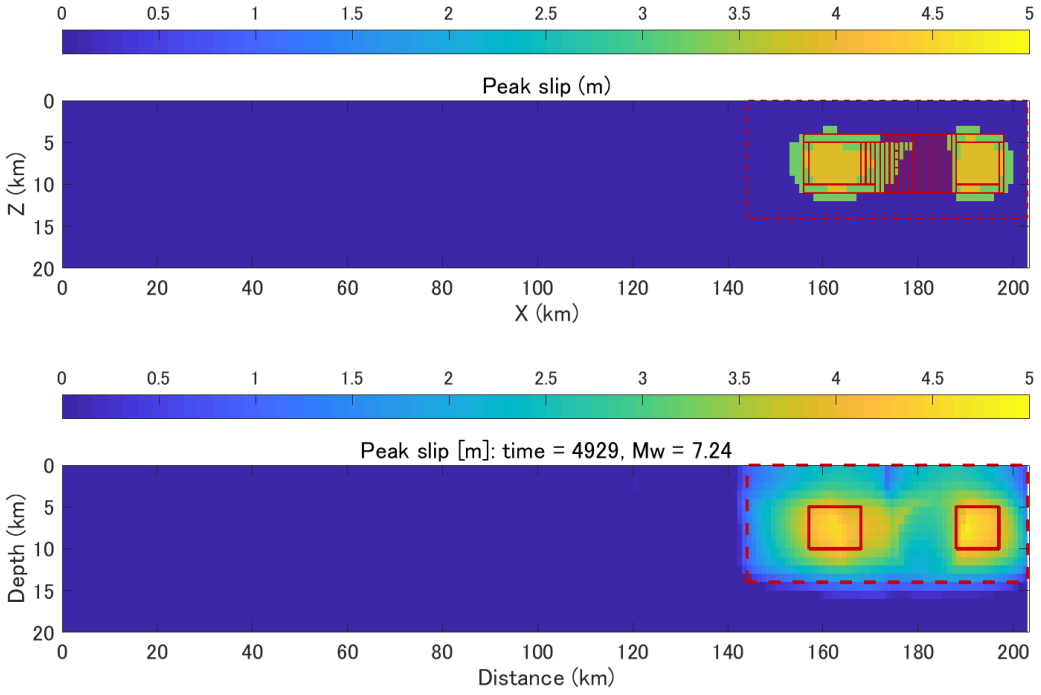

Figure A.3.6-17. Trimming for the slip asperity: procedure (top) and trimming result (bottom) for Event 20, 4929.0 year, *Mw*7.24

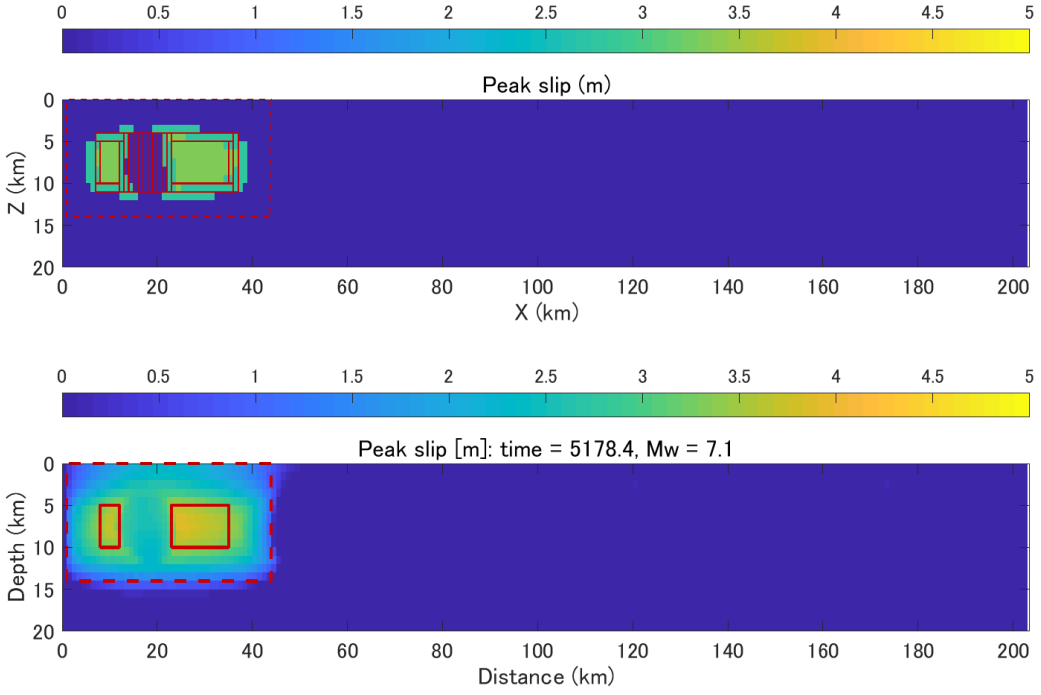

Figure A.3.6-18. Trimming for the slip asperity: procedure (top) and trimming result (bottom) for Event 21, 5178.4 year, *Mw*7.1

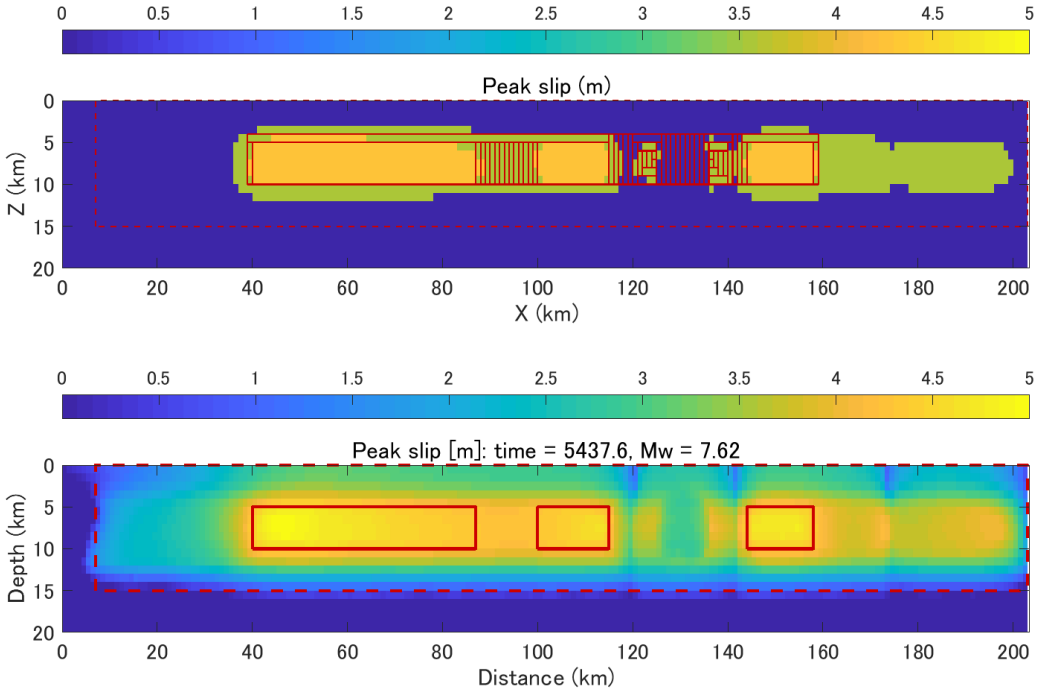

Figure A.3.6-19. Trimming for the slip asperity: procedure (top) and trimming result (bottom) for Event 22, 5437.6 year, *Mw*7.62

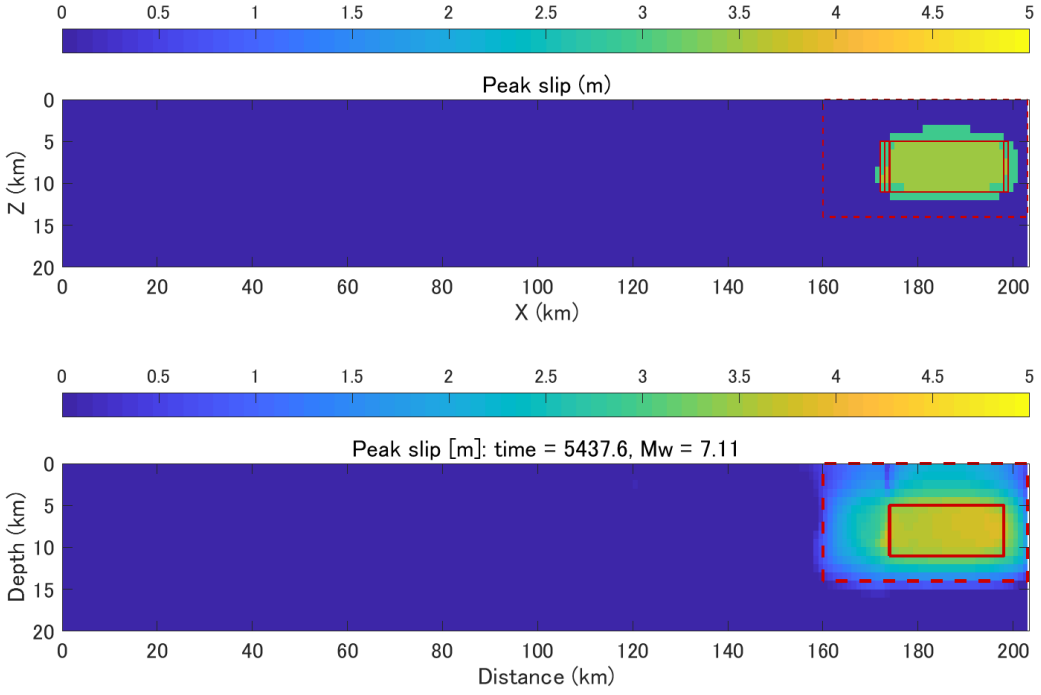

Figure A.3.6-20. Trimming for the slip asperity: procedure (top) and trimming result (bottom) for Event 23, 5437.6 year, *Mw*7.11

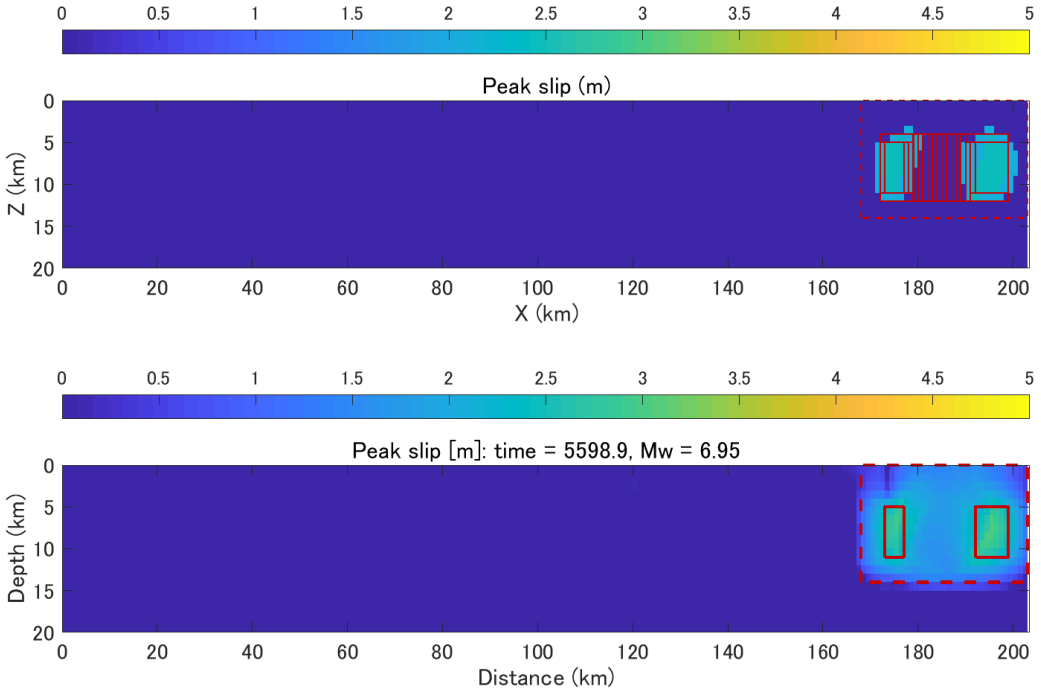

Figure A.3.6-21. Trimming for the slip asperity: procedure (top) and trimming result (bottom) for Event 24, 5598.9 year, *Mw*6.95

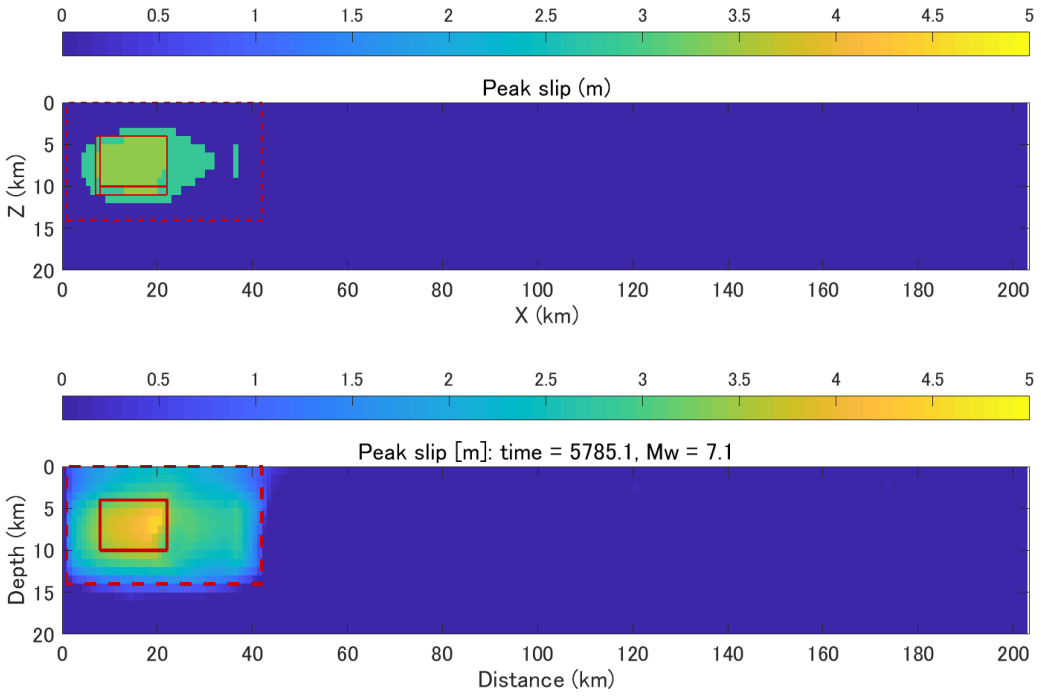

Figure A.3.6-22. Trimming for the slip asperity: procedure (top) and trimming result (bottom) for Event 25, 5785.1 year, *Mw*7.1

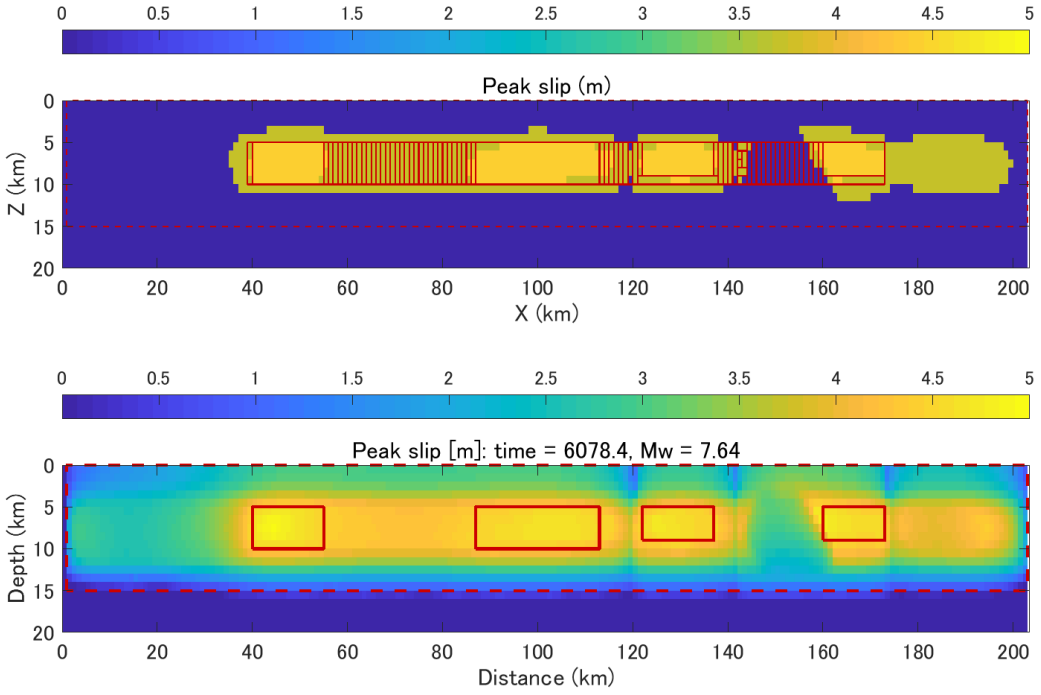

Figure A.3.6-23. Trimming for the slip asperity: procedure (top) and trimming result (bottom) for Event 26, 6078.4 year, *Mw*7.64

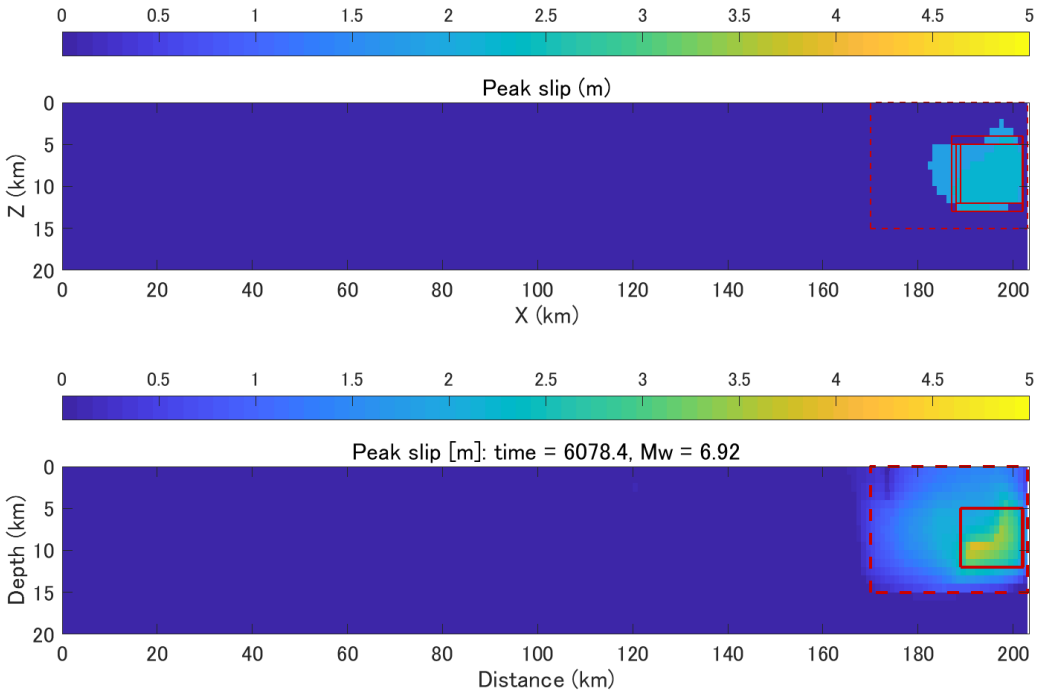

Figure A.3.6-24. Trimming for the slip asperity: procedure (top) and trimming result (bottom) for Event 27, 6078.4 year, *Mw*6.92

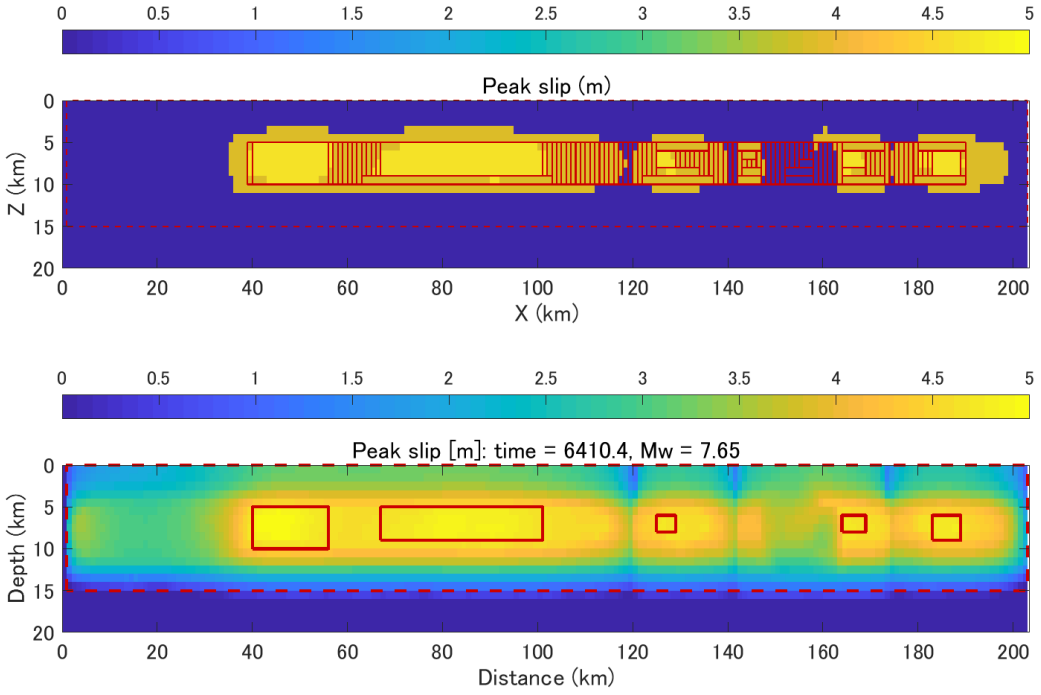

Figure A.3.6-25. Trimming for the slip asperity: procedure (top) and trimming result (bottom) for Event 28, 6410.4 year, *Mw*7.65

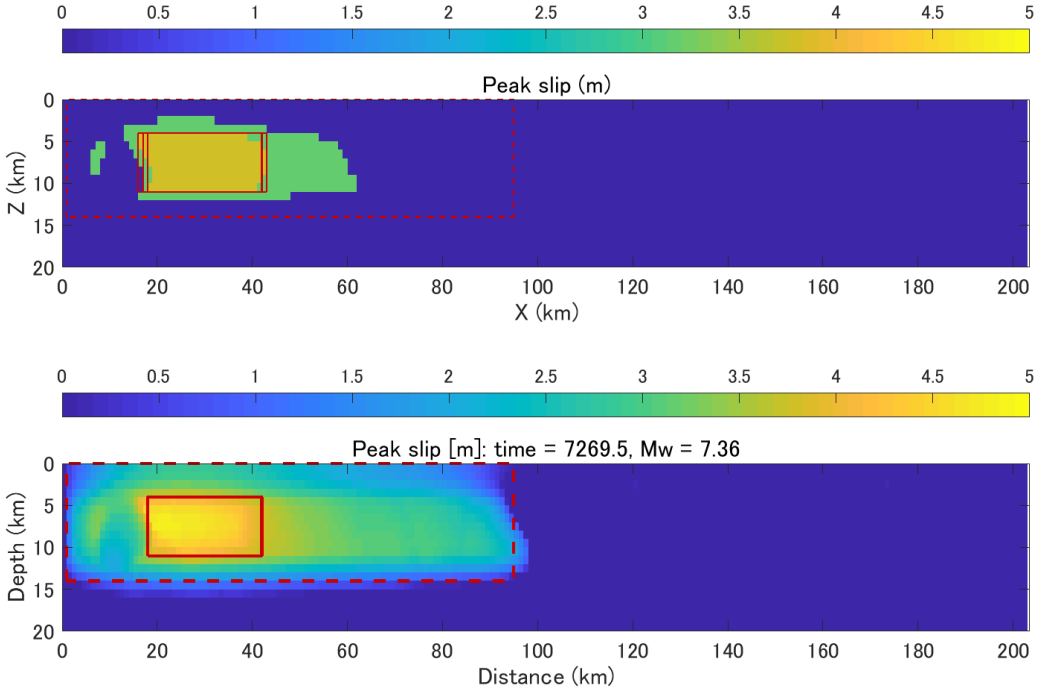

Figure A.3.6-26. Trimming for the slip asperity: procedure (top) and trimming result (bottom) for Event 29, 7269.5 year, *Mw*7.36

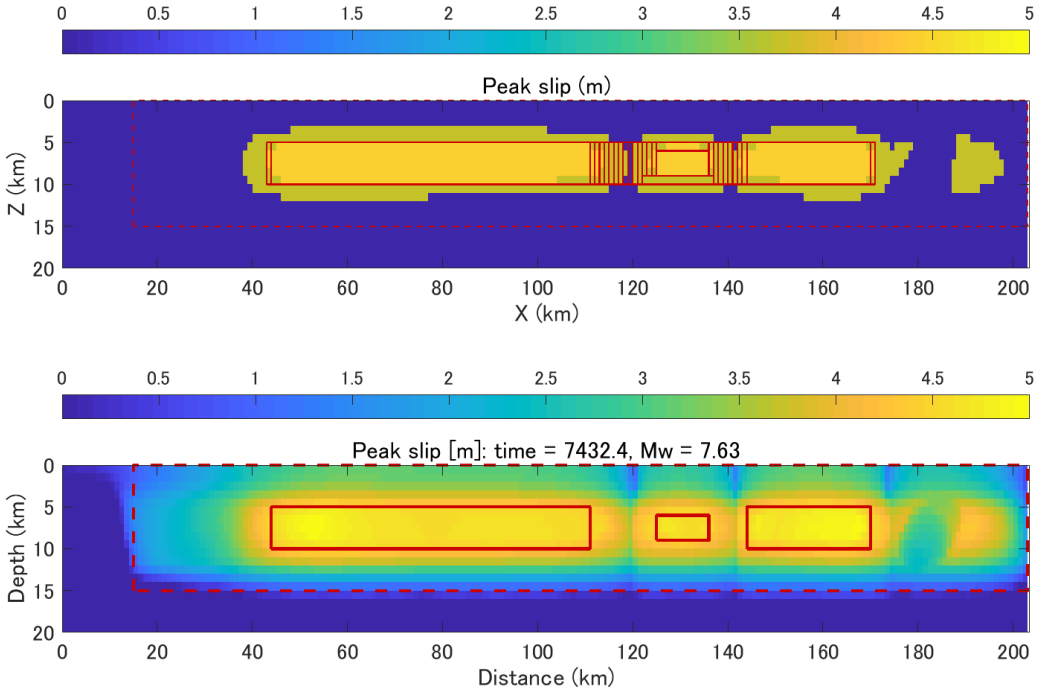

Figure A.3.6-27. Trimming for the slip asperity: procedure (top) and trimming result (bottom) for Event 30, 7432.4 year, *Mw*7.63

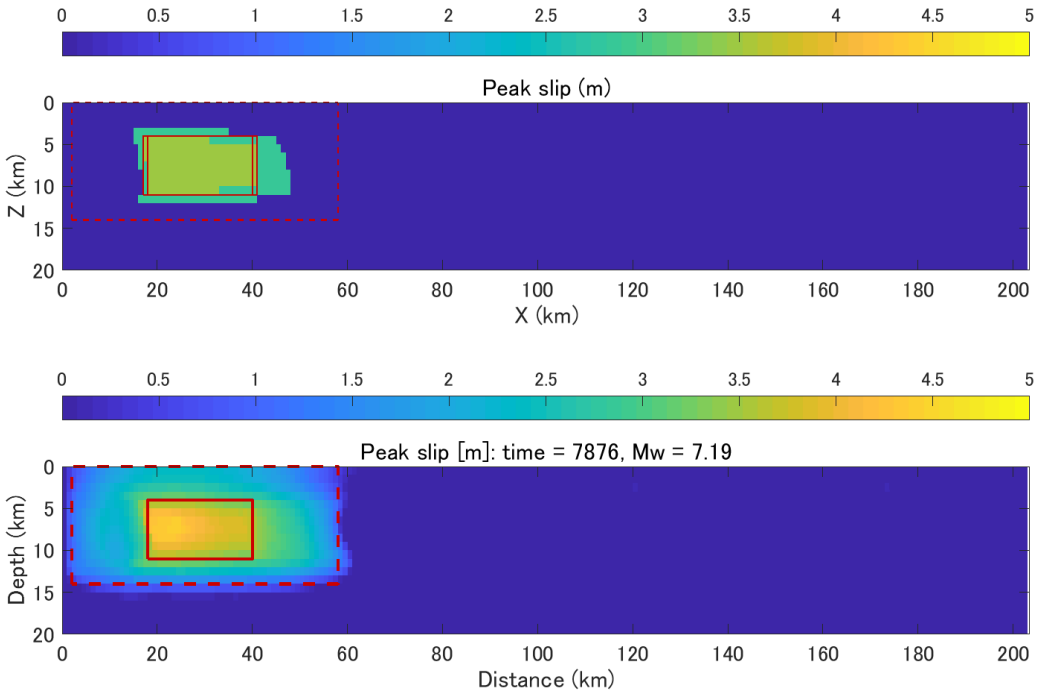

Figure A.3.6-28. Trimming for the slip asperity: procedure (top) and trimming result (bottom) for Event 31, 7876.0 year, *Mw*7.19

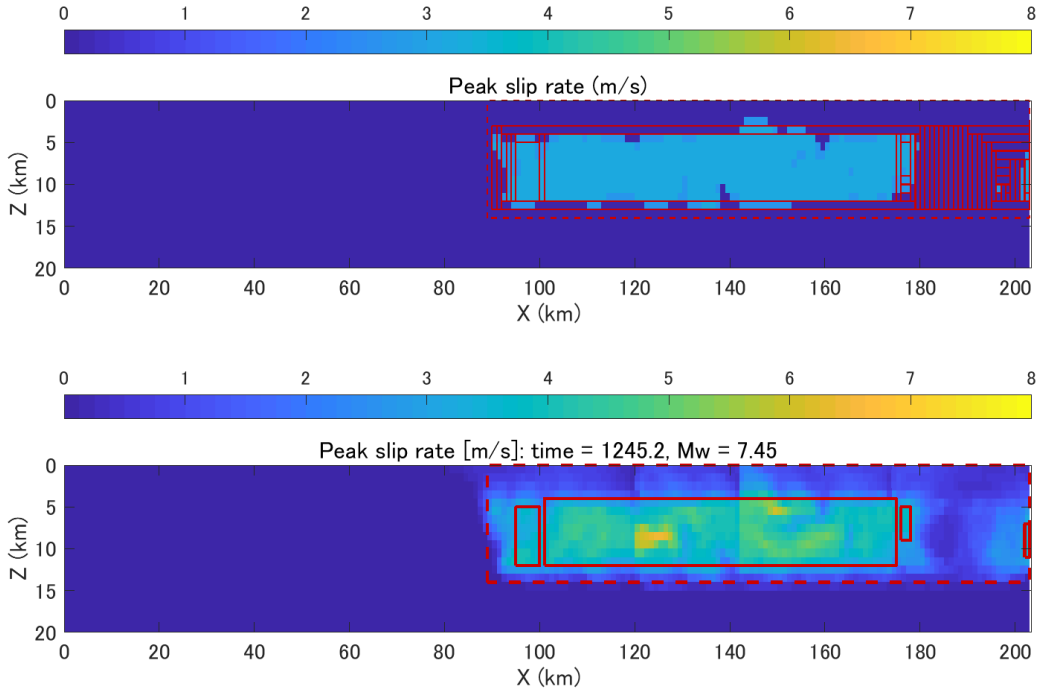

Figure A.3.6-29. Trimming for the slip-rate asperity: procedure (top) and trimming result (bottom) for Event 1, 1245.2 year, *Mw*7.45

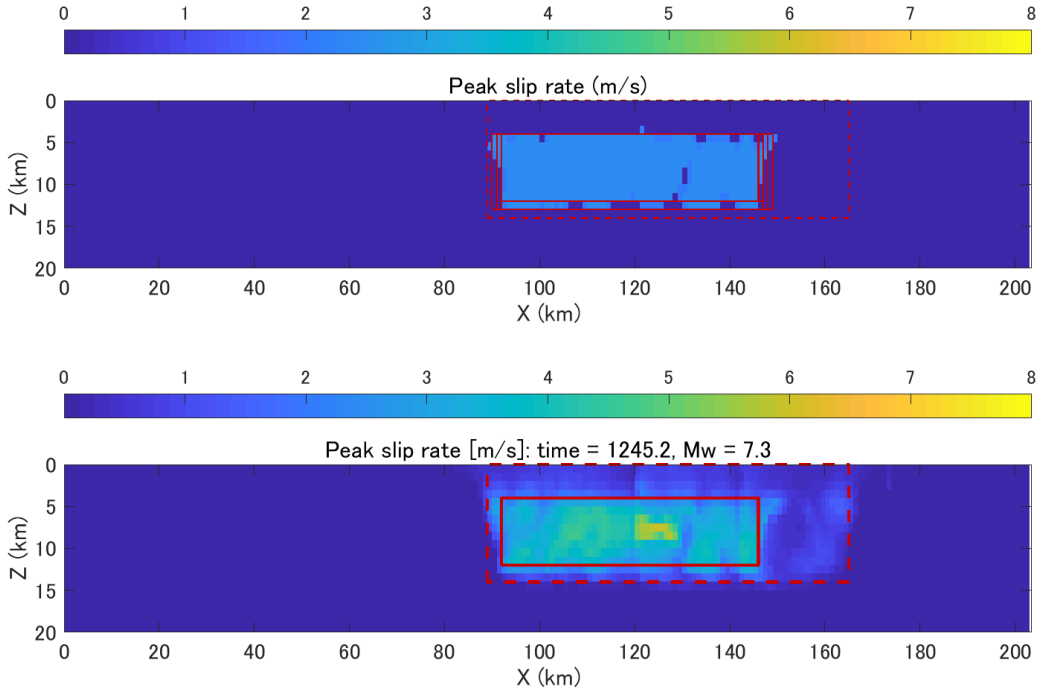

Figure A.3.6-30. Trimming for the slip-rate asperity: procedure (top) and trimming result (bottom) for Event 2, 1245.2 year, *Mw*7.3

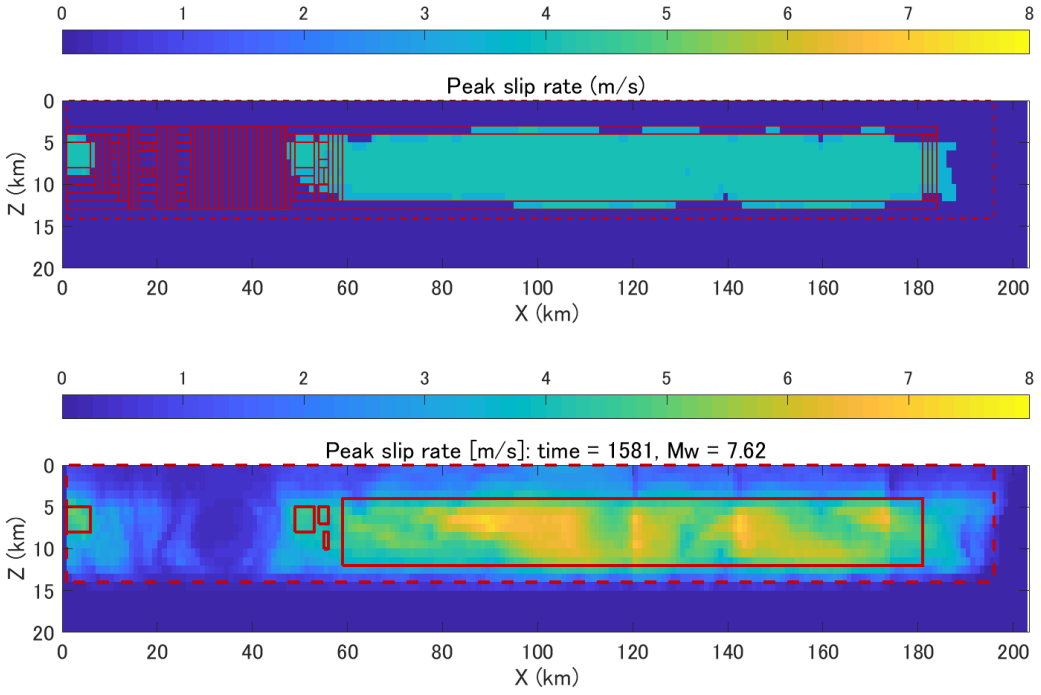

Figure A.3.6-31. Trimming for the slip-rate asperity: procedure (top) and trimming result (bottom) for Event 3, 1581.0 year, *Mw*7.62

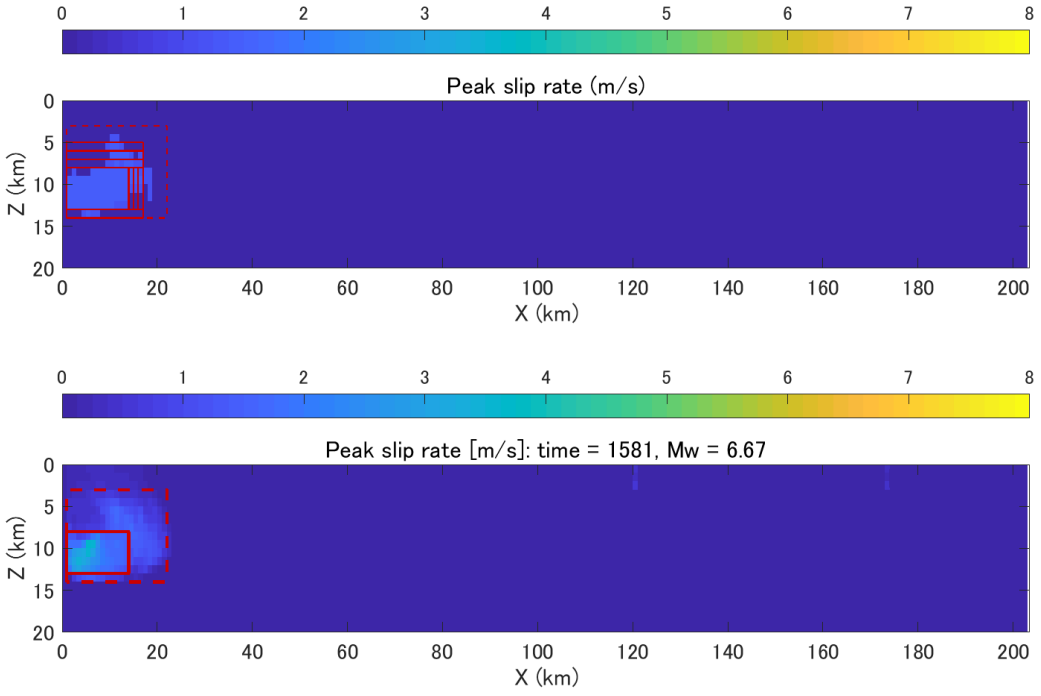

Figure A.3.6-32. Trimming for the slip-rate asperity: procedure (top) and trimming result (bottom) for Event 4, 1581.0 year, *Mw*6.67

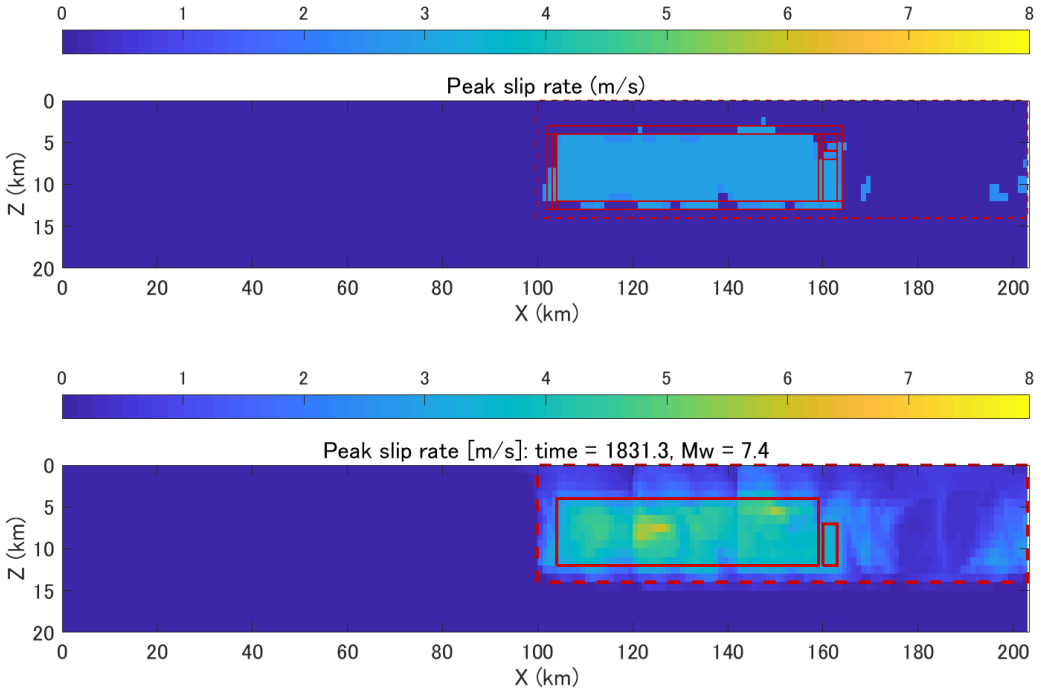

Figure A.3.6-33. Trimming for the slip-rate asperity: procedure (top) and trimming result (bottom) for Event 5, 1831.3 year, *Mw*7.4

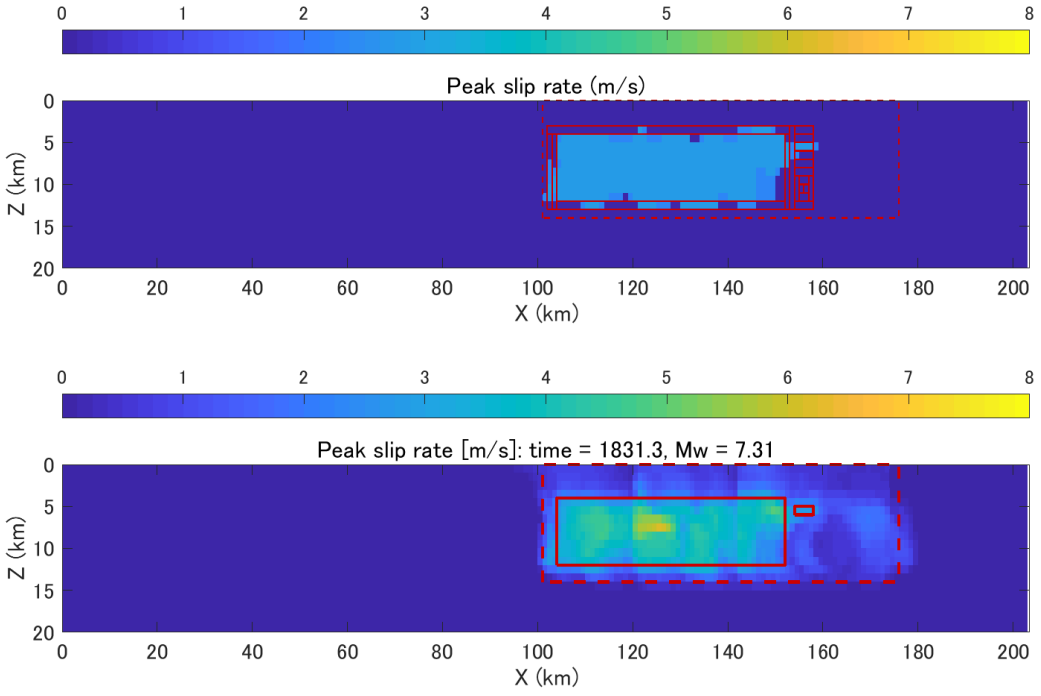

Figure A.3.6-34. Trimming for the slip-rate asperity: procedure (top) and trimming result (bottom) for Event 6, 1831.3 year, *Mw*7.31

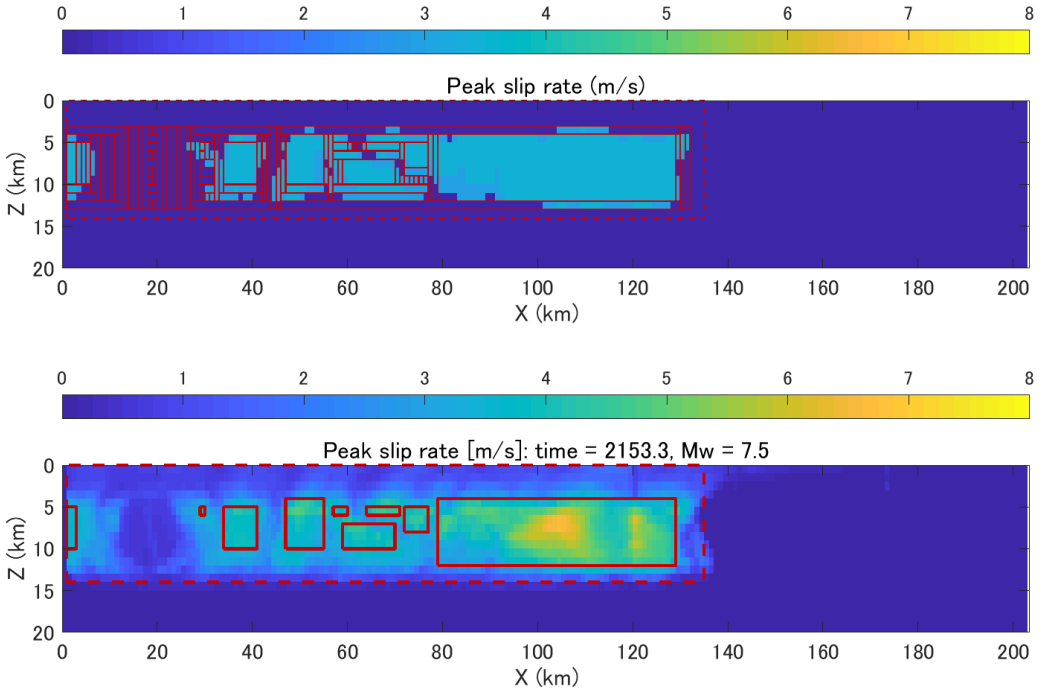

Figure A.3.6-35. Trimming for the slip-rate asperity: procedure (top) and trimming result (bottom) for Event 7, 2153.3 year, *Mw*7.5

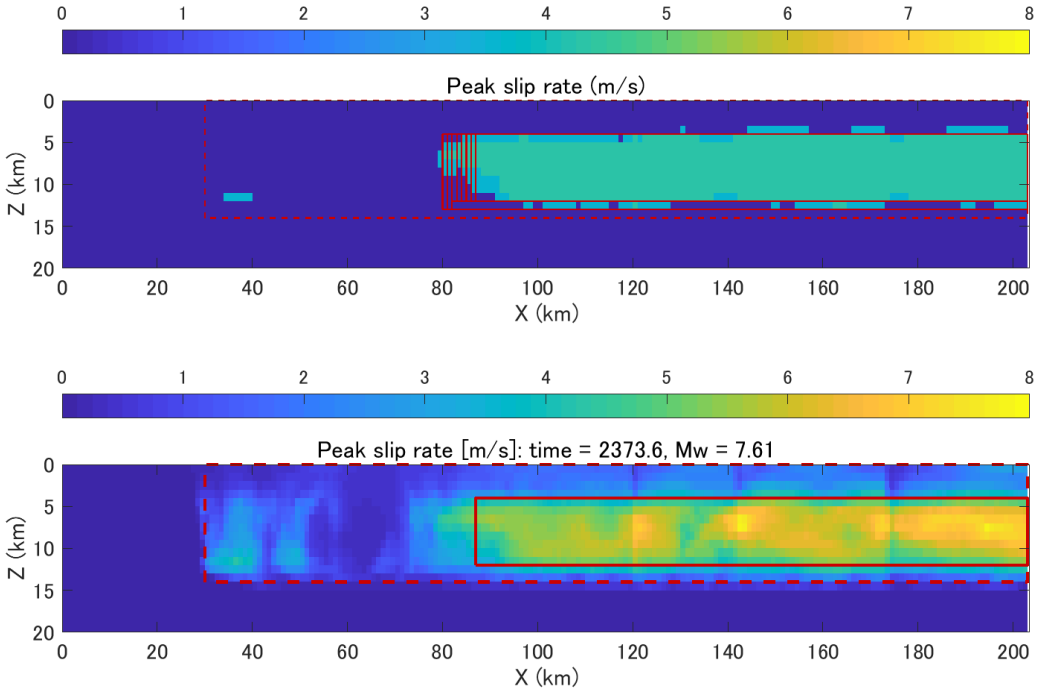

Figure A.3.6-36. Trimming for the slip-rate asperity: procedure (top) and trimming result (bottom) for Event 8, 2373.6 year, *Mw*7.61

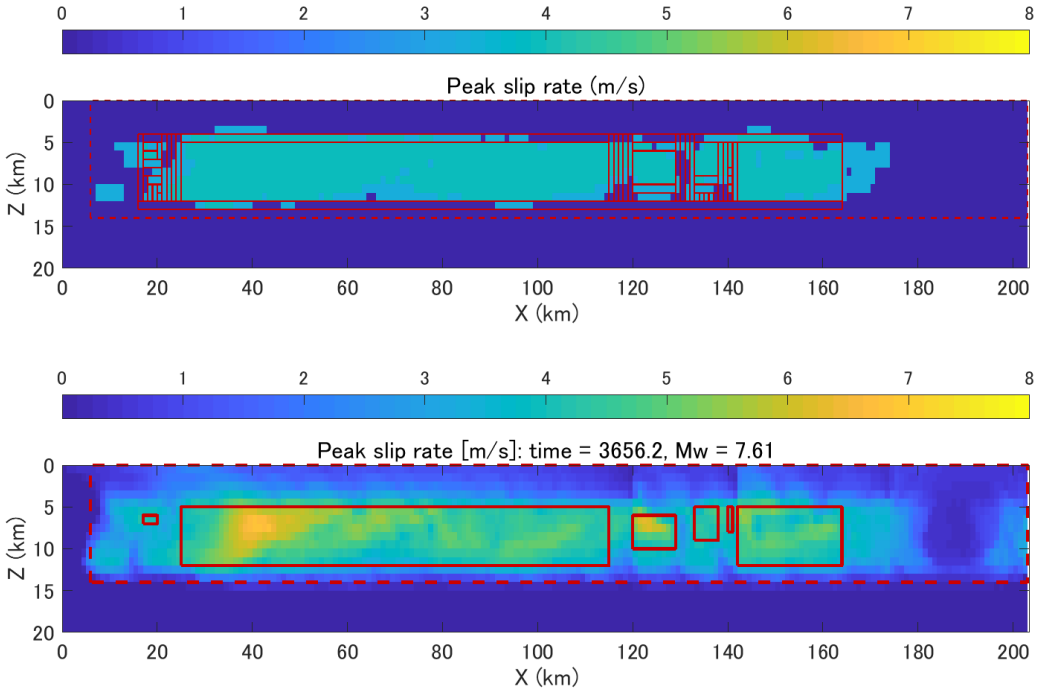

Figure A.3.6-37. Trimming for the slip-rate asperity: procedure (top) and trimming result (bottom) for Event 12, 3656.2 year, *Mw*7.61

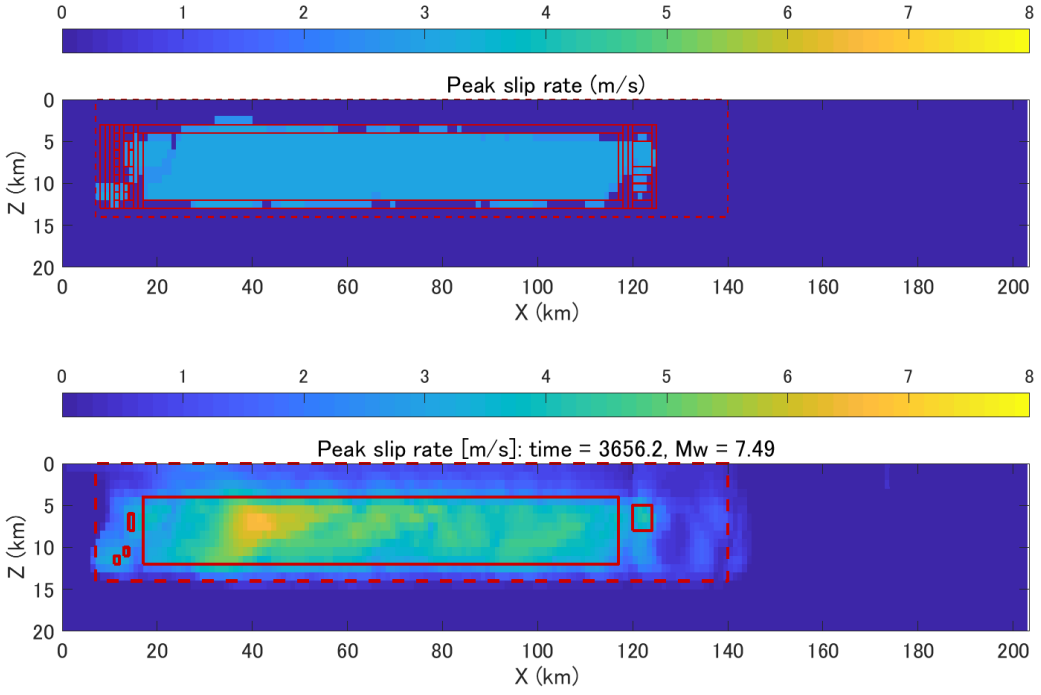

Figure A.3.6-38. Trimming for the slip-rate asperity: procedure (top) and trimming result (bottom) for Event 13, 3656.2 year, *Mw*7.49

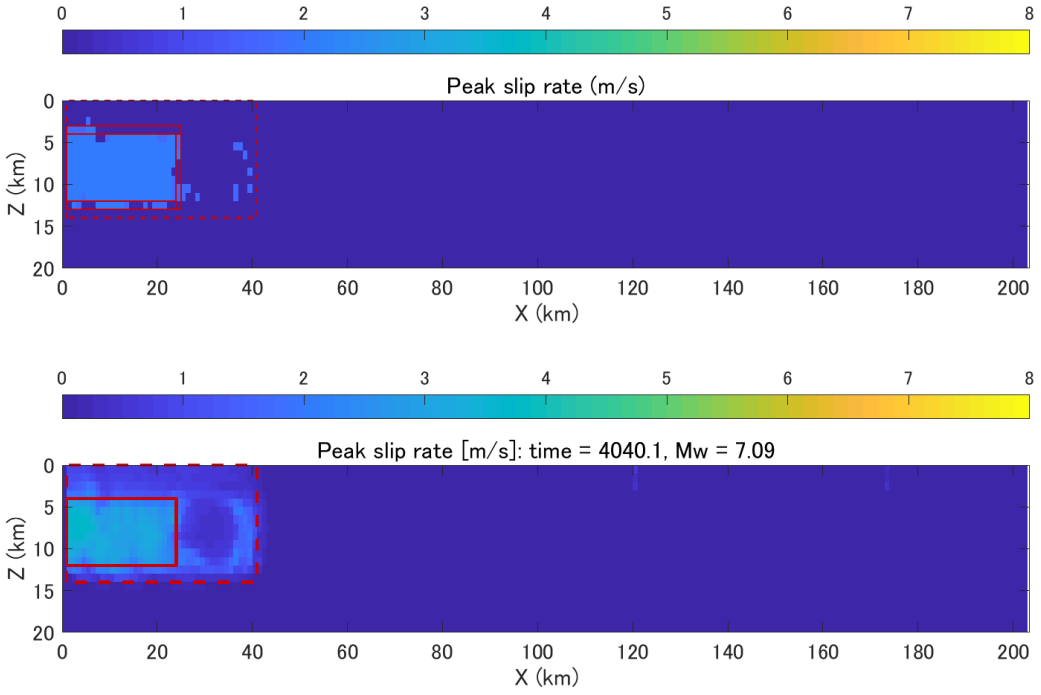

Figure A.3.6-39. Trimming for the slip-rate asperity: procedure (top) and trimming result (bottom) for Event 14, 4040.1 year, *Mw*7.09

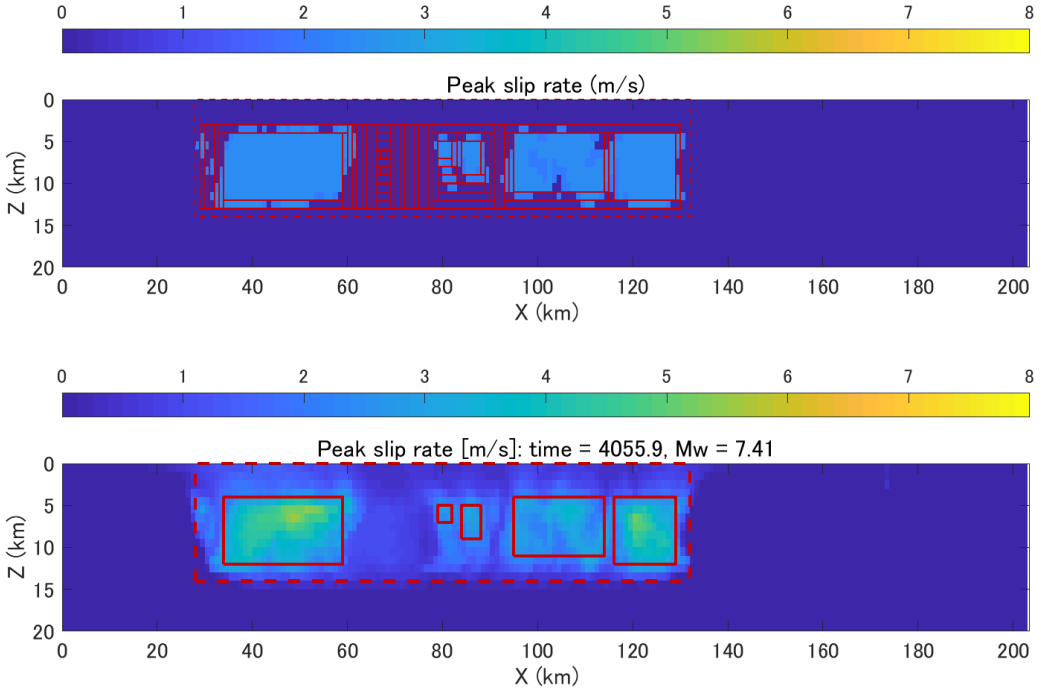

Figure A.3.6-40. Trimming for the slip-rate asperity: procedure (top) and trimming result (bottom) for Event 15, 4055.9 year, *Mw*7.41

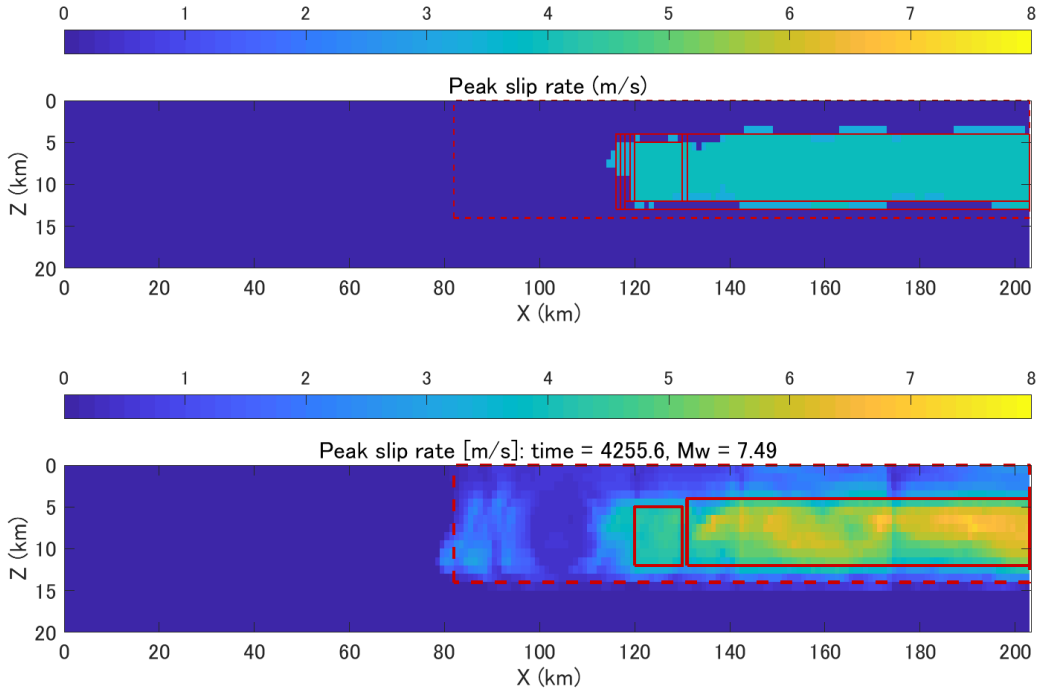

Figure A.3.6-41. Trimming for the slip-rate asperity: procedure (top) and trimming result (bottom) for Event 16, 4255.6 year, *Mw*7.49

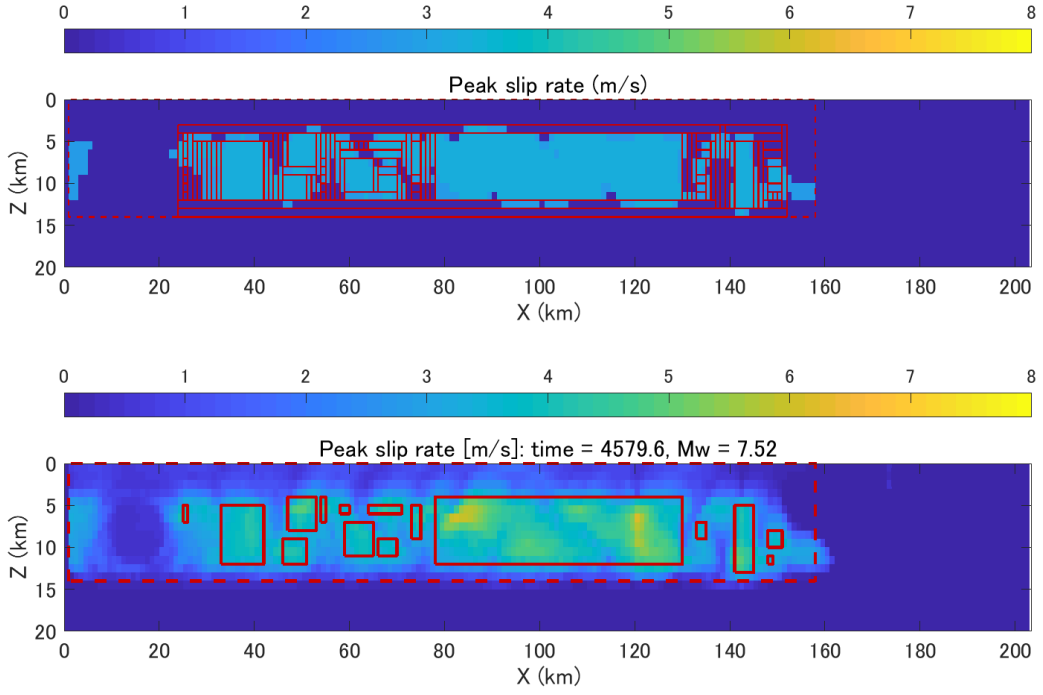

Figure A.3.6-42. Trimming for the slip-rate asperity: procedure (top) and trimming result (bottom) for Event 17, 4579.6 year, *Mw*7.52

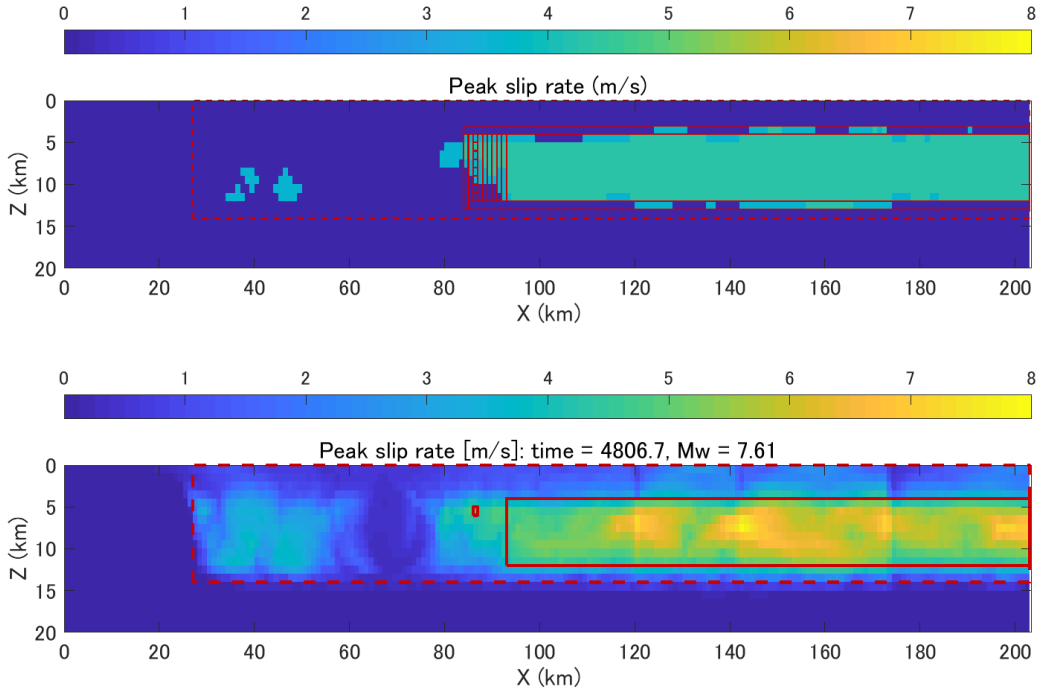

Figure A.3.6-43. Trimming for the slip-rate asperity: procedure (top) and trimming result (bottom) for Event 18, 4806.7 year, *Mw*7.61

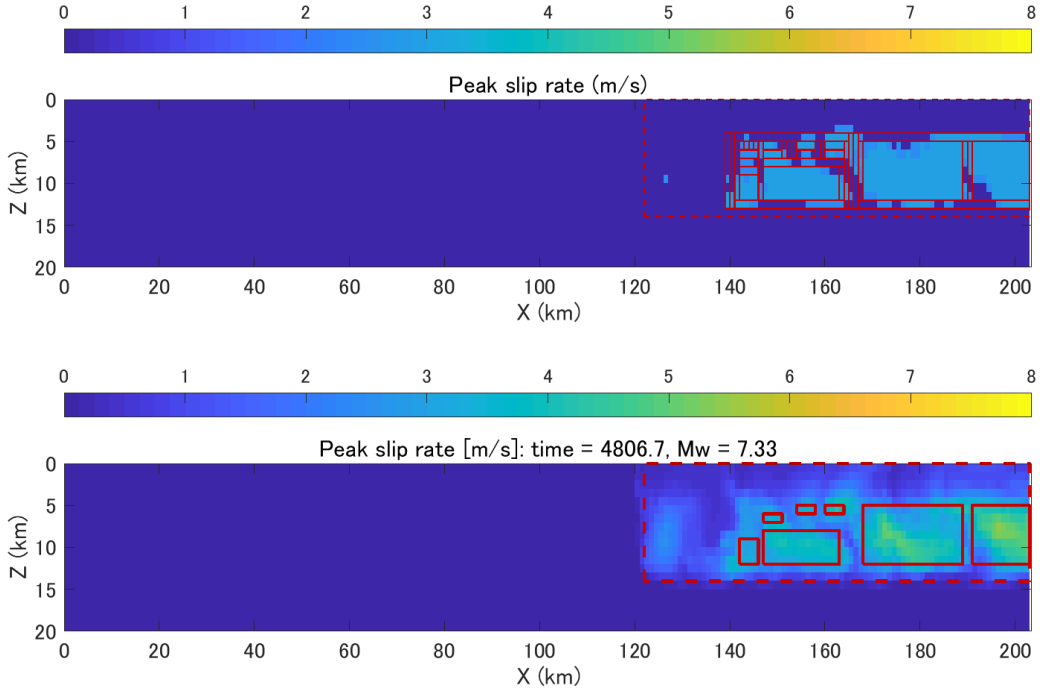

Figure A.3.6-44. Trimming for the slip-rate asperity: procedure (top) and trimming result (bottom) for Event 19, 4806.7 year, *Mw*7.33

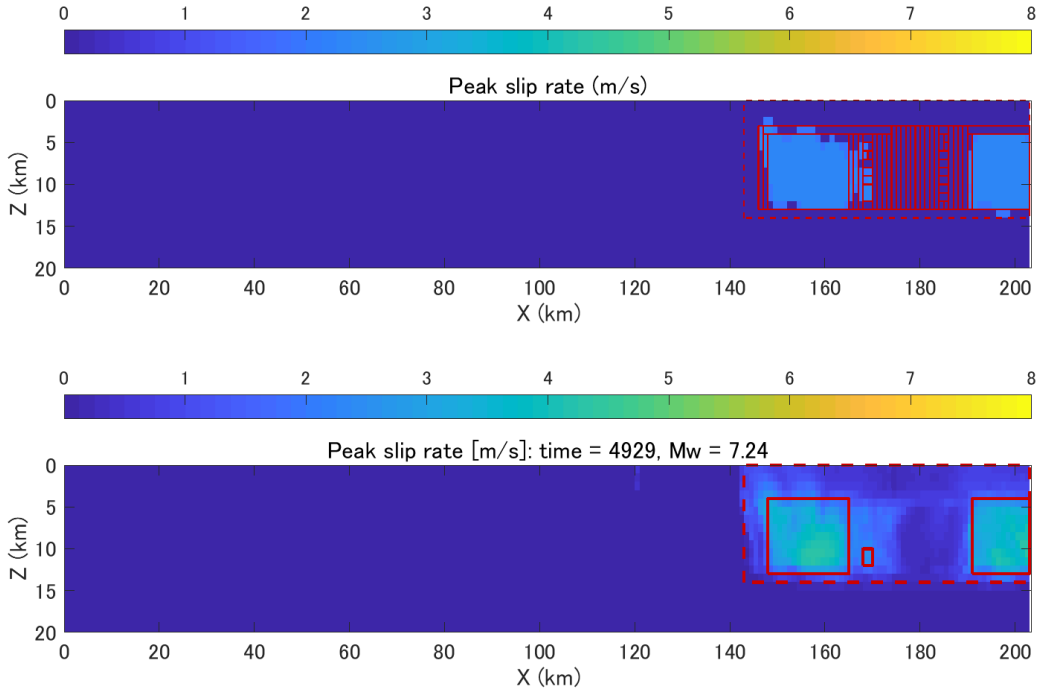

Figure A.3.6-45. Trimming for the slip-rate asperity: procedure (top) and trimming result (bottom) for Event 20, 4929.0 year, *Mw*7.24

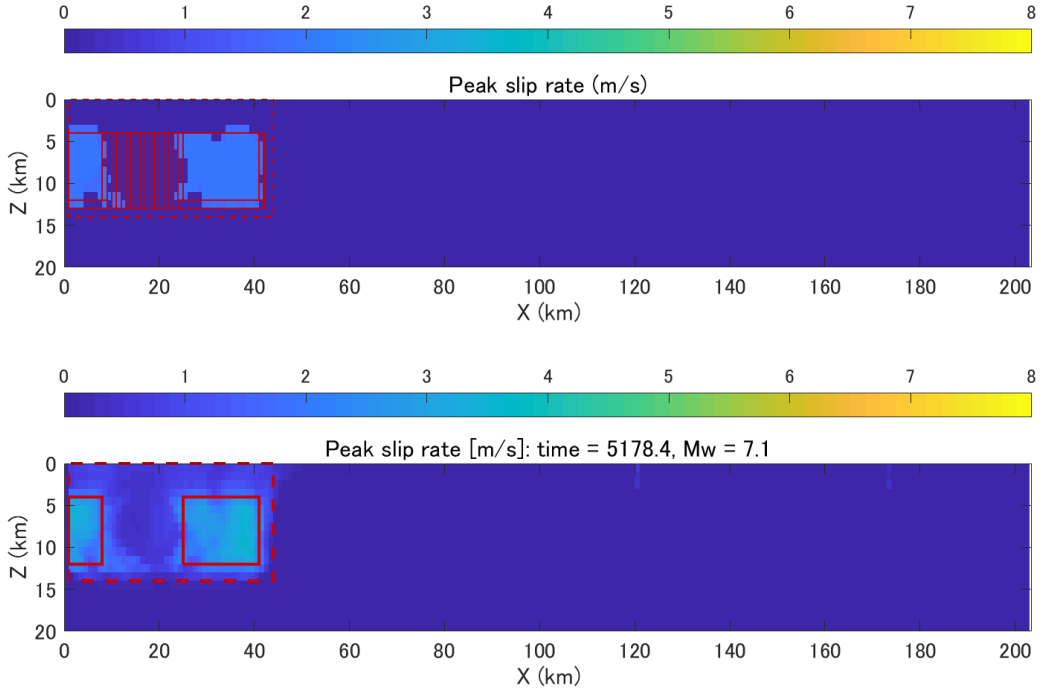

Figure A.3.6-46. Trimming for the slip-rate asperity: procedure (top) and trimming result (bottom) for Event 21, 5178.4 year, *Mw*7.1

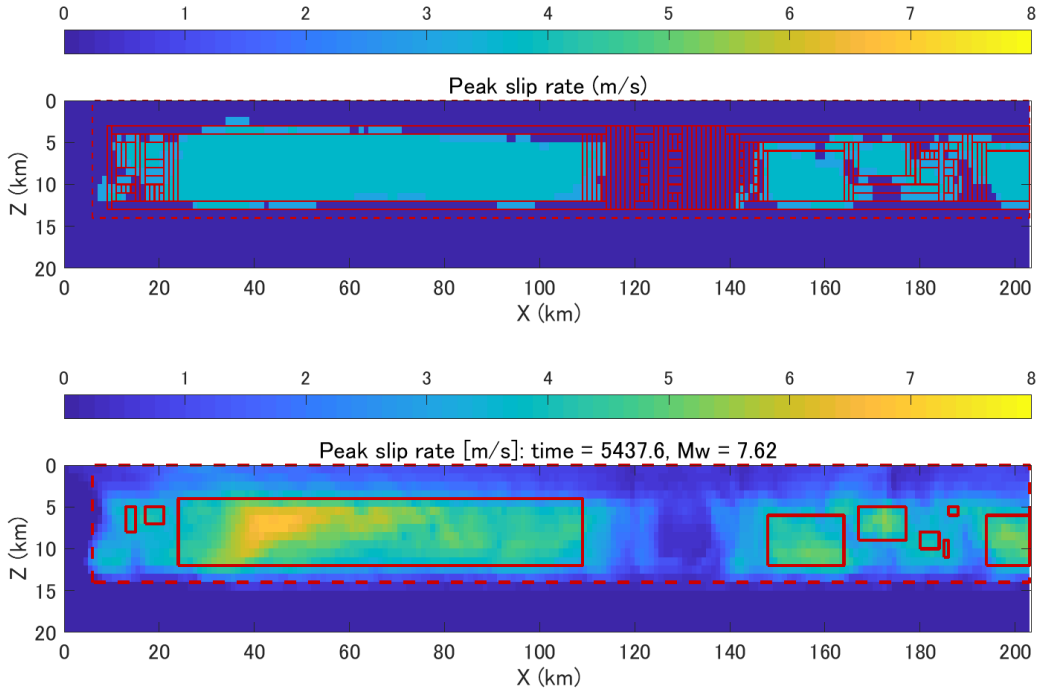

Figure A.3.6-47. Trimming for the slip-rate asperity: procedure (top) and trimming result (bottom) for Event 22, 5437.6 year, *Mw*7.62

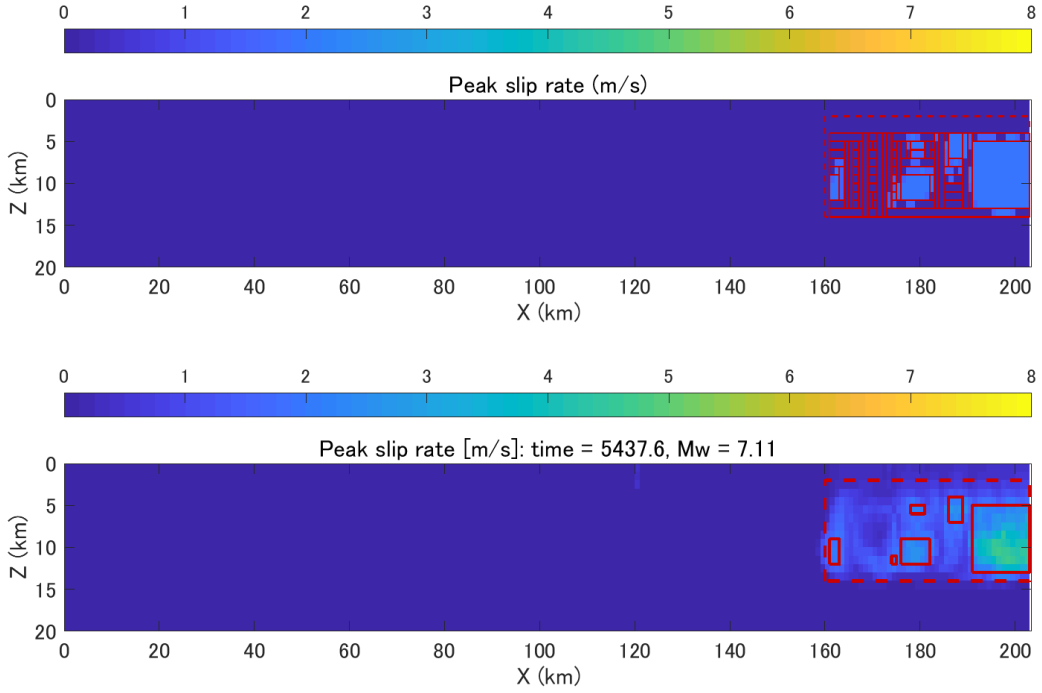

Figure A.3.6-48. Trimming for the slip-rate asperity: procedure (top) and trimming result (bottom) for Event 23, 5437.6 year, *Mw*7.11

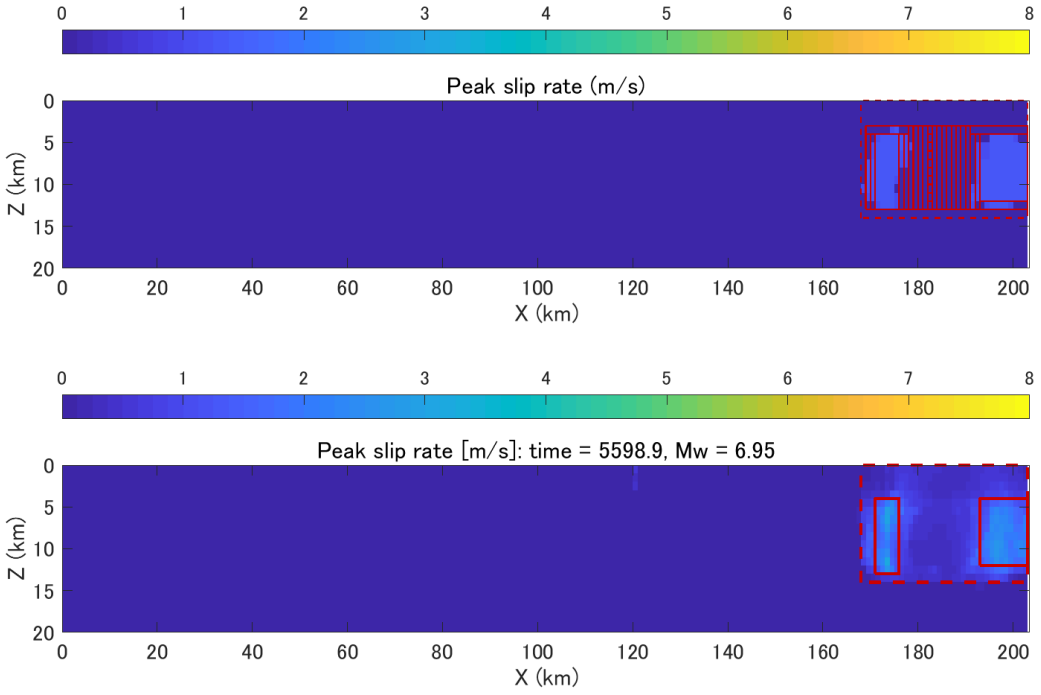

Figure A.3.6-49. Trimming for the slip-rate asperity: procedure (top) and trimming result (bottom) for Event 24, 5598.9 year, *Mw*6.95

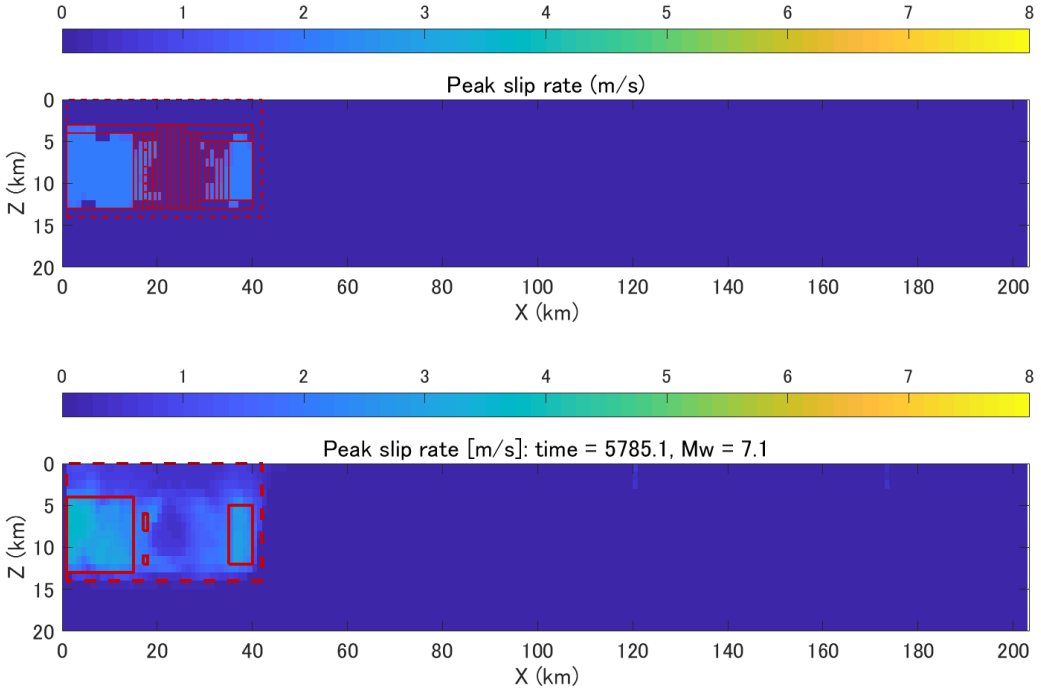

Figure A.3.6-50. Trimming for the slip-rate asperity: procedure (top) and trimming result (bottom) for Event 25, 5785.1 year, *Mw*7.1

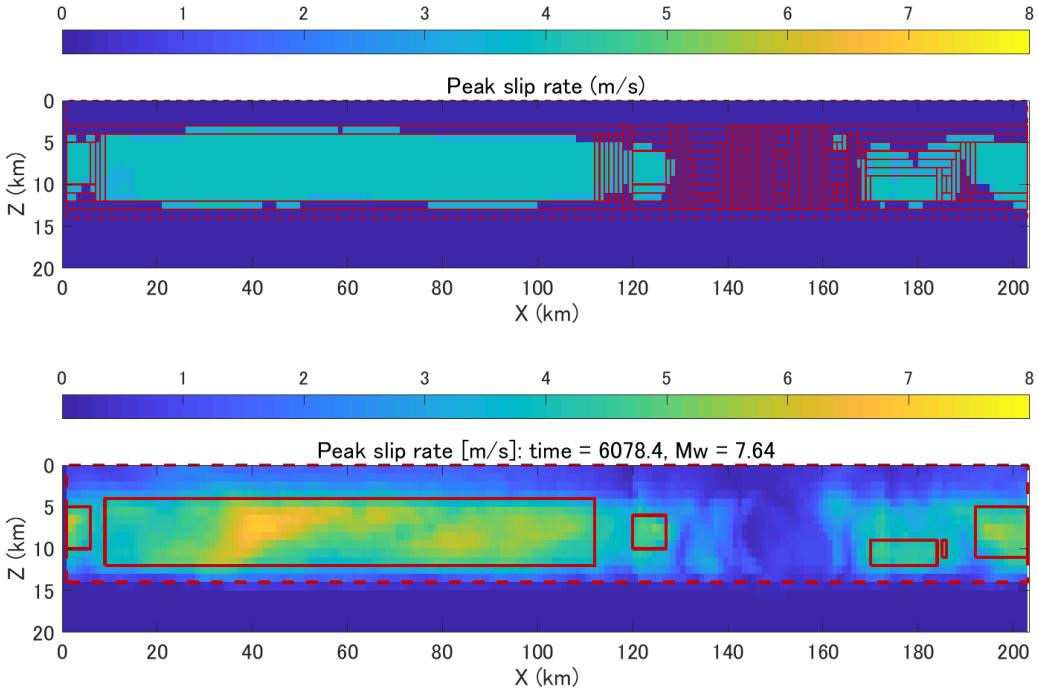

Figure A.3.6-51. Trimming for the slip-rate asperity: procedure (top) and trimming result (bottom) for Event 26, 6078.4 year, *Mw*7.64

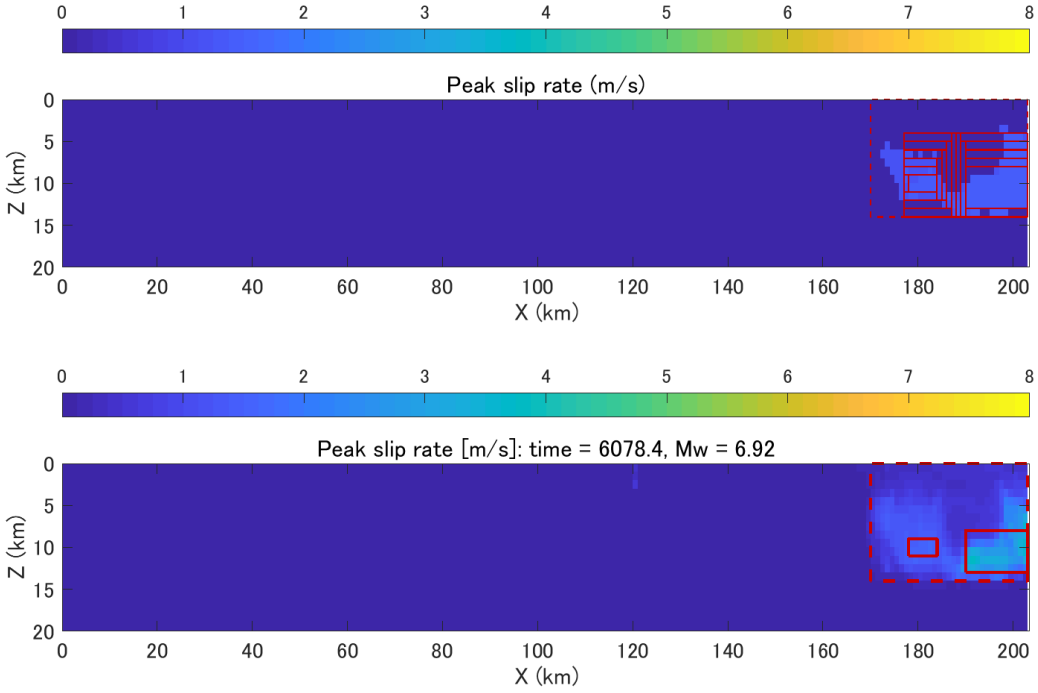

Figure A.3.6-52. Trimming for the slip-rate asperity: procedure (top) and trimming result (bottom) for Event 27, 6078.4 year, *Mw*6.92

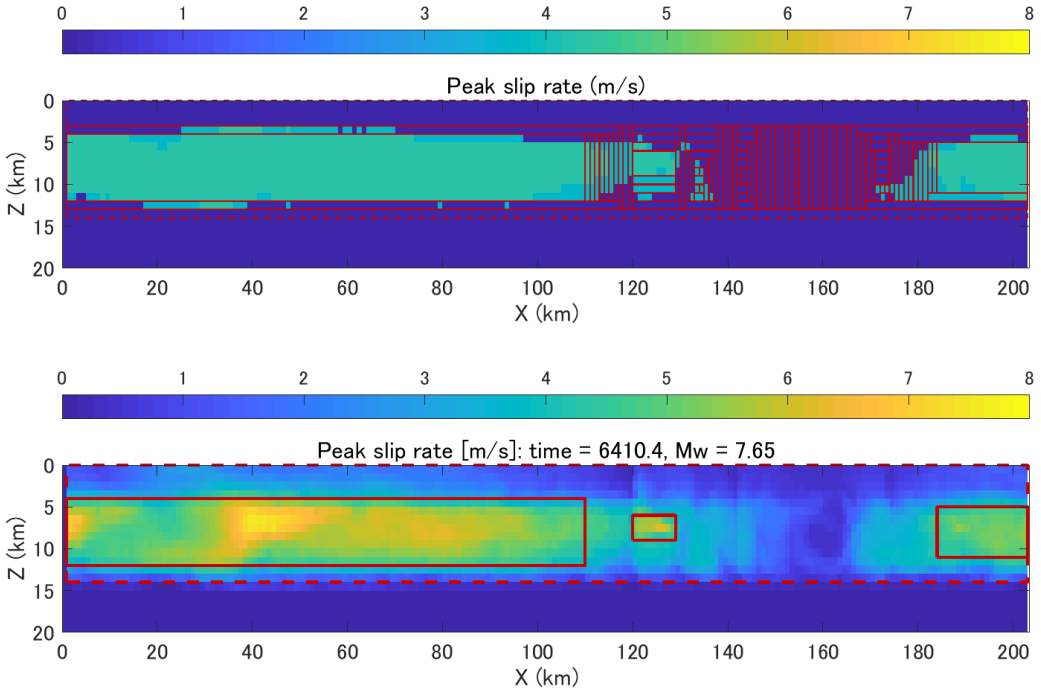

Figure A.3.6-53. Trimming for the slip-rate asperity: procedure (top) and trimming result (bottom) for Event 28, 6410.4 year, *Mw*7.65

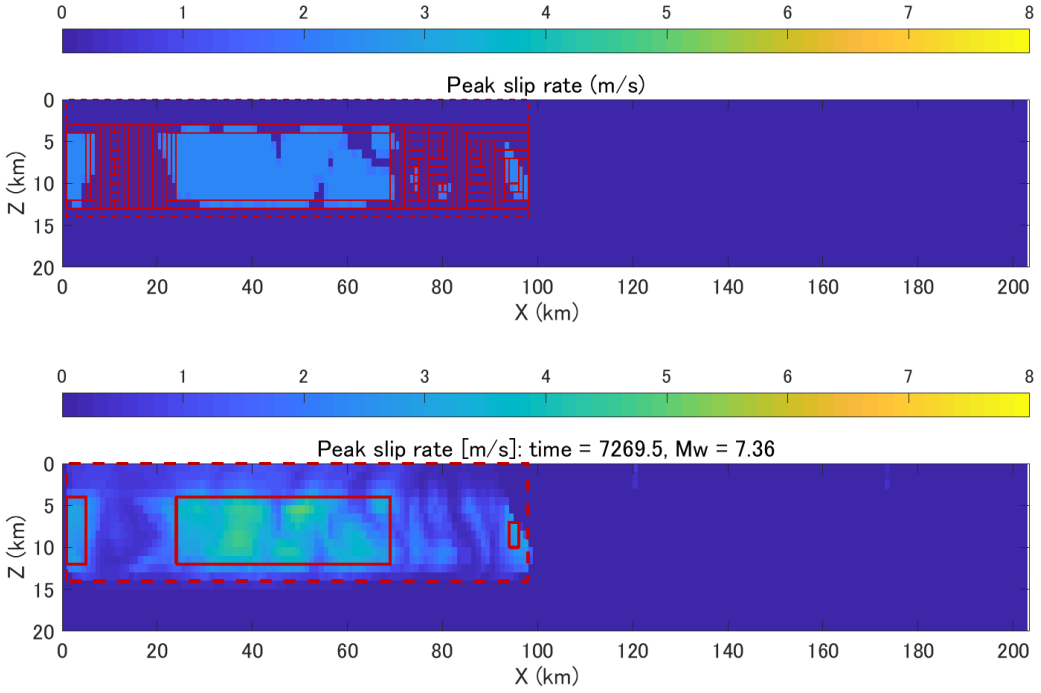

Figure A.3.6-54. Trimming for the slip-rate asperity: procedure (top) and trimming result (bottom) for Event 29, 7269.5 year, *Mw*7.36

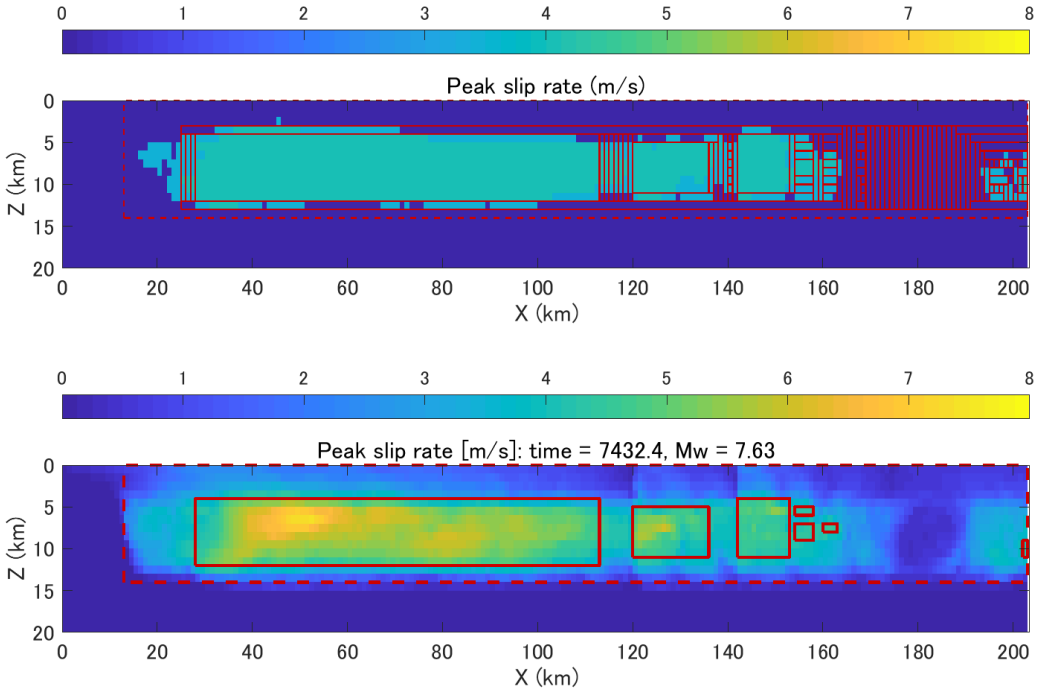

Figure A.3.6-55. Trimming for the slip-rate asperity: procedure (top) and trimming result (bottom) for Event 30, 7432.4 year, *Mw*7.63

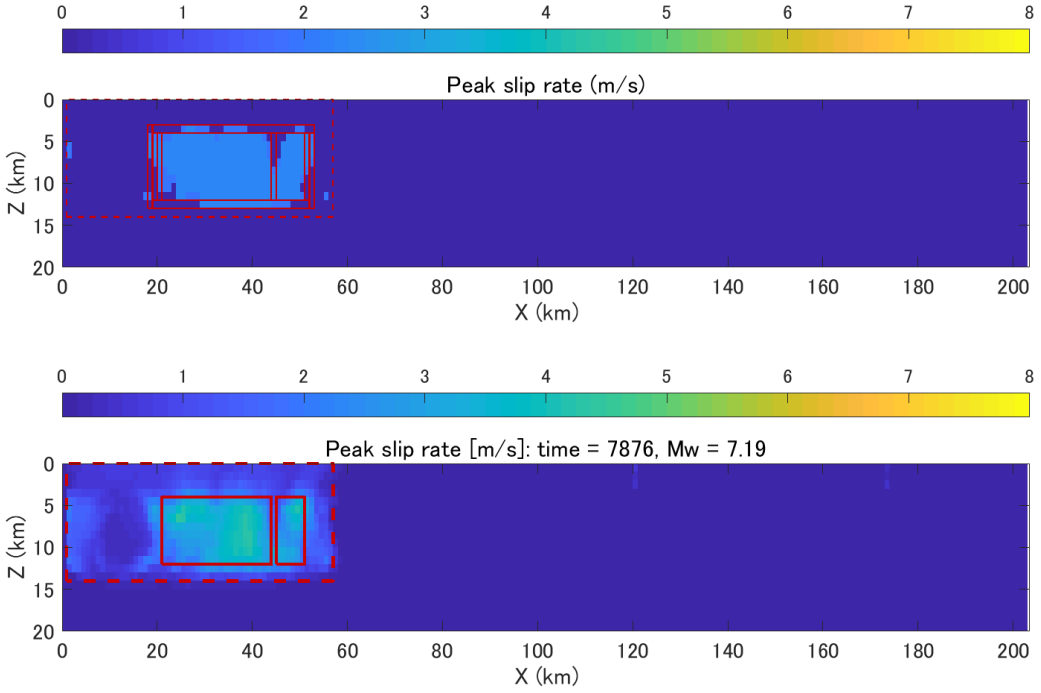

Figure A.3.6-56. Trimming for the slip-rate asperity: procedure (top) and trimming result (bottom) for Event 31, 7876.0 year, *Mw*7.19